

Copyright

by

Korede Fiyinfoluwa Akinpelumi

2021

**The Dissertation Committee for Korede Fiyinfoluwa Akinpelumi Certifies that this
is the approved version of the following Dissertation:**

Amine Aerosol in Aqueous Scrubbing for CO₂ Capture

Committee:

Gary T. Rochelle, Supervisor

Lea Hildebrandt Ruiz

Roger T. Bonnecaze

Hanna Knuutila

Eric Chen

Amine Aerosol in Aqueous Scrubbing for CO₂ Capture

by

Korede Fiyinfoluwa Akinpelumi

Dissertation

Presented to the Faculty of the Graduate School of

The University of Texas at Austin

in Partial Fulfillment

of the Requirements

for the Degree of

Doctor of Philosophy

The University of Texas at Austin

December 2021

Dedication

To my mum, Mrs. Eunice Omokehinde Akinpelumi, and my late father, Dr. Abiodun Ayotunde Akinpelumi.

Acknowledgments

I give God the glory for the completion of this training. My graduate school journey is like the Israelites through the wilderness: promised land, but not without many shortcomings and help.

First, I am very grateful to you, Dr. Rochelle, for your dedication to my professional development. What distinguishes you as an advisor is a fatherly touch you bring to mentorship while not sacrificing the quality of training. You are wise and have a large heart. I really couldn't have wished for a better advisor or a more apt project to have spent the last five years on. Over those years, I have watched and learned as you have led by example and managed the group culture to emphasize quality presentations, critical thinking, and a healthy work-life balance. I appreciate the opportunity you gave me to communicate and manage deliverables with several of our collaborators directly and to gain valuable experience through summer internships. While the skills I have learned under your tutelage will stay with me, the warmth and respect I have received will be passed on to others.

I also appreciate the support I have received from the other members of my dissertation committee: Roger Bonneau, Lea Hildebrandt, Eric Chen, and Hanna Knuutila. I have had the opportunity to interact with you through classes, conferences, departmental activities, or research collaborations and have only become better from such. Your inputs to the quality of my research publications and dissertation are deeply cherished.

My graduate study would not be a success without my interactions with members of the Rochelle group. I was fortunate to have overlapped with two very bright minds who

mentored me and provided a soft landing for my research. First is Matt Beaudry, whose research I inherited. I cannot thank you enough for your help in my first year of grad school. You were a pace-setter who initiated an excellent relationship with our collaborators at the National Carbon Capture Center (NCCC) and laid the groundwork for gas sampling at NCCC and UT-SRP. While your shoes were large to fill, your detailed documentation of procedures provided some cushion. Second is Kent Fischer, whom I traveled with on several road trips to the NCCC in Alabama. I learned a lot watching your commitment to work and positive spirit in the face of the most daunting challenges. To the other senior colleagues I met in the group: Yue Zhang, Ye Yuan, Paul Nelson, and Di Song, thank you for setting an excellent example of a healthy work-life balance. I hope I have been as good a resource to my colleagues as you were to me. To my more recent colleagues: Ching-Ting Liu, Tianyu Gao, Yuying Wu, Athreya Suresh, Miguel Abreu, Ben Drewry, Chih-I Chen, and Ariel Plantz, I thank you for your contributions to my work, and I wish you the best with completing your training. To my undergraduate research assistants: Monica Ogbonnaya and Syed Hassan, thank you for your help with my research. I enjoyed training you both, and I hope you take the learnings with you to your future endeavors. To Maeve Cooney, the administrative assistant for the group, I am thankful for all our conversations through the years. I hope my writing of this dissertation is proof that consistent feedback yields results. I am also glad to see I have matured from running away from your dogs to waving from a distance!

My research involved several field trips to the National Carbon Capture Center (NCCC) at Wilsonville, Alabama, in 2018 and 2019. Tony Wu, Robert Charles Lambrecht, and John Carroll were instrumental in supplying the necessary engineering and analytical support I needed during my time there. I also appreciate the process engineering support I received from Graham Bingham and Laura Uhrig of Southern Company and the analytical

support from Chiranjib Saha of the Southern Research Institute. I also want to thank Daniel Culpepper, Janelle Engel, and other staff at the UT-SRP pilot plant for being very resourceful in troubleshooting the analytical equipment I used for my research. I have learned a lot working close to Frank Seibert, Eric Chen, and Fred Closmann, who have managed operations at the UT-SRP pilot plant over the years.

Summers 2019 and 2020 were very memorable times spent as an intern with Equinor and ExxonMobil, respectively. I especially want to thank Andrea Carolina Machado Miguens, my manager, and Auristela Carolina Vasquez Quintero, my mentor, during my time with the Shale Oil and Gas Research and Technology group at Equinor. I enjoyed working on the low-carbon project, given my passion for the subject, and gained much confidence from the visibility and level of ownership I was accorded. At ExxonMobil, Alden Daniel, my mentor, was exceptional at engaging me and making sure I delivered an impactful project despite the challenges of COVID. I learned a lot from the brilliant minds at the Upstream Research Fractionations and Separations team and always looked forward to my biweekly meetings with Shwetha Ramkumar.

My gratitude goes to the Texas Carbon Management Program, the United States Department of Energy, and the Carbon Capture Simulation for Industry Impact (CCSI²) for funding my research. I am also grateful to have received the Howard A. Halff Graduate Fellowship and the Cindy and Mike Zeglin Endowed Graduate Fellowship in Chemical Engineering.

I could not have completed this program without the support groups that helped keep and restore my spiritual, emotional, and physical wellbeing during my time here: Eternal Glorious Fountain Ministries (EGFM), Brethren in Diaspora (BiD), friends from the UT Austin Nigerian community, and the ChE intramural soccer team.

Most importantly, thank you to my family: Eunice Omokehinde Akinpelumi, Niyi Akinpelumi, and Bonike Akinpelumi, for your overwhelming love and support.

Abstract

Amine Aerosol in Aqueous Scrubbing for CO₂ Capture

Korede Fiyinfoluwa Akinpelumi, Ph.D.

The University of Texas at Austin, 2021

Supervisor: Gary T. Rochelle

Sustained amine emissions above one ppm are prohibitive to amine scrubbing and prevalent with aerosol in the flue gas. The development, demonstration, and quantification of mitigation strategies for amine aerosol will ensure sustainable CO₂ capture operations. This work supports that goal by conducting systematic aerosol tests and developing aerosol models for 2nd and 3rd generation CO₂ capture solvents.

SO₃ generation by catalytic conversion and plasma oxidation of SO₂ were compared and adapted for aerosol tests. The catalytic bed was proven highly effective at pilot scale with the demonstration of 97% conversion and 8 ppm SO₃ injection into 4000 lb/hr flue gas. Plasma oxidation had a much lower conversion but showed great promise due to its relative cost and ease of start-up/shut down.

Amine aerosol can be sustainably mitigated upstream of CO₂ capture or within the absorber and water wash and are reduced at NGCC conditions. The hydrated lime addition rate is the critical indicator for upstream SO₃ reduction and inlet aerosol mitigation in baghouse operations. The threshold for SO₃ slippage is at half the normal lime rate. As inlet flue gas SO₃ increases, amine emissions increase, and the water wash performance decreases. There exists a tradeoff between capital or energy costs and amine aerosol

control. A 98% reduction in PZ aerosol was demonstrated for flue gas with 2 ppm SO₃ by increasing the lean solvent to 58 °C and using a 2-stage water wash. Particulate measurements showed that PZ aerosol grows and gets collected at higher lean solvent temperatures.

The growth of amine aerosol in the absorber is driven by amine-limited diffusion, and the aerosol is in equilibrium with water in the bulk gas phase. More volatile solvents grow bigger drops due to the larger driving force for amine transfer, and the effect of aerosol concentration on drop size is diminished. Therefore, aerosol mitigation with mist eliminators should be feasible for highly volatile solvents. As the volatility of the amine in a solvent system increases, vapor emissions will become more significant than aerosol emissions.

Table of Contents

List of Tables	xviii
List of Figures	xxi
Chapter 1: Introduction	1
1.1 Motivation for CO ₂ Capture by Amine Scrubbing	1
1.2 Relevant Advances in CO ₂ Capture by Amine Scrubbing	1
1.2.1 Piperazine Advanced Stripper (PZAS™)	2
1.2.2 Aqueous Blend (AB) of proprietary amines AM1 and AM2	3
1.2.3 Non-Aqueous Solvent Blend (NAB)	4
1.3 The Challenge of Amine Emissions in Amine Scrubbing	4
1.4 Gaps in Amine Aerosol Research	6
1.5 Research Objectives of this Work	8
1.5.1 Develop and Demonstrate Amine Aerosol Generation and Measurement at Pilot-Scale	8
1.5.2 Demonstrate Amine Aerosol Mitigation at Pilot-Scale	8
1.5.3 Evaluate Amine Emissions at NGCC Conditions	8
1.5.4 Improve PZ Aerosol Model and Develop New Aerosol Models for Solvent Blends	8
Chapter 2: Amine Aerosol Generation and Measurement at Pilot-Scale	10
2.1 Amine Measurement with Fourier Transform Infrared Gas Analyzer (FTIR) ...	10
2.1.1 Principles of Infrared Spectroscopy	10
2.1.2 FTIR Sampling Hardware and Specifications	13
2.1.2.1 FTIR Analyzer	13
2.1.2.2 Heated Sample Filter and Probe	17

2.1.2.3	Heated Sample Pads	18
2.1.2.4	Heated Sample Lines.....	19
2.1.3	FTIR Sampling Setup at NCCC.....	19
2.1.3.1	2018 Coal Campaign.....	20
2.1.3.2	2019 NGCC Campaign	26
2.1.4	Data Analysis	30
2.2	Aerosol Concentration and Size Distribution Measurement	32
2.2.1	Phase Doppler Interferometry (PDI).....	32
2.2.2	Electrical Low-Pressure Impactor (ELPI)	35
2.3	Aerosol Nuclei Generation	38
2.3.1	Catalytic Bed.....	38
2.3.1.1	Design.....	38
2.3.1.2	Experimental Setup	40
2.3.1.3	Bench-scale Results.....	42
2.3.1.4	Pilot-scale Results	47
2.3.2	Plasma Generator	49
2.3.2.1	Design.....	49
2.3.2.2	Reaction Mechanism	54
2.3.2.3	Experimental Setup	55
2.3.2.4	Results	57
2.3.2.5	Challenges and Recommendations for Future Work	58
2.4	Recommendations for Gas and Aerosol Sampling at UK CAER.....	61
2.4.1	Baseline Particulate Measurements at Wyoming ITC	61

2.4.2	Gas and Aerosol Sampling Setup for UK CAER	61
2.4.3	Sampling Port Requirements	64
2.4.3.1	FTIR Sample Ports	64
2.4.3.2	PDI Sample Ports	65
2.4.3.3	Space requirements	66
Chapter 3: PZ Aerosol Emissions and Mitigation at Pilot Scale		68
3.1	Introduction.....	68
3.2	Pilot Plant Overview	71
3.3	Methods	73
3.3.1	Gas Concentration Measurements	73
3.3.2	Aerosol Concentration and Size Distribution Measurement	76
3.4	PZ Aerosol Mitigation with Baghouse	76
3.5	SO ₃ Generation for Aerosol Tests	79
3.5.1	Calibration and SO ₂ –SO ₃ Conversion Results.....	80
3.5.2	SO ₃ Injection Runs.....	82
3.6	Effect of Inlet SO ₃ on PZ Emission.....	84
3.7	PZ Aerosol Mitigation in Absorber and Water Wash.....	86
3.7.1	Lean Solvent Temperature	87
3.7.2	Solvent Intercooling.....	88
3.7.3	Wash Wash	89
3.8	Effect of Aerosol Mitigation Strategy on CO ₂ Capture.....	92
3.9	Effect of Mitigation Strategies on PZ Aerosol Count and Size Distribution	95
3.10	Mechanisms of Aerosol Mitigation	99

3.11	Conclusions.....	100
Chapter 4: PZ Emissions from CO ₂ Capture at NGCC Conditions.....		102
4.1	Introduction.....	102
4.2	Pilot Plant Overview	104
4.3	Methods	105
4.4	Results and Discussions.....	108
4.4.1	Emission Trends from 2018 Coal and 2019 NGCC Campaigns .	108
4.4.2	Emissions from NGCC Steady-State Operations	110
4.4.3	Wash Tower Performance.....	116
4.5	Conclusions.....	117
Chapter 5: Modeling Aerosol Growth for Piperazine.....		118
5.1	Introduction.....	118
5.2	Modeling Approach	120
5.2.1	Absorber and Water Wash Profiles.....	120
5.2.2	Aerosol Size Calculations	121
5.3	Base Case	122
5.4	Effect of Long-Term Design Conditions on PZ Aerosol.....	124
5.4.1	Absorber Operating Conditions	125
5.4.2	Absorber Packing Volume	129
5.4.3	Absorber Packing Type.....	132
5.4.4	Water Wash Operating Conditions	135
5.5	Effect of Parametric Changes in Absorber Operating Conditions on PZ Aerosol.....	136
5.5.1	Lean Solvent Temperature	136

5.5.2	Intercooling Temperature.....	139
5.6	Effect of Input Models on PZ Aerosol.....	141
5.6.1	Equilibrium Model.....	141
5.6.2	Flow Model.....	146
5.6.3	Heat and Mass Transfer Models	149
5.6.4	Physical Property Models	153
5.7	Conclusions and Recommendations	155
Chapter 6:	Modeling Aerosol Growth for Solvent Blends	157
6.1	Introduction.....	157
6.2	Modeling Approach	158
6.2.1	Process Modeling with ProTreat [®] and Aspen Plus [®]	159
6.2.2	Column Specifications and Run Conditions	159
6.2.3	Stage-wise Composition and Physical Properties.....	161
6.3	Development of Aerosol Transport Model (ATM) for Solvent Blends	161
6.3.1	gPROMS ProcessBuilder.....	161
6.3.2	Model Equations	162
6.3.3	Model Assumptions	165
6.3.4	Surrogate Equilibrium Model	165
6.3.4.1	Surrogate Equilibrium Model Development for Aqueous Blend (AB).....	166
6.3.4.2	Surrogate Equilibrium Model Development for Non-Aqueous Blend (NAB).....	167
6.4	Results and Discussion	169
6.4.1	Amine Aerosol Growth Profile.....	170

6.4.2	Limiting Mechanisms for Aerosol Growth.....	173
6.4.3	Effect of Water Wash Temperature and Packed Height on Aerosol Growth for the Aqueous Blend (AB).....	181
6.5	Conclusions and Recommendations	184
Chapter 7:	Conclusions and Recommendations	186
7.1	Summary	186
7.2	Conclusions and Recommendations	186
7.2.1	Conclusions from the Demonstration of Amine Aerosol Generation and Measurement at Pilot-Scale.....	186
7.2.2	Conclusions from the Demonstration of Amine Aerosol Mitigation at Pilot-Scale	188
7.2.3	Conclusions from the Evaluation of Amine Emissions at NGCC Conditions.....	190
7.2.4	Conclusions from the Improvement of PZ Aerosol Model and Development of New Aerosol Models for Solvent Blends	191
7.3	Future Directions for Amine Aerosol Research	193
Appendix A:	Codes for PZ Aerosol Transport Model in gPROMS® ModelBuilder.....	194
A.1	Aerosol Integration	194
A.2	Physical Properties Model	201
A.3	Process Flowsheet.....	206
Appendix B:	Codes for Aerosol Transport Model of Solvent Blends in gPROMS® ModelBuilder	207
B.1	Aerosol Integration	207
B.2	Physical Properties Model	215
B.3	Process Flowsheet.....	219

References.....	221
Vita.....	226

List of Tables

Table 2.1:	Functional group wavenumbers	11
Table 2.2:	Analysis regions used for gas components in this work	13
Table 2.3:	FTIR analyzer technical specifications (Gasmel™ CX-4000)	15
Table 2.4:	FTIR filter technical specifications (Atmoseal® FPD-4-7/1-B02).....	16
Table 2.5:	FTIR sample pump technical specifications (Baldor® Super-E®)	16
Table 2.6:	Heated filter and probe specifications (Universal Analyzers Model 277S)	17
Table 2.7:	Heated sample pad specifications (CleanAir® SKU 1233).....	18
Table 2.8:	Heated sample line specifications (Clayborn Labs).....	19
Table 2.9:	Specifications of the Carbolite HST 12/900 furnace	39
Table 2.10:	Properties of the V ₂ O ₅ catalyst used in the catalytic bed (Research Catalysts, Inc.)	39
Table 2.11:	Results of experimental runs with catalytic bed at bench-scale conditions of the UT-SRP lab.....	44
Table 2.12:	Results from Plasma generator test to produce SO ₃ from SO ₂	57
Table 2.13:	Comparison of the Plasma Generator to the Catalytic Bed and the Liquid Vaporizer and Injector (LVI)	59
Table 2.13:	Comparison of the Plasma Generator to the Catalytic Bed and the Liquid Vaporizer and Injector (LVI) (continued).....	60
Table 2.14:	Three sampling locations, six sample ports, and three FTIR analyzers are recommended for UK CAER.....	64
Table 3.1:	Duration and quantity of SO ₃ injection at NCCC coal campaign in 2018....	83
Table 3.2:	Summary of pilot plant absorber performance during the aerosol tests at 2018 coal campaign	94

Table 4.1:	Steady state run summary for NGCC campaign.....	112
Table 4.1:	Steady state run summary for NGCC campaign (continued)	113
Table 4.1:	Steady state run summary for NGCC campaign (continued)	114
Table 4.1:	Steady state run summary for NGCC campaign (continued)	115
Table 4.2:	Average PZ emissions from absorber configurations tested.....	116
Table 5.1:	Base case design with PZ at conditions of the NCCC	123
Table 5.2:	Design conditions varied in the absorber.....	125
Table 5.3:	Design conditions varied in the water wash	125
Table 5.4:	Results of absorber design conditions at constant CO ₂ removal and variable L/G	127
Table 5.4:	Results of absorber design conditions at constant CO ₂ removal and variable L/G (continued).....	128
Table 5.5:	Range of column dimensions evaluated	129
Table 5.6:	Interfacial area and liquid hold-up for Mellapak 252Y	133
Table 5.7:	Range of packing types evaluated.....	133
Table 5.8:	Results of parametric test on lean solvent temperature at constant solvent flow rate simulated in Aspen Plus®	137
Table 5.9:	Results of parametric test on intercooling T at constant solvent flow rate simulated in Aspen Plus®	139
Table 5.10:	Empirical models for CO ₂ , PZ, and water equilibrium partial pressures from experimental data and Aspen Plus®	142
Table 5.11:	Flow models in Aspen Plus®	146
Table 5.12:	Effect of assuming constant values in physical property models on aerosol calculations. Base case conditions are defined in Table 5.1.	154
Table 6.1:	Summary of run conditions for the aqueous blend (AB).....	160

Table 6.2:	Summary of run conditions for the non-aqueous blend (NAB).....	160
Table 6.3:	Regressed equilibrium partial pressures for the aqueous blend (AB) over bulk liquid and aerosol conditions	166
Table 6.4:	Regressed equilibrium partial pressures for the non-aqueous blend (NAB) over aerosol conditions	167
Table 6.5:	Average amine and H ₂ O relative driving force for PZ, aqueous blend (AB), and non-aqueous blend (NAB) solvents in the absorber at 1–10 ⁸ particles/cm ³	176

List of Figures

Figure 1.1: Process flow diagram for PZAS™ as operated at the National Carbon Capture Center (NCCC) during 2018 coal and 2019 NGCC campaigns (Rochelle et al., 2021).....	3
Figure 2.1: Sample spectrum showing absorption bands	13
Figure 2.2: Detailed drawing for Model 277S heated probe showing conduit ports and internal wiring	18
Figure 2.3: Simplified absorber PFD showing the gas sampling system for the 2018 coal campaign at NCCC.....	20
Figure 2.4: Sampling probe, pad, and line installations at the absorber inlet and mid bed locations during the 2018 coal campaign.....	22
Figure 2.5: Gasmeter™ DX-4000 FTIR sampling setup for the absorber inlet and mid bed locations during 2018 coal campaign.....	23
Figure 2.6: Sampling probe, pad, and line installations at the water wash and absorber gas outlets during the 2018 coal campaign	24
Figure 2.7: Gasmeter™ CX-4000 FTIR sampling setup for the absorber and water wash gas outlets during the 2018 coal campaign.....	24
Figure 2.8: Manual stream switching box with valves to direct flow from either absorber gas, water wash gas, or N ₂ into the FTIR analyzer during the 2018 coal campaign	25
Figure 2.9: Custom electrical box with PID controllers to maintain sample line, pad, and probe temperatures at 180 °C (356 °F).....	26
Figure 2.10: Simplified absorber PFD showing the gas sampling system for the 2019 NGCC campaign at the NCCC	27

Figure 2.11: Gasetm™ CX-4000 FTIR sampling setup for the water wash gas outlet during the 2019 NGCC campaign.....	28
Figure 2.12: Gasetm™ DX-4000 FTIR sampling setup for the absorber gas outlet during the 2019 NGCC campaign.....	29
Figure 2.13: Separate stream switching boxes with valves to direct gas flow from the absorber and water wash to the 2 FTIR analyzers used in the 2019 NGCC campaign.....	30
Figure 2.14: Calcmnet display screenshot during 2018 coal campaign	31
Figure 2.15: Results showing gas compositions measured by the FTIR at the water wash gas outlet. Step changes in PZ were in response to step changes in inlet flue gas SO ₃ . Results were extracted on June 28, 2018, during the coal campaign at NCCC.....	32
Figure 2.16: Sampling setup showing PDI analyzer strapped firmly to a bench to reduce vibrational impact.....	34
Figure 2.17: PDI extractive sampling setup at the water wash gas outlet during the 2018 coal campaign.	34
Figure 2.18: Oscilloscope display showing no detectable particles flowing through the PDI test cell.....	35
Figure 2.19: Schematic of the isokinetic sample extraction system for ELPI measurements.....	36
Figure 2.20: ELPI sampling setup by SRI at the NCCC showing sample port, probe, and cascade impactors.....	37
Figure 2.21: ELPI setup and display at the NCCC during the 2018 coal campaign. SRI managed the setup and operation of the ELPI.....	37

Figure 2.22: Schematic of the catalytic bed design for SO ₃ production (Beaudry, 2018)	39
Figure 2.23: Bench-scale experimental setup for SO ₃ generation with the catalytic bed at the UT-SRP lab	40
Figure 2.24: Experimental setup for SO ₃ generation with the catalytic bed during the 2018 coal campaign at NCCC.....	41
Figure 2.25: MFC calibration for SO ₂ flow at the UT-SRP bench scale.	43
Figure 2.26: SO ₂ –SO ₃ conversion with the tube furnace at bench-scale conditions of the UT-SRP lab.....	45
Figure 2.27: Plot showing time taken to saturate the catalyst bed. No significant SO ₂ was recorded until flow was increased from 13 mL/min to 300 mL/min.....	46
Figure 2.28: Calibration curve for SO ₃ production from SO ₂ with the tube furnace at bench-scale conditions of the UT-SRP lab.....	47
Figure 2.29: Calibration curve for SO ₃ production from SO ₂ with the tube furnace during the 2018 coal campaign at NCCC.....	48
Figure 2.30: SO ₂ –SO ₃ conversion with the tube furnace during the 2018 coal campaign at NCCC. 97% average conversion was obtained.....	49
Figure 2.31: Custom-made plasma generator showing the materials, electrodes, and gas flow path	51
Figure 2.32: Front and side projections of the plasma generator showing the dimensions	52
Figure 2.33: Mechanical drawing for the Teflon bushing at the top of the plasma generator	53
Figure 2.34: Mechanical drawing for the Teflon bushing at the bottom of the plasma generator	54

Figure 2.35: Picture of fabricated plasma generator showing tubular glass reactor and power supply	56
Figure 2.36: Picture of the plasma generator inside a fume hood at the UT-SRP lab.....	56
Figure 2.37: SO ₂ –SO ₃ conversion with the plasma generation. 10% average conversion was obtained.....	58
Figure 2.38: Process flow diagram of UK CAER CO ₂ capture pilot plant with recommended gas and aerosol sampling.....	63
Figure 2.39: FTIR sample port requirements. 3” full port ball valves are required for Port A at the absorber gas inlet, Port B at the absorber gas outlet, and Port D at the water wash gas outlet.....	65
Figure 2.40: PDI sample port requirements. 1” full port ball valves are required for ports E and F at the water wash gas outlet.....	66
Figure 3.1: Flue gas treatment steps at NCCC Gaston Unit 5.....	72
Figure 3.2: Simplified absorber PFD and gas sampling system for the 2018 coal campaign	73
Figure 3.3: Sampling probe, pad, and line installations at the absorber and water wash gas outlets during the 2018 coal campaign.....	74
Figure 3.4: Gasmeter™ CX-4000 FTIR sampling setup for the absorber and water wash gas outlets during the 2018 coal campaign.....	75
Figure 3.5: Daily average PZ emission from water wash (primary vertical axis) and hydrated lime rates upstream of the baghouse (secondary vertical axis) during the campaign. Aerosol tests with SO ₃ injection are excluded.	78
Figure 3.6: Correlation between rates of hydrated lime injection upstream of the baghouse, lean T, and PZ emissions during steady-state operations of the 2018 coal campaign. Aerosol tests with SO ₃ injection are excluded.....	79

Figure 3.7: Calibration curve for SO ₃ production from SO ₂ with the tube furnace	81
Figure 3.8: SO ₂ -SO ₃ conversion with the tube furnace. 97% average conversion.....	82
Figure 3.9: Effect of SO ₃ on PZ emission in absorber and water wash gas outlets. Results were collected at steady-state conditions of 90% CO ₂ capture, 43 °C lean solvent, 33 °C intercooling, 4000 lbs/hr gas, 13,000 lbs/hr solvent, 0.22 mol CO ₂ /mol alkalinity, and single water wash.	85
Figure 3.10: Water wash efficiency as a function of flue gas SO ₃ concentration. Absorber and water wash operating conditions were held constant for all runs.....	86
Figure 3.11: Effect of lean solvent temperature on PZ emission exiting the absorber at varying flue gas SO ₃ . Results collected at steady-state conditions of 90% CO ₂ capture, 33 °C intercooling, 4000 lbs/hr gas, 13,000 lbs/hr solvent, and 0.22 mol CO ₂ /mol alkalinity.....	88
Figure 3.12: Effect of absorber intercooling on PZ emission exiting the water wash. Results were collected at steady-state conditions of 44 °C lean T, 33 °C intercooling, 4000 lbs/hr gas, 13,000 lbs/hr solvent, 0.22 mol CO ₂ /mol alkalinity, and single water wash.	89
Figure 3.13: Effect of water wash on PZ emission at 43 °C lean solvent and varying flue gas SO ₃ . Results were collected at steady-state conditions of 90% CO ₂ capture, 43 °C lean T, 33 °C intercooling, 4000 lbs/hr gas, 13,000 lbs/hr solvent, and 0.22 mol CO ₂ /mol alkalinity.....	91
Figure 3.14: Effect of water wash on PZ emission at 58 °C lean solvent and varying flue gas SO ₃ . Results were collected at steady-state conditions of 90% CO ₂ capture, 58 °C lean T, 33 °C intercooling, 4000 lbs/hr gas, 13,000 lbs/hr solvent, and 0.22 mol CO ₂ /mol alkalinity.....	92

Figure 3.15: Effect of absorber temperature on CO ₂ removal and wash tower circulation flow	93
Figure 3.16: Effect of SO ₃ injection on aerosol number concentration at wash tower outlet for cold (Lean T of 43 °C) absorber case. Results were collected at steady-state conditions of 43 °C lean T, 33 °C intercooling, 4000 lbs/hr gas, 13,000 lbs/hr solvent, 0.22 mol CO ₂ /mol alkalinity, and single water wash.	96
Figure 3.17: Effect of SO ₃ injection on aerosol number concentration at wash tower outlet for hot (Lean T of 54 °C) absorber case. Results were collected at steady-state conditions of 54 °C lean T, 33 °C intercooling, 4000 lbs/hr gas, 13,000 lbs/hr solvent, 0.22 mol CO ₂ /mol alkalinity, and single water wash.	97
Figure 3.18: Larger particles dominate the aerosol profile at elevated lean temperatures (a) 2 ppm SO ₃ in flue gas and (b) 4 ppm SO ₃ in flue gas.....	98
Figure 3.19: Effect of Lean solvent temperature on total aerosol number count at wash tower outlet for varying SO ₃	99
Figure 4.1: Simplified absorber PFD and gas sampling system for the 2019 NGCC campaign	105
Figure 4.2: Experimental sampling set up for gas measurements at the absorber outlet with a Gaset DX-4000 FTIR analyzer.	106
Figure 4.3: Experimental sampling set up for gas measurements at the water wash outlet with a Gaset CX-4000 FTIR analyzer fitted in rackmount support.....	107
Figure 4.4: Emission trends from 2018 coal and 2019 NGCC campaigns. Each data point represents the average daily PZ exiting the water wash.	108

Figure 4.5: Effect of lime rate on emissions during coal and NGCC campaigns. Lime rate is normalized to maximum injection during both campaigns. All data points represent daily averages.	109
Figure 4.6: PZ emission from the absorber and wash tower gas outlets for steady- state operations during the NGCC campaign.....	111
Figure 4.7: Effect of bypassing DCC on PZ emission during NGCC campaign. Lean solvent T was set to 40 °C and remained unchanged throughout the campaign. PZ data point represents hourly steady-state averages of PZ in absorber gas outlet.	111
Figure 4.8: Evaluation of wash tower performance during NGCC campaign with DCC bypassed. Each data point represents steady-state averages (runs 41–70) of PZ in the absorber gas outlet.	117
Figure 5.1: Absorber and water wash configuration at base case conditions.....	124
Figure 5.2: Effect of different absorber design conditions on PZ aerosol leaving the absorber.....	126
Figure 5.3: Effect of absorber column height on PZ aerosol growth.....	130
Figure 5.4: Effect of absorber column diameter on PZ aerosol growth.....	131
Figure 5.5: Effect of changes in packing volume at constant inlet gas flow on residence time	131
Figure 5.6: Effect of absorber column diameter on drop velocity	132
Figure 5.7: Effect of liquid hold-up in absorber on PZ aerosol growth.....	134
Figure 5.8: Effect of interfacial area in absorber on PZ aerosol growth.....	135
Figure 5.9: Effect of absorber packing type on PZ aerosol growth.....	135
Figure 5.10: Effect of changes in water wash operating conditions on PZ aerosol leaving the water wash.....	136

Figure 5.11: Effect of lean solvent temperature on PZ aerosol in the absorber. Constant: 40 °C IC, 0.24 lldg, 5 m PZ, and solvent flow rate. Varied: lean solvent (40–60 °C).....	137
Figure 5.12: Gas temperature profile in absorber at different lean solvent temperatures. Constant: 40 °C IC, 0.24 lldg, 5 m PZ, and solvent flow rate. Varied: lean solvent (40–60 °C).....	138
Figure 5.13: Driving force for PZ transfer from gas to aerosol in absorber at different lean solvent temperatures. Constant: 40 °C IC, 0.24 lldg, 5 m PZ, and solvent flow rate. Varied: lean solvent (40–60 °C).....	138
Figure 5.14: Effect of intercooling temperature on PZ aerosol in the absorber. Constant: 40 °C lean solvent, 0.24 lldg, 5 m PZ, and solvent flow rate. Varied: intercooler (35–45 °C).....	140
Figure 5.15: Gas temperature profile in absorber at different intercooling temperatures with base case conditions. Constant: 40 °C lean solvent, 0.24 lldg, 5 m PZ, and solvent flow rate. Varied: intercooler (35–45 °C).	140
Figure 5.16: Driving force for PZ transfer from gas to aerosol in absorber at different intercooling temperatures with base case conditions. Constant: 40 °C lean solvent, 0.24 lldg, 5 m PZ, and solvent flow rate. Varied: intercooler (35–45 °C).....	141
Figure 5.17: Drop growth comparison between equilibrium models from Aspen Plus® (solid lines) and empirical correlations (dashed lines) at base case conditions defined in Table 5.1.....	143
Figure 5.18: CO ₂ solubility comparison between Aspen Plus® regressed model (solid lines) and empirical correlation by Xu (2011) (dashed lines).....	144

Figure 5.19: PZ volatility comparison between Aspen Plus [®] regressed model (solid lines) and empirical correlation by Xu (2011) (dashed lines).....	145
Figure 5.20: Water vapor pressure comparison between Aspen Plus [®] regressed model (solid lines) and empirical correlation by DIPPR (1998) (dashed lines)....	146
Figure 5.21: Gas temperature profile in the absorber at different flow models	147
Figure 5.22: Liquid temperature profile in the absorber at different flow models.....	148
Figure 5.23: Temperature difference between gas and drop in the absorber at different flow models.....	148
Figure 5.24: Effect of flow models in Aspen Plus [®] on PZ aerosol growth.....	149
Figure 5.25: Gas temperature profile in the absorber for different Chilton-Colburn weighting parameter values	150
Figure 5.26: Liquid temperature profile in the absorber for different Chilton-Colburn weighting parameter values	151
Figure 5.27: Difference between gas and drop temperatures in the absorber for different Chilton-Colburn weighting parameter values	152
Figure 5.28: Effect of Chilton-Colburn weighting parameter in Aspen Plus [®] on PZ aerosol growth.....	153
Figure 6.1: Process flow diagram for the aqueous blend (AB). Process conditions: Run 1 “blue”, Run 2, “red”.....	159
Figure 6.2: Process flow diagram for the non-aqueous blend (NAB).....	160
Figure 6.3: Solvent volatility regressed in this work compared to PZ (Xu, 2011) and MEA (Xu, 2011) at bulk liquid conditions. Aqueous blend (AM1 and AM2). Non-aqueous blend (Amine A and Organic B).....	169

Figure 6.4: Aerosol growth in absorber for Aqueous Blend (AB), Non-aqueous blend (NAB), and PZ at base conditions and 10^7 particles/cm ³ . AB and NAB grow to 15 and 20 μm in the absorber, respectively.	171
Figure 6.5: AB Drop composition in the absorber and water wash for Run 1 (solid lines) and Run 2 (dashed lines). AB Drop grows by picking large amounts of water, AM1, and CO ₂ in the absorber; only water in the water wash.	172
Figure 6.6: NAB Drop composition in the absorber. Drop grows by picking up only Amine A, CO ₂ , and water.	173
Figure 6.7: Higher aerosol concentration ($1-10^8$ particles/cm ³) reduces the growth of the non-aqueous blend, aqueous blend, and PZ in the absorber by 5, 25, and 41%, respectively.	175
Figure 6.8: PZ relative driving force ($\emptyset\text{PZ}$) in the absorber at $1-10^8$ particles/cm ³ . Higher aerosol concentration decreases gas-phase amine driving force. ...	176
Figure 6.9: Amine relative driving force ($\emptyset\text{AM1}$ and $\emptyset\text{AM2}$) for the aqueous blend (AB) in the absorber at $1-10^8$ particles/cm ³ . Higher aerosol concentration decreases gas-phase amine driving force.	177
Figure 6.10: Amine relative driving force ($\emptyset\text{Amine A}$) for the non-aqueous blend (NAB) in the absorber at $1-10^8$ particles/cm ³ . Higher aerosol concentration decreases gas-phase amine driving force.	178
Figure 6.11: Gas-phase amine driving force for Aqueous Blend (AB), Non-aqueous blend (NAB), and PZ at base conditions and 10^7 particles/cm ³ . The driving force is greatest for NAB.	179

Figure 6.12: Aerosol growth in the absorber and water wash for the Aqueous Blend (AB) at Run 1 (lean solvent, intercooler, and water wash at 40 °C) and Run 2 (lean solvent at 60 °C, intercooler at 30 °C, and water wash at 40 °C). Drop grows to 18 μm in Run 1 and 17 μm in Run 2.....	180
Figure 6.13: Higher kg' (2x) increases the growth of the non-aqueous blend (NAB), Aqueous Blend (AB), and PZ in the absorber by 85, 10, and 16%, respectively.	181
Figure 6.14: Circulation water flow required to maintain water balance for Runs 1 and 2 with AB solvent at temperature set points.	182
Figure 6.15: Effect of water wash temperature on AB aerosol growth in the water wash. Colder water wash grows bigger drops for Run 2 (dashed lines); minimal effect for Run 1 (solid lines).....	183
Figure 6.16: Effect of water wash packed height on AB aerosol growth in the water wash. 6.64 ft (solid lines) and 10ft (dashed lines). More packing grows bigger drops.	184

Chapter 1: Introduction

1.1 MOTIVATION FOR CO₂ CAPTURE BY AMINE SCRUBBING

CO₂ is a greenhouse gas and precursor of global warming, and its continued emission will cause further warming. Reaching net-zero CO₂ emissions is virtually impossible without carbon capture technologies (IEA, 2021). The capture of CO₂ from large point sources like coal and natural gas combined cycle (NGCC) power plants is feasible and can significantly reduce CO₂ emissions and help mitigate global warming.

Of the possible technologies for CO₂ capture from fuel combustion, amine scrubbing, a subset of post-combustion CO₂ capture, is considered the most mature (Rochelle, 2009). First patented by (Bottoms, 1930), amine scrubbing has been used to separate CO₂ from large point sources for over eight decades. The process involves the counter-current contact of an amine solvent with the flue gas at a low temperature in an absorber. The CO₂ absorbed from the flue gas is then desorbed from the CO₂-rich solvent in a stripping column using heat from a reboiler.

1.2 RELEVANT ADVANCES IN CO₂ CAPTURE BY AMINE SCRUBBING

CO₂ capture has received much attention from a wide range of industries, policymakers, and non-governmental organizations over the past decade, emphasizing the need for scale-up to commercially viable operations. These have played a key role in promoting the development of 2nd and 3rd generation CO₂ capture technologies focused on improving CO₂ capture efficiency and reducing cost. Also, coal is rapidly being replaced by natural gas for electricity generation, and future advances in CO₂ capture technologies must demonstrate reliable operations with Natural Gas Combined Cycles (NGCC).

This work evaluates three of such technologies that fall under the 2nd and 3rd generation categories at coal and NGCC conditions. The first uses Piperazine (PZ), a superior solvent to the traditional monoethanolamine (MEA), with the advanced stripper configuration (PZASTM) that improves conventional stripper designs. The second is an aqueous solvent blend (AB) of proprietary amines AM1 and AM2 that collectively allow for faster CO₂ absorption kinetics and are operated with a two-stage solvent regeneration configuration to improve power plant efficiency. The third is a 3rd generation capture technology that utilizes a non-aqueous solvent blend (NAB) of Amine A and Organic B, significantly reducing the regeneration energy.

1.2.1 Piperazine Advanced Stripper (PZASTM)

Aqueous piperazine (PZ) is considered a superior solvent to MEA because of its fast absorption rate, relatively wide solubility range, good energy performance, and moderate volatility (Rochelle et al., 2011). The use of PZ, together with the advanced stripper, provides an excellent opportunity for cost and energy reduction. Figure 1.1 shows the PZASTM process flow diagram. Before the flue gas enters the PZASTM process, it undergoes several pretreatment steps to remove fine particulates, nitrogen oxides, and sulfur oxides. The flue gas exiting the pretreatment processes enters a direct contact cooler (DCC), where excess moisture is removed before being fed to the bottom of the absorber. Aqueous PZ is introduced at the top of the absorber to contact and remove CO₂ from the upward flowing gas. The CO₂-depleted gas then flows into a water wash with circulating water to recover any vapor amines and maintain the system water balance. As PZ flows down the absorber, it becomes richer in CO₂ and is sent through heat recovery exchangers for regeneration in the stripper. The regenerated PZ is sent back to the absorber top to complete the cycle, while CO₂ flashed in the stripper is transported to its end-use.

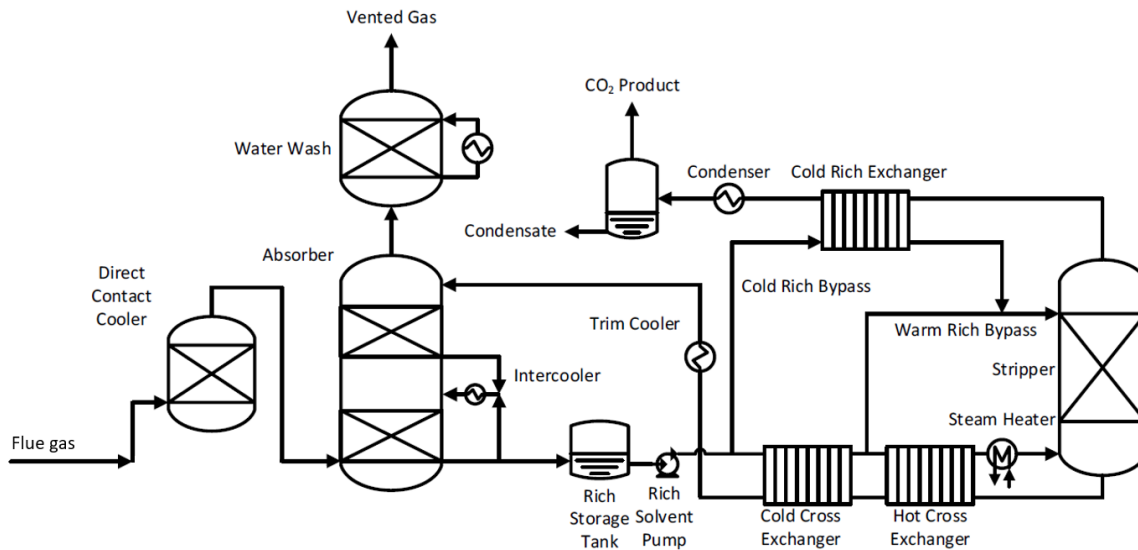


Figure 1.1: Process flow diagram for PZAS™ as operated at the National Carbon Capture Center (NCCC) during 2018 coal and 2019 NGCC campaigns (Rochelle et al., 2021).

1.2.2 Aqueous Blend (AB) of proprietary amines AM1 and AM2

The University of Kentucky Center for Applied Energy Research (UK CAER) large pilot CO₂ capture unit has tested a proprietary solvent, an aqueous blend (AB) of two amines: AM1 and AM2. This proprietary solvent can reduce the cost of CO₂ capture by 50% compared to existing technologies and has also been tested at the Technology Centre Mongstad (TCM) pilot plant. In addition, UK CAER has validated their heat-integrated solvent system by operating for more than 4,000 hours using a 0.7 MWe slipstream of flue gas at the E.W. Brown Power Generating Station (Thompson et al., 2017). Combining the proprietary solvent with the heat integrated technology provides the potential for significant energy savings and improved absorber performance.

1.2.3 Non-Aqueous Solvent Blend (NAB)

This study evaluates a proprietary non-aqueous blend (NAB) of Amine A and Organic B. These 3rd generation solvents with low water content have been developed to improve their aqueous counterparts and reduce the cost of CO₂ capture further (Heldebrant et al., 2017). Researchers argue that water lean solvents reduce both heats of absorption and vaporization, resulting in up to 50% reduction in regeneration energy compared to traditional aqueous solvents (Guo et al., 2019; Lail et al., 2014; Zhou et al., 2018). While non-aqueous solvents show great promise for CO₂ capture, they might be limited by their volatility and viscosity challenges (Yuan & Rochelle, 2018).

1.3 THE CHALLENGE OF AMINE EMISSIONS IN AMINE SCRUBBING

Amine loss from the absorber as vapor and aerosol has been reported in several pilot plants, with emissions in some instances exceeding 1000 ppm (Kamijo et al., 2013a; Moser et al., 2014; Thompson et al., 2017). These pilot studies have shown that a water wash section can absorb most of the vapor amine exiting the absorber but becomes ineffective when amine aerosol is present (Mertens et al., 2013). The water wash under regular operation fails to mitigate these emissions as the particulates are too small (below 1 μm) to be captured by impaction with the bulk washing action in the column. Amine aerosol is formed and emitted when particles such as fly ash or liquid aerosol resulting from sulfur trioxide (SO₃) are present in the flue gas (Anderlohr et al., 2015; Bade et al., 2015; Khakharia et al., 2016, 2013). Aerosol concentrations measured at pilot plants ranged from 10⁶ to 10⁸ particles/cm³ (Brachert et al., 2013; Saha & Irvin, 2017). This suggests that pretreatment processes that reduce inlet particulate concentration to 10⁵ particles/cm³ will mitigate amine aerosol. Beaudry (2018) concluded that the baghouse installed at the National Carbon Capture Center must have reduced SO₃ aerosol nuclei in

the flue gas due to the resultant 10-fold reduction in amine emissions observed at the CO₂ capture facility. However, these baghouse units are not used in all coal power plants and would be costly if installed solely to manage amine aerosol. Sustained amine emissions above one ppm are prohibitive to CO₂ capture due to safety, regulatory concerns, and cost of solvent replacement (Shao & Stangeland, 2009).

The oxidation of sulfur contained in fossil fuels forms sulfur dioxide (SO₂), which can be further oxidized to SO₃ in selective catalytic reduction (SCR) of nitrogen oxides (NO_x) or at other points in the combustion process (Srivastava et al., 2004). Gas-phase SO₃ quenched upstream of the CO₂ capture absorber produces acidic aerosol, resulting in amine aerosol emissions in the scrubbed gas. Beaudry et al. (2019) investigated the effect of SO₂ and SO₃ in flue gas on amine emissions. They concluded that SO₃ was the more potent nuclei for amine emissions with up to 7.6 mol piperazine (PZ) emitted per mol SO₃.

A few attempts have been made to hypothesize the mechanisms for amine aerosol formation and growth in the absorber and its mitigation by altering absorber operating parameters. Existing literature suggests that amine aerosol grows in the absorber through the uptake of water, CO₂, and amine on existing aerosol. Khakharia et al. (2015) studied the effect of lean solvent temperature, lean solvent pH, and flue gas CO₂ on emissions with aminomethyl propanol (AMP)/piperazine (PZ). They concluded that the amine aerosol particle number concentration, supersaturation, and reactivity were crucial for emission reductions. Bade et al. (2015) patented a method to inhibit amine aerosol formation in the absorption zone of the absorber by avoiding quenching or rapid cooling of the gas mixture in the absorber. They claim that if the temperature of the lean solvent entering the absorber is less than 5 °C lower than the maximum temperature in the absorption section of the absorber, cooling of the gas will be avoided, and aerosol formation in the absorption zone also be substantially reduced. They also suggest that although the top of the absorber has

greater amine partial pressure, operating the absorber with an elevated lean solvent temperature prevents amine aerosol formation at the absorber top and results in emission mitigation. Mertens et al. (2014) formulated a hypothesis for predicting aerosol formation based on the particle concentration and size distribution (PSD) in the inlet flue gas. They related number concentrations measured upstream of different capture pilot plants to the formation of amine aerosol and identified a threshold below which amine emissions were non-existent.

Other modeling studies show that emission mitigation at elevated lean solvent temperature may be due to amine aerosol growth and collection rather than the prevention of amine aerosol formation. Fulk (2016) developed an aerosol model for PZ and concluded that aerosol growth is limited in the absorber by uptake of CO₂ and PZ from bulk gas and in the water wash by uptake of water due to the lower water activity of the aerosol. Kang et al. (2017) improved on the Fulk aerosol model by including gas-phase PZ depletion. Using the upgraded PZ model, Zhang (2018) showed that amine aerosol growth in the absorber is driven by amine-limited diffusion. Khakharia (2015) and Majeed et al. (2017) agree with the aerosol growth mechanisms presented.

1.4 GAPS IN AMINE AEROSOL RESEARCH

While growth models from existing literature show trends for aerosol mitigation, the demonstration, and quantification of these strategies for PZ on the pilot-scale has not been done. The aerosol growth models have also not been validated with pilot plant results. Earlier studies with other solvents have largely considered amine emissions in response to process changes without creating a dedicated test plan for long-term emissions control. There has been minimal comprehensive data presented to demonstrate the effect on amine

emission of increasing the flue gas SO_3 , lean solvent temperature, and the residence time of the gas at water wash conditions for piperazine or other solvents.

More guidance for aerosol management at the pilot scale is still required for PZ and will require accurate modeling of aerosol growth. The modeling analyses performed in previous works do not quantify or clearly distinguish the effect of operational changes on solvent rate and CO_2 removal. The sensitivity of the PZ aerosol model to empirical correlations of the physical property and vapor-liquid equilibrium has also not been thoroughly evaluated. Finally, it is unclear how changes in flow models and heat and mass transfer calculations used by process simulators affect absorber bulk gas and liquid profiles and aerosol growth profiles.

Natural Gas Combined Cycle (NGCC) plants have started to replace coal as the primary electricity generation source and contribute a third of total U.S. energy-related CO_2 emissions (EIA, 2019). Future advances in CO_2 capture technologies must demonstrate reliable CO_2 capture from NGCC. Although long-term amine emissions with capture from coal have been reported, the literature is sparse for NGCC. Emissions from both sources should differ because the flue gas composition and absorber operating conditions differ. NGCC flue gas has a lower CO_2 content, requires a lower liquid to gas (L/G) ratio, and has a cleaner composition with a lower concentration of aerosol nuclei. Pilot studies with 90% capture over extended periods must be conducted for NGCC to monitor solvent emissions.

Although aerosol models for single amine solvents have been developed, none have been reported for blended amine solvents. Previous work on PZ- CO_2 (Fulk, 2016; Kang et al., 2017) and MEA- CO_2 (Kang et al., 2020; Majeed et al., 2017b) do not consider mass and heat transfer for a solvent blend. Also, the models are solvent-specific and cannot model the aerosol dynamics for other 2nd and 3rd generation CO_2 capture technologies. The

presence of a second amine in the bulk liquid might affect the current understanding of aerosol growth mechanisms, composition, and size.

1.5 RESEARCH OBJECTIVES OF THIS WORK

This work is focused on the measurement, modeling, and mitigation of amine aerosol at pilot plants and is summarized into four objectives.

1.5.1 Develop and Demonstrate Amine Aerosol Generation and Measurement at Pilot-Scale

The first objective is to develop and demonstrate experimental techniques for SO₃ generation and amine aerosol measurement at pilot scale. The results from this objective are documented in Chapter 2 of this dissertation.

1.5.2 Demonstrate Amine Aerosol Mitigation at Pilot-Scale

The second objective of this work is to demonstrate amine aerosol mitigation at the pilot scale for the piperazine advanced stripper (PZAS™) with flue gas at varying SO₃ concentration. This work is documented in Chapter 3 of this dissertation.

1.5.3 Evaluate Amine Emissions at NGCC Conditions

The third objective of this work is to evaluate amine emissions from pilot plant operations at NGCC conditions and compare them to coal. This work is documented in Chapter 4 of this dissertation.

1.5.4 Improve PZ Aerosol Model and Develop New Aerosol Models for Solvent Blends

The fourth and final objective is to develop a framework for aerosol growth modeling of solvent blends and compare the aerosol mechanisms of two proprietary solvent

blends (aqueous blend (AB) and non-aqueous blend (NAB)) to a modified PZ aerosol model. This work is documented in Chapters 5 and 6 of this dissertation.

Chapter 2: Amine Aerosol Generation and Measurement at Pilot-Scale

This chapter outlines the analytical techniques and experimental setup used for amine aerosol measurements and aerosol nuclei generation during the 2018 coal and 2019 natural gas combined cycle (NGCC) campaigns at the National Carbon Capture Center (NCCC). It also provides recommendations for amine aerosol measurements at the University of Kentucky Center for Applied Energy Research (UK CAER) large pilot CO₂ capture unit. Aerosol size distribution and concentration measurements with the ELPI were set up and operated by the Southern Research Institute (SRI). An extensive review of FTIR and PDI theory can be found in Fulk (2016), while detailed documentation of standard operating procedures for amine emission measurements can be found in Beaudry (2018).

2.1 AMINE MEASUREMENT WITH FOURIER TRANSFORM INFRARED GAS ANALYZER (FTIR)

Gasmet™ CX and DX-series FTIR gas analyzers were used to monitor CO₂, SO₂, PZ, NH₃, and water in the gas streams entering and exiting the absorber and the gas stream leaving the water wash. They operate by infrared spectroscopy and can simultaneously measure up to 50 gas components.

2.1.1 Principles of Infrared Spectroscopy

Infrared (IR) spectroscopy measures the concentration of a gas mixture by tracking the absorbance of light by each molecule in that mixture. Each molecule contains functional groups that stretch and bend at different frequencies. IR passing through the gas mixture is absorbed if the frequency of the light matches the vibrational frequency of any functional groups present. This produces IR spectra with absorption bands that help to identify key functional groups present in a molecule. The basis for IR spectroscopy is that

specific functional groups correspond to specific absorption bands at particular frequencies or wavenumbers.

Symmetrical non-polar bonds are IR inactive and will not absorb IR light because there is no change in the dipole moment during vibration. The more polar the bond, the stronger the absorption and wider the stretch on the IR spectra. Molecules with stronger bonds and lighter atoms are absorbed at higher frequencies or wavenumbers. Table 2.1 shows the wavenumbers corresponding to a range of functional groups. The gaseous components of interest to this work (CO₂, SO₂, PZ, NH₃, and water) contain polar bonds and are readily detected by the FTIR analyzer.

Table 2.1: Functional group wavenumbers

Bond	Wavenumber	Intensity
O—H	3650–3200	Strong, broad
C—H	3300–2700	Medium
N—H	3500–3300	Medium, broad
C≡N	2260–2220	Medium
C≡C	2260–2100	Weak-medium
C=C	1680–1600	Medium
C=N	1650–1550	Medium
C=O	1780–1650	Strong
C—O	1250–1050	Strong

The IR spectrum plots the transmission of the IR through the gas as a function of wavenumber. The transmittance ratio is the IR intensity that passed through the sample gas to the IR intensity that entered the sample gas. The absorbance of a sample is obtained by comparing its transmittance spectrum to a background spectrum. The background

spectrum is one with 100% transmittance and obtained using IR-inactive species such as N₂. The concentration of the sample gas can be obtained using the Beer-Lambert Law (Equation 2.1), which relates the measured absorbance of the sample spectrum to the concentration.

$$A = \log\left(\frac{I_o}{I}\right) = \log\left(\frac{1}{T}\right) = \varepsilon(\lambda)C X \quad (2.1)$$

where:

A = Absorbance

I_o = Incident light intensity

I = Transmitted light intensity

T = Transmittance

$\varepsilon(\lambda)$ = Absorptivity (depends on wavelength)

C = Sample concentration

X = Optical path length

The concentration of each gas component in a given sample may be obtained if the reference spectra for all the gas components for that sample exist. Each reference spectrum is unique for one single gas component and can be combined to replicate the sample spectrum. Reference spectrum for the gas components used in this work was obtained by passing individual known compositions through the FTIR analyzer and labeling the IR spectrum produced accordingly. Figure 2.1 shows a sample spectrum, and Table 2.2 shows the analysis regions used in this work.

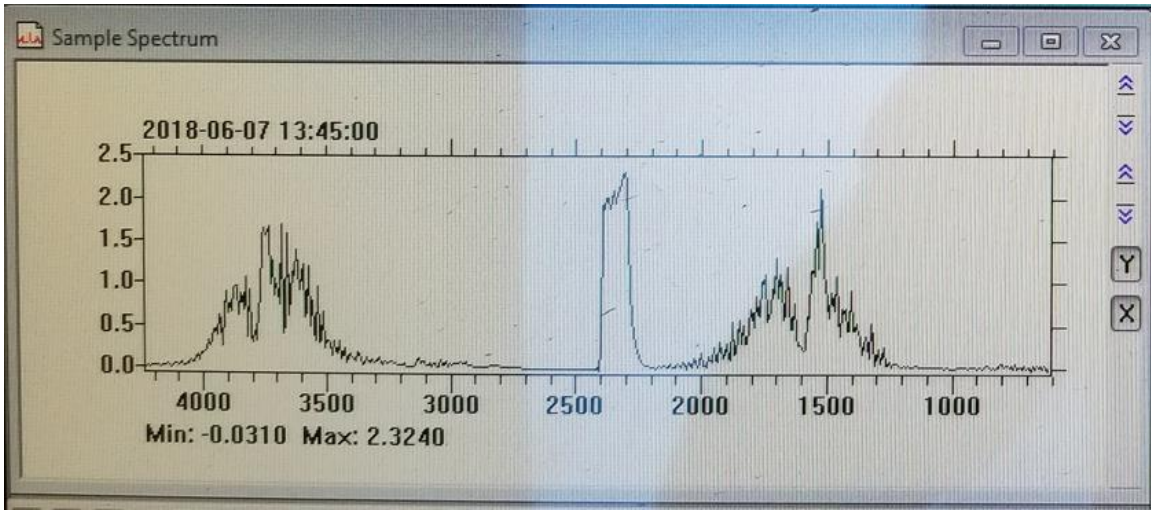


Figure 2.1: Sample spectrum showing absorption bands

Table 2.2: Analysis regions used for gas components in this work

Component	Concentration	Range 1 (cm^{-1})	Range 2 (cm^{-1})	Range 3 (cm^{-1})	Number of references
H ₂ O	vol %	—	2475–2600	3000–3375	7
CO ₂	vol %	926–1150	2065–2245	2550–2700	11
PZ	ppmv	—	2500–2600	2550–3100	11
NH ₃	ppmv	895–1300	2475–2600	—	8
SO ₂	ppmv	1050–1450	2500–2600	—	7

2.1.2 FTIR Sampling Hardware and Specifications

2.1.2.1 FTIR Analyzer

This work used a portable Gasmet™ DX-4000 (serial number 071203) and a rack-mount Gasmet™ CX-4000 (serial number 142840) FTIR analyzer for gas sampling. The technical specifications for the instrument are presented in Table 2.3. Both analyzers are identical in operation with differences in the housing structures. The Gasmet™ DX-4000

is designed for field operations with modular units and a protective casing against weather and vibrational disturbances. Gaset™ CX-4000, on the other hand, is integrated into a rackmount set up with all components placed in server racks that can be moved together as a unit.

The sample gas extracted from the process is sucked at 5 Lpm into the FTIR analyzer with an Air Dimensions, Inc.® Dia-Vac-R201 heated sample pump. The sample gas goes through an Atmoséal® FPD-4-7/1-B02 filter that removes particulates. The technical specifications of the filter and pump are presented in Tables 2.4 and 2.5, respectively.

Table 2.3: FTIR analyzer technical specifications (Gasmeter™ CX-4000)

Parameter	Value/Description
Model #	CX-4000
Mounting Position	Horizontal
Line Voltage	120 VAC
Fittings	¼" Imperial, Compression
Gaskets	Kalrez [®]
Software	Calcmeter™ V11.110, Windows 7 (64-bit)
<hr/>	
Interferometer	
Interferometer Type	Temet Carousel Interferometer (GICCOR)
Beamsplitter/Window Material	ZnSe
Wavenumber Range	900-4200 cm ⁻¹
<hr/>	
Sample Cell	
Temperature	180 °C
Path Length	5.0 m
Sample Cell Volume	0.4 L
Gasket Material	Kalrez [®]
Coating	Ni + Rh + CVD Au
Mirrors	Fixed, protected Au coating
Protective Coating	MgF ₂
Window Material	BaF ₂
Sample Cell Pressure	Yes
Detector Type	Mercury, Cadmium, Tellurium, Pelletier Cooled (MCPT)
IR Source	SiC, 1550K
<hr/>	
DSP/Power Board Settings	
Speed Setting	5 Hz
Resolution	8 cm ⁻¹
Scan Frequency	10 spectra/s
Comport Speed	57600 bps
EPRM Type	Standard
Digital Interface	9-pole D-connector RS232 protocol serial
<hr/>	
Measuring Parameters	
Zero-point calibration	Every 24 hours with N ₂
Zero-point drift	<2% of measuring range per zero point calibration interval
Accuracy	2% of measuring range
Temperature drift	<2% of measuring range per 10K change
Pressure influence	1% of measuring range per 1% sample pressure change

Table 2.4: FTIR filter technical specifications (Atmoseal[®] FPD-4-7/1-B02)

Specifications	Values
Part number	FPD-4-7/1-B02
Voltage	120 VAC (60 Hz)
Full load amps	2.0 A
Enclosure	316 SS
Thermocouple Type	K
Filter Type	Bayonet
Maximum Temperature	400 °F
Port Size and Type	¼” NPT
Element Length and ID	7” x 1”

Table 2.5: FTIR sample pump technical specifications (Baldor[®] Super-E[®])

Specifications	Values
Model number	R201-FP-IE3-M
Heater power	150 W (2 x 75 W)
Voltage	115 VAC (60 Hz)
Current Draw	1.3 A
Head material	316SS
Diaphragm material	Teflon [®]
Temperature range	30–400 °F
Max. ambient temperature	140 °F
Enclosure	Explosion proof
Port connectors	1/4” NPT
Pump Motor	
Catalog number	1202035119-000010
Specification number	M35J302P862
Serial number	X1702M23881
Horsepower	0.5
Voltage	230/460 VAC (60 Hz)
Phase(s)	3
Full load amps	1.54/0.77 A
RPM	1735
NEMA nominal efficiency	82.5%
Power factor	74%
Service factor	1.25
Frame	56C
Enclosure	TEFC
Insulation class	F
KVA code	K
Design code	B

2.1.2.2 Heated Sample Filter and Probe

A Universal Analyzers Model 277S heated filter with an extended probe was inserted into the absorber and water wash sample ports to extract gas for FTIR analysis. It has heating elements that prevent the condensation of water vapor in the filter. The temperature in the probe and filter elements was maintained at 180 °C with PID controllers in an electrical box. Table 2.6 shows the specifications for the heated probe, and Figure 2.2 shows the mechanical and electrical internals of the heated probe.

Table 2.6: Heated filter and probe specifications (Universal Analyzers Model 277S)

Specifications	Values
Sample flow rate	0–20 L/min
Calibration gas requirement	Sample flow rate plus 10%
Operating pressure drop at 10 L/min.	12” water column (3.0 kPa)
Maximum stack gas temperature	700 °F (371 °C)
Oven and vaporizer temperature	350 °F (176 °C)
Dimensions	9” x 9” x 10” (H x W x D)
Weight	20 lb. (9.1 kg)
Input power requirement	350 W (Custom)
Input voltage requirement	115 VAC, 50/60 Hz
Filter chamber heater type	Rod heaters in aluminum tube and PID controlled
Filter chamber material	316SS
Filter element type	Ceramic 2µm (Standard Option)
Chamber material	316SS

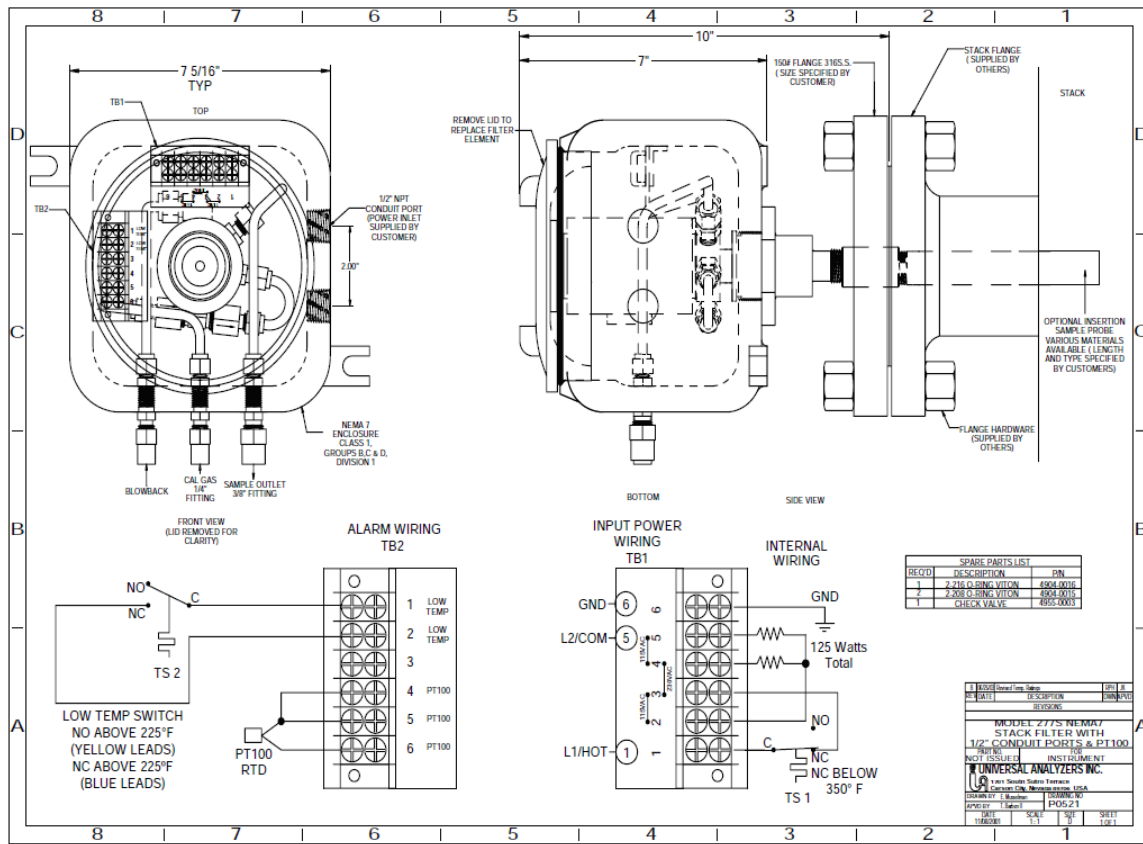


Figure 2.2: Detailed drawing for Model 277S heated probe showing conduit ports and internal wiring

2.1.2.3 Heated Sample Pads

CleanAir® SKU 1233 heated electrical blankets, more commonly called sample pads, were used to insulate the connection between the sample probe and sample lines. The temperature in the pad was maintained at 180 °C to prevent condensation and was controlled with external PID controllers in an electrical box. Table 2.7 shows the specifications for the heated pads.

Table 2.7: Heated sample pad specifications (CleanAir® SKU 1233)

Specifications	Values
Max. Operating Temperature	400 °F
Ambient Temperature	0 °F

Heat Output	42.7 W
Operating Voltage	120 VAC
Measured Resistance	337.1 Ω
Latch Mechanism	Velcro [®] Release
Dimensions (Open)	4" x 3" x 1" (L x W x H)
Dimensions (Closed)	4" x 6" x 1/2" (L x W x H)

2.1.2.4 Heated Sample Lines

The gas extracted from the sample probes was conveyed to the FTIR via heated sample lines. The sample lines used in this work were procured from Clayborn Labs with varying lengths from 3 ft to 30 ft. The lines were maintained at 180 °C with external PID controllers in an electrical box. The technical specifications for the sample lines are presented in Table 2.8.

Table 2.8: Heated sample line specifications (Clayborn Labs)

Specifications	Values
Carrier Tube Material	PFA
Carrier Tube Diameter	0.5"
Carrier Tube Wall Thickness	0.062"
Insert Tube Material	PTFE
Insert Tube Diameter	3/8"
Insert Tube Wall Thickness	0.047"
Max Temperature	200 °C
Min Environmental Temperature	-10 °C
Thermocouple Type	K-Type
Thermocouple Positioning	Midpoint
Operating Voltage	208 AC

2.1.3 FTIR Sampling Setup at NCCC

FTIR sampling was conducted for two major pilot plant campaigns at the NCCC: the 2018 coal campaign and the 2019 NGCC campaign. A portable Gasetm™ DX-4000 and a rack-mount Gasetm™ CX-4000 FTIR analyzer were used to analyze gas stream

compositions for both campaigns. The results of continuous emission monitoring during these campaigns are presented later in Chapters 3 and 4 of this dissertation.

2.1.3.1 2018 Coal Campaign

During the coal campaign, FTIR sampling was performed at 4 locations (Figure 2.3). A DX-4000 FTIR analyzer was devoted to sampling between the absorber gas inlet and absorber mid-bed locations. Similarly, a CX-4000 FTIR analyzer sampled gas from the absorber and water wash outlets.

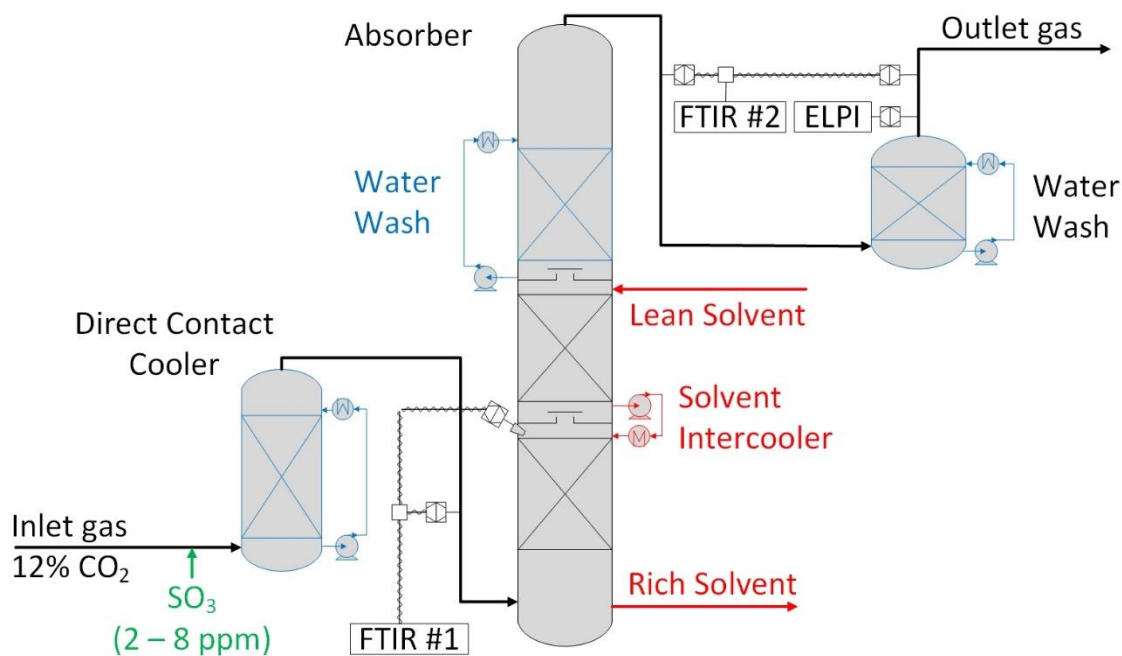


Figure 2.3: Simplified absorber PFD showing the gas sampling system for the 2018 coal campaign at NCCC

Figures 2.4–2.7 show the sampling setup during the coal campaign. Sample probes with heated probe tubes were inserted into pre-existing ports on the absorber and water wash. The gas was conveyed in heated sample lines into the analyzer through a stream switching box. Heated pads were used to insulate the exposed junctions between the probes

and sample lines to prevent condensation. The stream switching box was designed to allow flow from one sample location into the FTIR analyzer while bypassing the other to vent (Figure 2.8). This meant that at any given time, only data from either the absorber gas outlet or water wash could be sampled and recorded. The flow exiting the stream switching box was controlled using manual quarter-turn valves. During routine background scans, the sample valves on the box were turned to bypass, and N₂ was fed into the analyzer. All the pads, probes, sample lines, and stream switching boxes were heated and maintained at 180 °C to prevent condensation. The thermocouple and power elements for all the heated components were assembled into a custom electrical box with PID controllers to maintain the temperature setpoint (Figure 2.9). Unfortunately, sampling at the absorber mid-bed location was discontinued due to excessive condensation on the lines. An extractive sampling system is recommended for future sampling from that location.

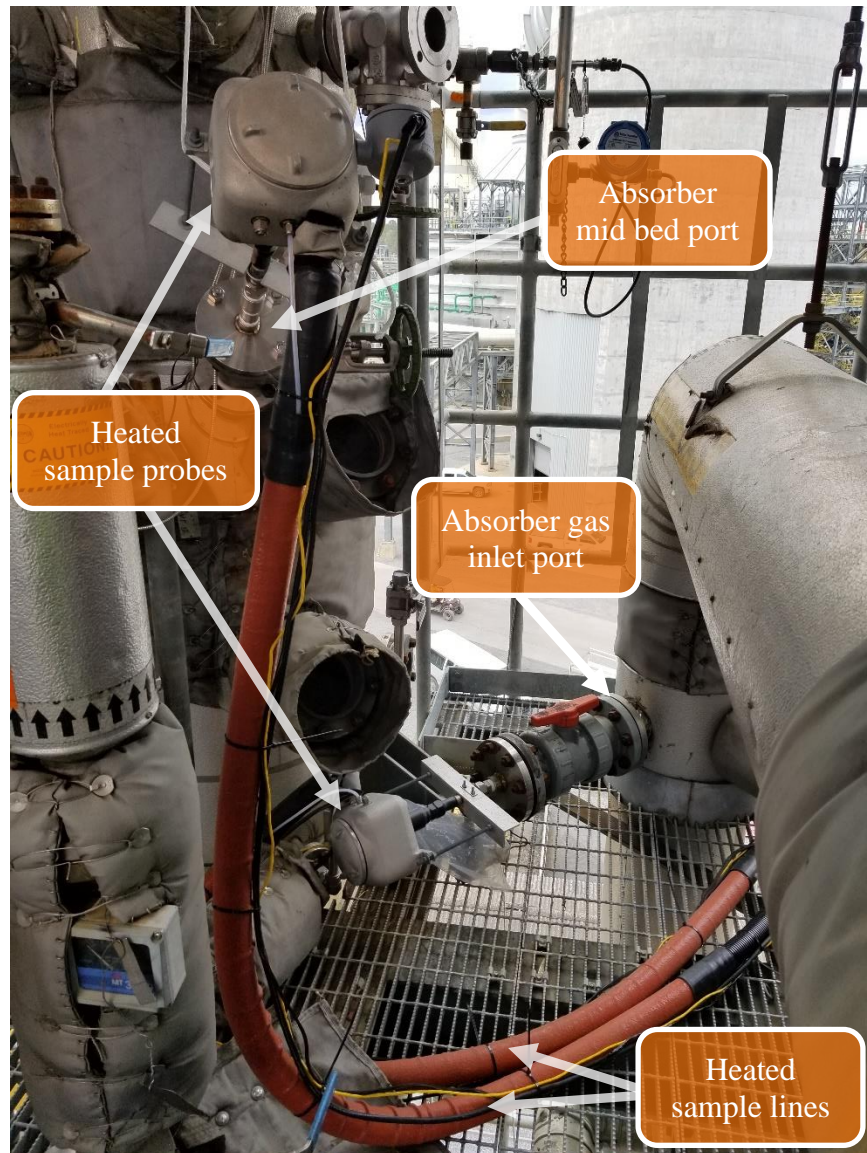


Figure 2.4: Sampling probe, pad, and line installations at the absorber inlet and mid bed locations during the 2018 coal campaign

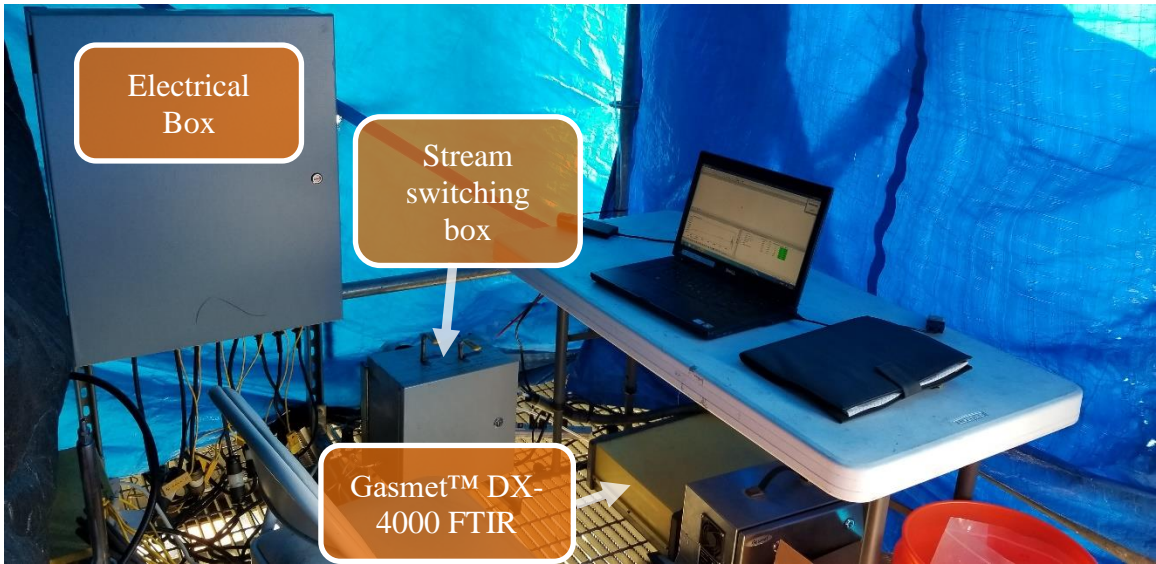


Figure 2.5: Gasmeter™ DX-4000 FTIR sampling setup for the absorber inlet and mid bed locations during 2018 coal campaign

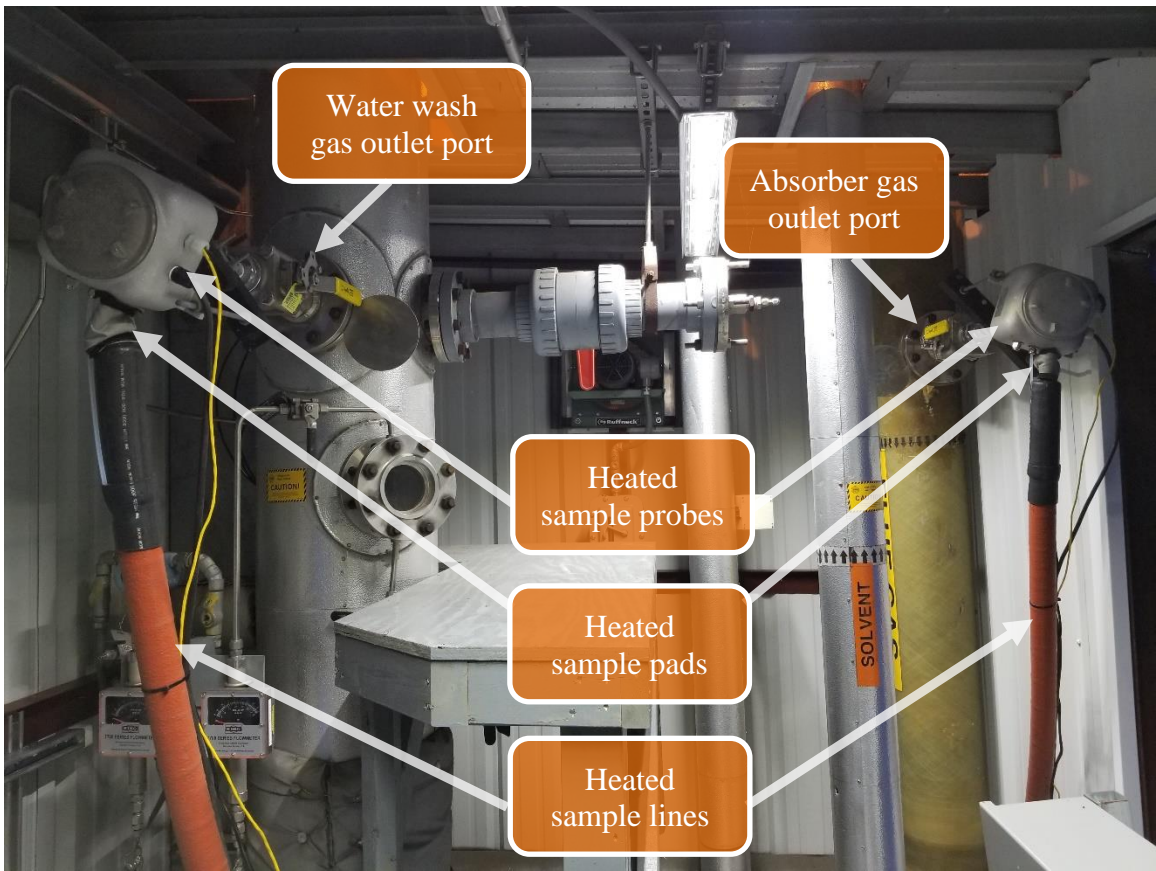


Figure 2.6: Sampling probe, pad, and line installations at the water wash and absorber gas outlets during the 2018 coal campaign

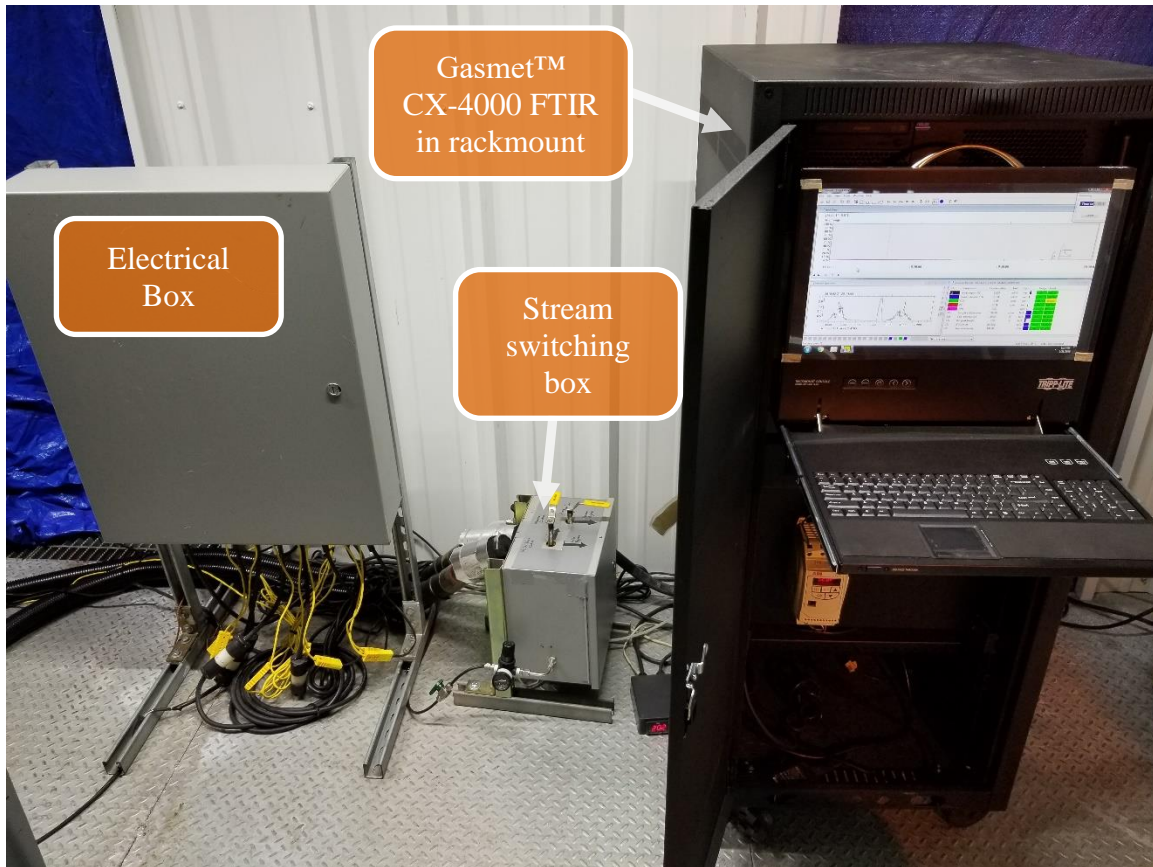


Figure 2.7: Gasetm™ CX-4000 FTIR sampling setup for the absorber and water wash gas outlets during the 2018 coal campaign



(a) Both absorber and water wash sample valves bypassed. N_2 flow open

(b) Water wash gas is sampled. Absorber and N_2 flow closed/bypassed to vent

Figure 2.8: Manual stream switching box with valves to direct flow from either absorber gas, water wash gas, or N_2 into the FTIR analyzer during the 2018 coal campaign



Figure 2.9: Custom electrical box with PID controllers to maintain sample line, pad, and probe temperatures at 180 °C (356 °F)

2.1.3.2 2019 NGCC Campaign

During the NGCC campaign, FTIR sampling was performed at 2 locations: absorber and water wash gas outlets (Figure 2.10). Gas compositions from both locations were measured with separate FTIR analyzers—providing a real-time evaluation of the

wash tower performance and significantly improving the 2018 coal campaign sampling setup. A Gasetm DX-4000 FTIR analyzer was used at the absorber outlet, while a Gasetm CX-4000 FTIR analyzer measured concentration exiting the water wash. At the beginning of the 2019 NGCC campaign, probe failure and condensation in the sample lines were observed at the absorber gas outlet port and were replaced later in the campaign leading to some loss of results.

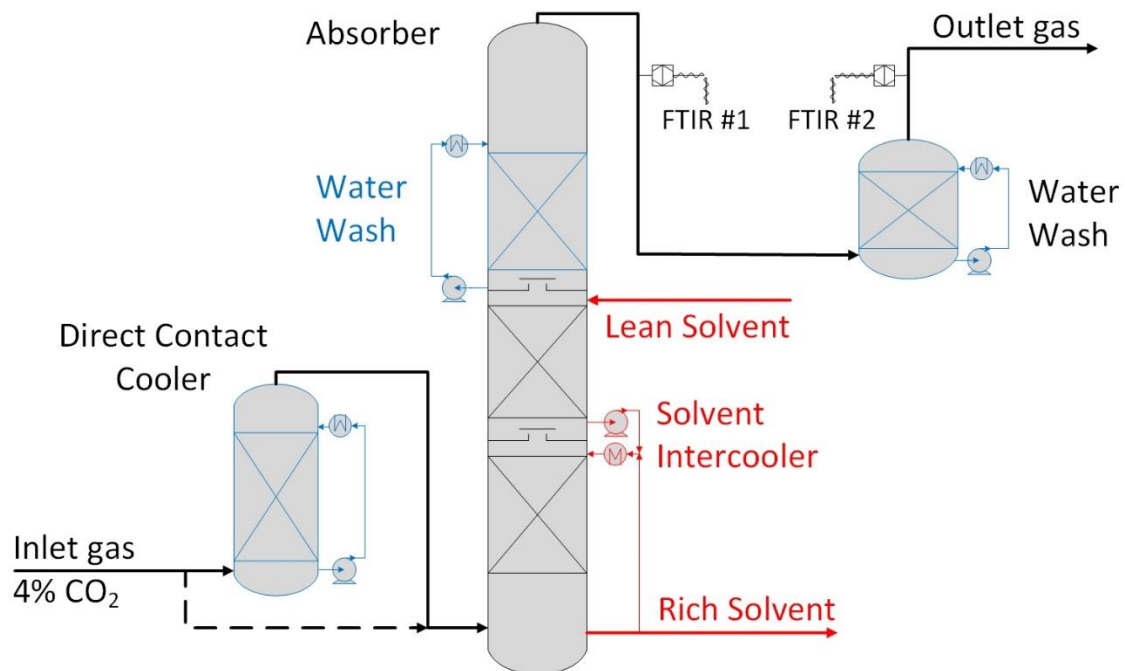


Figure 2.10: Simplified absorber PFD showing the gas sampling system for the 2019 NGCC campaign at the NCCC

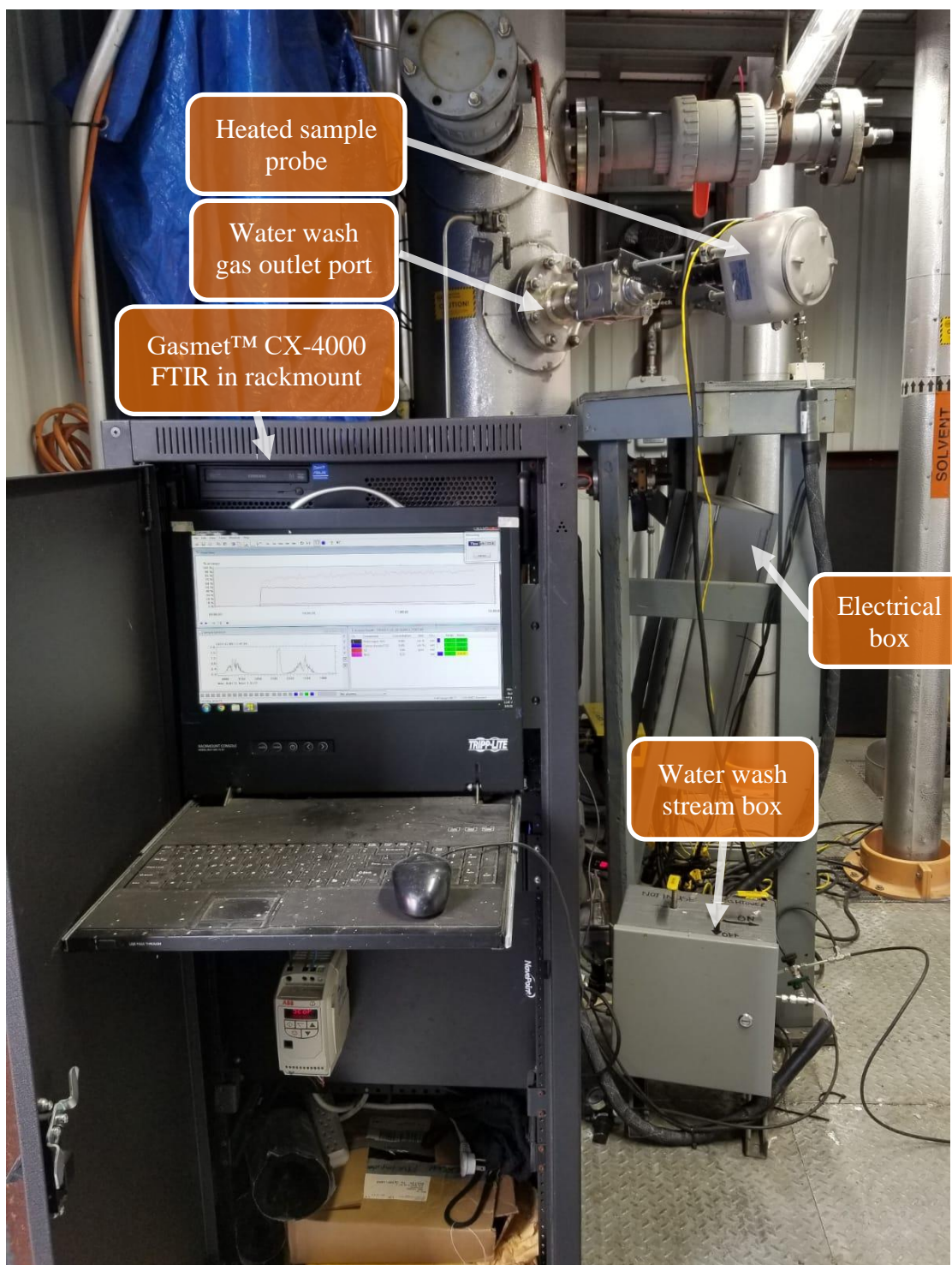


Figure 2.11: Gasetm™ CX-4000 FTIR sampling setup for the water wash gas outlet during the 2019 NGCC campaign

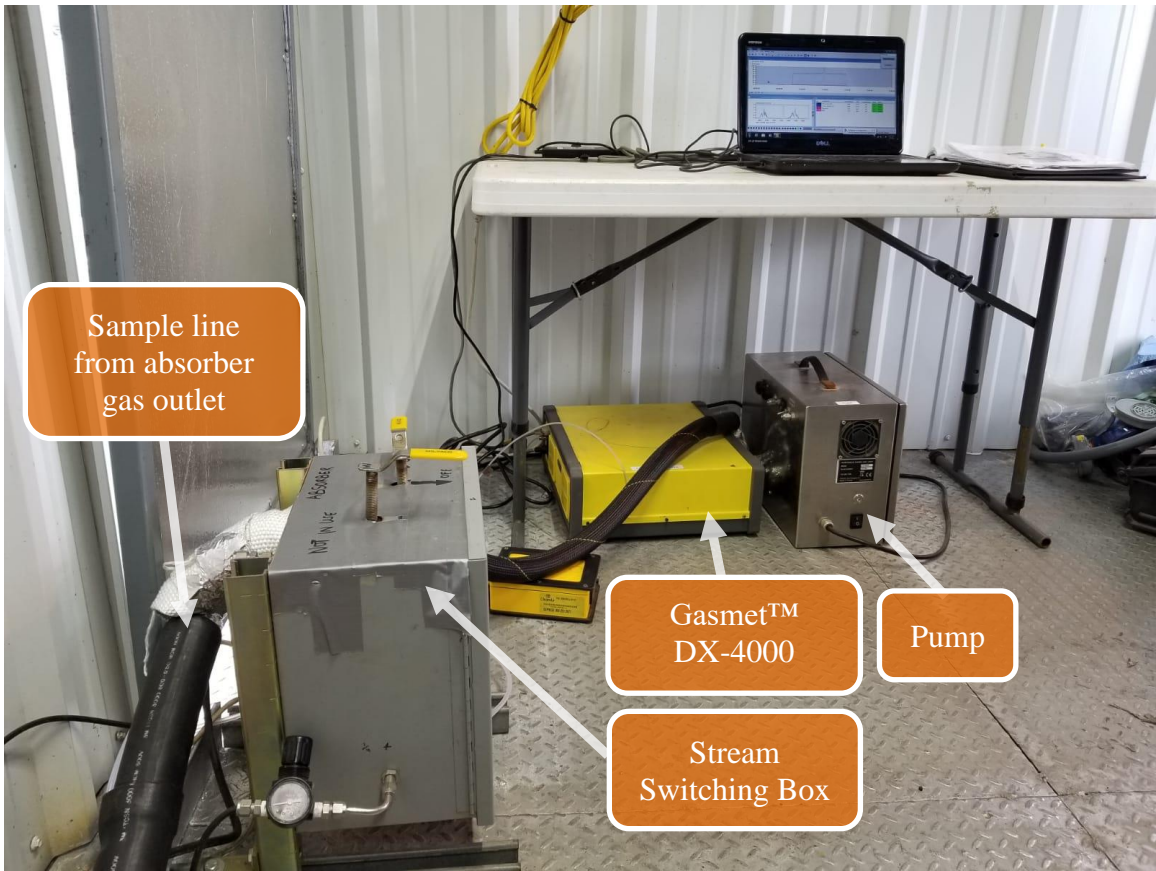
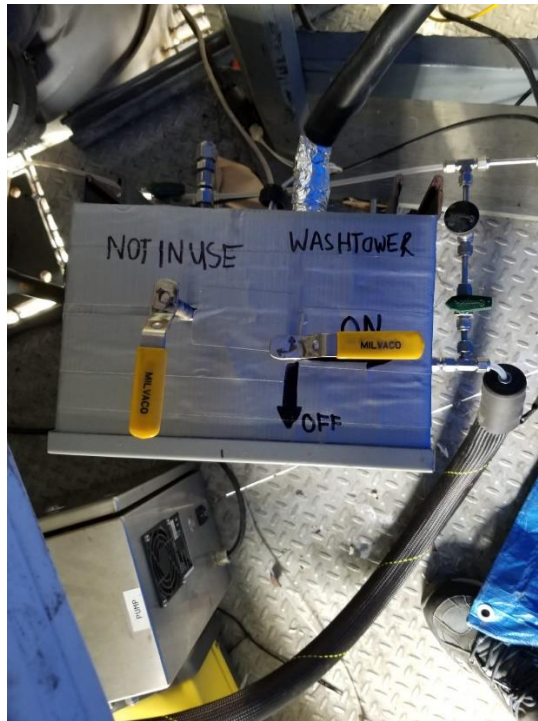


Figure 2.12: Gasetm™ DX-4000 FTIR sampling setup for the absorber gas outlet during the 2019 NGCC campaign



(a) Absorber gas is sampled, and N₂ flow closed.



(b) Water wash gas is sampled, and N₂ flow closed.

Figure 2.13: Separate stream switching boxes with valves to direct gas flow from the absorber and water wash to the 2 FTIR analyzers used in the 2019 NGCC campaign.

2.1.4 Data Analysis

The Gaset FTIR analyzers were operated and controlled with the Calcmet software installed on an external computer and linked to the analyzer via an RS232 cable. Figure 2.14 shows a screenshot of the Calcmet display. The sample spectrum window shows the absorbance vs. wave number plot, while the analysis results show the concentration of each component identified. The concentrations as a percentage of user-defined ranges are shown in the trend view plot to help track real-time compositional changes.

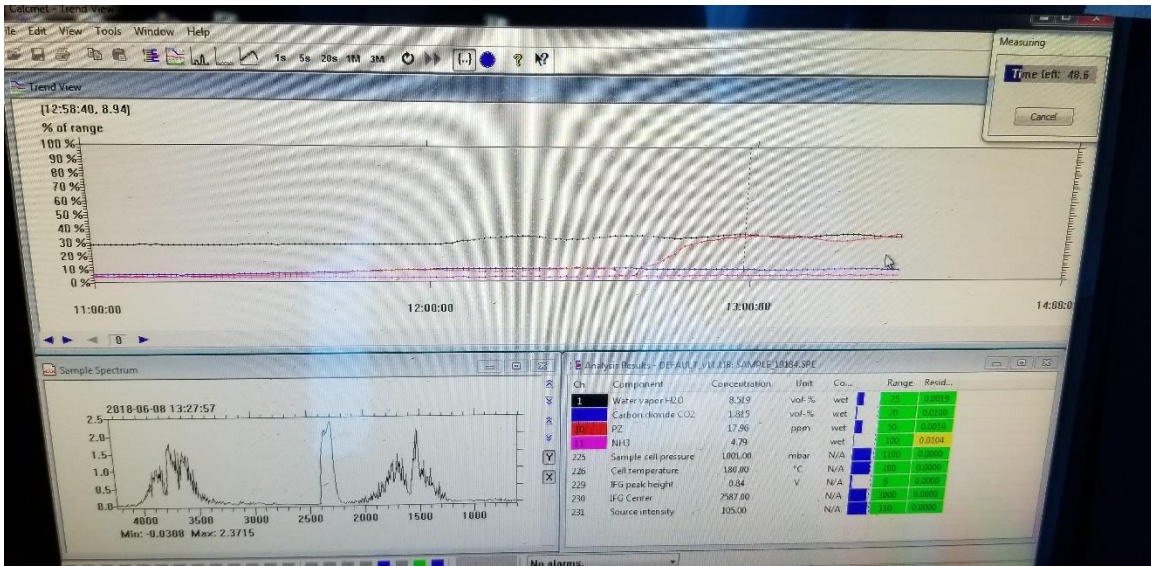


Figure 2.14: Calcmet display screenshot during 2018 coal campaign

The results were automatically saved with a timestamp and downloaded for data analysis in excel. A measuring time interval of 1-minute was used during the campaigns to capture instantaneous changes in emissions with operating conditions. When changes in absorber operating conditions or inlet flue gas SO₃ were made, a 15–20 minute wait time was enforced before recording concentrations. This ensured that a steady state is reached and allows enough time for the gas entering the absorber to travel to the water wash gas outlet where sampling was being done. Changes in SO₃ concentration had an almost immediate impact on PZ exiting the water wash, while temperature changes in the absorber took longer. Results showing the changes in concentrations as a function of time are presented as an example in Figure 2.15.

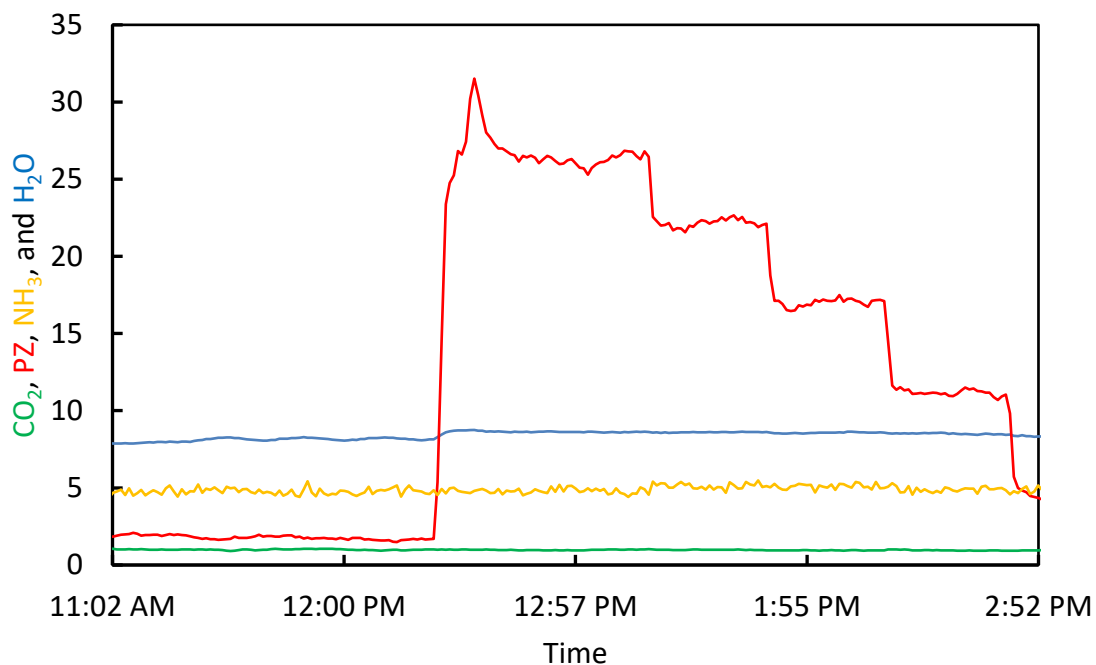


Figure 2.15: Results showing gas compositions measured by the FTIR at the water wash gas outlet. Step changes in PZ were in response to step changes in inlet flue gas SO₃. Results were extracted on June 28, 2018, during the coal campaign at NCCC.

2.2 AEROSOL CONCENTRATION AND SIZE DISTRIBUTION MEASUREMENT

2.2.1 Phase Doppler Interferometry (PDI)

The PDI is a laser-based technique used to measure particle concentration and size distribution. As the particles travel through the cell, they scatter light in an alternating high and low-intensity pattern. The scattered light pattern is observed by photodetectors and referred to as Doppler burst. A signal analyzer transforms the doppler signals to determine the Doppler frequency and phase shift between each pair of photodetectors. The PDI determines the particle size and particle size distribution of particles passing through the test cell by measuring the phase shift of the Doppler signal.

A third-generation PDI instrument built by Artium Technologies and modified for amine aerosol measurements was used for this work. The PDI instrument can measure a size range of 0.1–12 μm and concentrations above 10^6 particles/ cm^3 . This instrument has been used successfully at previous amine aerosol campaigns at the University of Texas at Austin Separations Research Program (UT-SRP) pilot plant and the NCCC. Beaudry (2018) and Fulk (2016) provide an extensive description of the design and working principles.

An attempt was made to use the PDI to measure particle concentration and size distribution at the water wash gas outlet during the 2018 coal campaign. Figures 2.16 and 2.17 show the sampling setup with the PDI strapped firmly to a bench to reduce vibrational impact. Sample gas was extracted using a blower and returned 3 ft below the extraction port. Unfortunately, the PDI instrument failed to function correctly, and a decision was made to conduct aerosol sampling with an Electrical Low-Pressure Impactor (ELPI) instead. Figure 2.18 shows the readout from the oscilloscope showing no data acquired through the channels.

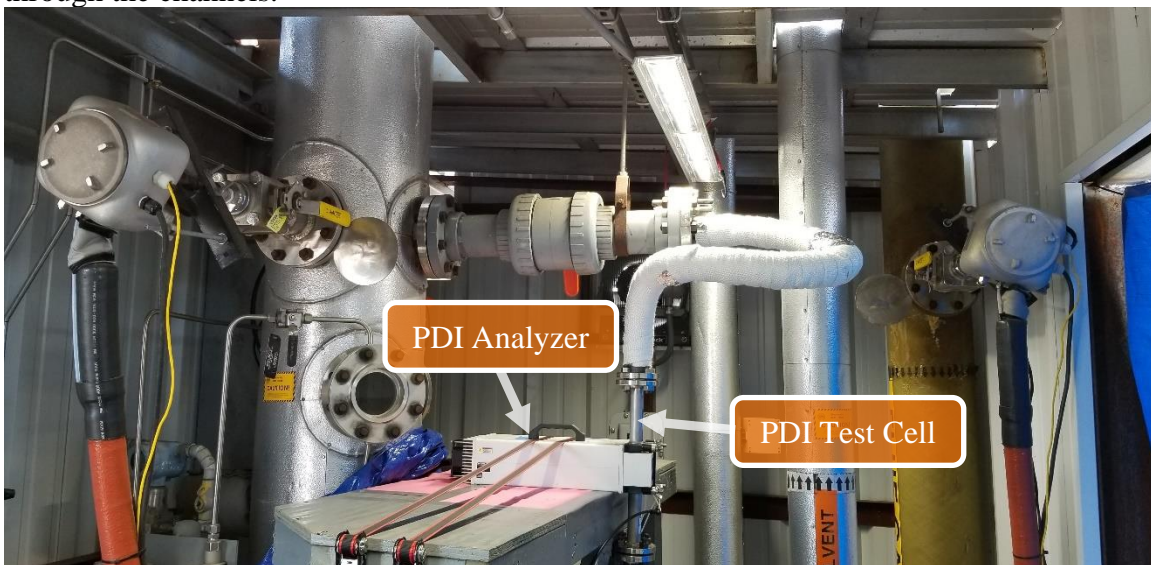


Figure 2.16: Sampling setup showing PDI analyzer strapped firmly to a bench to reduce vibrational impact.

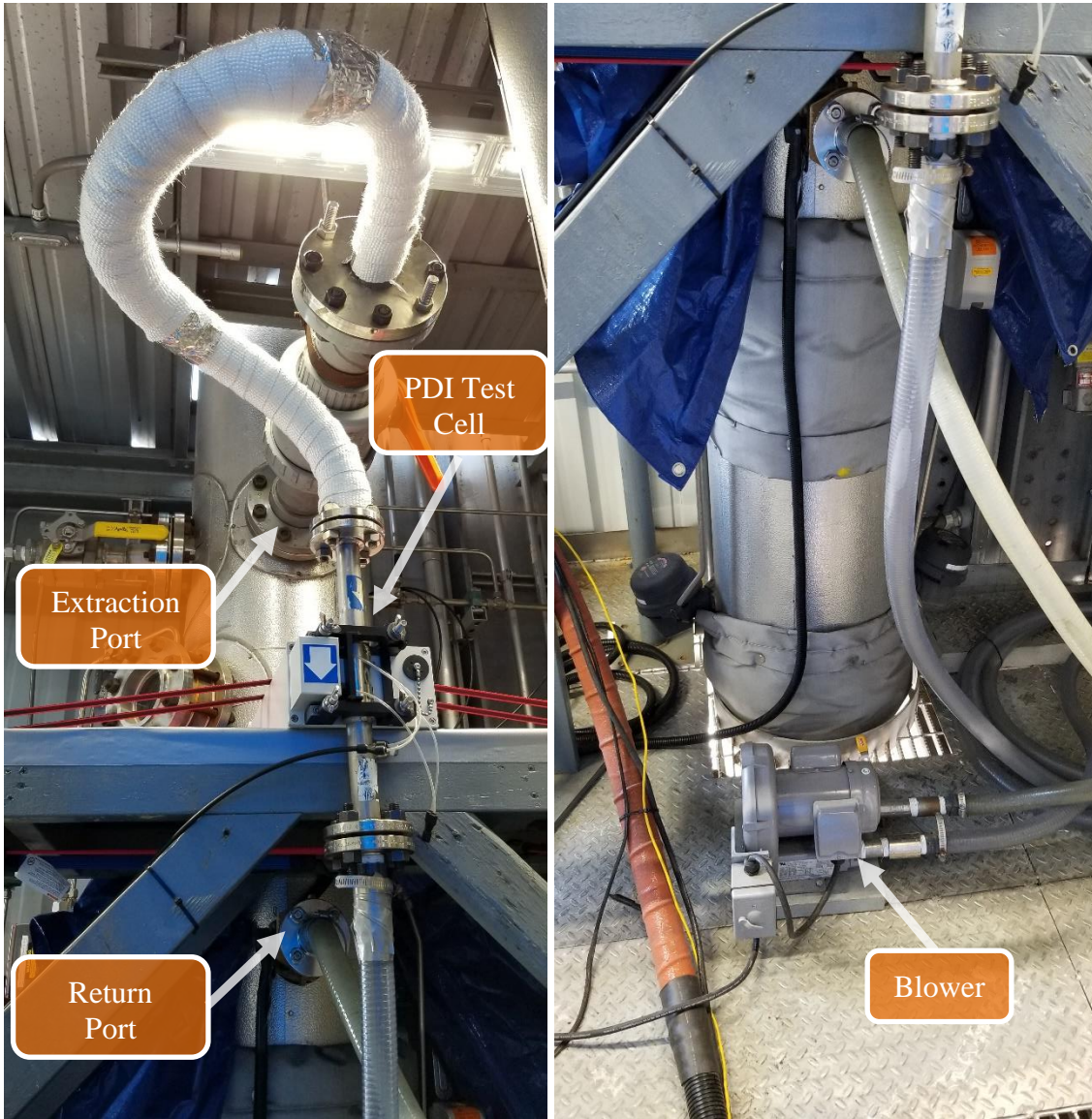


Figure 2.17: PDI extractive sampling setup at the water wash gas outlet during the 2018 coal campaign.

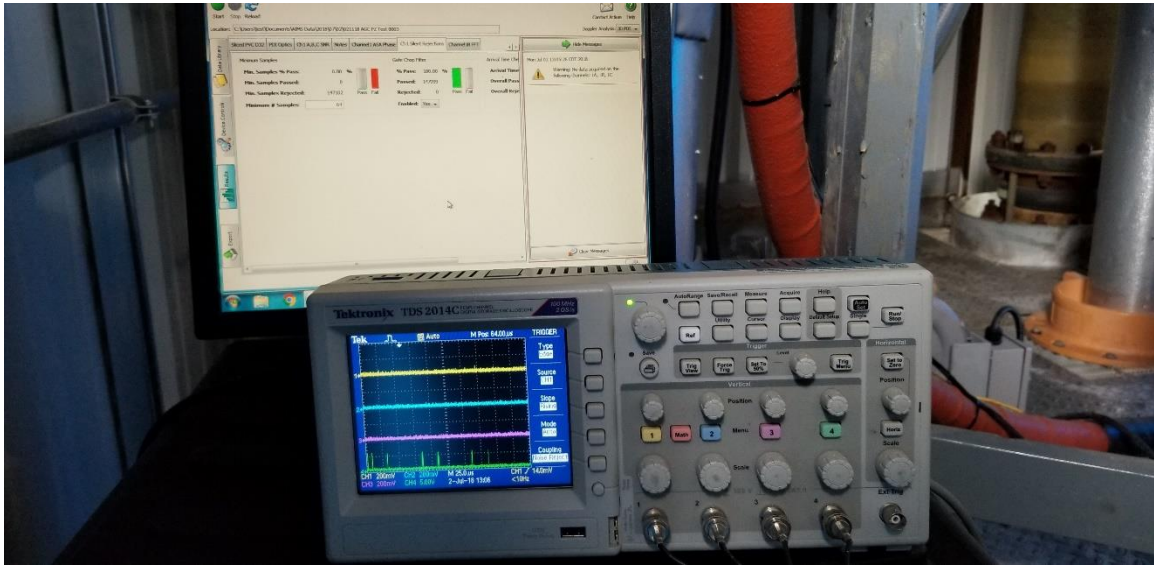


Figure 2.18: Oscilloscope display showing no detectable particles flowing through the PDI test cell.

2.2.2 Electrical Low-Pressure Impactor (ELPI)

The Southern Research Institute (SRI) set up and operated the ELPI used in this work at the NCCC. The ELPI classifies charged particles across a broad range of 6 nm to 10 μm in a low-pressure cascade impactor. It characterizes the aerodynamic size distribution by the number of impactor stages and their corresponding cut-off diameters in real-time. The schematic of the ELPI setup is shown in Figure 2.19. An ejector type control was used to dilute the sample with heated air to avoid condensation on the impactor plates of the ELPI stages. The dilution air is passed through a moisture trap and filtered to dry the air and collect any particles. The dilution air is then heated, and diluted samples from the outlet of the dilution chamber are drawn to the ELPI for aerosol characterization.

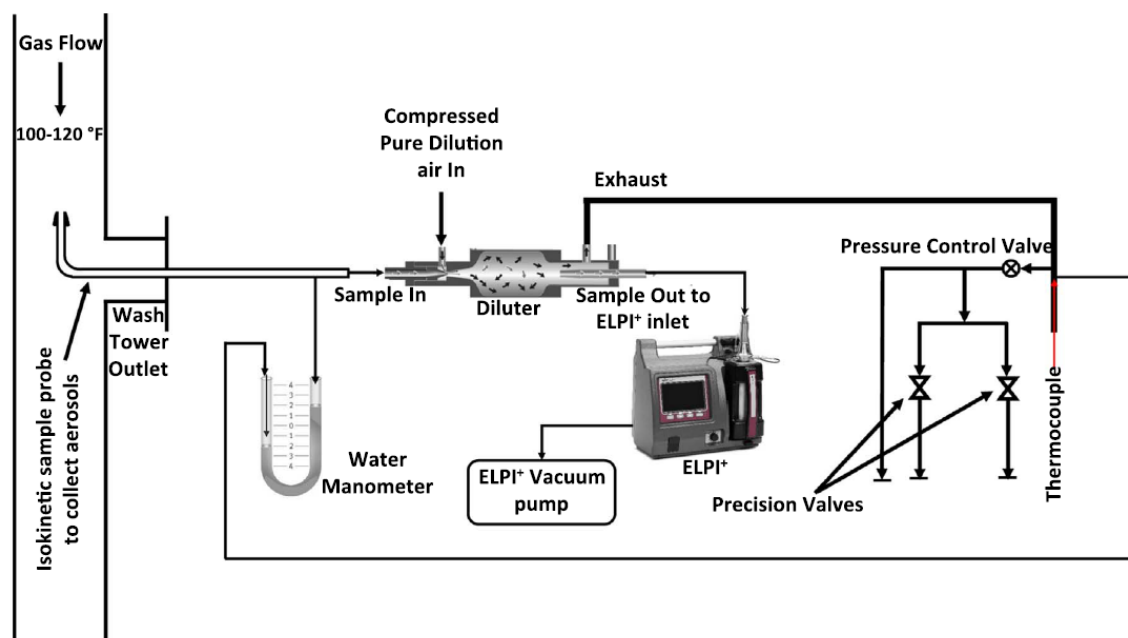


Figure 2.19: Schematic of the isokinetic sample extraction system for ELPI measurements

A downside to using the ELPI is the evaporation and loss of particles during dilution and extractive sampling. The dilution effects have been reported to affect the particle size distribution (Mertens et al., 2014; Saha & Irvin, 2017). Due to previous difficulties using a typical Dekati[®] diluter, a custom-made diluter was used in this work. The experimental setup and operation of the diluter and ELPI system used in this work were based on previous work by Saha & Anthony (2018) and Saha & Irvin (2017). The dilution ratio used varied from 4 to 7 for several tests, in good agreement with the optimal dilution of 5 from open literature. Real-time ELPI measurements were taken at the wash tower outlet using isokinetic probes. Figures 2.20 and 2.21 show the ELPI sampling setup used at the NCCC during the 2018 coal campaign.

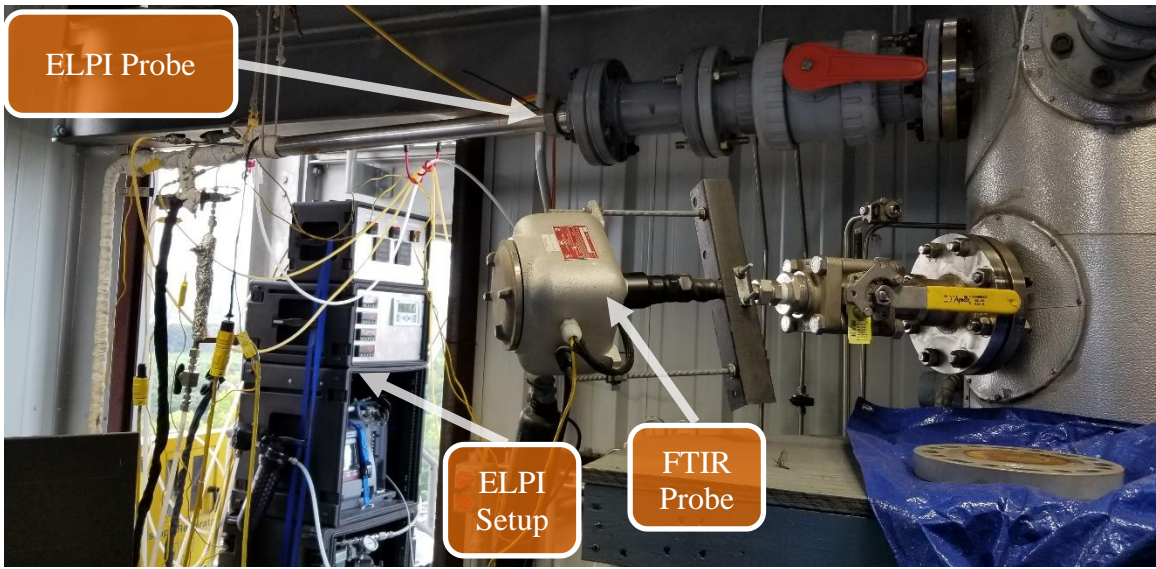


Figure 2.20: ELPI sampling setup by SRI at the NCCC showing sample port, probe, and cascade impactors

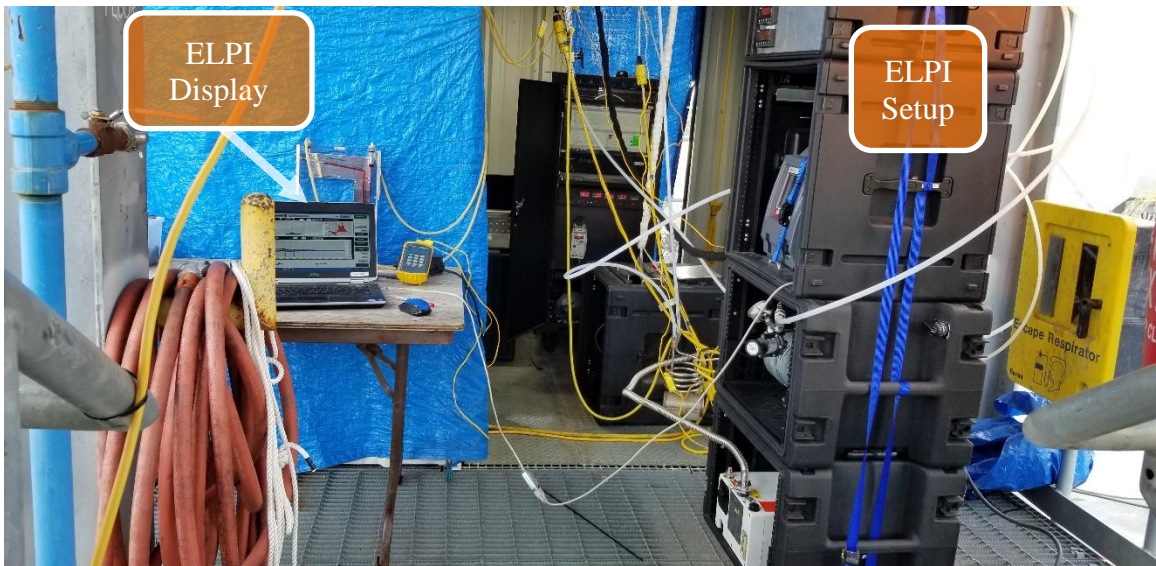


Figure 2.21: ELPI setup and display at the NCCC during the 2018 coal campaign. SRI managed the setup and operation of the ELPI.

2.3 AEROSOL NUCLEI GENERATION

There is a need for aerosol nuclei generation at pilot plants where aerosol research is carried out. A synthetic mix of air and CO₂ is used to simulate the flue gas composition for many experiments at the bench scale and pilot scale. These lack aerosol nuclei necessary for investigating aerosol emission. Some pilot plants like the NCCC, which use coal flue gas, have a baghouse and hydrated lime pretreatment process that removes a significant fraction of SO₃ entering the CO₂ capture process. In this work, two methods for generating SO₃ were applied and tested on bench and pilot scales: catalytic conversion of SO₂ to SO₃ and plasma-assisted oxidation of SO₂ to SO₃.

2.3.1 Catalytic Bed

2.3.1.1 Design

A catalytic bed, previously fabricated and tested at the UT-SRP pilot plant by Beaudry (2018), was adapted for SO₃ production during aerosol tests in this work. The catalytic bed takes a feed of SO₂ and air and produces SO₃ by catalyzing the reaction between SO₂ and O₂ (Equation 2.2). It consists of a two-pass catalyst bed filled with vanadium pentoxide (V₂O₅) catalysts and operates optimally at 520 °C (Beaudry, 2018). The bed is a Carbolite HST 12/900 furnace with a heated length of 36". The schematic for the SO₃ generator is shown in Figure 2.22. The specifications for the furnace and catalyst are shown in Tables 2.9 and 2.10, respectively.



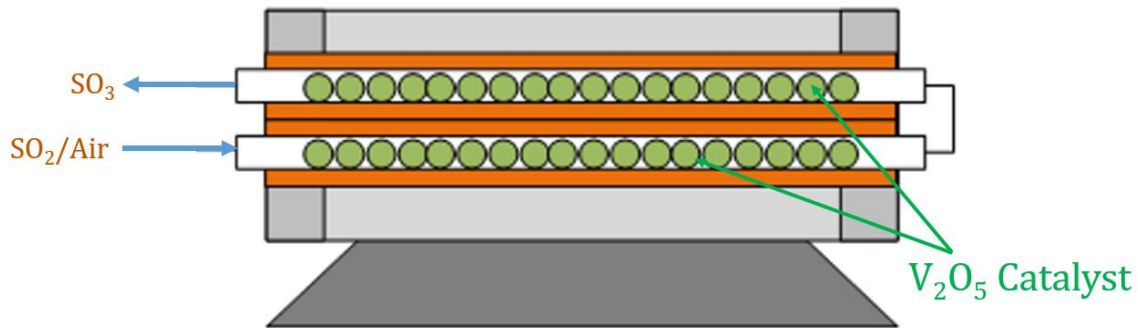


Figure 2.22: Schematic of the catalytic bed design for SO_3 production (Beaudry, 2018)

Table 2.9: Specifications of the Carbolite HST 12/900 furnace

Specifications	Value
Max Temperature ($^{\circ}\text{C}$)	1200
Number of heated zones	1
Max Tube Diameter (mm)	110
Heated Length (mm)	900
Tube length (mm)	1050
Furnace Length (mm)	1050
Furnace Height (mm)	350
Furnace Depth (mm)	410
Heat-up time (min)	45
Control Module Height (mm)	222
Control Module Width (mm)	370
Control Module Depth (mm)	376
Uniform Length $\pm 5^{\circ}\text{C}$ (mm)	450
Max Power (W)	4500
Holding Power (W)	1450
Thermocouple Type	N
Weight (kg)	60

Table 2.10: Properties of the V_2O_5 catalyst used in the catalytic bed (Research Catalysts, Inc.)

Specifications	Value
Form	Extrudes
Diameter (mm)	8
Bulk Density (lb/L)	1.35

Knife Edge Hardness (kg)	4.5
Ignition T (°C)	380
Operating T (°C)	415-630

2.3.1.2 Experimental Setup

The catalytic bed was tested and calibrated for SO₃ production at the bench and pilot scales. Figure 2.23 shows the setup at the UT-SRP lab. Two rotameters were used to control the flow of SO₂/air and N₂.

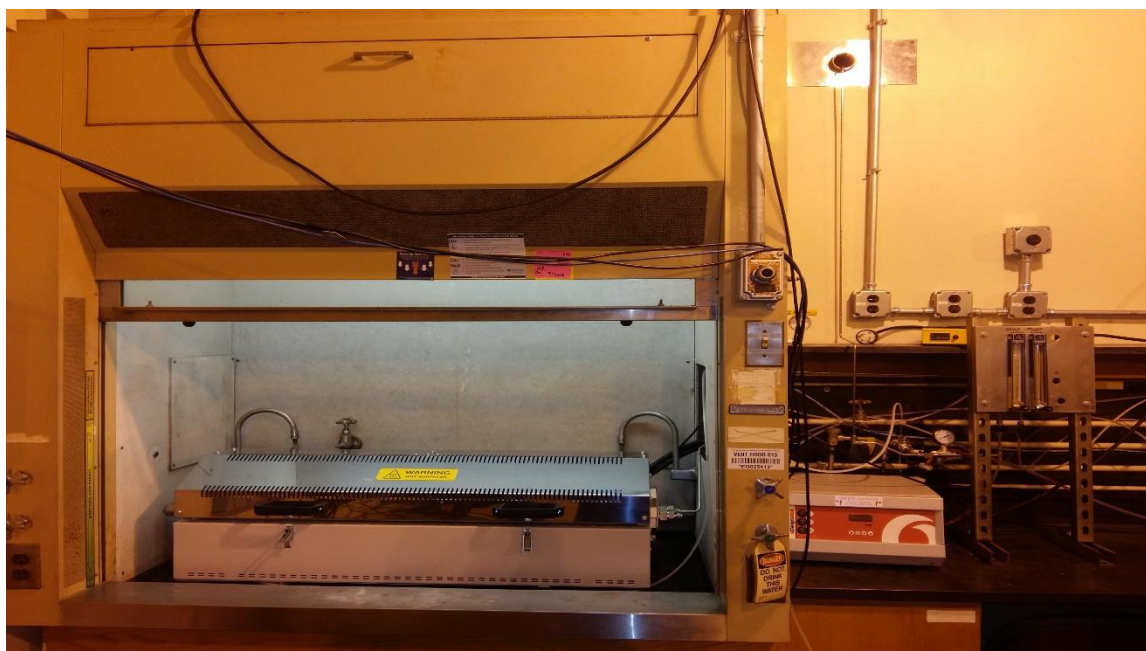


Figure 2.23: Bench-scale experimental setup for SO₃ generation with the catalytic bed at the UT-SRP lab

The bed was tested for the first time at the NCCC during the 2018 coal campaign. In this campaign, a total of 34 runs of SO₃ injections were made over two weeks. SO₃ concentration up to 8 ppm were produced and injected with the flue gas entering the absorber. Several cylinders of 8% SO₂ in air were used during the injection. These cylinders were situated in a well-vented enclosure several feet away from the pilot plant.

A safety shed with emergency shut down controls was built on the pilot skid to house the furnace. The SO_2 from the cylinders were routed in jacketed stainless steel tubing to the safety shed. The SO_3 produced was allowed to cool in a coiled tube before injection into the process. Figure 2.24 presents the experimental setup at the NCCC during the 2018 coal campaign.



Figure 2.24: Experimental setup for SO_3 generation with the catalytic bed during the 2018 coal campaign at NCCC.

2.3.1.3 Bench-scale Results

The flow rate of inlet SO₂ required to produce 10 ppm SO₃ will be much lower at the bench scale compared to the pilot-scale due to the lower gas flow rate. A precision rotameter was initially tested but found to provide unstable flow rates at flow rates less than 20 mL/min. The rotameter was replaced with a 10 mL/min mass flow controller (MFC). The MFC adapted for this work was previously calibrated for CO₂ and needed to be recalibrated for SO₂. This is because the signal generated by the MFC is dependent on the specific heat capacity of the gas flowing through it. Three calibration methods for SO₂ measurement by the MFC were performed and compared: bubble column experiment, sensor factor approximation, and molar mass approximation. The bubble column experiment was conducted by measuring the time taken for a bubble to rise through a height of 9 ml in a bubble column. The equations for the sensor factor and molar mass approximations are shown in Equations 2.3 and 2.4. Figure 2.25 shows the results from the calibration methods. The bubble column and sensor factor methods were found to be in close agreement, with the SO₂ flow rate being equal to 0.14 times the controller setpoint. The MFC set point was calibrated using the calibration factor from the bubble column experiment.

$$\text{New gas (SO}_2\text{)} = \text{Calibrated gas (CO}_2\text{)} \times \frac{\text{Sensor factor of new gas}}{\text{Sensor factor of calibrated gas}} \quad (2.3)$$

$$\text{New gas (SO}_2\text{)} = \text{Calibrated gas (CO}_2\text{)} \times \frac{\text{Molar mass of new gas}}{\text{Molar mass of calibrated gas}} \quad (2.4)$$

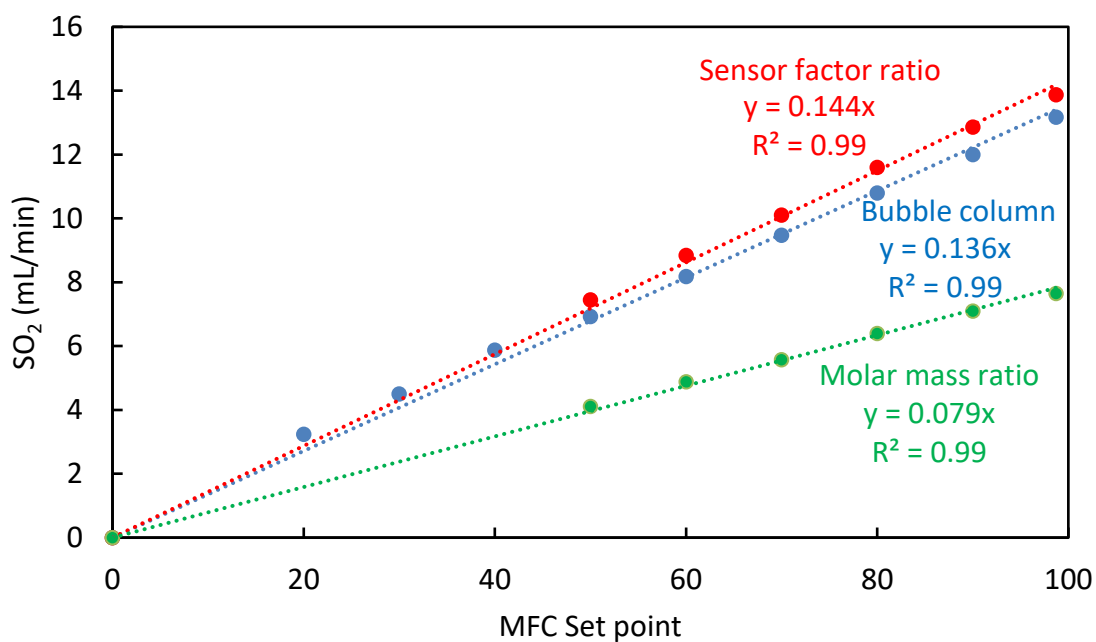


Figure 2.25: MFC calibration for SO₂ flow at the UT-SRP bench scale.

An essential requirement for evaluating the generator performance measures the conversion of SO₂ to SO₃ over the range of inlet gas flow rates. A low conversion means a significant portion of the SO₂ stream enters the absorber unconverted. The conversion was determined by tracking the SO₂ concentration exiting the furnace. With flow through the furnace, the SO₂ concentration should decrease as the furnace turns on. The decrease in SO₂ concentration was monitored by the FTIR analyzer and determined the production of SO₃. Based on the reaction stoichiometry (Equation 2.2), one mole SO₃ is produced for every mole SO₂ consumed.

The performance of the catalytic bed at low inlet SO₂ flows of 0–10 mL/min is presented in Table 2.11 and Figure 2.26. The blue trend line indicates the SO₂ entering/exiting the catalytic bed while it was turned OFF. As expected, the SO₂ concentration increased with inlet SO₂ flow. When the bed was turned ON, the SO₂

concentration dropped to negligible values indicating very high conversion from SO₂ to SO₃. An 84–93% conversion range was obtained for 0–10 mL/min inlet SO₂ flow with a positive slope indicating better conversion at higher inlet SO₂ flow. When the inlet SO₂ flow through the bed fell below 2 mL/min, the SO₂ outlet concentration never returned to zero even at zero inlet SO₂ flow. This indicates a constant bleed of about 2 ppm of SO₂ from the catalyst surface in the bed. Therefore, the catalyst bed should be flushed with N₂ after the conclusion of experiments to allow SO₂ to desorb fully.

Table 2.11: Results of experimental runs with catalytic bed at bench-scale conditions of the UT-SRP lab

Runs	MFC Setpoint	Inlet SO ₂ mL/min	Outlet SO ₂ (Bed OFF) ppm	Outlet SO ₂ (Bed ON) ppm	SO ₃ produced ppm	SO ₂ –SO ₃ Conversion %
1	73.6	10	8.36	0.57	7.79	93
2	58.9	8	7.17	0.49	6.68	93
3	44.2	6	5.77	0.46	5.31	92
4	29.5	4	4.33	0.37	3.96	91
5	14.7	2	3.03	0.29	2.74	90
6	7.4	1	1.74	0.28	1.46	84
7	0	0	1.52	0.23	1.29	85

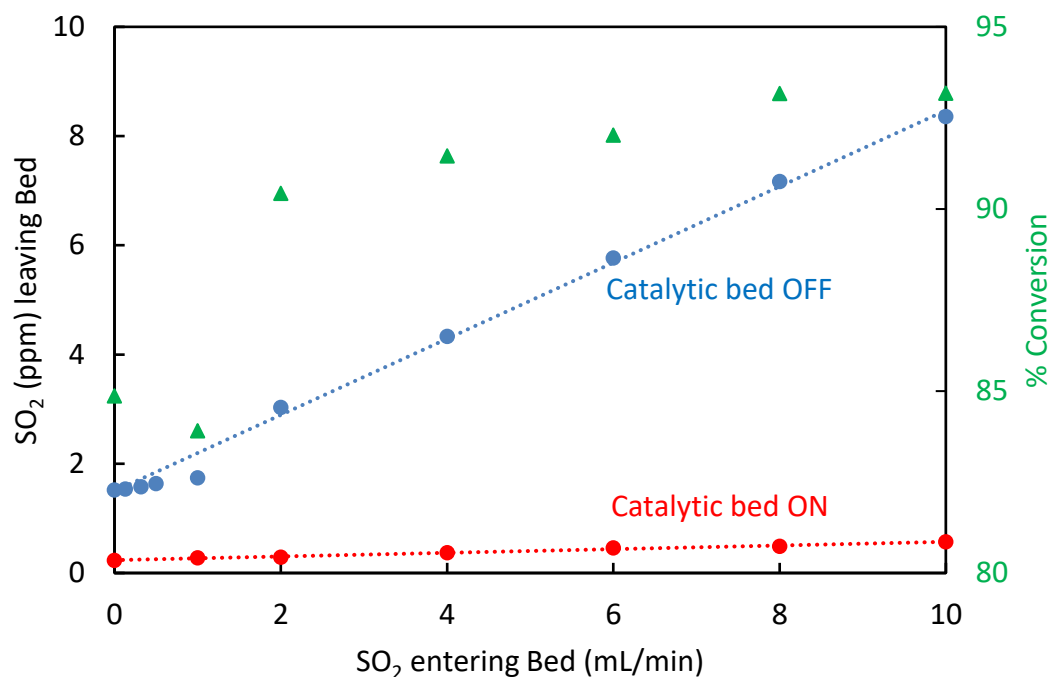


Figure 2.26: SO₂–SO₃ conversion with the tube furnace at bench-scale conditions of the UT-SRP lab.

The results in Figure 2.27 further confirm the saturation effect of the catalyst earlier identified. On a cold start, with the catalyst bed turned OFF and SO₂ flow increased from 0 to 13 mL/min, a steady outlet SO₂ concentration of 1.2–1.7 ppm was read on the FTIR, which is about one order of magnitude less than expected. This <2 ppm concentration was recorded for over 30 minutes. Significant SO₂ concentration only began to be recorded when the inlet flow was ramped up to 300 mL/min. While it is not clear how much initial SO₂ flow is required to saturate the catalytic bed upon startup, it can be concluded that nominal flow rates of 10 mL/min will take too long (>30 minutes). Therefore, it is necessary to saturate/flood the catalytic bed during startup with an excess flow of SO₂.

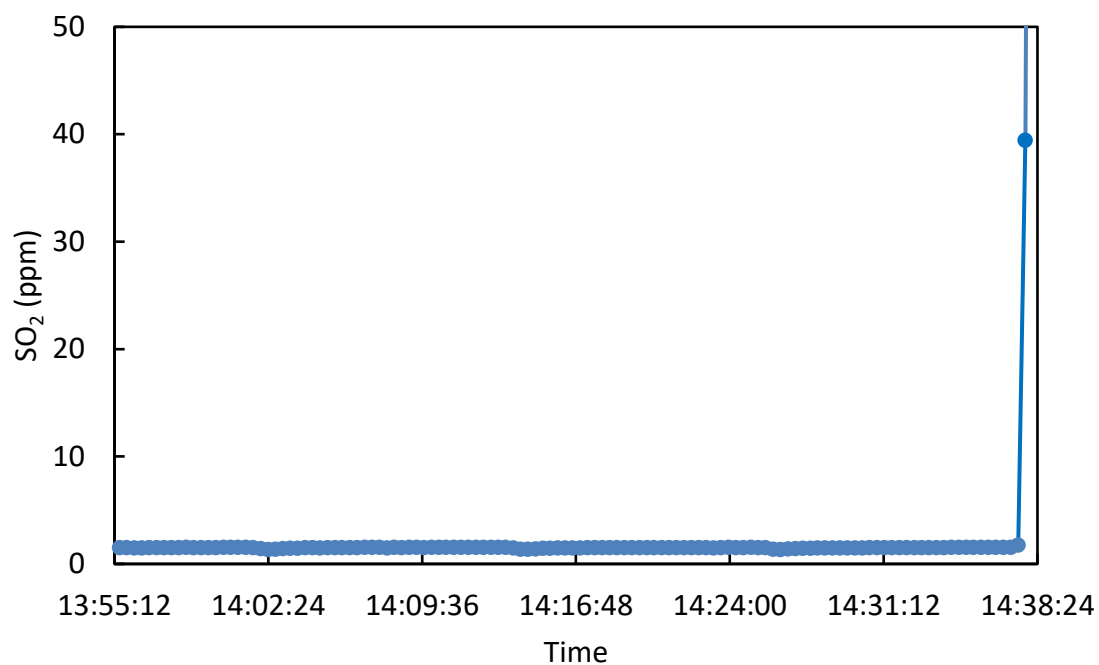


Figure 2.27: Plot showing time taken to saturate the catalyst bed. No significant SO₂ was recorded until flow was increased from 13 mL/min to 300 mL/min.

A calibration curve relating inlet SO₂ flow through the MFC to SO₃ produced is presented in Figure 2.28. The equation does not pass through the origin because of the saturation effect of the catalyst bed. Hence, for this equation to be valid, the catalytic bed must be fully saturated before the experimental runs.

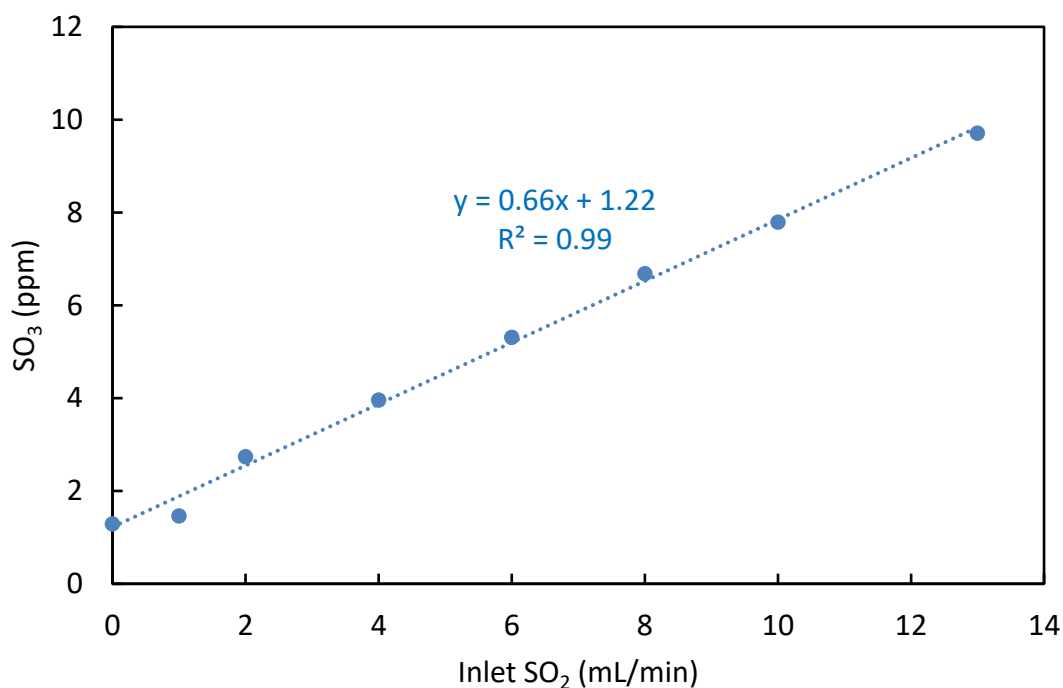


Figure 2.28: Calibration curve for SO₃ production from SO₂ with the tube furnace at bench-scale conditions of the UT-SRP lab.

2.3.1.4 Pilot-scale Results

During the 2018 coal campaign, the flow meter was calibrated for 2–8 ppm SO₃ by adjusting inlet SO₂ flow rates up to 12 SCFH and tracking the SO₂ measured by the FTIR while the furnace was ON/OFF. For example, when the furnace was OFF and inlet SO₂ flow was set to 4 SCFH, the SO₂ concentration read by the FTIR was 3.6 ppm. While maintaining the flow rate and turning the furnace ON, the reading dropped to a steady-state value of 1.66. The difference between the SO₂ measured by the FTIR with the furnace OFF and ON gives the SO₃ produced—which for this example is 1.94 ppm. Figure 2.29 shows the results of the calibration tests. The equation obtained relates the desired SO₃ concentration in the flue gas to the required SO₂ flow rate into the furnace. The conversion increased with inlet SO₂ flow rate or SO₃ produced and averaged 97% throughout the flow

rates tested (Figure 2.30). A greater average conversion was achieved at the pilot-scale (97%) than the bench-scale (90%), confirming that the catalytic bed is more efficient at larger flows.

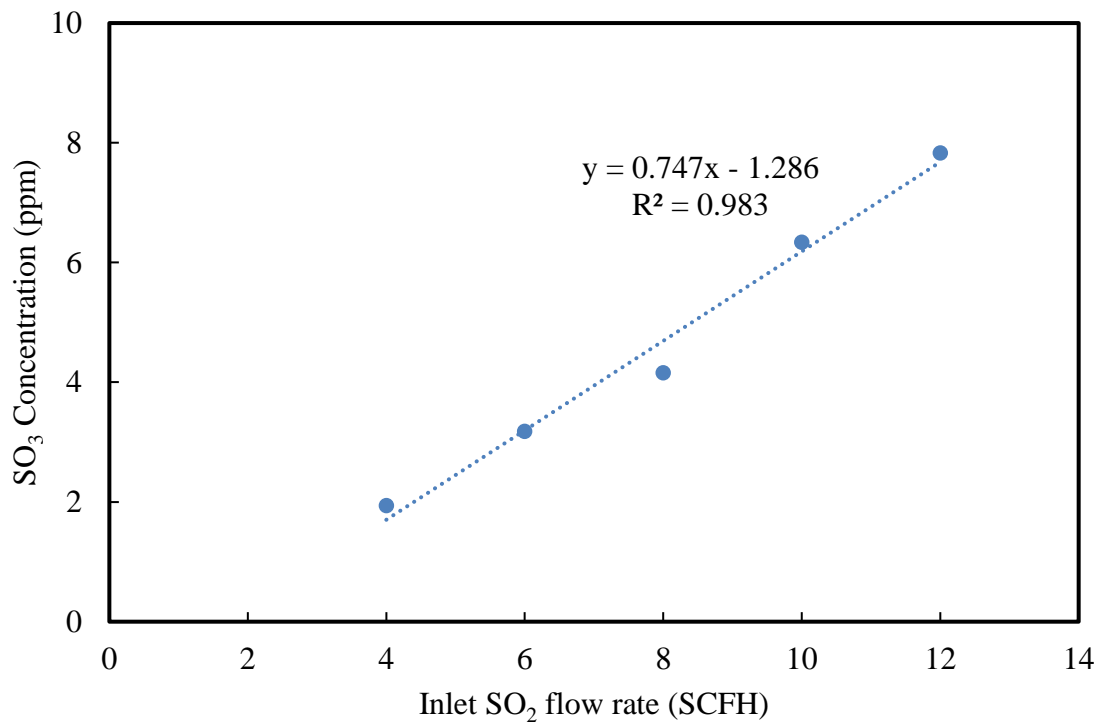


Figure 2.29: Calibration curve for SO₃ production from SO₂ with the tube furnace during the 2018 coal campaign at NCCC.

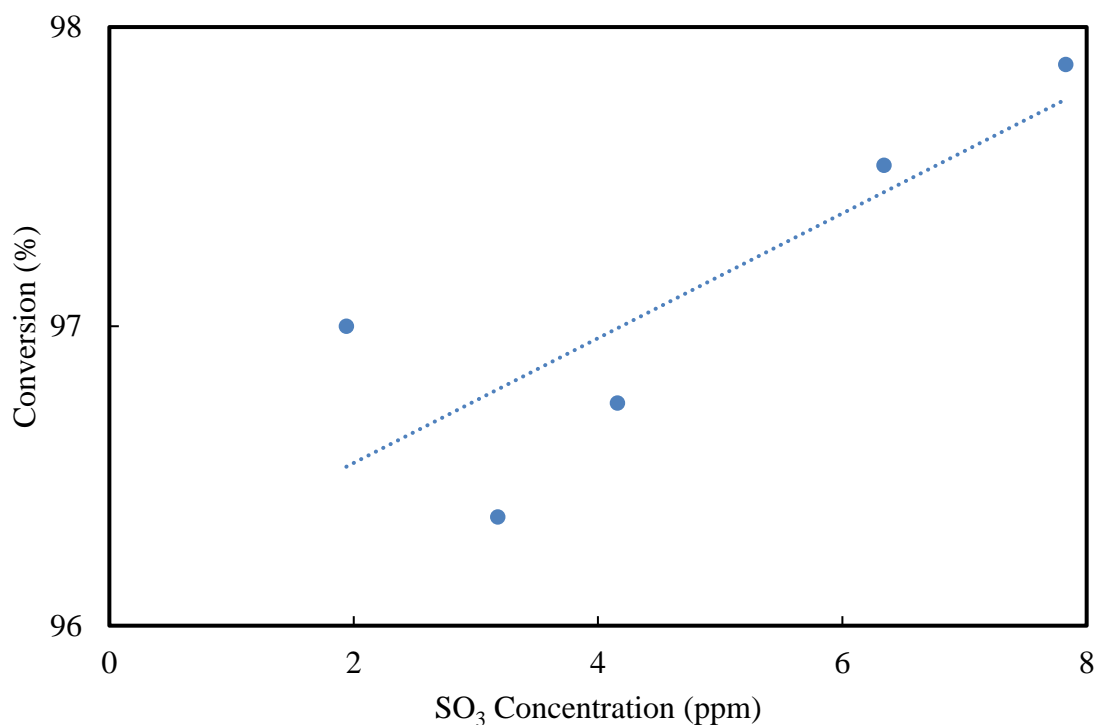


Figure 2.30: SO₂–SO₃ conversion with the tube furnace during the 2018 coal campaign at NCCC. 97% average conversion was obtained.

2.3.2 Plasma Generator

2.3.2.1 Design

A custom-made dielectric-barrier discharge (DBD) setup was adapted for SO₃ production in this work. The design involves plasma-assisted oxidation of SO₂ to SO₃ with a coaxial dielectric barrier discharge to generate the atomic oxygen. The schematic of the DBD experimental setup was modeled after Sardja & Dhali (1990) and has been widely used in the industry for ozone synthesis. Although this design has been previously applied to remove SO₂ from flue gas and collect the SO₃ produced over water, it has not been directly used to create aerosol nuclei for injection purposes (Sardja & Dhali, 1990; Saveliev et al., 2007).

The plasma generator operates on a dielectric barrier discharge principle: an electrical discharge between two electrodes separated by an insulating dielectric barrier. The dielectric barrier, in this case, is glass. One of the electrodes acts as the high voltage electrode with a connection to a high voltage power source, while the second is the ground electrode with ground wiring from the power source. The plasma region formed contains highly mobile electrons that dissociate the incoming oxygen, which then oxidizes SO_2 to SO_3 .

The plasma generator is designed to produce SO_3 from a feed of SO_2 in air. The SO_3 then rapidly hydrolyses when injected into a water vapor-saturated environment to form a sulfuric acid aerosol. The mechanical drawings for the plasma generator and Teflon bushings are shown in Figures 2.31–2.34. The setup consists of a tubular reactor with a high voltage power supply. The power supply has an output of up to 300 W and independent voltage control of 40kV pk-pk. It can easily be turned ON/OFF with the switch and finds excellent application to pilot plant operations where the ease of startup and shutdown is valuable. The single-tube reactor has a quartz glass tube of 0.5” diameter and wall thickness of 0.04”, wrapped with aluminum foil serving as a low voltage electrode. A stainless steel rod of 1/8” diameter centered inside the quartz tube serves as the high voltage electrode. The setup has a total capacitive load of 34pf per meter and a discharge gap of 0.14 inches.

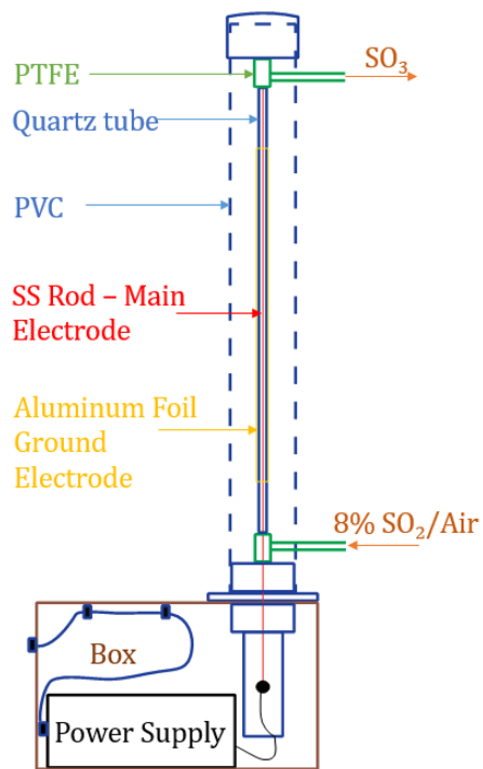


Figure 2.31: Custom-made plasma generator showing the materials, electrodes, and gas flow path

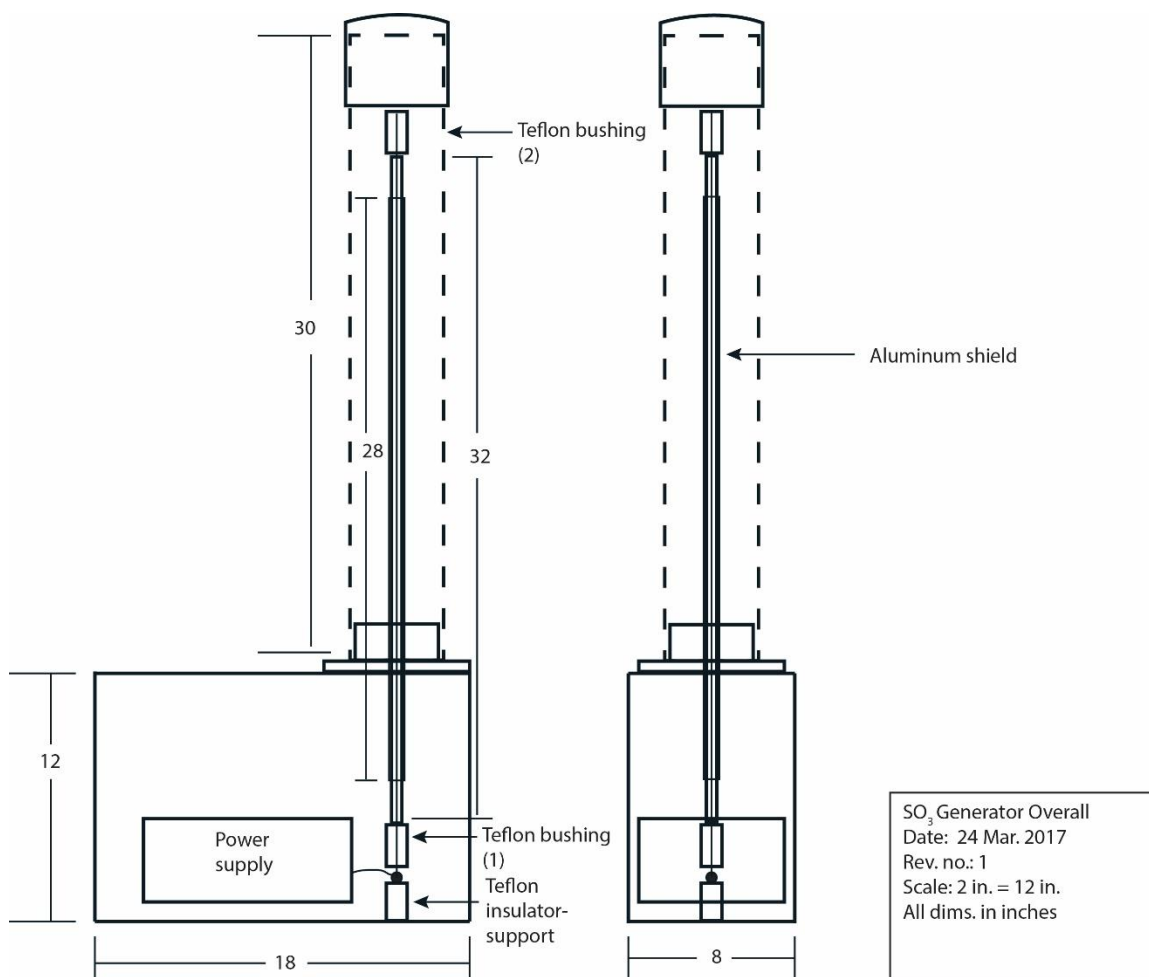


Figure 2.32: Front and side projections of the plasma generator showing the dimensions

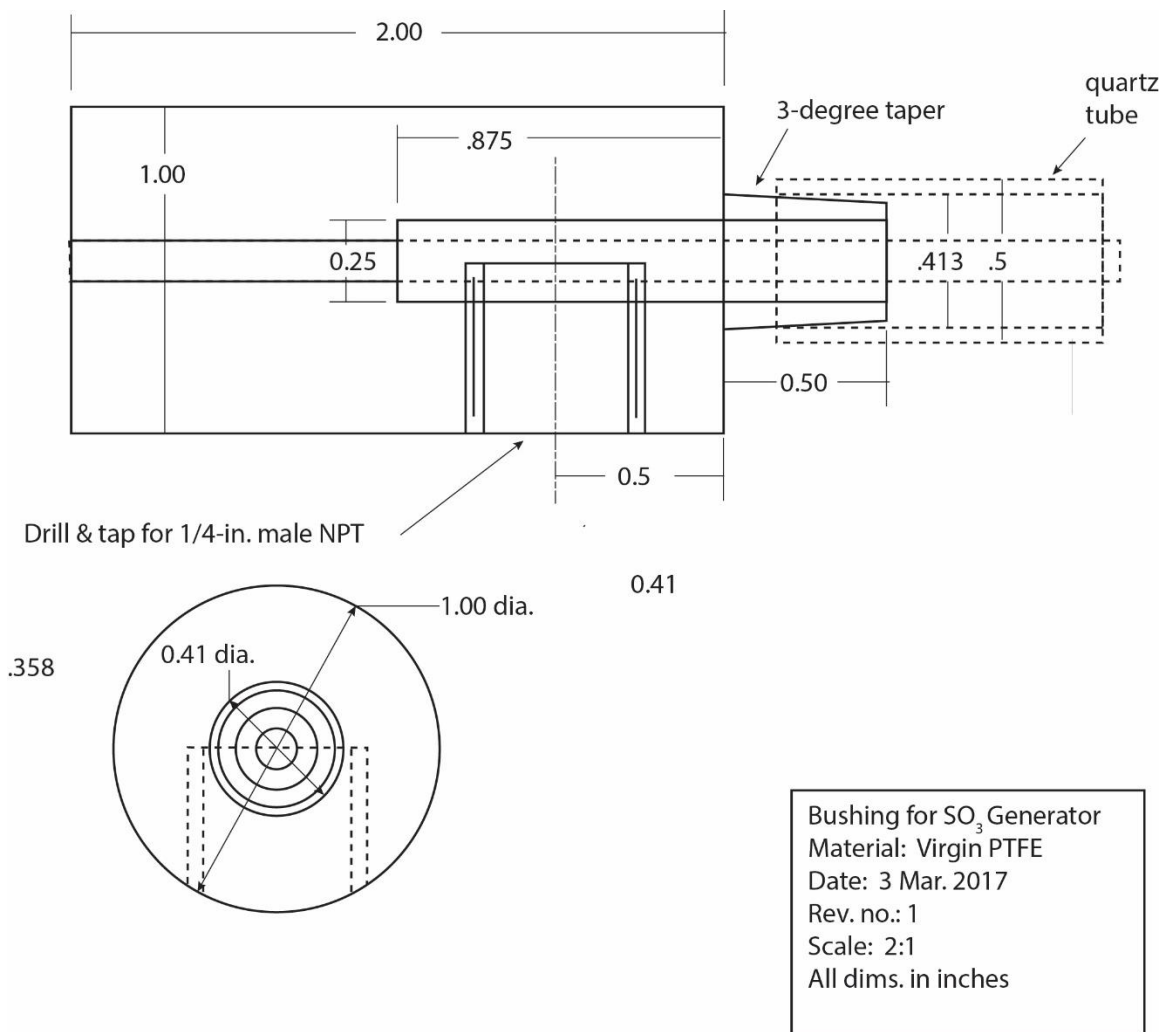


Figure 2.33: Mechanical drawing for the Teflon bushing at the top of the plasma generator

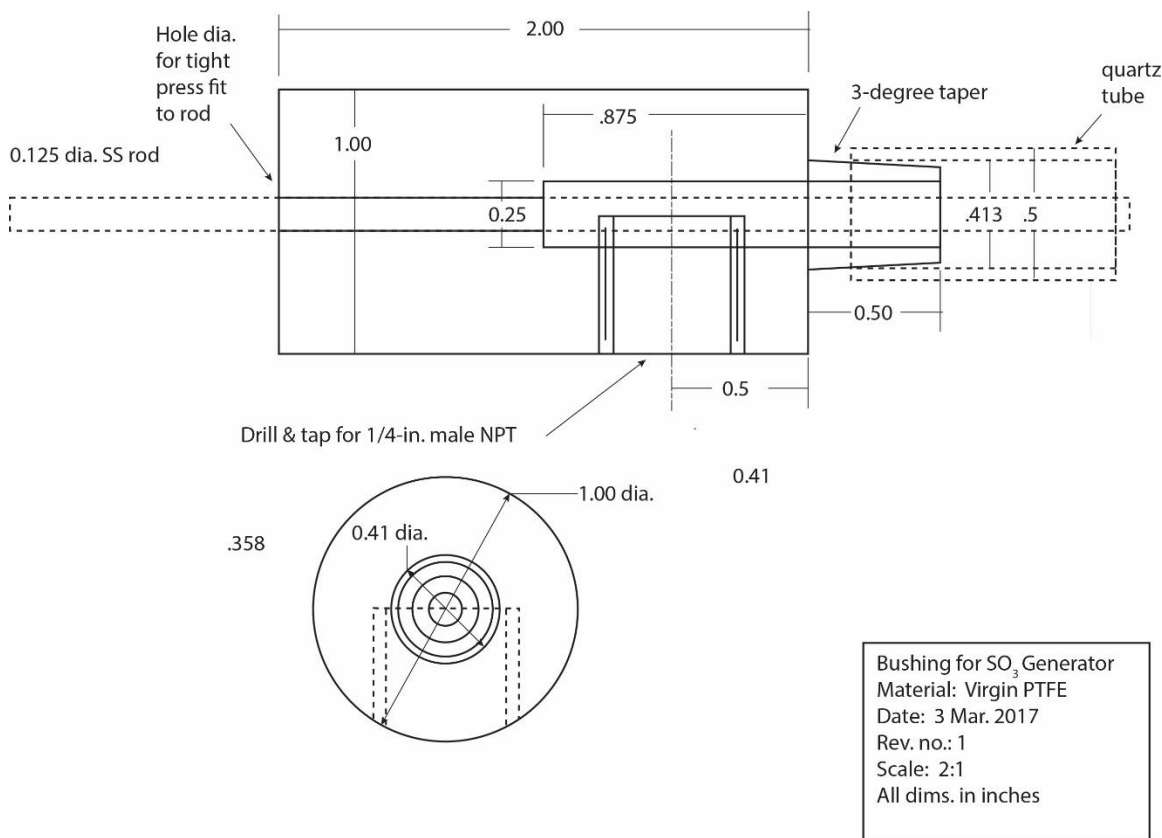


Figure 2.34: Mechanical drawing for the Teflon bushing at the bottom of the plasma generator

2.3.2.2 Reaction Mechanism

The reaction mechanism has been studied by Sardja & Dhali (1990) and involves the following four reactions:



where M is either O₂ or N₂.

The loss of atomic oxygen (O) through Equation 4 is not significant because the concentration of O₃ is orders of magnitude smaller than O₂. Assuming a pseudo-steady state hypothesis for the atomic oxygen, the resulting rate for the conversion of SO₂ to SO₃ is:

$$\frac{d[SO_3]}{dt} = \frac{2k_1k_2[e][O_2][SO_2]}{k_2[SO_2]+k_3[O_2]} \quad (2.9)$$

From the rate above, it is expected that the initial addition of oxygen molecules will increase the atomic oxygen concentration up to a threshold where further addition of oxygen molecules favors ozone formation. In other words, at a high O₂ concentration, the rate of SO₃ formation becomes independent of the inlet O₂ concentration.

2.3.2.3 Experimental Setup

The plasma generator was tested at a bench-scale aerosol growth column at UT-SRP. The inlet SO₂ flow to the plasma generator was diluted with N₂. One rotameter controlled the 8% SO₂/air flow between 0.3 L/min and 2 L/min, while another rotameter controlled N₂ flow at 4 L/min. The flow exiting the plasma generator was routed into a CX-4000 FTIR analyzer and vented to the atmosphere through a carbon bed. The pictures of the fabricated plasma generator and the experimental setup tested at UT-SRP are presented in Figures 2.35 and 2.36.

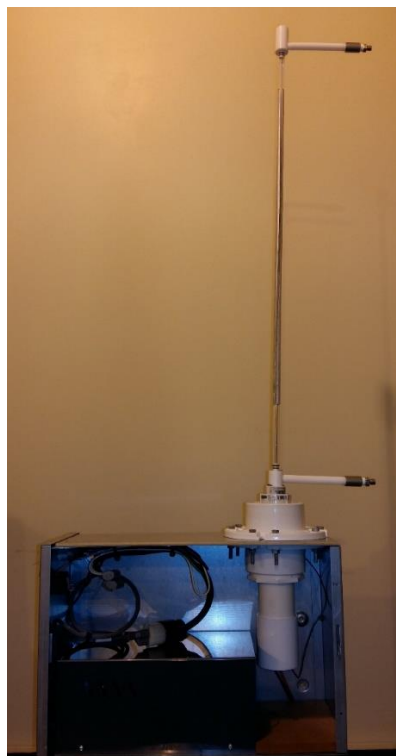


Figure 2.35: Picture of fabricated plasma generator showing tubular glass reactor and power supply



Figure 2.36: Picture of the plasma generator inside a fume hood at the UT-SRP lab

2.3.2.4 Results

The results from the plasma generator test are presented in Table 2.12 and Figure 2.37. The rotameter was calibrated for SO₃ by adjusting inlet SO₂ flow rates up to 2 L/min and tracking the SO₂ exiting the generator. When the Plasma was turned ON, the SO₂ concentration decreased, corresponding to SO₃ production. The conversion from SO₂ to SO₃ was inversely proportional to SO₂ flow and averaged 10%. The SO₃ concentrations produced were excessive for aerosol tests, and better conversion may be obtained at much lower SO₂ flow rates.

Table 2.12: Results from Plasma generator test to produce SO₃ from SO₂

Runs	SO ₂ Flow L/min	SO ₂ with Plasma OFF ppm	SO ₂ with Plasma ON ppm	SO ₃ Produced ppm	SO ₂ -SO ₃ Conversion %
1	0.3	1535	1306	230	15%
2	0.5	2957	2545	411	14%
3	1	6600	5778	822	12%
4	1.5	10419	10003	416	4%
5	2	13786	13141	645	5%

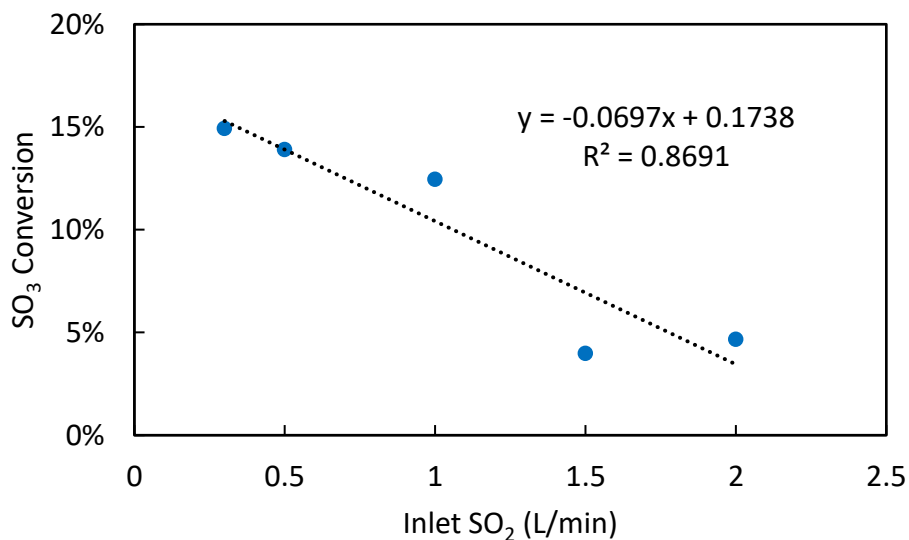


Figure 2.37: SO₂–SO₃ conversion with the plasma generation. 10% average conversion was obtained.

2.3.2.5 Challenges and Recommendations for Future Work

The SO₃ generation process via DBD poses significant health risks. SO₂ and SO₃ gases are harmful if inhaled. The quartz tube could shatter and lead to an SO₂/SO₃ leak. This safety concern was mitigated by sheltering the glass tube within a PVC pipe. Also, the return line from the FTIR was vented to the atmosphere through a carbon bed.

Another safety concern is the risk of high voltage exposure from the power supply. A decision was made to place the power supply within the box to prevent exposure to the power lines. The box was modified with control knobs to make the power switch accessible from the outside.

Although the 1st generation prototype of this setup was successfully designed, fabricated, and tested, the results of less than 15% conversion are underwhelming. Future upgrades to this setup should be made to maximize the conversion. Upgrades should focus on increasing the intensity of the plasma or increasing the residence time for reaction. The plasma intensity can be increased by reducing the discharge gap between the electrodes, selecting better electrodes, or increasing the power supply. The residence time can be increased by increasing the reactor length or fabricating a series/cascade reactor configuration. Table 2.13 compares the plasma generator to the catalytic bed and a previous aerosol nuclei generator designed by Fulk (2016) called the Liquid Vaporizer and Injector (LVI).

Table 2.13: Comparison of the Plasma Generator to the Catalytic Bed and the Liquid Vaporizer and Injector (LVI)

	Liquid Vaporizer and Injector (LVI) (Fulk 2016)	Catalytic Bed	Plasma Generator
Feed	H ₂ SO ₄	8 % SO ₂ in Air	8 % SO ₂ in Air
Operating Temperature	325 °C	520 °C	90 °C
Equation of Reaction	$H_2SO_4(l) \rightarrow H_2SO_4(g)$	$2SO_2 + O_2 \rightarrow 2SO_3$	$e + O_2 \rightarrow e^- + O + O$ $O + SO_2 + M \rightarrow SO_3 + M$
Max. SO ₂ conversion	–	98%	15%
Time required to start-up	60 minutes	90 minutes	Instant
Max. Power	–	4500W	300W
Total Fabrication Cost	\$5,000	\$11,000	\$1,500
Experimental Limitations	Eductor plugs due to corrosion, unstable injection rate, and pulsating aerosol stream	Bed saturation and desorption	Low SO ₂ conversion

Table 2.13: Comparison of the Plasma Generator to the Catalytic Bed and the Liquid Vaporizer and Injector (LVI)
(continued)

	Liquid Vaporizer and Injector (LVI) (Fulk 2016)	Catalytic Bed	Plasma Generator
Potential for Upgrades	Replace steel components with glass tubing	Optimize performance	Increase plasma intensity and reaction residence time
Safety Concerns	Corrosion leaks and burn	Harmful Catalyst	Gas leak
Best suited for	Bench scale	Bench and Pilot scales	Bench scale

2.4 RECOMMENDATIONS FOR GAS AND AEROSOL SAMPLING AT UK CAER

This section contains recommendations for gas and amine aerosol sampling at the UK CAER large pilot CO₂ capture unit. The gaseous components of interest are CO₂, NH₃, SO₂, amine, and water. A robust emission sampling system should measure a baseline for aerosol number concentration and aerosol size distribution of the flue gas entering the CO₂ capture process and continuously monitor the volatile amine species in the gas streams exiting the water wash.

2.4.1 Baseline Particulate Measurements at Wyoming ITC

The recommendation is to measure particulate (fly ash and SO₃) concentration in the flue gas from the Wyoming ITC to establish a baseline and identify the potential for aerosol episodes. The ITC facility collects SO₂ and alkaline ash with hydrated lime in a baghouse. The resulting concentrations of SO₃, submicron particulate, and alkali particulate will probably be too small to constitute a significant risk of aerosol emissions from the pilot plant. Published measurements in pilot plants have established that amine aerosol is not generally a problem if the particle count is less than 10⁵ particles/cm³. The SO₃ and particulate number concentration of the flue gas entering the CO₂ capture system should be tested to confirm low concentrations. A particle counter such as the ELPI, Condensation Particle Counter (CPC), or Scanning Mobility Particle Sizer (SMPS) should be used for the particle concentration measurements.

2.4.2 Gas and Aerosol Sampling Setup for UK CAER

The recommended sampling setup for volatile amines and amine aerosol at the UK CAER large pilot CO₂ capture unit is presented in Figure 2.38. Three locations were identified for gas and aerosol sampling: absorber gas inlet, absorber gas outlet, and water

wash gas outlet. The gas exiting the water wash should be monitored continuously with an FTIR analyzer for amine and amine degradation products. The aerosol size distribution at the outlet is expected to range from 0.01 to 10 μm , and its size and concentration can be effectively measured using a PDI or an ELPI. The amine concentrations from the absorber gas outlet should be measured to evaluate the effectiveness of the water wash in reducing amine emissions.

Aerosol concentration at the absorber gas inlet should be measured using a particle counter to provide a baseline and evaluate the effectiveness of the Wyoming ITC baghouse. The ELPI is recommended, but a CPC or SMPS can also be used for this location. Also, the vapor phase concentration should be monitored with FTIR spectroscopy for NH_3 slippage from the power plant.

Two approaches are highlighted for gas sampling with FTIR spectroscopy:

- (a) Sampling with portable FTIR analyzers: Three FTIR analyzers could be used to sample each of the three locations. The spectrometers should be located close to the sample locations. This setup is ideal for temporary or short-term sampling.
- (b) Sampling with centrally located FTIR analyzer(s): The FTIR analyzer(s) should be placed in a central location on the ground floor with sample lines from the three locations (absorber gas inlet, absorber gas outlet, and water wash gas outlet) running into the shed. Each location could be sampled with a dedicated FTIR analyzer. Alternatively, a single FTIR analyzer can be used to sample from all three locations. In this case, the sample lines from the different locations will be connected through valves with pneumatic controls to regulate gas flow from one port at a time. This method is ideal for continuous or long-term sampling and could be a permanent feature of the unit.

Although the results from the FTIR analyzers can be extracted manually from the CPU, we recommend that it is fully integrated into the pilot plant control scheme.

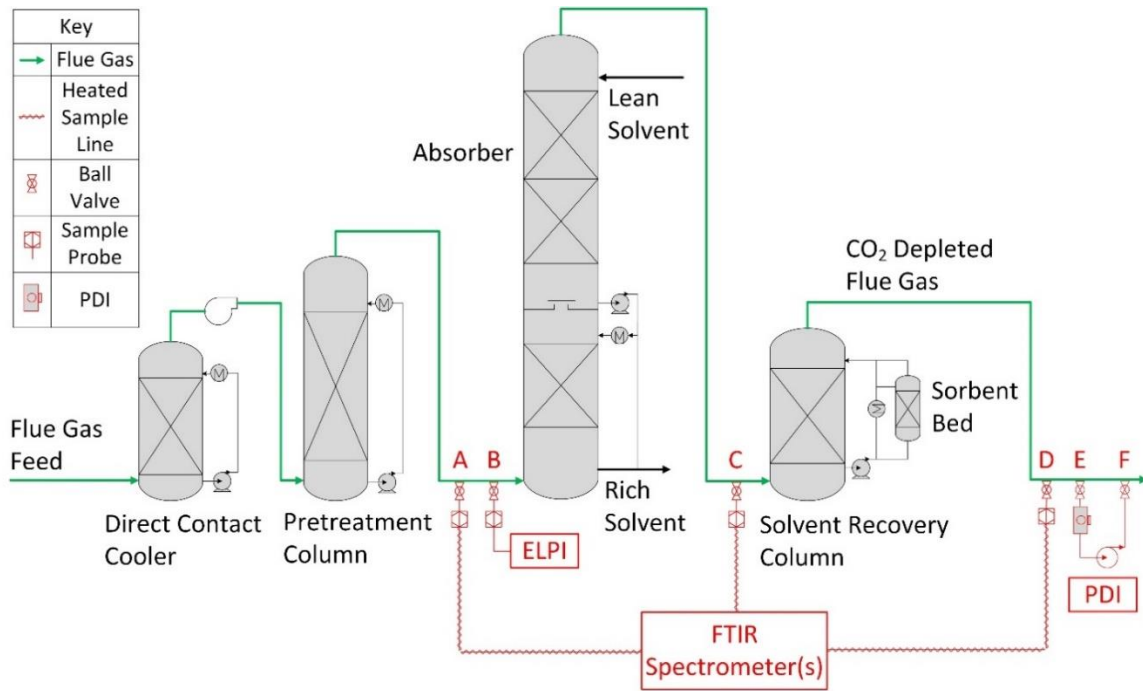


Figure 2.38: Process flow diagram of UK CAER CO₂ capture pilot plant with recommended gas and aerosol sampling

The recommended sampling locations, sample ports, ball valve size, analyzers, and function are presented in Table 2.14. A total of six sample ports were identified. Two ports at the absorber gas inlet for FTIR and ELPI measurements, one at the absorber gas outlet for FTIR measurements, and three at the water wash gas outlet for FTIR and PDI measurements. 1” ball valves are recommended for the PDI sample ports, while 3” ball valves are recommended for all other ports.

Table 2.14: Three sampling locations, six sample ports, and three FTIR analyzers are recommended for UK CAER

Sample Location	Sample port	Ball Valve	Analyzer	Gas sampled/Function
Absorber Gas Inlet	A	3"	FTIR #1 (Optional)	CO ₂ , water, NH ₃ , and SO ₂
	B	3"	ELPI #1 (Optional)	Aerosol concentration and size distribution
Absorber Gas Outlet	C	3"	FTIR #2	CO ₂ , water, NH ₃ , and amine
Water Wash Gas Outlet	D	3"	FTIR #3	CO ₂ , water, NH ₃ , and amine
Outlet	E (Extraction port)	1"	PDI #1	Aerosol concentration and size distribution
	F (Return port)	1"		

2.4.3 Sampling Port Requirements

Six sample ports (A–F) were identified, as shown in Figure 2.38. Three (Ports A, C, and D) are for the FTIR sample locations, while the other three are for ELPI (Port B) and PDI (Ports E and F) sample locations.

2.4.3.1 FTIR Sample Ports

Figure 2.39 presents the sample port requirements for gas sampling using the FTIR. The FTIR probe should be inserted through the ball valve and into the duct and must have sufficient clearance for the 1" probe tip diameter. 4" 150# sample ports are recommended for all sample locations. The sample ports should have 3" full port ball valves installed and adapted with flanges or bushings to a 1" MNPT. The 1" Swagelok compression fitting to 1" MNPT fitting will be connected at this point. The probe length should be modified to have at least 1.75" penetration into the duct to avoid pipe wall-flow effects.

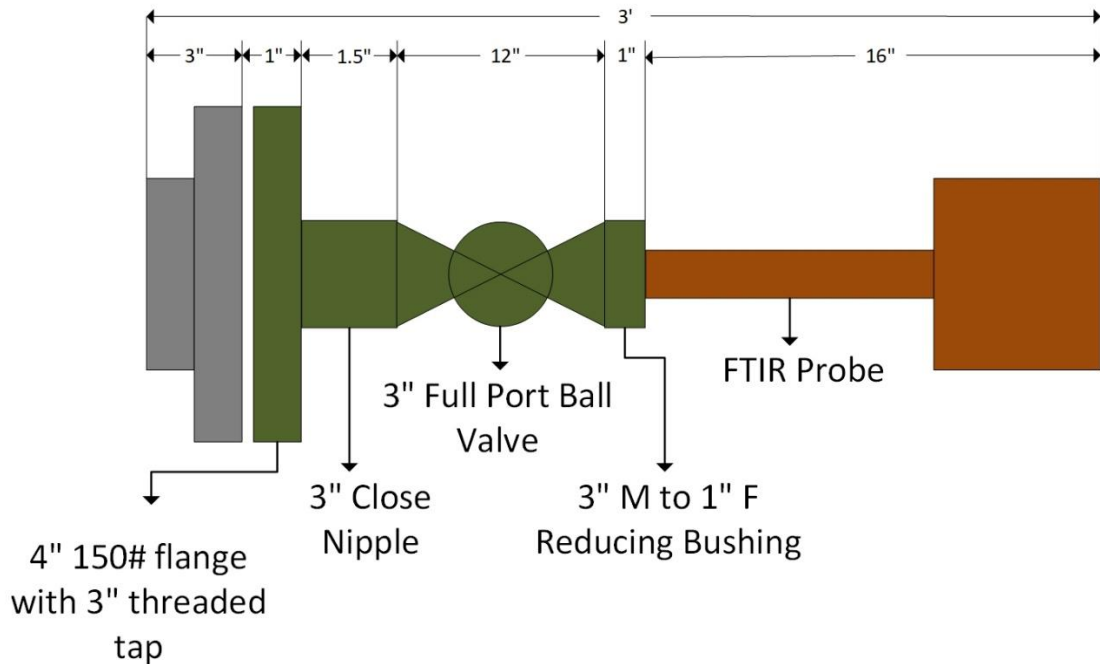


Figure 2.39: FTIR sample port requirements. 3" full port ball valves are required for Port A at the absorber gas inlet, Port B at the absorber gas outlet, and Port D at the water wash gas outlet.

2.4.3.2 PDI Sample Ports

For PDI measurements, 5–30 Lpm of gas will be extracted from port E and returned to port F with a blower. The return port should be at least 3 ft downstream of the extraction port. The gas pulled will flow through the PDI cell, where it is analyzed before returning to the duct. Figure 2.40 presents aerosol sampling requirements for the PDI.

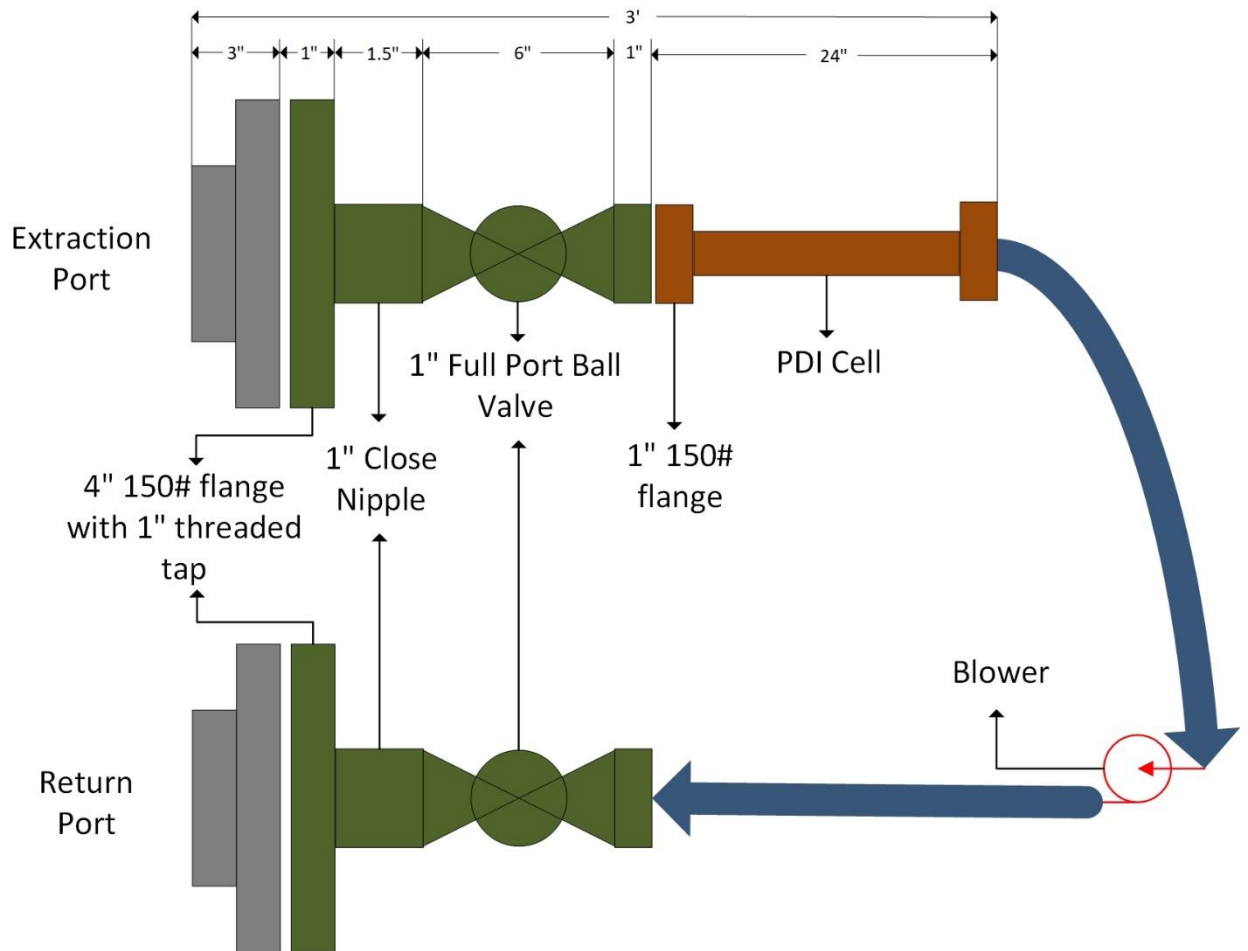


Figure 2.40: PDI sample port requirements. 1" full port ball valves are required for ports E and F at the water wash gas outlet.

2.4.3.3 Space requirements

The ports should be located to ensure that flue gas sample conditions are the same but sufficiently apart. That way, any flow disturbances introduced by upstream sample trains will not influence samples taken downstream. All the ports should preferably be at ground level, lower than 5 ft above the platform, with 10 ft of clearance around the duct. This will significantly help with the convenient installation of the probes and ease of moving the instruments. Mechanical supports such as ratchet straps should secure the

probe to the roof or a nearby structure. We recommend that a shed with heating and ventilation be provided on the ground level for the FTIR analyzer(s). Also, the shed location should be central to the sample ports to minimize the length of the sample lines.

Chapter 3: PZ Aerosol Emissions and Mitigation at Pilot Scale

This chapter presents the first demonstration of PZ aerosol mitigation at a pilot scale. It is also the first pilot-scale demonstration of emission reduction for any solvent with varying flue gas SO₃ concentrations. This work was conducted during the 2018 pilot plant campaign at the National Carbon Capture Center (NCCC) with coal flue gas and the piperazine advanced stripper (PZASTM). Southern Research Institute (SRI) set up, operated, and provided the raw data from ELPI measurements during the campaign. This chapter is based on a paper presented at the Greenhouse Gas Control Technologies (GHGT-14) conference and published with the International Journal of Greenhouse Gas Control (IJGGC) (Akinpelumi et al., 2019).

3.1 INTRODUCTION

The capture of CO₂ from large point sources is key to abating anthropogenic climate change. Adaptability, flexibility, and technological maturity have made amine scrubbing the technology of choice for post-combustion carbon capture, particularly for capture from coal-fired power plants (Rochelle, 2009). However, pivotal to its commercial deployment are long-term demonstrations of process reliability and reductions in capital and operational expenses. To this end, pilot-scale projects have been conducted in the past decade at several research facilities worldwide, focusing on energy performance, process configurations, and solvent choice.

Amine loss from the absorber as vapor and aerosol have been reported in several of these pilot plant projects, with emissions in some instances exceeding 1000 ppm (Kamijo et al., 2013a; Moser et al., 2014; Thompson et al., 2017). These pilot studies have shown that a water wash section can absorb most of the vapor amine after the absorber. However, amine aerosol is formed and emitted when particles such as fly ash or liquid aerosol

resulting from sulfur trioxide (SO_3) are present in the flue gas. The conventional wash tower alone becomes ineffective for mitigation (Mertens et al., 2013).

The oxidation of sulfur contained in fossil fuels forms sulfur dioxide (SO_2), which can be further oxidized to SO_3 in selective catalytic reduction (SCR) of nitrogen oxides (NO_x) or at other points in the combustion process (Srivastava et al., 2004). Gas-phase SO_3 quenched upstream of the CO_2 capture absorber produces acidic aerosol, resulting in amine aerosol emissions in the scrubbed gas. Beaudry et al. (2018) investigated the effect of SO_2 and SO_3 in flue gas on amine emissions. They concluded that SO_3 was the more potent nuclei for amine emissions with up to 7.6 mol piperazine (PZ) emitted per mol SO_3 . Depending on the cost, environmental regulations, and toxicity of the amine and degradation products, the loss of amine through aerosol emissions in the CO_2 -scrubbed gas could have significant economic, environmental, and safety implications (Shao & Stangeland, 2009).

A few attempts have been made to hypothesize the mechanisms for amine aerosol formation and growth in the absorber and its mitigation by altering absorber operating parameters. Existing literature suggests that amine aerosol grows in the absorber through the uptake of water, CO_2 , and amine on existing aerosol. Khakharia et al. (2015) studied the effect of lean solvent temperature, lean solvent pH, and flue gas CO_2 on emissions with aminomethyl propanol (AMP)/piperazine (PZ). They concluded that the amine aerosol particle number concentration, supersaturation, and reactivity were crucial for emission reductions. Bade et al. (2015) patented a method to inhibit amine aerosol formation in the absorption zone of the absorber by avoiding quenching or rapid cooling of the gas mixture in the absorber. They claim that if the temperature of the lean solvent entering the absorber is less than 5 °C lower than the maximum temperature in the absorption section of the absorber, cooling of the gas will be avoided and aerosol formation in the absorption zone

also substantially reduced. They also suggest that although the top of the absorber has greater amine partial pressure, operating the absorber with an elevated lean solvent temperature prevents amine aerosol formation at the absorber top and results in emission mitigation.

More recent modeling studies show that emission mitigation at elevated lean solvent temperature may be due to amine aerosol growth and collection rather than the prevention of amine aerosol formation. Kang et al. (2017) and Majeed et al. (2017) developed models that predict amine aerosol growth in the absorber and account for amine driving force depletion in the bulk gas phase. Zhang et al. (2017) show that PZ aerosol can grow up to 5 μm in the absorber and 12 μm in the water wash. They conclude that amine aerosol emission can be controlled by enhancing aerosol growth to large enough sizes for collection by impaction in the absorber. As PZ aerosol concentration increases, aerosol growth decreases, and the limiting driving force for aerosol growth shifts from gas-to-drop to liquid-to-gas (Zhang, 2018). The experimental results presented in this work will be interpreted using the theory from the more recent modeling results, but these experiments were not designed to validate this theory.

Aqueous PZ is considered a superior solvent to MEA because of its fast absorption rate, relatively wide solubility range, good energy performance, and moderate volatility (Rochelle et al., 2011). While growth models from existing literature show trends for aerosol mitigation, the demonstration and quantification of these strategies for PZ on the pilot-scale has not been done. The aerosol growth models have also not been validated with pilot plant results. Earlier studies done with other solvents have largely considered amine emissions in response to process changes without creating a dedicated test plan for long-term emissions control. There has been minimal comprehensive data presentation demonstrating the effect on amine emission of increasing the flue gas SO_3 , lean solvent

temperature, and the residence time of the gas at water wash conditions for piperazine or other solvents.

This paper presents results from research conducted at the National Carbon Capture Center (NCCC) in Wilsonville, Alabama, USA. Two mitigation strategies were successfully implemented during episodes of PZ aerosol emission. These episodes resulted from SO_3 in the flue gas due to periods of sub-optimal SO_3 removal upstream of the CO_2 capture facility. Four weeks of aerosol tests were also run with 0–6 ppm of SO_3 generated and injected into the flue gas to evaluate the resilience of the mitigation strategies. The first approach to aerosol emission mitigation was to remove aerosol nuclei present in the flue gas. The second approach was to run the absorber (with flue gas containing varying SO_3) at conditions that accelerate aerosol growth and collection within the packing.

3.2 PILOT PLANT OVERVIEW

The National Carbon Capture Center (NCCC), located in Wilsonville, Alabama, operates an amine scrubbing pilot plant with 0.6 MWe of coal-fired flue gas from Alabama Power Gaston Station Unit 5. The flue gas from the boiler was treated for particulates, nitrogen oxides, and sulfur oxides using electrostatic precipitators, selective catalytic reduction, baghouse, and flue gas desulfurization units (Figure 3.1). A slipstream of the treated gas was then sent to the Pilot Solvent Test Unit (PSTU), where CO_2 was removed using the piperazine advanced stripper (PZASTM) process. The PSTU was run with PZASTM for approximately 2000 h from February 22 to August 15, 2018.

The 2018 coal campaign started with two months of parametric testing followed by four months of long-term testing. A wide range of process conditions was used throughout the testing based on a robust test plan to evaluate emissions, energy performance, solvent degradation, and corrosion. The results from these tests are summarized in Rochelle et al.

(2019). Figure 3.2 shows a simplified flowsheet of the absorption columns and sampling locations for the campaign. The flue gas exiting the SO₂ pre-scrubber was first cooled in the direct contact cooler (DCC) to remove excess moisture and then fed to the bottom of the absorber. The absorber consists of 3 packed beds, each with 20 ft of Mellapak Plus[®] 252Y structured packing. During the campaign, the top bed was either operated dry or used as an additional water wash. Lean solvent from the advanced stripper was introduced to the top of the absorber and cooled between the mid and bottom absorber beds. The CO₂-depleted flue gas was then fed to a water wash column where volatile amine was removed, and the water balance was maintained.

Measured quantities of SO₃ were generated and injected into the flue gas during aerosol tests. Gas-phase concentrations were sampled at the absorber inlet, absorber mid bed, absorber outlet, and water wash outlet for 1500 hours using Fourier Transform Infrared (FTIR) analyzers. In addition, the aerosol concentration and particle size distribution of particles exiting the water wash were measured using an Electrical Low-Pressure Impactor (ELPI).

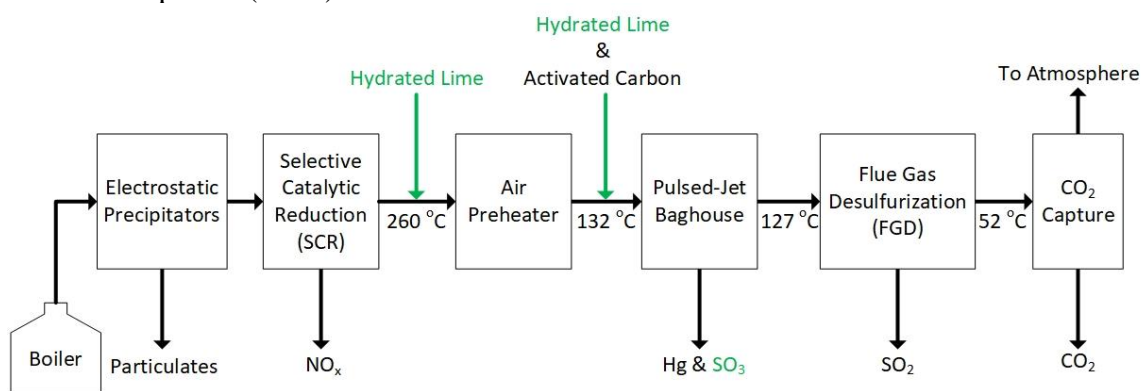


Figure 3.1: Flue gas treatment steps at NCCC Gaston Unit 5

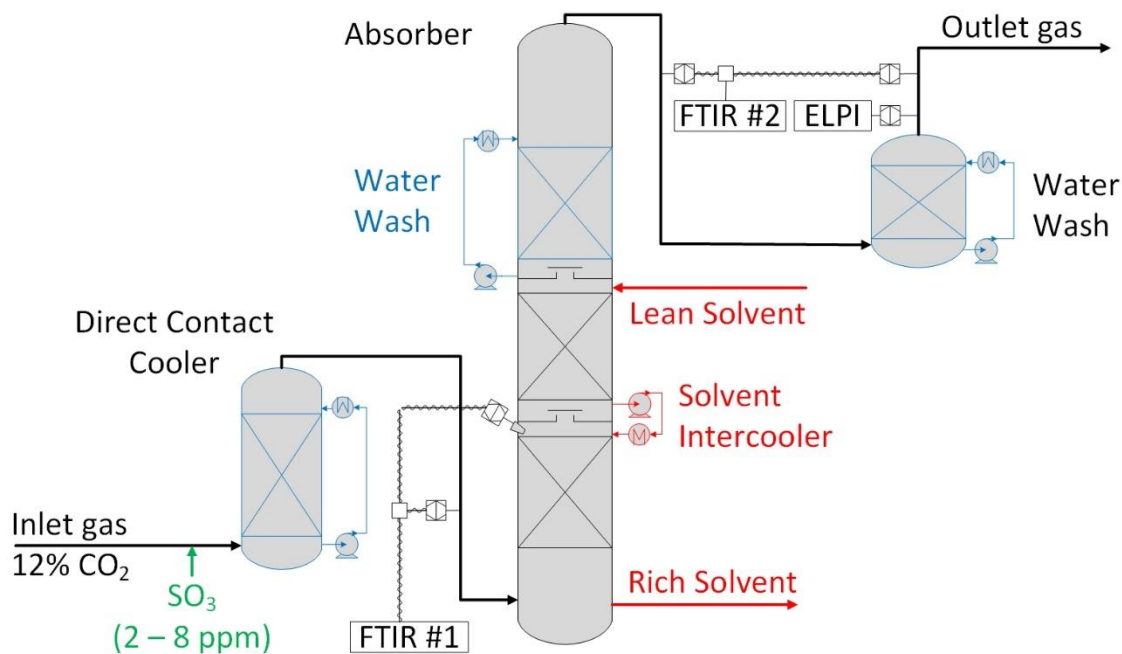


Figure 3.2: Simplified absorber PFD and gas sampling system for the 2018 coal campaign

3.3 METHODS

3.3.1 Gas Concentration Measurements

Gas-phase emissions were monitored and recorded using Fourier Transform Infrared (FTIR) analyzers. CO₂, SO₂, H₂O, NH₃, and PZ were measured at the absorber inlet, absorber mid-bed, absorber outlet, and water wash outlet. The FTIR measurements at the absorber gas inlet also validated the CO₂, SO₂, and H₂O data reported by the NCCC online analytical instruments.

A continuous stream of gas was extracted at all the sample locations using heated probes, heated pads, and heated sample lines at 180 °C to volatilize any amine aerosol and reduce the risk of condensation in the sampling system. A Gaset DX-4000 FTIR analyzer was used at the absorber inlet, while a Gaset CX-4000 FTIR analyzer alternated between

the absorber outlet and wash tower outlet. The locations of the sampling points and FTIR units are shown in Figures 3.2–3.4. In addition, the operation and adaptation of the FTIR gas analyzer for amine emission measurements at these locations are well documented in Chapter 2 of this dissertation.

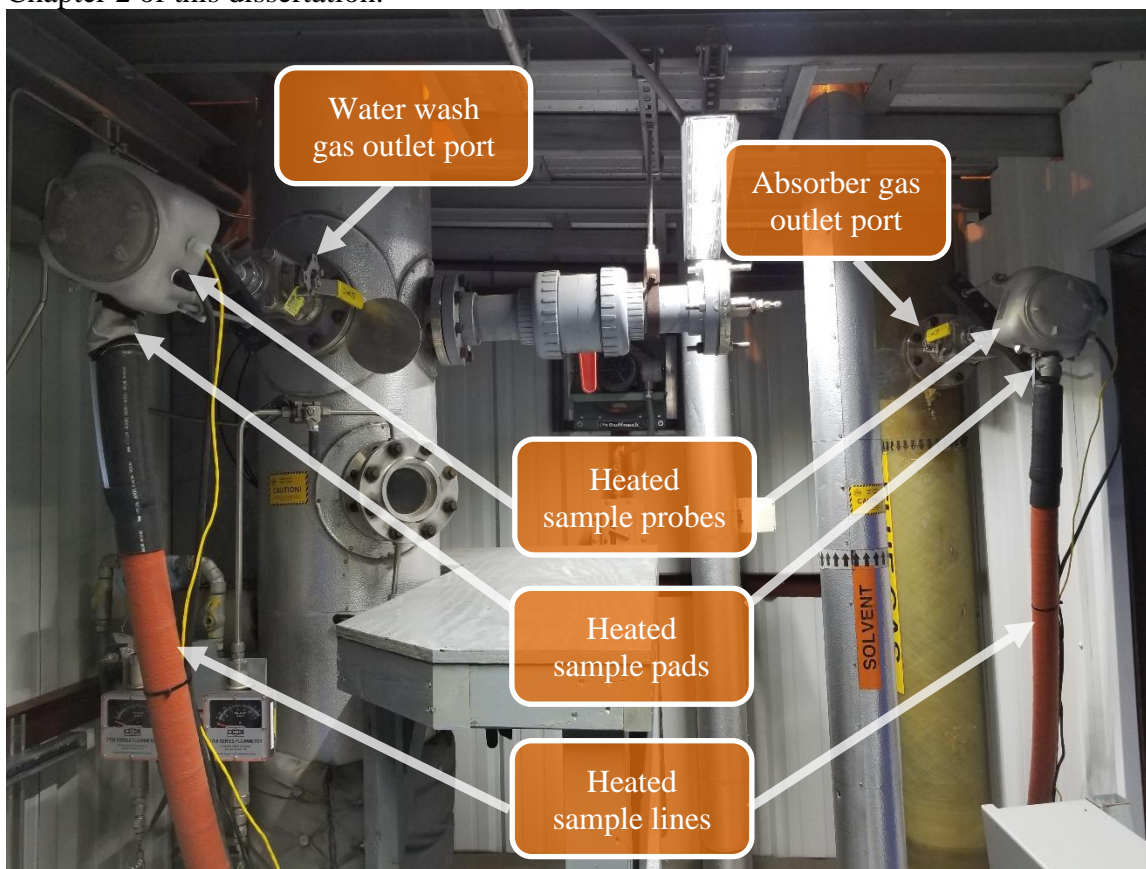


Figure 3.3: Sampling probe, pad, and line installations at the absorber and water wash gas outlets during the 2018 coal campaign

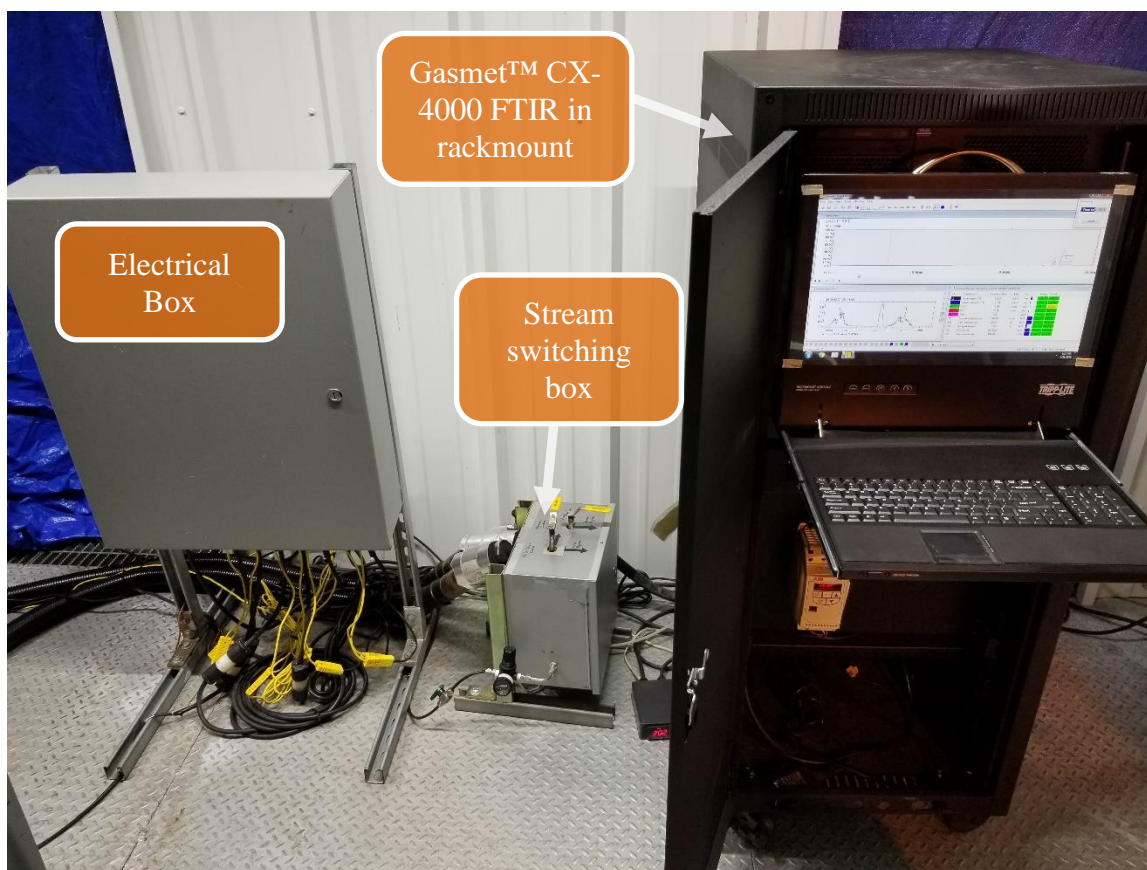


Figure 3.4: Gaset™ CX-4000 FTIR sampling setup for the absorber and water wash gas outlets during the 2018 coal campaign

During aerosol tests, up to 8 ppm SO_3 were generated and injected into the flue gas. The FTIR at the absorber gas inlet measured inlet SO_3 concentration by tracking the SO_2 conversion rate. The SO_3 was generated on-site by oxidizing SO_2 with oxygen in a catalytic bed with a vanadium pentoxide catalyst. The setup and operation of the catalytic bed during the campaign are reported more extensively in Chapter 2 of this dissertation.

The FTIR measurements were validated by comparing to cation chromatography for extracted condensates. The lab at the NCCC assisted by taking two sets of SKC sorbent sample tubes with matching pairs of impingers on the back end to measure vapor-phase products from the water wash gas outlet. The vapor-phase products from the water wash

gas outlet were condensed as liquid samples and analyzed using cation chromatography. Two samples were taken, one in the absence of injected SO₃ and the other during the 4ppm SO₃ injection test. The concentration ratio of PZ for both runs was 38 with the FTIR and 39 with the extracted condensate. This 3% error provides a close match and validates the gas measurements reported by the FTIR.

3.3.2 Aerosol Concentration and Size Distribution Measurement

Aerosol size distribution and concentration measurements with the ELPI were set up and operated by the Southern Research Institute (SRI). The ELPI classifies charged particles from 0.006 to 10 μm in a low-pressure cascade impactor. A custom-made dilutor was used for this experiment as designed by Southern Research and based on previous experimental setup and operation of the ELPI system by Saha & Anthony (2018) and Saha & Irvin (2017).

A downside to using the ELPI is the evaporation and loss of particles during dilution and extractive sampling. The dilution effects have been reported to affect the particle size distribution (Mertens et al., 2014; Saha & Irvin, 2017), so only the aerosol counts were used to make conclusions on aerosol mitigation in this work. Real-time ELPI measurements were taken at the water wash outlet using isokinetic probes at specific campaign periods. Tests were conducted to investigate the effect of mitigation strategies on the aerosol size distribution and concentration for various flue gas SO₃ concentrations.

3.4 PZ AEROSOL MITIGATION WITH BAGHOUSE

Beaudry (2018), in earlier work, concluded that the baghouse installation at NCCC must have reduced SO₃ in the flue gas due to the resultant 10-fold reduction in amine emissions observed at the CO₂ capture facility. Despite this finding, it was unclear what

particular operations of the baghouse at NCCC led to the SO₃ removal and subsequent amine emission reduction.

The NCCC operates a pulse-jet baghouse between the air preheater and flue gas desulfurization units. Hydrated lime and activated carbon are injected upstream of the baghouse to remove mercury and sulfur oxides. The baghouse itself has several individual filters which collect particulates as the gas flows into the bags. The bag filters are cleaned with bursts of compressed air through the collectors, and the cycle repeats. The flue gas treatment steps were shown in Figure 3.1.

Figure 3.5 shows the summary of PZ emissions from the water wash outlet for the campaign, excluding periods of aerosol tests. The PZ emissions shown are averaged for each 24-hr duration and include periods of unsteady-state operations. It can be noticed that the emissions dropped by order of magnitude past the 600 h operating time. This step-change in PZ emissions is remarkable, coinciding with a step-change in hydrated lime addition upstream of the baghouse. For the first 600 h when hydrated lime was below 0.5 normalized rates, emissions ranged 10–60 ppm; past the 600 h mark when hydrated lime rates were restored above 0.5, the maximum daily emissions dropped to 5 ppm.

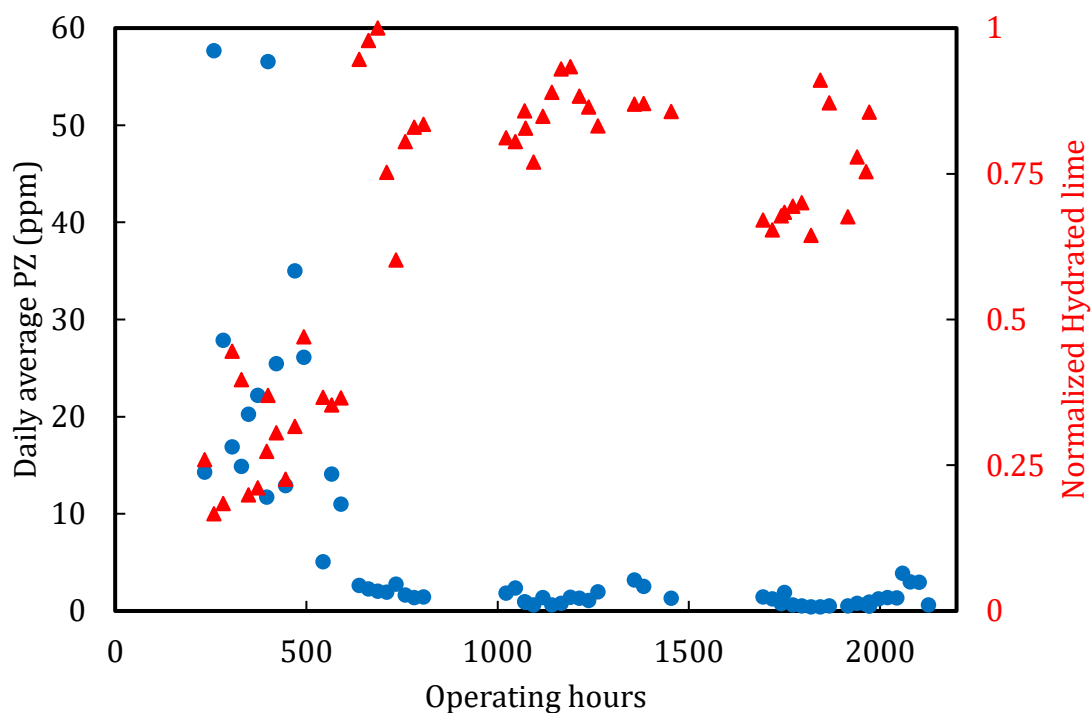


Figure 3.5: Daily average PZ emission from water wash (primary vertical axis) and hydrated lime rates upstream of the baghouse (secondary vertical axis) during the campaign. Aerosol tests with SO_3 injection are excluded.

Also, in Figure 3.6, the effect of hydrated lime on the emission is more evident for curated steady-state runs of the campaign. The step-change in emissions is not a function of lean solvent temperature or changes within the CO_2 capture plant. This finding shows that hydrated lime is critical in baghouse operations for SO_3 reduction and amine emission mitigation. There is a threshold for hydrated lime injection rates beyond which SO_3 slippage into the CO_2 capture plant occurs. For the NCCC, that threshold is at 0.5 of nominal rates.

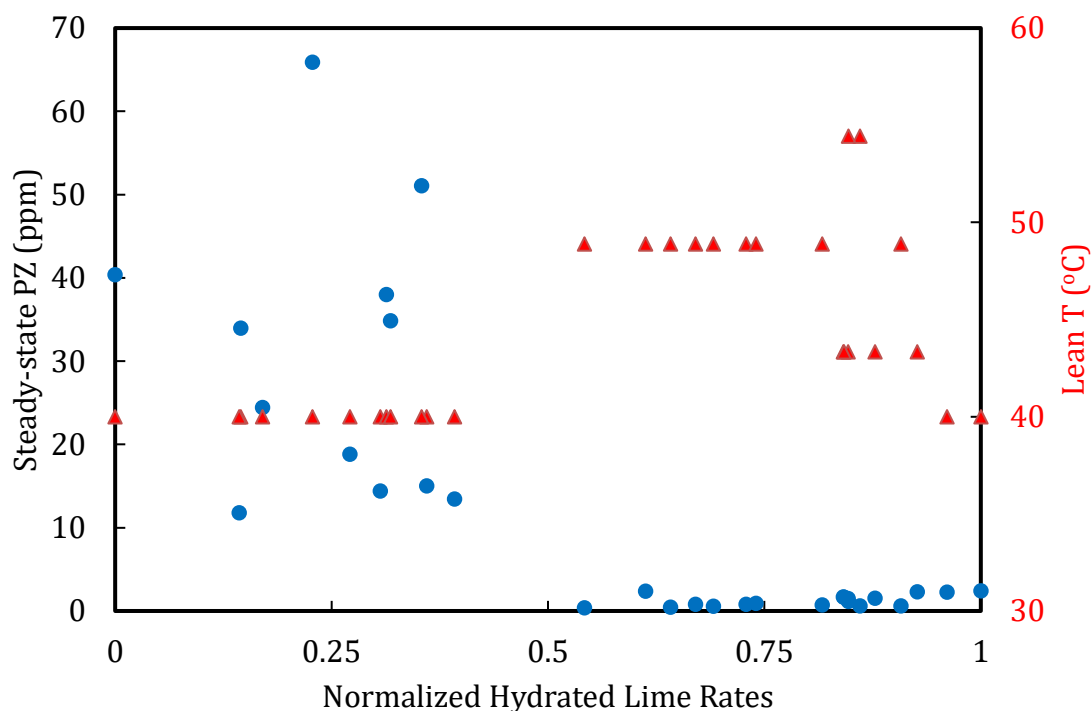


Figure 3.6: Correlation between rates of hydrated lime injection upstream of the baghouse, lean T, and PZ emissions during steady-state operations of the 2018 coal campaign. Aerosol tests with SO₃ injection are excluded.

3.5 SO₃ GENERATION FOR AEROSOL TESTS

Beaudry (2018) observed from earlier campaigns at the NCCC that the operation of a newly installed baghouse significantly reduced amine emissions and attributed this to SO₃ removal in the filters. Because of this, it was expected during this campaign that the flue gas might not contain sufficient aerosol concentration for scheduled aerosol tests, creating a need for SO₃ addition to the flue gas.

SO₃ was generated on-site using a Carbolite HST 12/900 tube furnace at 520 °C to oxidize a dilute stream of SO₂ and air over a vanadium pentoxide catalyst bed. The design and operation of this system are documented in Chapter 2 of this dissertation. The SO₃

generated was injected upstream of the DCC to allow for saturation, and the formation of tiny sulfuric acid drops as the gas enters the absorber.

3.5.1 Calibration and SO₂–SO₃ Conversion Results

An essential requirement for evaluating the generator performance measures the conversion of SO₂ to SO₃ over the range of inlet gas flow rates. A low conversion rate means a significant portion of the SO₂ stream enters the absorber unconverted. The conversion was determined by tracking the SO₂ concentration exiting the furnace. With flow through the furnace, the SO₂ concentration should decrease as the furnace turns on. The decrease in SO₂ concentration was monitored by the FTIR analyzer and determined the production of SO₃.

The flow meter was calibrated for 2–8 ppm SO₃ by adjusting inlet SO₂ flow rates up to 12 SCFH and tracking the SO₂ measured by the FTIR while the furnace was ON/OFF. For example, when the furnace was OFF and inlet SO₂ flow was set to 4 SCFH, the SO₂ concentration read by the FTIR was 3.6 ppm. While maintaining the flow rate and turning the furnace ON, the reading dropped to a steady-state value of 1.66. The difference between the SO₂ measured by the FTIR with the furnace OFF and ON gives the SO₃ produced—which for this example is 1.94 ppm. Figure 3.7 shows the results of the calibration tests. The equation obtained relates the desired SO₃ concentration in the flue gas to the required SO₂ flow rate into the furnace. The conversion increased with inlet SO₂ flow rate or SO₃ produced and averaged 97% throughout the flow rates tested (Figure 3.8).

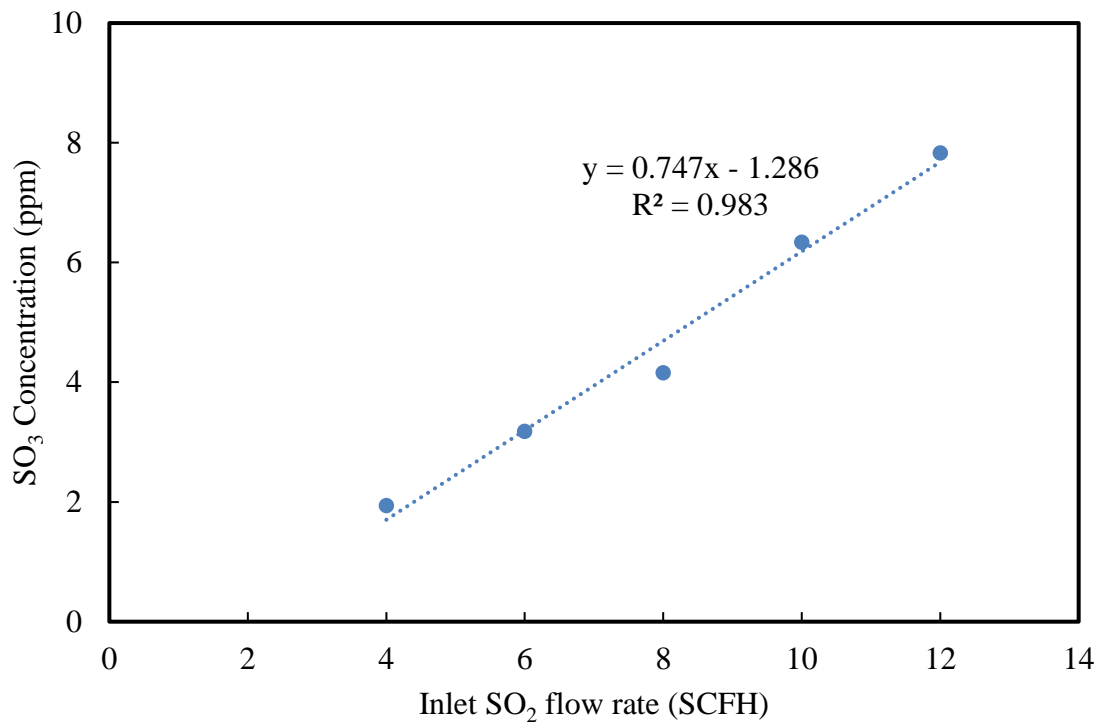


Figure 3.7: Calibration curve for SO₃ production from SO₂ with the tube furnace

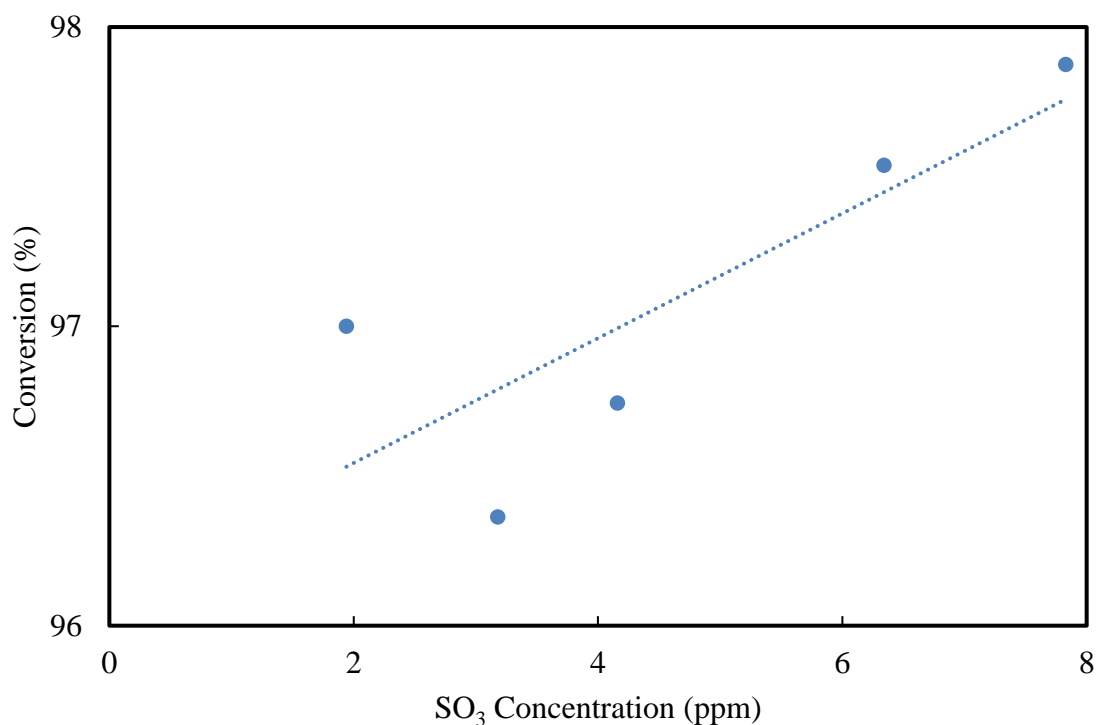


Figure 3.8: SO₂-SO₃ conversion with the tube furnace. 97% average conversion.

3.5.2 SO₃ Injection Runs

A total of 34 runs of SO₃ injection into the flue gas were made over two weeks. Eleven of these runs were for calibration tests, while the other 23 were to demonstrate aerosol mitigation. A range of 2–8 ppm SO₃ was generated and injected. In addition, SO₂ concentrations were measured using FTIR at the absorber gas inlet duct. The run times and conditions are presented in Table 3.1.

Table 3.1: Duration and quantity of SO₃ injection at NCCC coal campaign in 2018

S/N	Date	Total Injection Time (hr:min)	Start Time	Stop Time	SO ₂ Setpoint (SCFH)	SO ₃ Injected (ppm)
1	6/27/2018	3:15	11:45	12:30	12	8
			12:30	13:00	10	6
			13:00	13:30	8	5
			13:30	14:00	6	3
			14:00	14:30	4	2
			14:30	15:00	2	0
2	6/28/2018	2:38	12:22	13:15	12	8
			13:15	13:45	10	6
			13:45	14:15	8	5
			14:15	14:45	6	3
			14:45	15:00	4	2
3	6/29/2018	2:44	10:35	13:19	4.5	2
4	7/2/2018	3:00	12:30	15:30	4.5	2
5	7/3/2018	3:20	9:40	13:00	12	8
6	7/5/2018	6:11	9:00	14:11	4.5	2
			14:11	14:40	7	4
			14:40	14:59	10	6
			14:59	15:11	12	8
7	7/6/2018	4:35	10:00	14:05	12	8
			14:05	14:35	4.5	2
8	7/10/2018	2:55	11:00	12:39	4.5	2
			12:39	13:55	10	6
9	7/11/2018	3:37	12:23	13:56	4.5	2
			13:56	14:31	7	4
			14:31	15:25	10	6
			15:25	15:49	12	8
			15:49	16:00	10	6
10	7/12/2018	2:37	10:38	11:59	4.5	2
			11:59	12:45	7	4
			12:45	13:15	10	6
11	7/13/2018	4:32	11:28	15:28	7	4
			15:28	16:00	4.5	2
Total Injection Time		15:24				

3.6 EFFECT OF INLET SO₃ ON PZ EMISSION

PZ emissions in the absorber and water wash gas outlets were monitored as measured quantities of SO₃ were dosed into the flue gas. Figure 3.9 shows the PZ emissions in the absorber and water wash gas outlets at steady-state conditions of 90% CO₂ capture, 43 °C lean solvent, 33 °C intercooling, 4000 lbs/hr gas, 13,000 lbs/hr solvent, 0.22 mol CO₂/mol alkalinity, and a single water wash stage. PZ emissions exiting both the absorber and water wash were proportional to SO₃. This finding is consistent with previous work by Beaudry (2018) and Khakharia et al. (2016). Without SO₃ injection, the baseline concentration was 11 ppm in the absorber and 2 ppm in the water wash. However, with SO₃ in the flue gas, the PZ in the absorber gas outlet increased by 14 times the inlet SO₃. This factor was reduced to 11 in the water wash. Using the trendlines from Figure 3.9, the water wash efficiency was compared at the different flue gas SO₃ concentrations (Figure 3.10). The result shows that the water wash was most effective in mitigating vapor emissions (zero SO₃ concentration in the flue gas), and its efficiency diminished with SO₃ load.

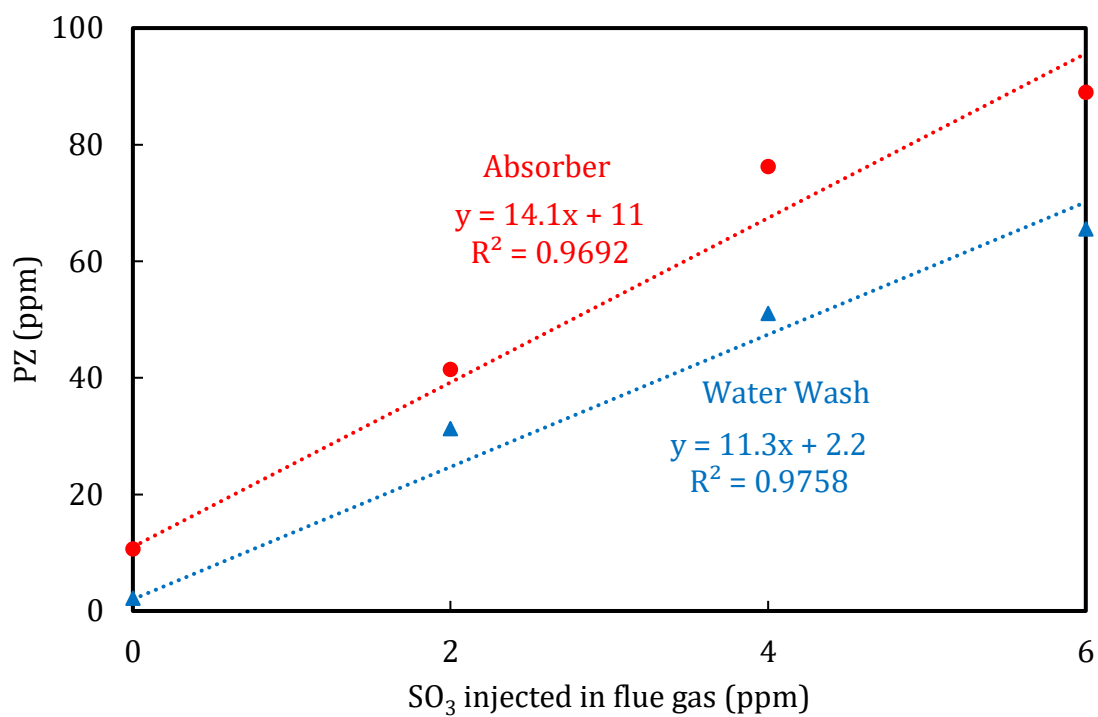


Figure 3.9: Effect of SO₃ on PZ emission in absorber and water wash gas outlets. Results were collected at steady-state conditions of 90% CO₂ capture, 43 °C lean solvent, 33 °C intercooling, 4000 lbs/hr gas, 13,000 lbs/hr solvent, 0.22 mol CO₂/mol alkalinity, and single water wash.

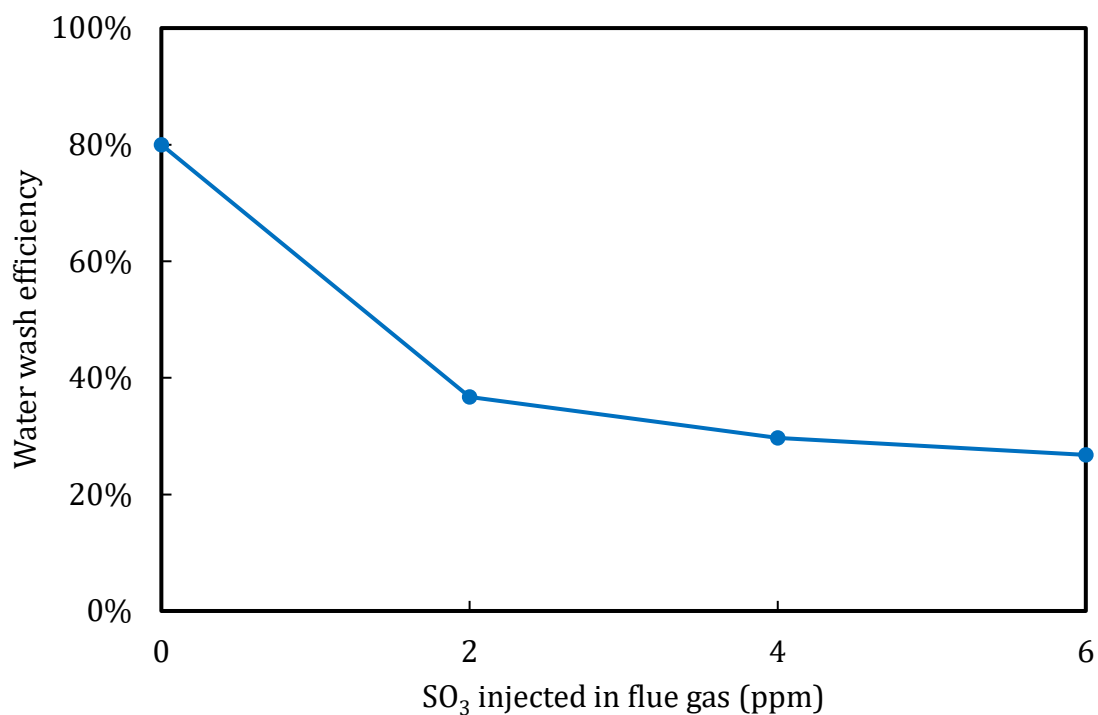


Figure 3.10: Water wash efficiency as a function of flue gas SO₃ concentration. Absorber and water wash operating conditions were held constant for all runs.

3.7 PZ AEROSOL MITIGATION IN ABSORBER AND WATER WASH

Aerosol modeling work on PZ has shown that the limiting mechanism for PZ aerosol growth shifts from gas-to-drop to bulk liquid-to-gas (Zhang, 2018). Hence, it was of interest to investigate the potential of mitigating PZ aerosol emissions by using critical handles in the absorber and water wash that help increase the bulk gas partial pressures of the amine. Therefore, the lean solvent temperature, solvent intercooling, and water wash stages were adjusted while measured quantities of SO₃ were dosed into the flue gas.

3.7.1 Lean Solvent Temperature

A test plan to vary the lean solvent entering the absorber at 43 °C, 49 °C, and 54 °C was set up to investigate the potential for PZ aerosol mitigation. Figure 3.11 shows PZ emission for variable SO₃ at these conditions. Each data point is a 10–20 minute time-averaged concentration of PZ at the wash tower outlet. The results were collected at steady-state conditions of 90% CO₂ capture, 4000 lbs/hr gas, 13,000 lbs/hr solvent, and lean loading of 0.22 mol CO₂/equivalent PZ.

Regardless of lean temperature, step-change increases in SO₃ resulted in a corresponding rise in absorber outlet emissions. The results show that PZ emissions were suppressed at higher lean solvent temperatures for all ranges of SO₃ in the flue gas. With 2 ppm SO₃ in the flue gas, increasing the lean solvent temperature from 43 to 58 °C reduced PZ exiting the absorber by 65%. More SO₃ nuclei in the flue gas increase the competition for the available volatile PZ; hence, the PZ aerosol does not grow enough for collection within the absorber packing. Raising the lean solvent temperature increases the partial pressure of PZ and H₂O in the gas phase and hence the driving force for PZ and H₂O mass transfer from gas to aerosol. Therefore, the bigger aerosol is collected by the absorber packing and mist eliminator, resulting in lower emission.

With no SO₃ added, PZ emission should be proportional to PZ volatility and should be lower for the cold solvent case. However, even with no added SO₃, PZ emissions were greater at reduced lean temperature. This suggests the presence of trace SO₃ in the flue gas despite upstream SO₃ removal by the baghouse.

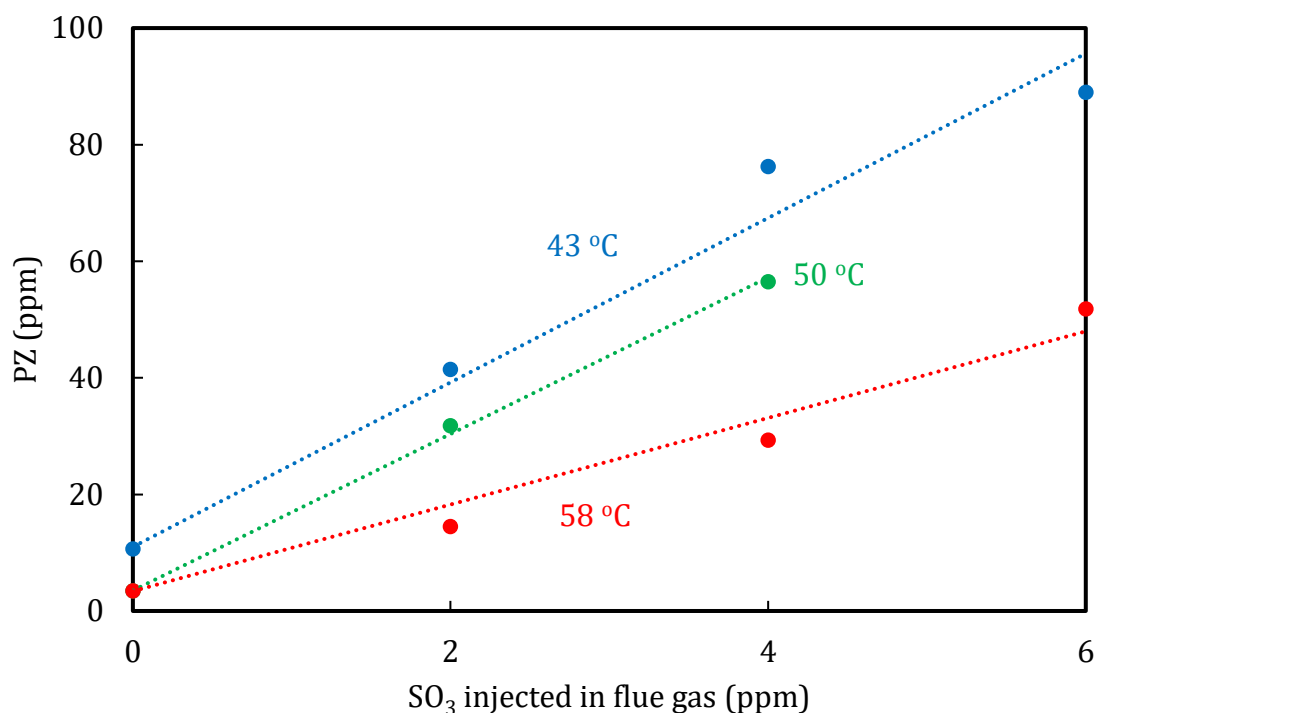


Figure 3.11: Effect of lean solvent temperature on PZ emission exiting the absorber at varying flue gas SO₃. Results collected at steady-state conditions of 90% CO₂ capture, 33 °C intercooling, 4000 lbs/hr gas, 13,000 lbs/hr solvent, and 0.22 mol CO₂/mol alkalinity.

3.7.2 Solvent Intercooling

The effect of solvent intercooling on PZ emission is shown in Figure 3.12. The intercooler was bypassed from 18:00 on 6/5/18 through 8:00 the next day. During this time, all process conditions were maintained, and PZ emission exiting the water wash averaged 7 ppm. The intercooler was then turned ON with a flow of about 20 GPM and an intercooling temperature of 33 °C at 8:00 6/6/18. This change resulted in an immediate and sustained surge in PZ emission with an average of 20 ppm over a 14-hr period. The lean solvent temperature was maintained at 44 °C throughout the 28-hr test, and all other process conditions were also kept constant.

Although no SO₃ was dosed into the flue gas during these tests, by extrapolating from results presented later in Figure 3.13, it can be concluded that there must have been about two ppm SO₃ slippage from upstream processes. The results show that the avoidance of solvent intercooling raised the bulge temperature in the absorber from 66 to 74 °C and reduced PZ emissions by 65%.

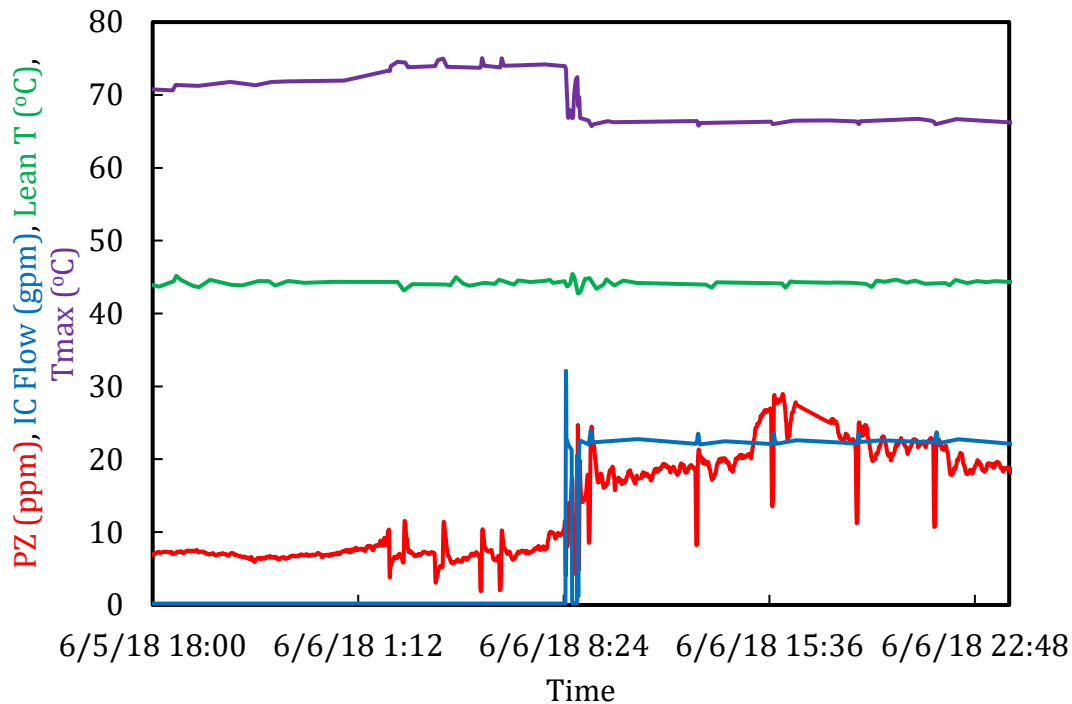


Figure 3.12: Effect of absorber intercooling on PZ emission exiting the water wash. Results were collected at steady-state conditions of 44 °C lean T, 33 °C intercooling, 4000 lbs/hr gas, 13,000 lbs/hr solvent, 0.22 mol CO₂/mol alkalinity, and single water wash.

3.7.3 Wash Wash

Unlike PZ vapor, PZ aerosols are not easily condensable in conventional water wash designs (Mertens et al., 2013). Zhang (2018) predicted PZ aerosol growth in the wash tower is due to a large amount of H₂O transfer from gas to aerosol. In this campaign,

the significance of increased residence time for aerosol growth through an additional water wash section was investigated. Figures 3.13 and 3.14 show PZ emissions with no water wash, a single water wash, and a two-stage water wash for lean solvent at 43 °C and 58 °C, respectively. The results were collected at steady-state conditions of 90% CO₂ capture, 4000 lbs/hr gas rate, 13,000 lbs/hr solvent circulation rate, and a lean loading range of 0.22–0.24 mol CO₂/equivalent PZ.

For both cold and hot lean solvent cases, fewer emissions are seen as more washing sections were used. For any given SO₃ concentration, the hot solvent case in Figure 3.14 shows lower emissions when compared to the cold solvent case in Figure 3.13. Overall, PZ emissions were managed to less than one ppm with 2 ppm flue gas SO₃ using a lean solvent temperature of 58 °C and a 2-stage water wash. Compared to the case with cold solvent at 43 °C and no water wash, a 98% reduction in PZ emission was achieved for flue gas with 2 ppm SO₃ by increasing the lean solvent to 58 °C and using a 2-stage water wash.

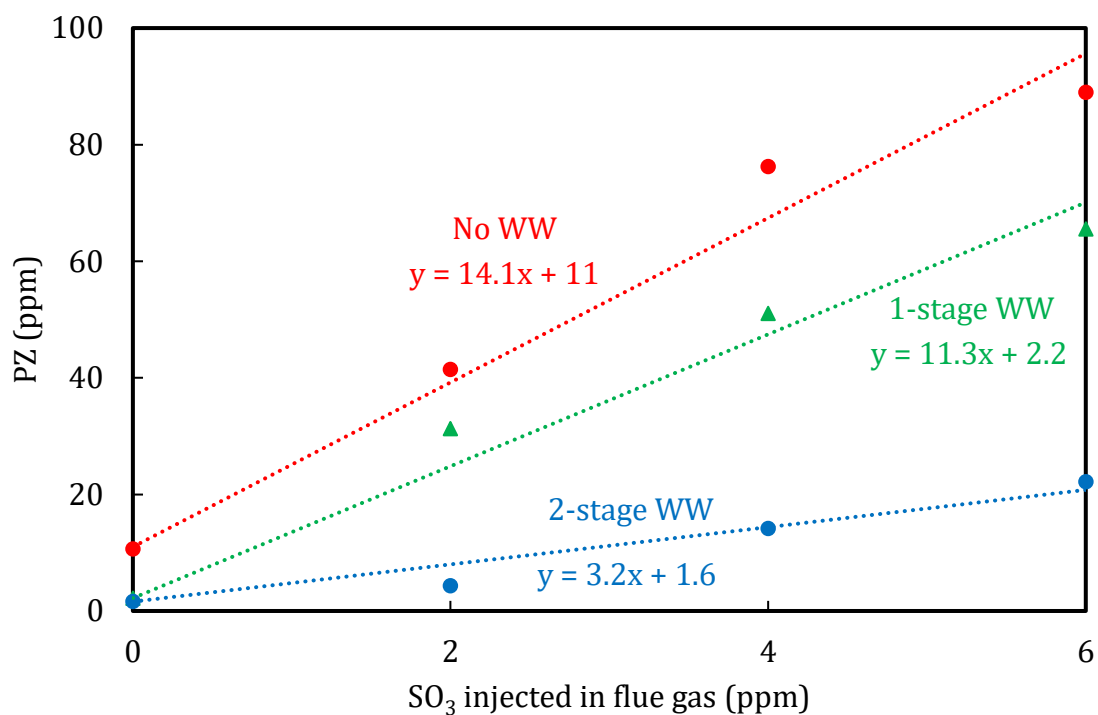


Figure 3.13: Effect of water wash on PZ emission at 43 °C lean solvent and varying flue gas SO₃. Results were collected at steady-state conditions of 90% CO₂ capture, 43 °C lean T, 33 °C intercooling, 4000 lbs/hr gas, 13,000 lbs/hr solvent, and 0.22 mol CO₂/mol alkalinity.

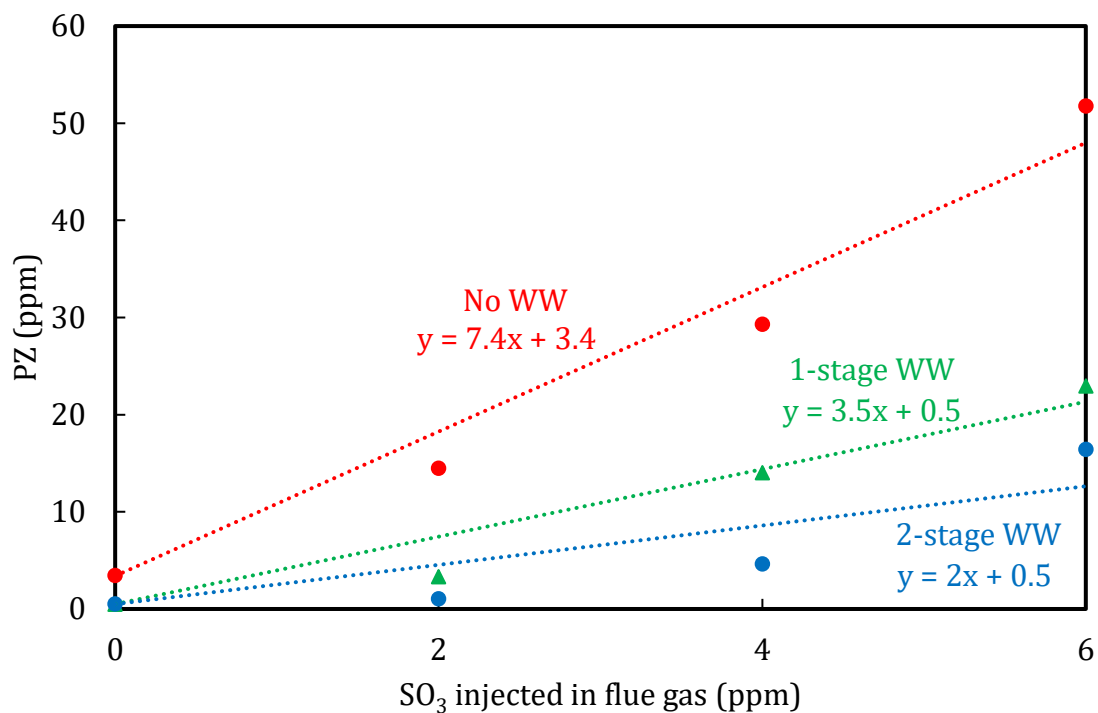


Figure 3.14: Effect of water wash on PZ emission at 58 °C lean solvent and varying flue gas SO₃. Results were collected at steady-state conditions of 90% CO₂ capture, 58 °C lean T, 33 °C intercooling, 4000 lbs/hr gas, 13,000 lbs/hr solvent, and 0.22 mol CO₂/mol alkalinity.

3.8 EFFECT OF AEROSOL MITIGATION STRATEGY ON CO₂ CAPTURE

Running the absorber at a high lean solvent temperature does not favor CO₂ absorption because the CO₂ driving force is reduced. This constraint on CO₂ capture efficiency was avoided with solvent intercooling in the absorber between the 1st and 2nd packing beds. The solvent was cooled up to 32 °C during the aerosol tests. Figure 3.15 shows CO₂ removal at varying lean solvent temperatures. At 54 °C lean solvent, CO₂ removal greater than 90% was achieved. In addition to the contribution of solvent intercooling to enhanced CO₂ absorption, the large amount of packing in the absorber also maintained CO₂ absorption. Two 20 ft beds of packing were used with a mass transfer

pinch in the absorber, so CO₂ absorption should be a weak function of the change in driving force (Gao et al., 2019).

Figure 3.15 also shows the cooling water requirement of the wash tower. As the lean solvent temperature is raised, the temperature of the gas exiting the absorber and entering the wash tower rises equally. This results in an increased requirement for wash tower circulation water to cool the gas to a few degrees hotter than the inlet gas and maintain the overall water balance of the system. The summary of the pilot plant absorber performance during the emission tests is presented in Table 3.2.

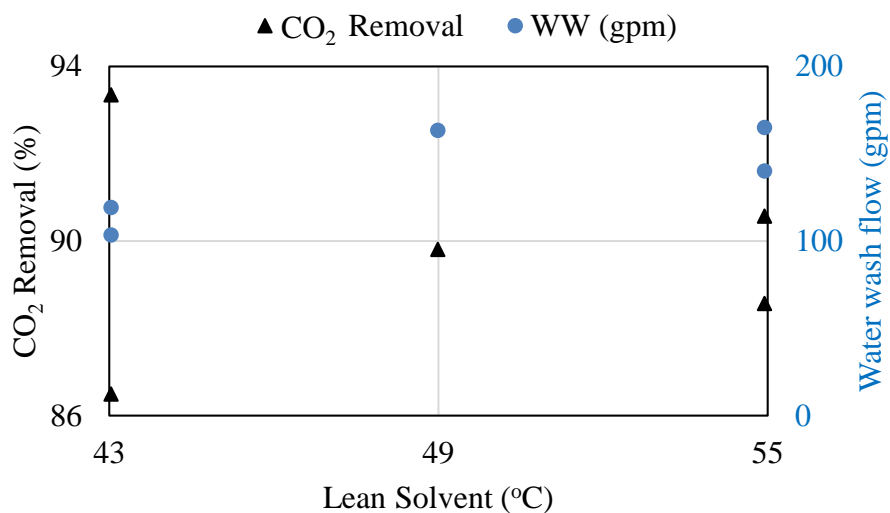


Figure 3.15: Effect of absorber temperature on CO₂ removal and wash tower circulation flow

Table 3.2: Summary of pilot plant absorber performance during the aerosol tests at 2018 coal campaign

Run	Abs		WW	Lean	Abs	Abs	Abs	Abs	WW	Abs	WW		PZ	Removal	WW		
	Inlet SO ₃	Outlet PZ	Outlet PZ	Solvent T	Inlet Gas T	T _{bulge}	T _{bulge} - LST	Outlet Gas T	Outlet Gas T	IC T	L/G	Water T				Lean ldg	Rich ldg
	ppm	ppm	ppm	°C	°C	°C	°C	°C	°C	°C		°C	m/m	m/m	m	%	
1a	0	4	0.5														
1b	2	14	3	54	45	67	13	62	51	34	3.2	59.5	0.22	0.40	4.6	89	One-stage
1c	4	29	14														
1d	6	49	23														
2a	0	11	2.2														
2b	2	50	31	43	46	66	23	53	44	33	3.1	51.6	0.22	0.40	4.6	86	One-stage
2c	4	76	51														
2d	6	90	66														
3a	0	4	0.6														
3b	2	24	13	49	44	67	18	56	45	34	3.2	54.1	0.22	0.40	4.5	90	One-stage
3c	4	57	37														
4a	0	3	0.5														
4b	2	5	1.0	54	44	67	13	58	47	34	3.2	54.5	0.24	0.40	4.8	91	Two-stage
4c	4	14	5														
4d	6	30	16														
5a	0	7	1.6														
5b	2	16	4.3	43	45	66	23	49	45	35	3.2	48.3	0.22	0.40	4.8	93	Two-stage
5c	4		14														
5d	6		22														

3.9 EFFECT OF MITIGATION STRATEGIES ON PZ AEROSOL COUNT AND SIZE DISTRIBUTION

This section presents particle counts and size distributions measured by the ELPI at the water wash gas outlet. The results were collected at steady-state conditions of 90% CO₂ capture, 4000 lbs/hr gas, 13,000 lbs/hr solvent, lean loading of 0.22 mol CO₂/equivalent PZ, and a single water wash stage. The lean solvent temperature was varied between 43 °C and 54 °C, and a single-stage wash was used. Earlier research with the ELPI has highlighted the dependence of its particle size distribution on dilution ratio and temperature (Mertens et al., 2014; Saha & Irvin, 2017). Also, particle loss due to shrinkage through dilution makes it challenging to accurately interpret the ELPI particle size distribution. However, the ELPI aerosol number concentration and count remain correct and helpful in evaluating aerosol mitigation.

Figures 3.16 and 3.17 show the particle size distributions for aerosol collected with the ELPI at the wash tower outlet. A general trend of increase in particle number count with SO₃ was seen for the cold (Lean T of 43 °C) and hot (Lean T of 54 °C) absorber cases. No significant aerosol was found at sizes greater than 3 μm. This is most likely due to the cut-off efficiency of the mist-eliminator used on the wash tower. Most demisters are known to have a 3–10 μm cut-off diameter, and aerosol larger than 3 μm will coalesce on contact with the wire surface and ultimately drain into the vessel (Glitsch, 2012). A less likely reason could be the intrinsic dilution effect and reduction of drop size specific to the ELPI sampling technique.

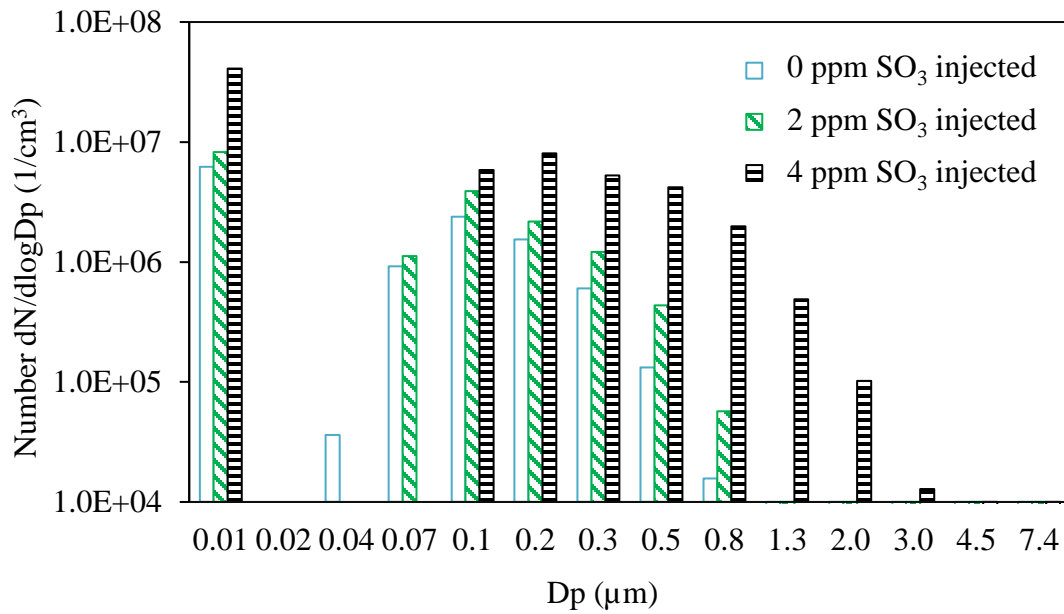


Figure 3.16: Effect of SO₃ injection on aerosol number concentration at wash tower outlet for cold (Lean T of 43 °C) absorber case. Results were collected at steady-state conditions of 43 °C lean T, 33 °C intercooling, 4000 lbs/hr gas, 13,000 lbs/hr solvent, 0.22 mol CO₂/mol alkalinity, and single water wash.

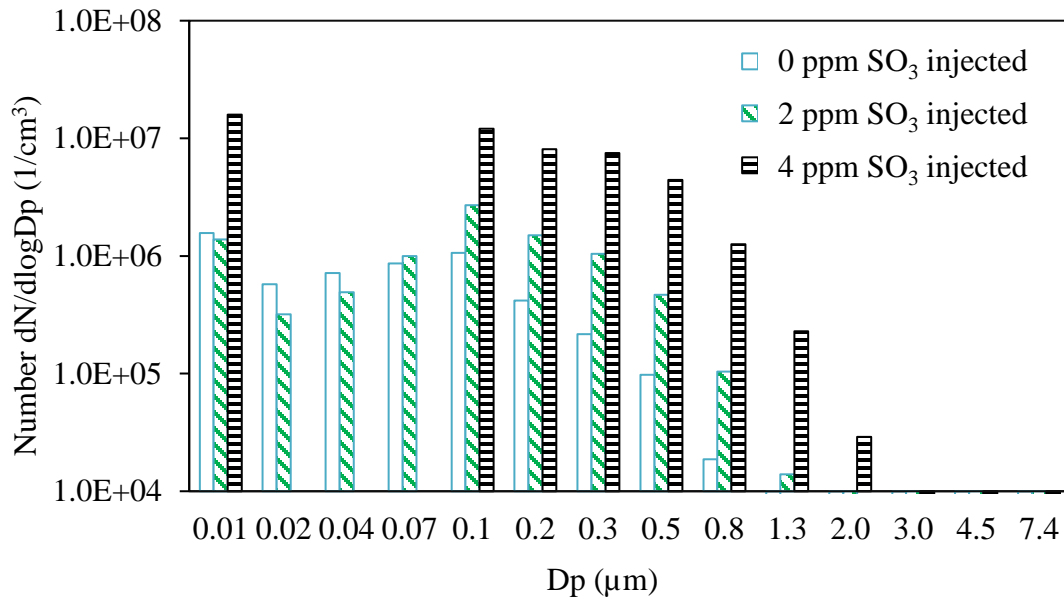
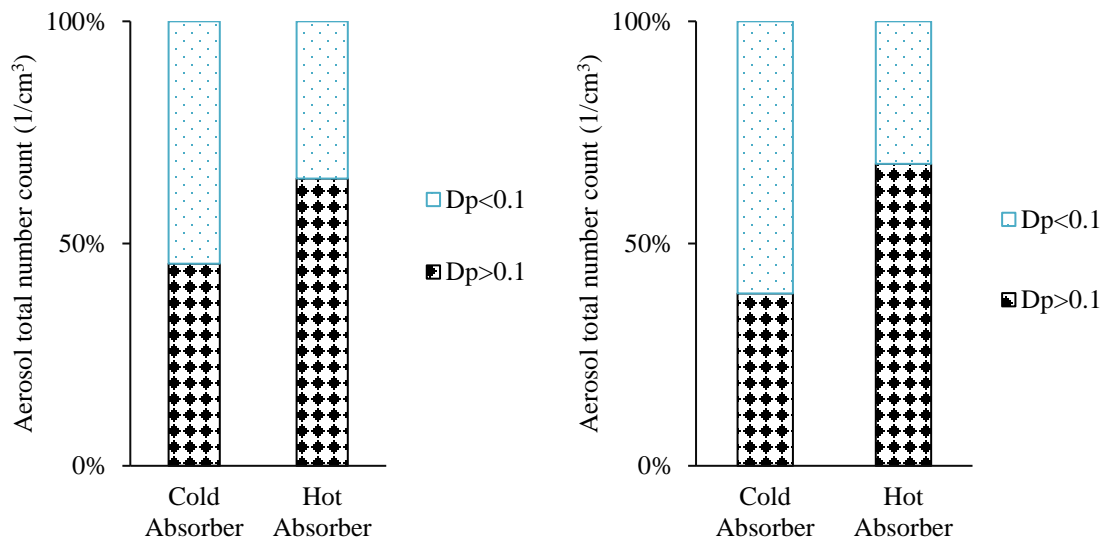


Figure 3.17: Effect of SO₃ injection on aerosol number concentration at wash tower outlet for hot (Lean T of 54 °C) absorber case. Results were collected at steady-state conditions of 54 °C lean T, 33 °C intercooling, 4000 lbs/hr gas, 13,000 lbs/hr solvent, 0.22 mol CO₂/mol alkalinity, and single water wash.

To quantify and better understand the effect of the lean temperature on outlet aerosol count and size distribution, the aerosol from the cold and hot absorber cases was divided into two groups: $D_p < 0.1 \mu\text{m}$ and $D_p > 0.1 \mu\text{m}$. The fraction of aerosol count in these size groups for variable SO₃ is shown in Figure 3.18. Running the absorber at an elevated lean solvent temperature resulted in a smaller total aerosol count of the smaller particles ($D_p < 0.1 \mu\text{m}$) and a larger total aerosol count of larger particles ($D_p > 0.1 \mu\text{m}$). The fraction of larger particles increased from 46 to 65% in the 2 ppm case and 39 to 68% in the 4 ppm case by increasing the lean solvent temperature. This increase in the count of larger particles confirms aerosol growth due to condensation at elevated lean temperatures.



a) 2 ppm SO₃

b) 4 ppm SO₃

Figure 3.18: Larger particles dominate the aerosol profile at elevated lean temperatures
(a) 2 ppm SO₃ in flue gas and (b) 4 ppm SO₃ in flue gas

Although the fraction of larger particles is smaller at cold lean temperatures, Figure 3.19 shows that the total aerosol number count is greater. For 2 ppm SO₃, increasing the lean solvent temperature resulted in a 47% decrease in the total aerosol number count. Running a hot absorber increased the aerosol size and reduced the total number counts. There is a significantly greater number count of particles with the cold absorber, and most of these particles have a diameter less than 0.1 μm. It is thus likely that the aerosol that grew to sizes greater than the 3 μm cut-off diameter were collected within the packing, resulting in the reduced total aerosol count.

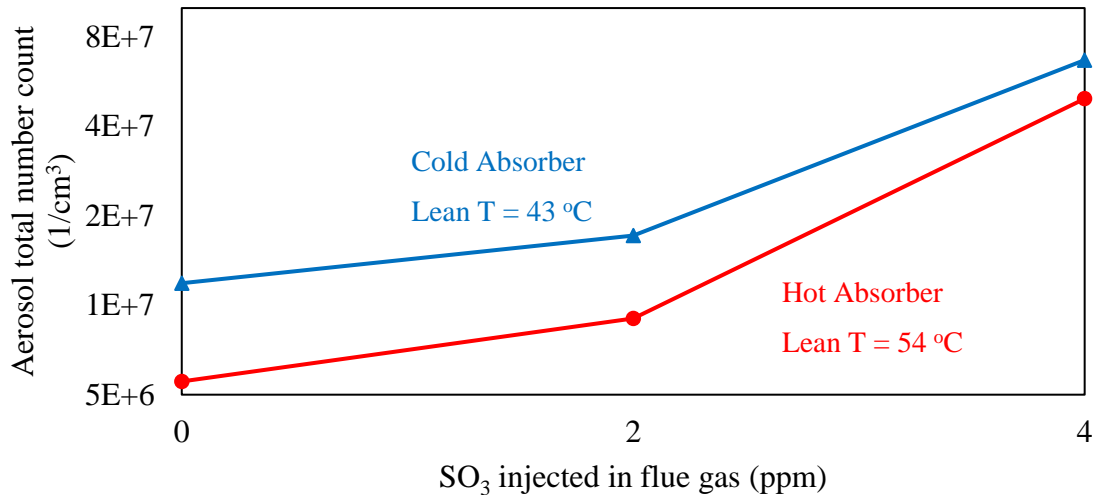


Figure 3.19: Effect of Lean solvent temperature on total aerosol number count at wash tower outlet for varying SO₃

3.10 MECHANISMS OF AEROSOL MITIGATION

PZ aerosol emissions are probably mitigated by increased lean solvent temperature because the increased temperature at the top of the absorber increases the rate of growth of the aerosol to the point that it is large enough to be collected. Zhang (2018) modeled aerosol growth at the conditions of the NCCC pilot plant and showed that the driving force for amine transfer to the aerosol is greater at higher lean solvent temperature, resulting in larger aerosol leaving the absorber and the water wash. The measurements by the ELPI suggest that the number of aerosol drops leaving the water wash decreased by a factor of two with the elevated lean solvent temperature.

Bade et al. (2015) claimed that increased lean solvent temperature would reduce the “formation of mist” by avoiding “rapid cooling of the gas mixture streaming upwards in the absorption zone of the absorber.” The Bade patent claims the use of “temperature of the aqueous amine solvent introduced into the CO₂ absorption section is less than or

equal to a maximum temperature in the absorption section and not more than 5 °C lower than the maximum temperature in the absorption section of the absorber.” In the systematic testing performed at NCCC, the difference between the maximum temperature in the absorber and the lean solvent temperature varied from 13 to 23 °C (Table 3.2) and was always substantially greater than the zero to 5 °C claimed by Bade. It is possible that greater lean solvent temperature would be even more effective at mitigating the amine emissions. Future work to clarify and validate these mechanisms could include ELPI measurements at different stages throughout the absorber.

3.11 CONCLUSIONS

Hydrated lime is the critical function in baghouse operations for SO₃ reduction and amine emission mitigation. There is a threshold for hydrated lime injection rates beyond which SO₃ slippage into the CO₂ capture plant occurs. For the NCCC, that threshold is at 0.5 of nominal rates.

Using a tube furnace, up to 8 ppm of SO₃ was successfully generated at a pilot scale from an SO₂-air mixture. The conversion increased with inlet SO₂ flow rate or SO₃ produced and averaged 97% throughout the flow rates tested.

PZ emissions in both the absorber and water wash are proportional to inlet SO₃. With no SO₃ injected in the flue gas, PZ was 11 ppm and 2 ppm in the absorber and water wash outlets, respectively. The water wash is more effective for vapor emission reduction where flue gas SO₃ is negligible and diminishes in performance with flue gas SO₃. PZ increased up to 20 mol PZ/mol SO₃ when no mitigation strategy was implemented. By using a combination of higher lean solvent temperature and double water wash stages, this ratio was reduced to 0.5 mol PZ/mol SO₃.

Increasing the lean solvent temperature, turning off the intercooler, and increasing the water wash stages help mitigate PZ emissions in the presence of SO₃. Increasing the lean solvent from 43 to 58 °C resulted in a 65% reduction in PZ exiting the absorber. Likewise, the avoidance of intercooling also reduced PZ by 65%. Overall, PZ emissions were reduced to 1ppm for flue gas with 2 ppm SO₃ by increasing the lean solvent temperature and water wash stages. Compared to the case with cold solvent at 44 °C and no water wash, a 98% reduction in PZ emission was achieved for flue gas with two ppm SO₃ by increasing the lean solvent to 58 °C and using a 2-stage water wash.

The ELPI aerosol concentration measurements showed that runs at higher lean solvent temperatures shifted the aerosol size distribution to the right and reduced the total number count. The fraction of larger particles ($D_p > 0.1 \mu\text{m}$) increased from 39 to 68% by increasing the lean solvent temperature, confirming growth due to amine condensation at the higher temperature. Also, increasing the lean solvent temperature resulted in a 47% decrease in the total aerosol number count, confirming that many particles had grown above the 3 μm threshold for removal and were collected in the packing and mist eliminator of the column.

Long-term operations at elevated lean solvent temperatures can be sustained. Although running the absorber at higher lean solvent temperatures does not favor CO₂ absorption, 90% CO₂ removal was maintained by intensive solvent intercooling to 32 °C. A large amount of packing in the NCCC absorber also helped sustain CO₂ absorption at the operating conditions evaluated during the aerosol tests. The water balance of the system was maintained by increasing the circulation water flow to cool the gas exiting the water wash within 4–7 °C of the absorber inlet gas temperature.

Chapter 4: PZ Emissions from CO₂ Capture at NGCC Conditions

Coal is rapidly being replaced by natural gas for electricity generation, and future advances in CO₂ capture technologies must demonstrate reliable operations with Natural Gas Combined Cycles (NGCC). In this work, solvent emissions are reported for 2000 h of CO₂ capture with PZASTM at NGCC conditions at the National Carbon Capture Center (NCCC). The results show that NGCC capture conditions may have suppressed emissions even at significant aerosol nuclei penetration. Average PZ emissions were below 1 ppm. The emissions increased by a factor of 5 when the DCC was bypassed and hot inlet gas fed to the absorber. Changes in the intercooling configurations did not affect emissions. On average, only 6% of PZ entering the wash tower was emitted.

4.1 INTRODUCTION

Flue gases from fossil fuel-based power plants are the major concentrated CO₂ sources in the United States. The capture of CO₂ from these plants is an essential solution to meeting energy demand economically and sustainably. Natural Gas Combined Cycle (NGCC) plants have replaced coal as the primary electricity generation source and contribute a third of total U.S. energy-related CO₂ emissions (EIA, 2019). Future advances in CO₂ capture technologies must demonstrate reliable CO₂ capture operations from NGCC.

Solvent emissions in the CO₂-scrubbed gas concern amine-based CO₂ capture units and must be monitored and managed below 1 ppm. Pilot studies have shown that emissions are influenced mainly by the flue gas composition and absorber operating conditions. SO₂, SO₃, and fly ash in the flue gas nucleate aerosol on which the solvent condenses. Absorber operating conditions also play a critical role in creating or mitigating emissions in the presence of aerosols (Akinpelumi et al., 2019; Bade et al., 2015). These factors are crucial

because the flue gas composition and absorber conditions for CO₂ capture from NGCC differ from coal.

First, NGCC flue gas has a lower CO₂ content, reducing the partial pressure driving force for absorption and requiring lower lean loading for equivalent capture to coal. Because amines are more volatile at lower lean loading, this can affect the mass transfer of species from gas to aerosol. Second, because of the lower CO₂, the NGCC flue gas requires a lower liquid to gas (L/G) ratio, which shifts the temperature bulge higher up the absorber compared to capture from coal. The magnitude and location of the temperature bulge can influence the supersaturation of the upward streaming gas and nucleation of aerosols. Intercooling configurations can also affect the temperature bulge location and thus have significant effects on solvent volatility and emission control. Third, the NGCC flue gas has a cleaner composition with a lower concentration of aerosol nuclei. The absence of significant concentrations of SO₂, SO₃, and fly ash should result in much lower amine emissions.

Although long-term emissions from capture from coal have been reported, the literature is sparse for NGCC. A bench-scale emission study of capture from varying inlet CO₂ showed an initial increase of inlet CO₂ to 4% doubled PZ emission, while further increases in inlet CO₂ had negligible effects (Fulk & Rochelle, 2014). Beaudry (2018) found that higher inlet CO₂ increased the mean diameter of aerosols. Although both studies show that inlet CO₂ can have some effect on solvent emission, they only demonstrated instantaneous changes in CO₂ over a short duration of 30 minutes. Furthermore, the experiments were not under optimal capture conditions, and the solvent loadings and concentrations were not tracked. Pilot studies with 90% capture over extended periods must be conducted for NGCC to monitor solvent emissions.

This work reports solvent emissions over extended periods of capture from NGCC using the PZASTM process. The emission trends during the NGCC campaign were compared to the 2018 coal campaign at the National Carbon Capture Center (NCCC). The effect of intercooling configurations and the direct contact cooler (DCC) on emissions was investigated. This work also evaluated water wash performance through continuous emissions sampling upstream and downstream of the water wash.

4.2 PILOT PLANT OVERVIEW

Following the success of the 2018 coal campaign at the National Carbon Capture Center (NCCC), the Pilot Solvent Test Unit (PSTU) was modified for NGCC testing with pump-around intercooling in the absorber. The 2019 NGCC campaign also used the PZASTM process for CO₂ removal and spanned for an additional 2000 h from February 14 to May 20, 2019. The test system for CO₂ absorption is shown in Figure 4.1. Flue gas containing 12% CO₂ from the Alabama Power coal boiler was diluted with air to 4.3% CO₂ to simulate NGCC conditions. The DCC was bypassed for specific periods of the campaign, and hot inlet gas at 76 °C was fed directly to the absorber. The first two beds of the absorber were used for absorption while the 3rd bed was operated dry. Two intercooling configurations were tested in the absorber: in-and-out (IO) and pump-around (PA). Gas compositions upstream and downstream of the water wash were measured with separate FTIR analyzers—providing a real-time evaluation of the water wash performance and significantly improving the 2018 coal campaign sampling setup. Details on the energy performance and other non-emissions-related results from this campaign are reported by Rochelle et al. (2021).

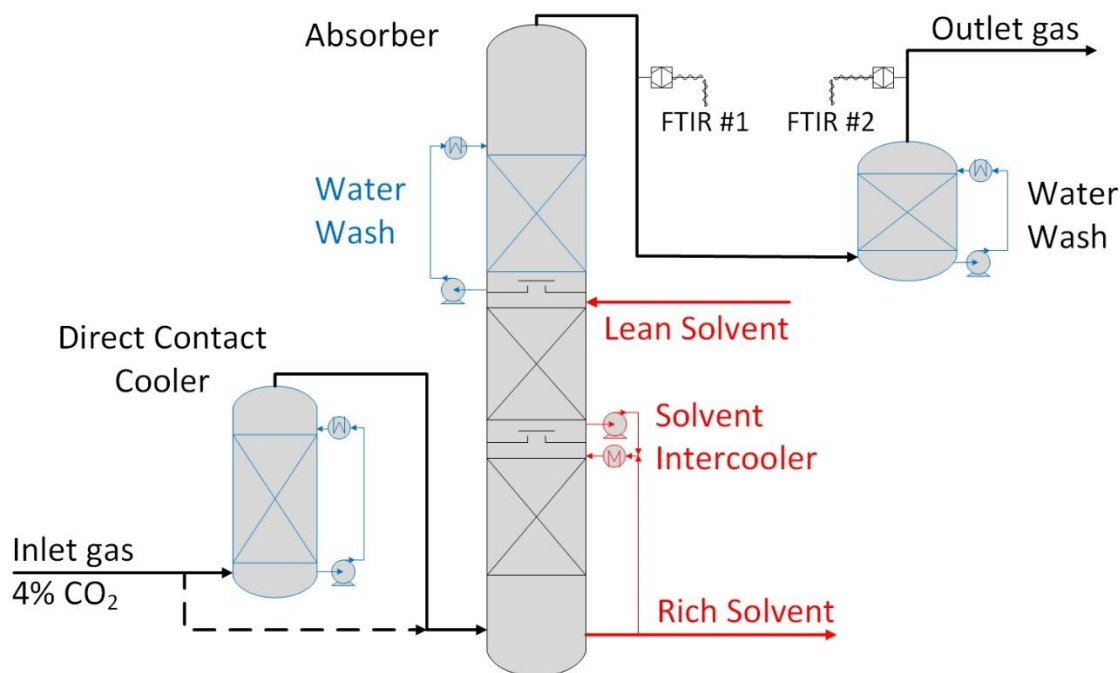


Figure 4.1: Simplified absorber PFD and gas sampling system for the 2019 NGCC campaign

4.3 METHODS

Gas-phase emissions were monitored and recorded using Fourier Transform Infrared (FTIR) analyzers. CO₂, H₂O, NH₃, and PZ were measured at the absorber and water wash outlets. A continuous stream of gas was extracted at the sample locations using heated probes, heated pads, and heated sample lines at 180 °C to volatilize any amine aerosol and reduce the risk of condensation in the sampling system. Gas compositions upstream and downstream of the water wash were measured with separate FTIR analyzers—providing a real-time evaluation of the wash tower performance and significantly improving the 2018 coal campaign sampling setup. A Gasetm DX-4000 FTIR analyzer was used at the absorber outlet, while a Gasetm CX-4000 FTIR analyzer measured concentrations exiting the water wash. Figures 4.2 and 4.3 present the sampling set up at

both locations. In addition, the operation and adaptation of the FTIR gas analyzer for amine emission measurements at these locations are well documented in Chapter 2 of this dissertation. At the beginning of the 2019 NGCC campaign, probe failure and condensation in the sample lines were observed at the absorber gas outlet port and only replaced later, leading to some data loss.



Figure 4.2: Experimental sampling set up for gas measurements at the absorber outlet with a Gaset DX-4000 FTIR analyzer.



Figure 4.3: Experimental sampling set up for gas measurements at the water wash outlet with a Gaset CX-4000 FTIR analyzer fitted in rackmount support.

4.4 RESULTS AND DISCUSSIONS

4.4.1 Emission Trends from 2018 Coal and 2019 NGCC Campaigns

The 2018 coal and 2019 NGCC campaigns each lasted about 2000 hours, with brief periods during which the capture plant was shut down. Figure 4.4 shows a summary of the emissions throughout both campaigns. Each data point represents the average daily PZ in the water wash gas outlet and includes unsteady state conditions. While this helps to analyze emissions from an operational standpoint, it introduces outliers resulting from erratic operations during process changes, such as startup or recommissioning of the sampling setup. During the coal campaign, two periods of emissions were observed: the first during the initial 600 hours of the campaign with high emissions ranging between 11–60 ppm; and the second during the last 1000 hours with emissions below 3 ppm. For NGCC, the PZ emissions were significantly lower, with a maximum of 2 ppm and an overall average below 1 ppm.

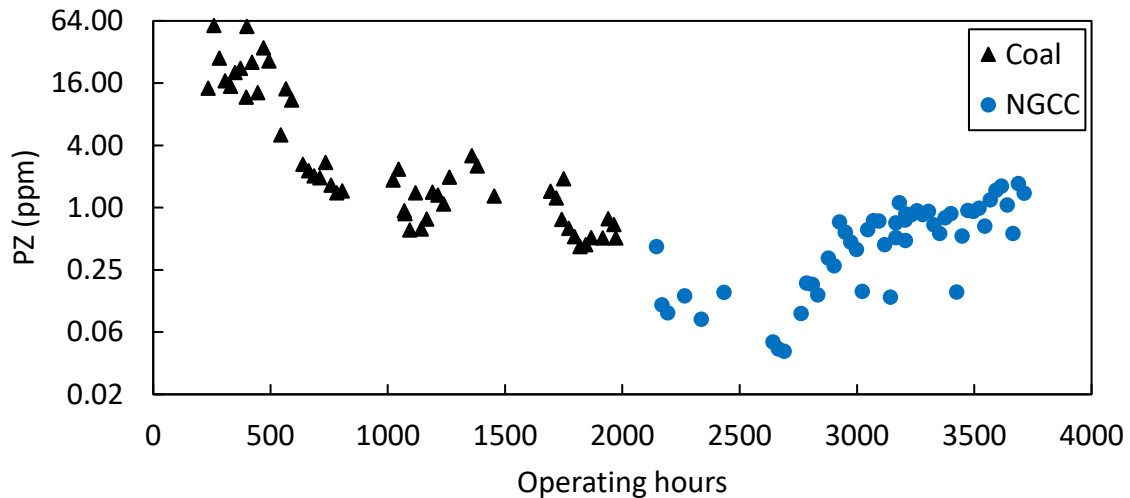


Figure 4.4: Emission trends from 2018 coal and 2019 NGCC campaigns. Each data point represents the average daily PZ exiting the water wash.

Akinpelumi et al. (2019) attributed the first period of excessive emissions during the coal campaign due to SO_3 penetration from the sub-optimal lime rate in the upstream pretreatment at the baghouse. In Figure 4.5, the lime rate for both coal and NGCC campaigns is presented against operating hours. The rates were normalized to the same maximum rate from both campaigns and averaged daily to correspond with the measured PZ. Although the lime rates during the latter part of the NGCC campaign were of a similar sub-optimal range as that of the first part of the coal campaign, the resulting PZ emissions were much lower. The data suggest that the capture conditions of NGCC suppressed emissions even at significant SO_3 penetration. It is possible the inlet aerosol concentration in the NGCC case was significantly reduced due to the flue gas dilution with air to meet the 4% CO_2 spec.

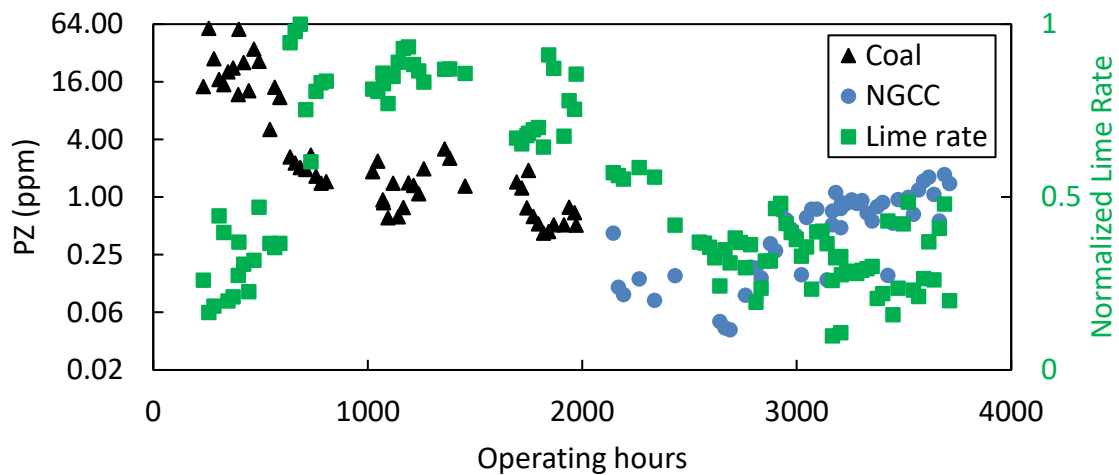


Figure 4.5: Effect of lime rate on emissions during coal and NGCC campaigns. Lime rate is normalized to maximum injection during both campaigns. All data points represent daily averages.

4.4.2 Emissions from NGCC Steady-State Operations

Of the 75 steady-state runs during the NGCC campaign, PZ measurements at the absorber and wash tower gas outlet were available for 36 and 56 runs, respectively (Table 4.1). PZ emissions from the water wash across all steady-state runs were below 3 ppm with an average of 0.72 ppm (Figure 4.6). PZ emissions from the absorber had two distinct sets: the first with a maximum of 0.4 ppm and the second with an average of 11 ppm. Figure 4.7 shows that the dramatic increase in emissions for the absorber gas corresponds with the bypass of the DCC. This bypass also resulted in a five-fold increase in PZ exiting the wash tower (Table 4.2). The intercooling configurations tested did not have a significant effect on emissions. When the DCC was bypassed, the inlet gas at 76 °C was introduced to the absorber resulting in possible aerosol formation due to quenching of hot gas with cold solvent (Bade et al., 2015). Throughout the test period, the lean solvent temperature was constant at 40 °C, and no significant changes in process operations that can explain the increase in emissions were identified. However, the initial blob of absorber outlet data could be an artifact of the FTIR sampling technique at the beginning of the campaign. Probe failure and condensation were observed at the absorber sampling port at the beginning of the campaign and were only corrected later. Nonetheless, even if the absorber data at the start of the campaign is discarded, the increase in wash tower PZ is still best explained by aerosol formation due to quenching of the hot gas.

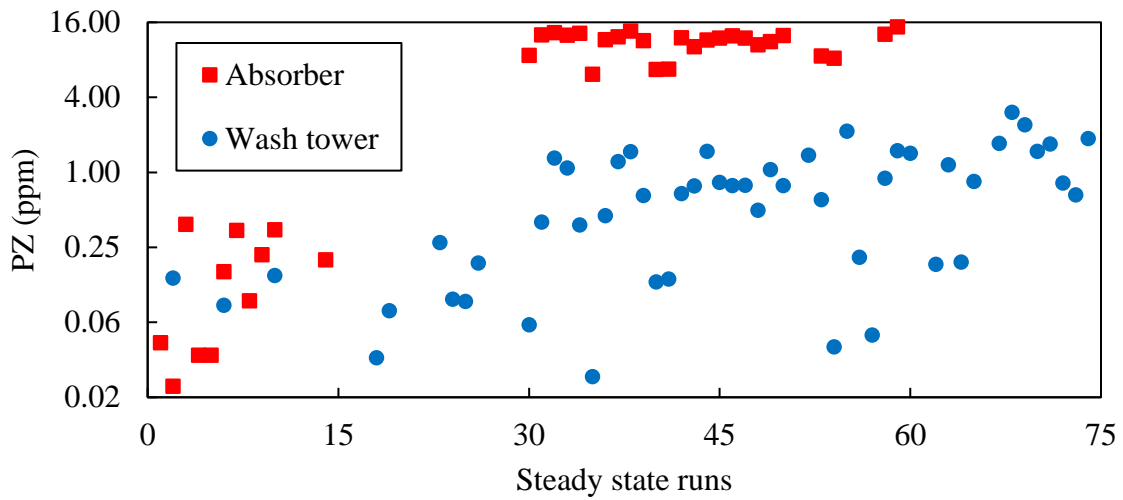


Figure 4.6: PZ emission from the absorber and wash tower gas outlets for steady-state operations during the NGCC campaign.

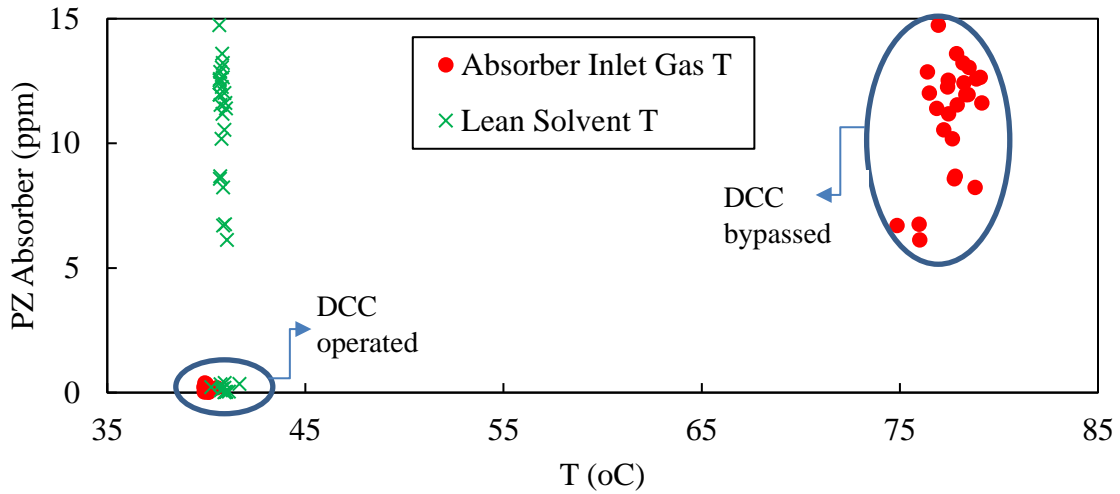


Figure 4.7: Effect of bypassing DCC on PZ emission during NGCC campaign. Lean solvent T was set to 40 °C and remained unchanged throughout the campaign. PZ data point represents hourly steady-state averages of PZ in absorber gas outlet.

Table 4.1: Steady state run summary for NGCC campaign

Run	PZ WW outlet ppm	PZ Abs outlet ppm	Abs Gas Inlet T C	Abs Gas Outlet T C	WW Outlet T C	Solvent Inlet T C	IC	DCC	Solvent Inlet kg/s	Gas Inlet kg/s	Abs Inlet CO ₂ %	CO ₂ Removal %	lldg m/m	rldg m/m
1		0.04	40.1	47.9	40.6	41.1	IO	ON	0.80	0.82	4.3	87	0.20	0.41
2	0.14	0.02	40.1	47.8	40.5	40.9	IO	ON	1.05	1.01	4.3	89	0.20	0.40
3		0.38	39.9	48.0	40.5	40.9	IO	ON	1.01	1.01	4.3	88	0.19	0.40
4		0.03	40.0	46.5	40.5	41.0	IO	ON	0.86	0.63	4.3	87	0.23	0.40
5		0.03	39.9	45.4	40.7	41.0	IO	ON	0.91	0.63	4.3	92	0.24	0.40
6	0.09	0.16	39.9	44.8	40.7	40.8	IO	ON	1.60	1.01	4.3	91	0.24	0.38
7		0.34	40.0	44.8	40.7	40.7	IO	ON	1.60	1.01	4.3	92	0.23	0.38
8		0.09	40.0	44.4	40.5	40.7	IO	ON	1.61	1.01	4.3	92	0.24	0.38
9		0.22	39.9	44.6	40.7	40.3	IO	ON	1.62	1.01	4.3	91	0.24	0.39
10	0.15	0.35	40.0	47.4	47.4	41.7	PA	ON	0.61	0.63	4.3	94	0.20	0.41
11			40.0	43.1	42.1	41.4	PA	ON	0.93	0.63	4.3	96	0.23	0.39
12			39.7	45.9	40.6	41.0	PA	ON	1.28	1.01	4.3	95	0.21	0.38
13			39.9	46.1	40.7	41.3	PA	ON	1.05	1.01	4.3	86	0.21	0.40
14		0.20	40.5	44.1	40.5	40.9	PA	ON	1.38	1.01	4.0	86	0.25	0.39
15			39.9	43.3	40.6	40.7	PA	ON	1.37	1.01	4.0	91	0.25	0.38
16			75.7	45.2	37.6	41.1	PA	OFF	0.84	0.63	4.3	85	0.25	0.40
17			75.8	41.5	35.0	41.1	PA	OFF	1.07	0.63	4.3	94	0.25	0.38
18	0.03		76.6	43.2	36.6	41.0	PA	OFF	0.97	0.63	4.3	92	0.25	0.39
19	0.08		73.9	43.2	36.6	40.9	PA	OFF	1.04	0.63	4.3	92	0.25	0.38
20	0.01		83.0	40.2	37.7	40.5	PA	OFF	1.77	1.01	4.3	92	0.25	0.36
21	0.00		82.7	41.4	37.8	40.5	PA	OFF	1.58	1.01	4.3	91	0.25	0.37

Table 4.1: Steady state run summary for NGCC campaign (continued)

Run	PZ WW outlet ppm	PZ Abs outlet ppm	Abs Gas Inlet T C	Abs Gas Outlet T C	WW Outlet T C	Solvent Inlet T C	IC	DCC	Solvent Inlet kg/s	Gas Inlet kg/s	Abs Inlet CO ₂ %	CO ₂ Removal %	lldg m/m	rldg m/m
22	0.01		82.6	41.9	37.8	40.6	PA	OFF	1.61	1.01	4.3	91	0.25	0.38
23	0.27		80.0	44.0	42.1	40.7	PA	OFF	1.49	1.01	4.3	90	0.24	0.38
24	0.10		80.4	42.4	41.7	40.7	PA	OFF	1.49	1.01	4.3	92	0.24	0.38
25	0.09		79.6	42.4	42.6	40.7	PA	OFF	1.48	1.01	4.3	92	0.24	0.38
26	0.19		77.9	42.5	37.7	40.6	PA	OFF	1.48	1.01	4.3	93	0.23	0.38
27			76.8	41.6	37.7	40.8	PA	OFF	1.48	1.01	4.3	93	0.24	0.37
28			75.8	41.4	37.6	40.7	PA	OFF	1.48	1.01	4.3	93	0.25	0.38
29			78.8	52.8	52.5	53.5	PA	OFF	1.49	1.01	4.3	73	0.23	0.38
30	0.06	8.68	77.8	42.5	42.8	40.7	PA	OFF	1.34	1.01	4.3	91	0.25	0.39
31	0.40	12.65	79.1	44.0	44.1	40.8	PA	OFF	1.23	1.01	4.3	85	0.24	0.40
32	1.31	13.22	78.2	43.5	40.6	40.8	PA	OFF	1.25	1.01	4.3	86	0.25	0.40
33	1.08	12.59	78.9	43.9	40.6	40.7	PA	OFF	1.24	1.01	4.3	86	0.24	0.40
34	0.38	13.05	78.5	43.5	40.5	40.8	PA	OFF	1.24	1.01	4.3	86	0.24	0.40
35	0.02	6.12	76.0	43.0	40.4	41.0	PA	OFF	1.24	1.01	4.3	85	0.25	0.40
36	0.45	11.62	79.1	43.7	37.8	41.0	PA	OFF	1.25	1.01	4.3	85	0.24	0.40
37	1.22	12.26	77.4	43.4	37.7	40.8	PA	OFF	1.25	1.01	4.3	86	0.25	0.40
38	1.47	13.60	77.9	43.6	37.7	40.8	PA	OFF	1.25	1.01	4.3	86	0.24	0.40
39	0.65	11.40	76.9	43.3	37.8	41.0	PA	OFF	1.20	1.01	4.3	86	0.25	0.40
40	0.13	6.70	74.9	43.2	37.7	40.9	PA	OFF	1.24	1.01	4.3	86	0.25	0.40
41	0.14	6.76	76.0	43.5	37.7	40.9	PA	OFF	1.25	1.01	4.3	86	0.24	0.40
42	0.67	12.02	76.5	43.8	37.7	40.9	PA	OFF	1.25	1.01	4.3	86	0.24	0.40
43	0.78	10.18	77.6	43.8	37.4	40.8	PA	OFF	1.22	1.01	4.3	85	0.25	0.40

Table 4.1: Steady state run summary for NGCC campaign (continued)

Run	PZ WW outlet ppm	PZ Abs outlet ppm	Abs Gas Inlet T C	Abs Gas Outlet T C	WW Outlet T C	Solvent Inlet T C	IC	DCC	Solvent Inlet kg/s	Gas Inlet kg/s	Abs Inlet CO ₂ %	CO ₂ Removal %	lldg m/m	rldg m/m
44	1.48	11.54	77.9	45.4	37.2	40.7	PA	OFF	1.22	1.01	4.3	85	0.24	0.40
45	0.83	11.96	78.4	44.1	37.8	40.7	PA	OFF	1.22	1.01	4.3	84	0.24	0.40
46	0.78	12.43	78.2	50.4	37.7	40.7	PA	OFF	1.22	1.01	4.3	86	0.24	0.40
47	0.79	11.95	78.3	46.1	37.7	40.7	PA	OFF	1.22	1.01	4.3	85	0.24	0.40
48	0.50	10.54	77.2	43.9	43.3	40.9	PA	OFF	1.21	1.01	4.3	86	0.24	0.40
49	1.05	11.18	77.5	44.2	37.9	40.8	PA	OFF	1.23	1.01	4.3	85	0.25	0.40
50	0.78	12.54	77.4	43.9	37.8	40.7	PA	OFF	1.23	1.01	4.3	85	0.24	0.40
51			77.7	45.7	37.5	40.7	PA	OFF	1.23	1.01	4.3	85	0.24	0.40
52	1.37		78.3	43.8	37.3	40.8	PA	OFF	1.23	1.01	4.3	87	0.24	0.40
53	0.60	8.57	77.7	44.0	37.7	40.7	PA	OFF	1.22	1.01	4.3	86	0.24	0.40
54	0.04	8.24	78.8	45.4	37.6	40.8	PA	OFF	1.22	1.01	4.3	86	0.24	0.40
55	2.14		78.4	43.3	40.6	40.8	PA	OFF	1.21	1.01	4.3	85	0.24	0.40
56	0.21		78.3	44.0	40.5	40.8	PA	OFF	1.22	1.01	4.3	85	0.25	0.40
57	0.05		77.5	43.8	40.5	40.8	PA	OFF	1.24	1.01	4.3	85	0.25	0.40
58	0.90	12.87	76.4	43.8	40.5	40.7	PA	OFF	1.23	1.01	4.3	86	0.24	0.40
59	1.49	14.74	76.9	44.3	37.9	40.6	PA	OFF	1.22	1.01	4.3	87	0.23	0.40
60	1.42		76.3	44.2	37.9	40.7	PA	OFF	1.21	1.01	4.3	86	0.24	0.41
61	0.00		76.7	44.8	37.4	40.7	PA	OFF	1.21	1.01	4.3	87	0.24	0.41
62	0.18		77.1	44.5	37.3	40.7	PA	OFF	1.22	1.01	4.3	87	0.23	0.41
63	1.15		77.2	44.7	37.7	40.7	PA	OFF	1.23	1.01	4.3	87	0.23	0.41
64	0.19		77.7	51.3	38.2	40.7	PA	OFF	1.22	1.01	4.3	86	0.23	0.41
65	0.84		77.5	45.0	37.4	40.7	PA	OFF	1.23	1.01	4.3	87	0.24	0.41

Table 4.1: Steady state run summary for NGCC campaign (continued)

Run	PZ WW outlet ppm	PZ Abs outlet ppm	Abs Gas Inlet T C	Abs Gas Outlet T C	WW Outlet T C	Solvent Inlet T C	IC	DCC	Solvent Inlet kg/s	Gas Inlet kg/s	Abs Inlet CO ₂ %	CO ₂ Removal %	lldg m/m	rldg m/m
66	0.00		77.4	45.1	37.8	40.8	PA	OFF	1.23	1.01	4.3	87	0.23	0.41
67	1.71		77.8	45.0	38.5	40.7	PA	OFF	1.22	1.01	4.3	87	0.24	0.41
68	3.03		77.9	45.3	39.1	40.5	PA	OFF	1.22	1.01	4.3	86	0.23	0.41
69	2.41		77.3	45.9	39.3	40.7	PA	OFF	1.22	1.01	4.3	86	0.23	0.41
70	1.48		77.7	45.4	39.3	40.5	PA	OFF	1.22	1.01	4.3	85	0.23	0.41
71	1.69		77.6	46.1	39.0	40.6	PA	OFF	1.22	1.01	4.3	85	0.23	0.41
72	0.82		77.4	44.9	38.5	40.6	PA	OFF	1.23	1.01	4.3	86	0.23	0.41
73	0.66		78.1	44.9	42.3	40.6	PA	OFF	1.22	1.01	4.3	86	0.24	0.41
74	1.87		78.0	45.5	42.1	40.5	PA	OFF	1.22	1.01	4.3	86	0.23	0.41
75			77.8	45.5	42.2	40.6	PA	OFF	1.23	1.01	4.3	85	0.23	0.41

Table 4.2: Average PZ emissions from absorber configurations tested.

DCC	Intercooling (IC)	PZ Water Wash Gas outlet (ppm)	PZ Absorber Gas outlet (ppm)
ON	IO	0.11	0.15
	PA	0.15	0.27
OFF	PA	0.75	11.1

4.4.3 Wash Tower Performance

The continuous measurement of gas compositions upstream and downstream of the water wash provides a real-time evaluation of the wash tower performance. For this analysis, steady-state runs 41–70 were chosen as reliable PZ data from both the absorber and wash tower outlets. Wash tower removal efficiency was defined as the fraction of PZ removed from the gas in the wash tower. Figure 4.8 shows an inverse correlation between PZ entering wash tower and wash tower removal efficiency. On average, a removal efficiency of 94% was obtained. This means that about 6% of PZ entering the wash tower was emitted.

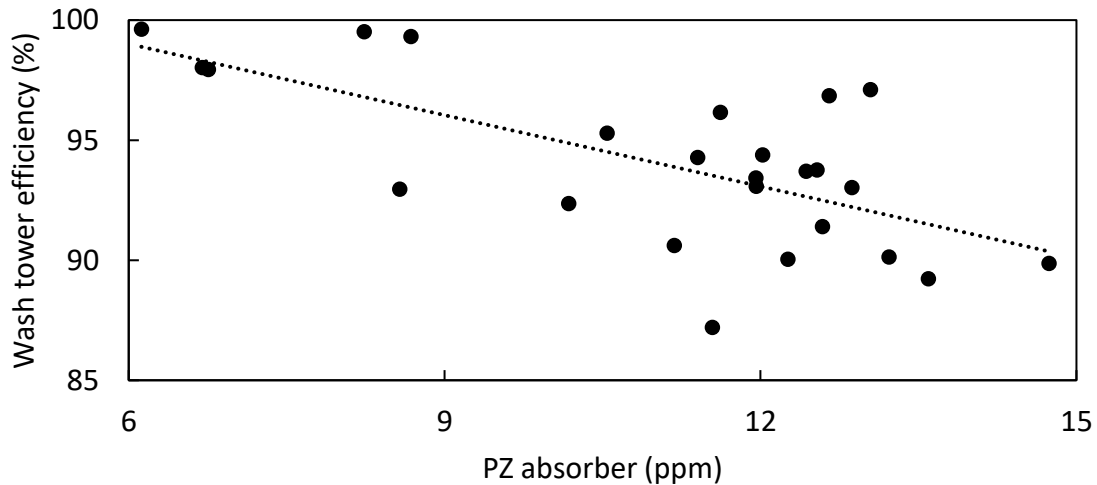


Figure 4.8: Evaluation of wash tower performance during NGCC campaign with DCC bypassed. Each data point represents steady-state averages (runs 41–70) of PZ in the absorber gas outlet.

4.5 CONCLUSIONS

For the same SO₃ penetration, emissions during the NGCC campaign were much lower than that of coal. PZ emissions exiting the water wash at NGCC conditions had a maximum of 2 ppm and an overall average below 1 ppm. The results suggest that the capture conditions of NGCC suppressed emissions even at significant SO₃ penetration. This could have resulted from diluting inlet aerosol as the coal flue gas was diluted with air to meet the 4% CO₂ spec for NGCC.

Bypassing the DCC resulted in a five-fold increase in PZ due to possible aerosol formation from the quenching of hot gas in the absorber. When the DCC was bypassed, the inlet gas at 76 °C was introduced to the absorber, resulting in a five-fold increase in PZ emission. This increase in emission is possibly due to aerosol formation from the quenching of hot gas with cold solvent in the absorber.

The water wash efficiency at NGCC conditions is high and inversely correlated with inlet PZ. The average removal efficiency at NGCC conditions was 94%. This efficiency is significantly higher than coal conditions which ranged from 30–80%, although at a more significant inlet SO₃ load. The water wash efficiency correlates inversely with the PZ concentration entering the water wash.

Chapter 5: Modeling Aerosol Growth for Piperazine

This chapter presents a modified aerosol growth model for PZ, a sensitivity analysis of PZ aerosol growth, and recommendations for aerosol management from design and operational standpoints. It improves upon previous work by Fulk (2016) and Zhang (2018) by using updated equilibrium and thermodynamic models, identifying operating conditions favorable for emission control, and determining the sensitivity of physical property models.

5.1 INTRODUCTION

The amine scrubbing technology for CO₂ capture is challenged by the potential for amine loss to the atmosphere. Several pilot studies have shown that particulates in the flue gas significantly increase amine concentration exiting the absorber and water wash columns (Akinpelumi et al., 2019; Anderlohr et al., 2015; Bade et al., 2015; Beaudry et al., 2019; Kamijo et al., 2013b; Khakharia et al., 2013, 2016). These particulates are aerosol with small drops below 1 μm and 10⁶ to 10⁸ particles/cm³ (Brachert et al., 2013; Saha & Irvin, 2017). The water wash under normal operation fails to mitigate these emissions as the particulates are tiny and travel through channels that evade the bulk washing action in the column. Furthermore, sustained amine emissions above one ppm are prohibitive to CO₂ capture due to regulatory concerns and economic penalties for solvent replenishing.

Extensive work to identify aerosol growth mechanisms and develop models that predict aerosol size and composition at normal operating conditions has been conducted. Fulk (2016) developed an aerosol model for PZ and concluded that aerosol growth is limited in the absorber by uptake of CO₂ and PZ from bulk gas and in the water wash by uptake of water due to the lower water activity of the aerosol. Kang et al. (2017) improved on the Fulk aerosol model by including gas-phase PZ depletion. Using the upgraded PZ model, Zhang (2018) showed that amine aerosol growth in the absorber is driven by amine-

limited diffusion. Khakharia (2015) and Majeed et al. (2017) also agree with the aerosol growth mechanisms presented.

While aerosol emissions can be mitigated by pretreating the flue gas to remove particulates, removing them in the absorber and water wash could be cheaper and more efficient. If the amine aerosol grows larger than 3 μm , it will be collected in the packing and mist eliminator. Fulk (2016) and Zhang (2018) hypothesized that specific operating conditions in the absorber and water wash would accelerate particle growth, aid removal by impaction, and reduce the emitted amine concentration. Using PZ as a case study, Fulk (2016) evaluated the effects of solvent intercooling in the absorber. Zhang (2018) improved this by investigating the impact of lean solvent temperature, lean loading, inlet aerosol concentration, and solvent volatility on aerosol growth. Khakharia (2015) also performed a similar analysis for lean solvent temperature effects on MEA. The overarching conclusions from these studies are that conditions that increase the absolute temperature profile in the absorber and increase the water partial pressure in the water wash will improve the driving force for growth.

More guidance for aerosol management at the pilot scale is still required for PZ and will require accurate modeling of aerosol growth. The modeling analyses performed in previous works do not quantify or clearly distinguish the effect of operational changes on solvent rate and CO_2 removal. The sensitivity of the PZ aerosol model to empirical correlations of the physical property and vapor-liquid equilibrium has also not been thoroughly evaluated. Finally, it is unclear how changes in flow models and heat and mass transfer calculations used by process simulators affect absorber bulk gas and liquid profiles and aerosol growth profiles.

This work presents a modified aerosol growth model for PZ, performs a sensitivity analysis of PZ aerosol growth, and provides recommendations for aerosol management

both from a design and operational standpoint. It extends from previous work by Fulk (2016) and Zhang (2018) in improving the modeling approach using updated equilibrium and thermodynamic models, identifying operating conditions favorable for emission control, and determining the sensitivity of physical property models.

5.2 MODELING APPROACH

The approach to modeling PZ aerosol growth involved two steps:

(1) obtain profiles for bulk gas and liquid compositions and physical properties for each run in the absorber and water wash, and

(2) track the growth of aerosol containing 10^7 particles/cm³ and traveling through the absorber and water wash using the PZ aerosol transport model (ATM).

5.2.1 Absorber and Water Wash Profiles

The absorber and water wash were modeled using the Independence model, developed by Frailie in Aspen Plus[®], with a rigorous e-NRTL thermodynamic framework and rigorous kinetics with reactions in the boundary layer. The packing characterization model is based on updated air-water column measurements (Song, 2017), improving previous work. Bulk-gas compositions and physical properties were extracted for each computational stage in the absorber and water wash. The following properties were extracted: vapor temperature, vapor volumetric flow rate, vapor thermal conductivity, vapor partial pressures of water, CO₂, and PZ, vapor diffusion coefficients of water and PZ, mass transfer coefficients of PZ, interfacial area, liquid temperature, liquid hold-up, and liquid mole fraction of water, CO₂, and PZ.

5.2.2 Aerosol Size Calculations

The size of aerosol with 10^7 particles/cm³ traveling through the columns was calculated using the PZ aerosol transport model developed by (Fulk, 2016) and modified by Kang et al. (2017). The model calculates the size and composition of the drop by tracking the water, CO₂, and PZ in the bulk gas and aerosol phases, with mass transfer occurring at the bulk gas-drop interface and the bulk gas-solvent interface. There are four major inputs to the PZ aerosol transport model:

- (1) Absorber profiles from Aspen Plus[®],
- (2) Equilibrium models for water, CO₂, and PZ,
- (3) Heat and mass transfer models,
- (4) Physical property models

The model equations and assumptions used in this work have been previously published by Kang et al. (2017) and Zhang (2018) and are provided in Appendix A. This work improves on the previous model by using a surrogate equilibrium model that better accounts for the temperature and composition ranges of the aerosol and more accurately matches the gas-phase partial pressure calculations. The equilibrium model used in this work was regressed using flash calculations from thermodynamic data of the Independence model in Aspen Plus[™] (Frailie, 2014). The model was regressed at a loading range of 0.2–0.4 mol CO₂/mol alkalinity, temperature range of 30–70 °C, concentration of 5 m PZ in the absorber, and 0.5–5 m PZ in the water wash. Previous works by Fulk and Zhang used experimental data from Xu (2011) at 0.25–0.4 mol CO₂/mol alkalinity, 4.7–11.3 m PZ, and 40–150 °C. The regression results are presented and compared to empirical models used in previous works in Section 5.6.1.

5.3 BASE CASE

A base case with column configuration and operating conditions similar to those run at the National Carbon Capture Center (NCCC) during the 2018 coal campaign is defined in Table 5.1. The absorber has three packing sections, with only the first and second used for absorption and intercooling between both beds of packing. 90% CO₂ removal was set by optimizing the lean solvent and intercooling flow rates. The absorber and water wash column configuration is shown in Figure 5.1. The sensitivity analyses performed in the rest of this section will be benchmarked against the base case conditions.

Table 5.1: Base case design with PZ at conditions of the NCCC

Inlet Flue Gas Specification	Value	Units
CO ₂	12	vol %
O ₂	6	vol %
N ₂	75	vol %
H ₂ O	7	vol %
Temperature	40	°C
Pressure	1	atm
Mass flow rate	4000	lb/hr
<hr/>		
Inlet Solvent Specification	Value	Units
Lean loading	0.24	mol CO ₂ /mol alk.
Piperazine	5	m
Temperature	40	°C
Pressure	1	atm
Lean solvent flow rate	14700	lb/hr
IC flow rate	14300	lb/hr
CO ₂ Removal	90	%
<hr/>		
Packing Specifications	Value	Units
Packing Height	40	ft
Packing Diameter	2.17	ft
Packing Type	Mellapak 252Y	
No. of Computational stages	60	

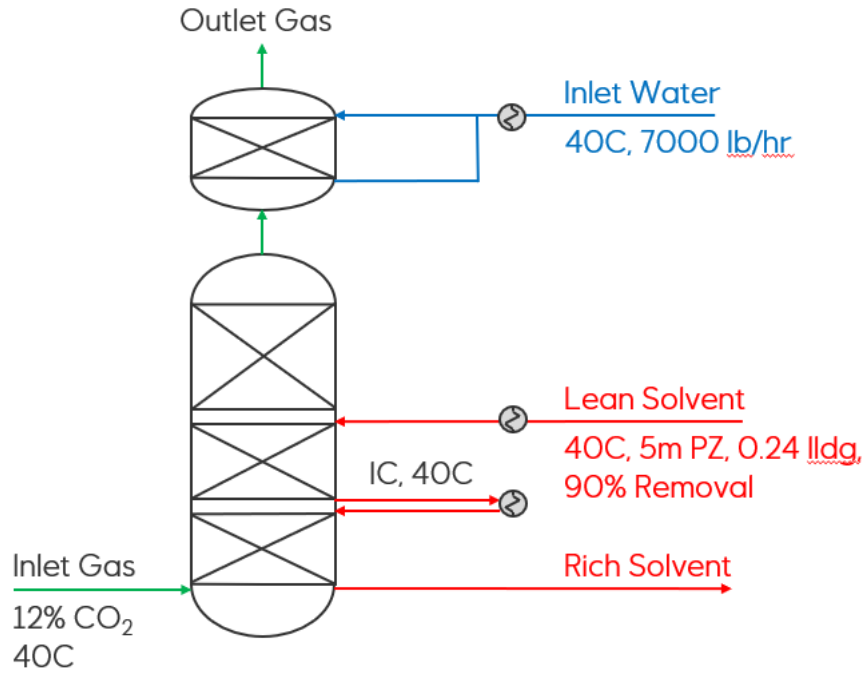


Figure 5.1: Absorber and water wash configuration at base case conditions

5.4 EFFECT OF LONG-TERM DESIGN CONDITIONS ON PZ AEROSOL

A target CO₂ removal is usually specified during long-term operations while other design variables in the absorber and water wash are controlled. This section evaluates the effect of such specifications of absorber and water wash design on PZ aerosol. Twenty operating conditions were modeled in the absorber (Table 5.2) and six conditions in the water wash (Table 5.3). Each design condition was obtained by making stepwise changes to the base conditions earlier defined in Table 5.1. In the absorber, lean solvent temperature, lean loading, intercooling temperature, CO₂ removal, and molality were varied, while in the water wash, the water temperature and rates were varied. At each condition, the solvent and intercooling flow rates were adjusted to obtain the specified CO₂ removal.

Table 5.2: Design conditions varied in the absorber

Design variables	Values	Unit
Lean solvent temperature	40, 50, and 60	°C
Intercooling temperature	35, 40, and 45	°C
Lean loading	0.22, 0.24, and 0.26	mol CO ₂ /mol alk.
CO ₂ removal	90, 93, and 95	%
Molality	4.5, 5, and 5.5	m

Table 5.3: Design conditions varied in the water wash

Operating condition	Values	Unit
Water temperature	35, 40, and 45	°C
Water rate	6000, 7000, and 8000	lb/hr

5.4.1 Absorber Operating Conditions

Figure 5.2 shows the results of the sensitivity analysis in the absorber. Aerosol size varies directly with lean solvent temperature, intercooling temperature, and molality; and varies inversely with lean loading. The impact of CO₂ removal on aerosol size is negligible. The effect of lean solvent and intercooling temperatures are consistent with previous findings by Zhang (2018).

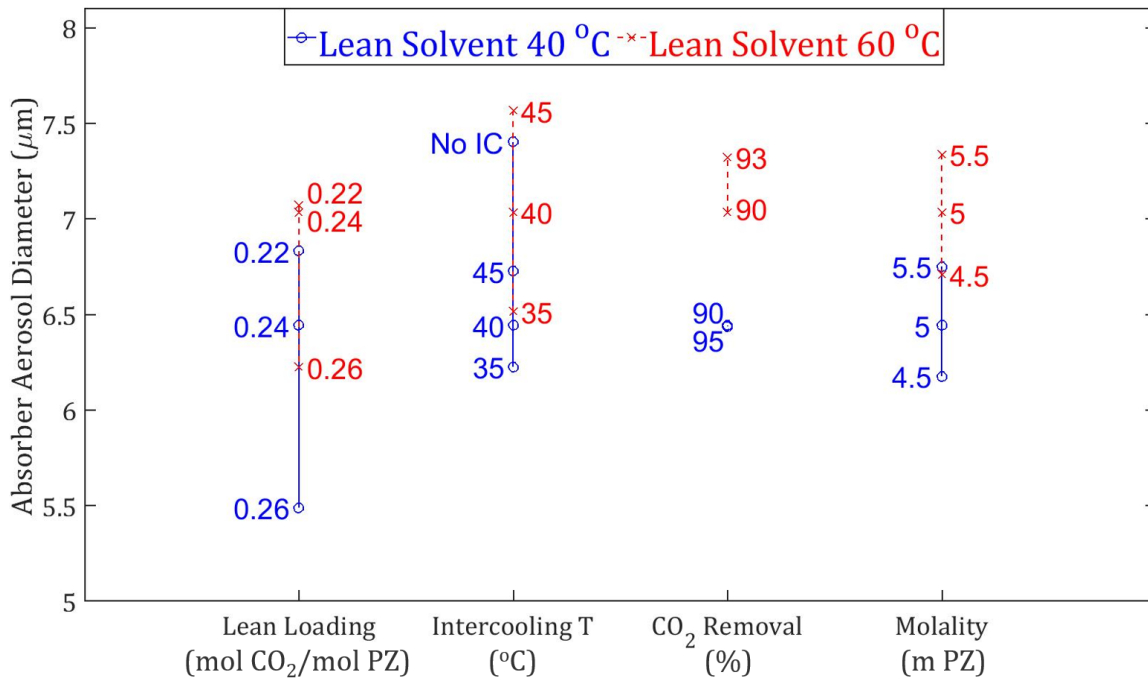


Figure 5.2: Effect of different absorber design conditions on PZ aerosol leaving the absorber

Design conditions in the absorber significantly impact CO₂ absorption in the absorber and solvent recovery downstream. Table 5.4 shows the solvent flow requirement and rich loading for each run. The results show that at constant CO₂ removal, there is a tradeoff between capital or energy costs and PZ aerosol control. Conditions that lead to larger drop sizes exiting the absorber, such as higher lean solvent and intercooling temperatures, also require more solvent flow to maintain CO₂ removal specifications, leading to more capital costs for larger heat exchangers. There are, however, some savings from the avoidance of capital and energy expenses required for additional cooling of the solvent. A lower lean loading does not have the solvent flow penalty but demands a higher energy cost for solvent regeneration in the stripper.

Table 5.4: Results of absorber design conditions at constant CO₂ removal and variable L/G

Run	Description	Lean		Rich	Removal	L/G	IC T	Drop
		Lean T	Loading	Loading				Diameter
		°C	mol CO ₂ /mol alk.		%	lb/lb	°C	m
1	Base Case	40	0.24	0.38	90	3.7	40	6.4
2	With 50 °C Lean T	50	0.24	0.37	90	4.0	40	6.7
3	With 60 °C Lean T	60	0.24	0.36	90	4.4	40	7.0
4	With 0.22 Lean Loading	40	0.22	0.38	90	3.2	40	6.8
5	With 0.26 Lean Loading	40	0.26	0.39	90	4.1	40	5.5
6	With 4.5 m PZ	40	0.24	0.39	90	3.9	40	6.2
7	With 5.5 m PZ	40	0.24	0.38	90	3.6	40	6.8
8	With 35 °C Intercooling	40	0.24	0.39	90	3.5	35	6.2
9	With 45 °C Intercooling	40	0.24	0.37	90	3.9	45	6.7
10	With No Intercooling	40	0.24	0.34	90	5.2	N/A	7.4
12	With 95% CO ₂ Removal	40	0.24	0.38	95	3.9	40	6.4
13	With 60 °C Lean T and 0.22 lldg	60	0.22	0.37	90	3.4	40	7.1

Table 5.4: Results of absorber design conditions at constant CO₂ removal and variable L/G (continued)

Run	Description	Lean	Rich	Removal	Gas	Drop		
		Lean T	Loading		Loading	L/G	Out T	Diameter
		°C	mol CO ₂ /mol alk.	%	lb/lb	°C	m	
14	Base Case, 60 °C Lean T, and 0.26 lldg	60	0.26	0.35	90	5.6	40	6.2
15	Base Case, 60 °C Lean T, and 4.5 m PZ	60	0.24	0.36	90	4.6	40	6.7
16	Base Case, 60 °C Lean T, and 5.5 m PZ	60	0.24	0.36	90	4.2	40	7.3
17	Base Case, 60 °C Lean T, and 35 °C IC	60	0.24	0.37	90	4.0	35	6.5
18	Base Case, 60 °C Lean T, and 45 °C IC	60	0.24	0.35	90	4.9	45	7.6
20	Base Case, 60 °C Lean T, and 93% CO ₂ Removal	60	0.24	0.33	93	6.2	40	7.3

5.4.2 Absorber Packing Volume

In this section, the effect of packing dimensions and type on aerosol growth is studied. The packing volume was adjusted by making changes to the packing height and diameter. While the volume is directly proportional to height, it scales to the square of the diameter. The packing type and dimensions of the NCCC absorber are defined as the base case and are offset at $\pm 20\%$ (Table 5.5). The solvent flow rate was adjusted to maintain 90% CO₂ removal for each run.

Table 5.5: Range of column dimensions evaluated

	Packing Height (ft)	Packing Diameter (ft)
Base case	40	2.17
-20%	32	1.7
+20%	48	2.6

Aerosol growth is directly proportional to absorber height and diameter at constant gas flow rates (Figures 5.3 and 5.4). A 20% increase in absorber height and diameter results in a 5% and 12% increase in outlet aerosol size, respectively. This effect is due to the increase in residence time for growth as the drop travels through the absorber column. The residence time is the ratio of the packing volume and inlet gas flow rate. Increasing the column height increases the residence time for growth at constant gas rates due to the extra distance traveled (Figure 5.5). Similarly, increasing the column diameter at constant gas rates increases residence time for growth due to the reduced drop velocity (Figure 5.6). Therefore, the residence time is the key variable that clarifies the effect of absorber packing volume on aerosol growth.

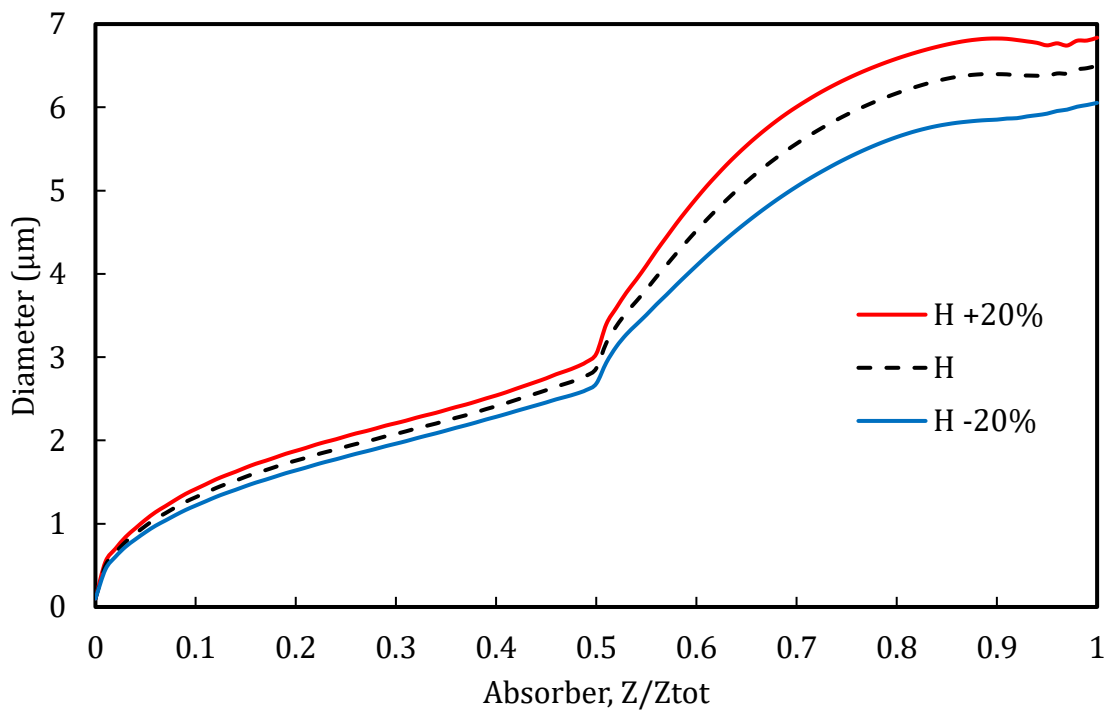


Figure 5.3: Effect of absorber column height on PZ aerosol growth

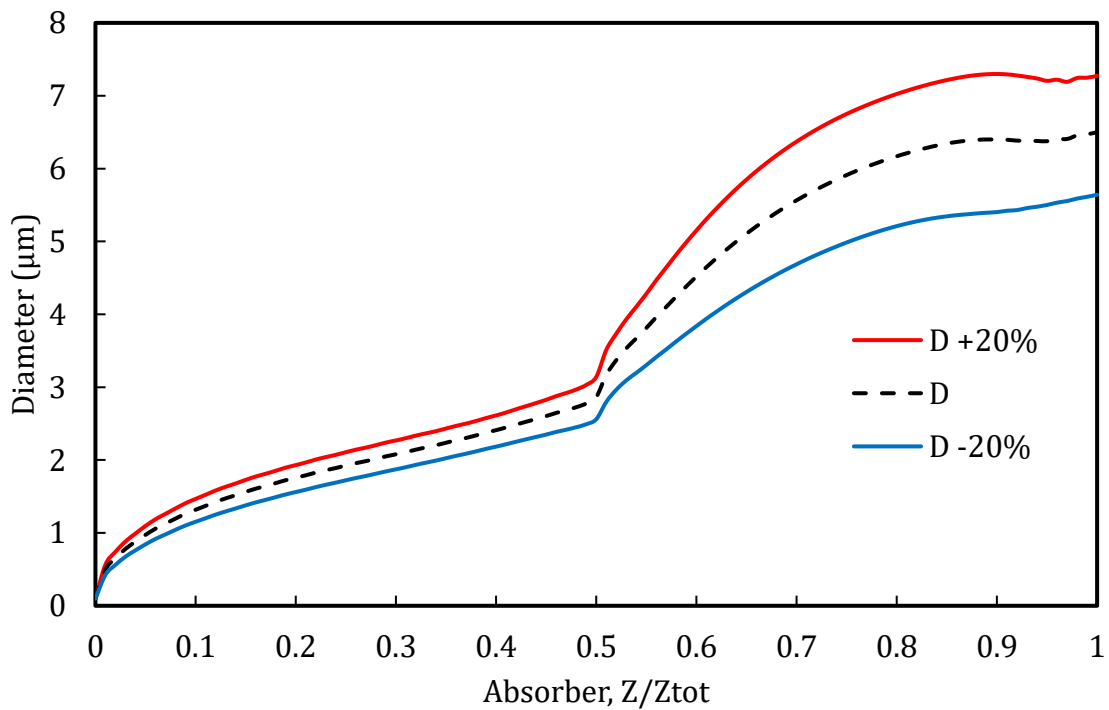


Figure 5.4: Effect of absorber column diameter on PZ aerosol growth

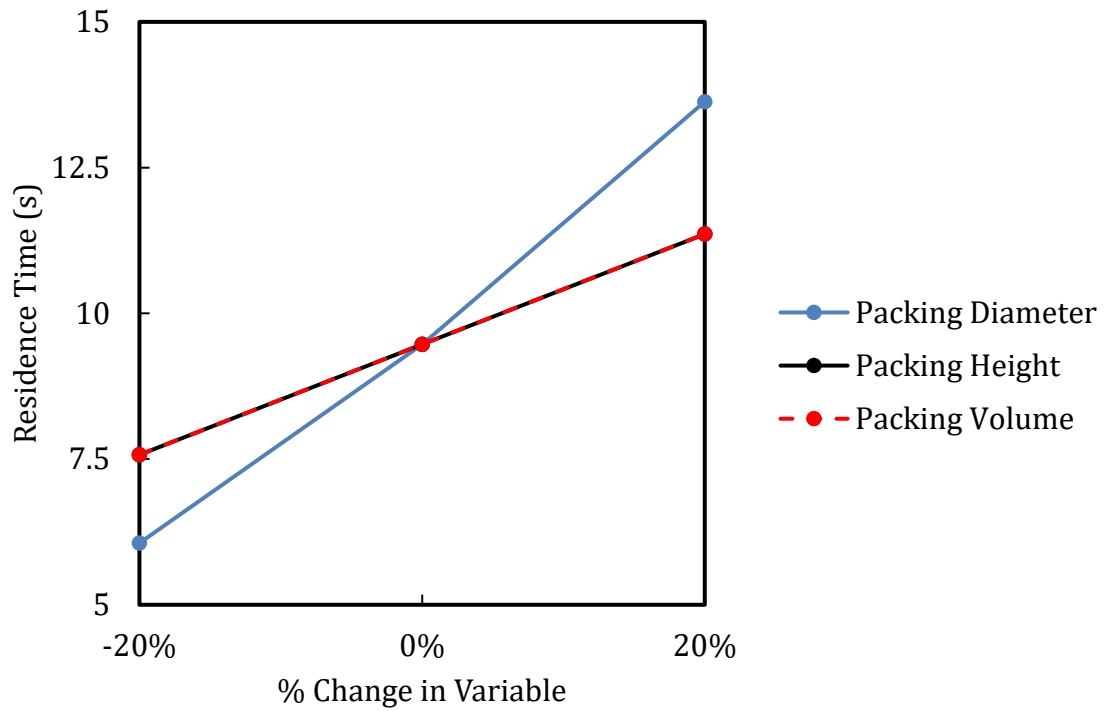


Figure 5.5: Effect of changes in packing volume at constant inlet gas flow on residence time

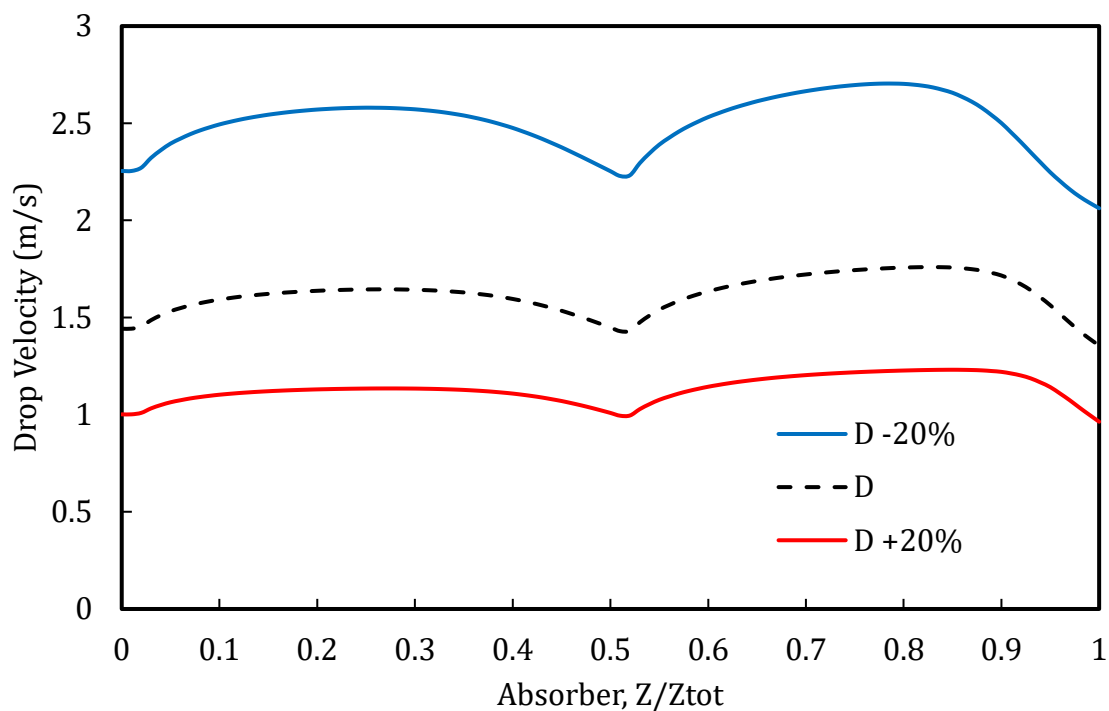


Figure 5.6: Effect of absorber column diameter on drop velocity

5.4.3 Absorber Packing Type

The effect of packing-specific properties on aerosol growth is evaluated for three commercial packing. The interfacial area and liquid hold-up for the base case Mellapak 252Y packing is shown in Table 5.6. These variables are offset at $\pm 20\%$ to evaluate their effect on aerosol growth. The interfacial area and hold-up of Mellapak 252Y are compared to KG 2.5Y and KG 250Y (Table 5.7). They all have comparable interfacial areas and hold-ups except for KG 2.5Y, which has a 30% smaller interfacial area.

Table 5.6: Interfacial area and liquid hold-up for Mellapak 252Y

	Interfacial Area (m ²)	Liquid Hold-up
Base	13.7	0.0061
-20%	11	0.0049
+20%	16.4	0.0073

Table 5.7: Range of packing types evaluated

Packing Type	Interfacial area (m ²)	Hold-up (m ³)
Mellapak 252Y	14	0.0061
KG 2.5Y	9.5	0.0060
KG 250Y	14	0.0058

Figures 5.7 and 5.8 show that a lower hold-up and higher interfacial area create bigger drops. A 20% offset on the interfacial area and hold-up increased drop size by 2% and 1%, respectively. This effect of IA and hold-up on drop size is confirmed by comparing the packing (Figure 5.9). KG 2.5Y, which has a 30% lower interfacial area (Table 5.7), produces the smallest drop.

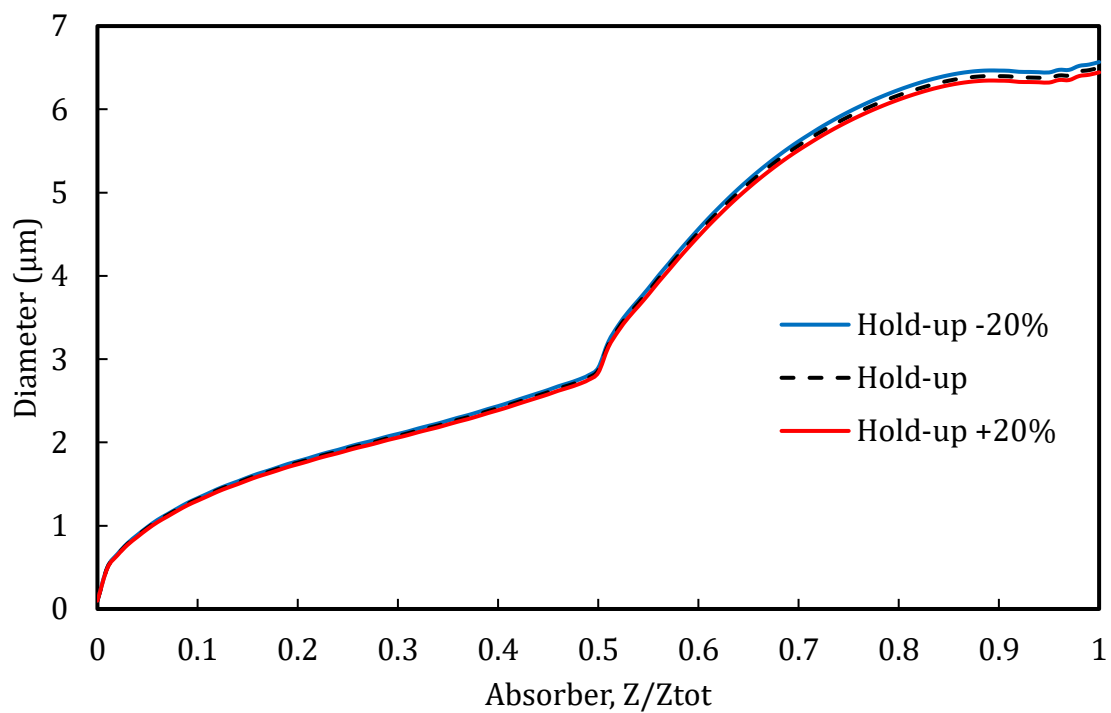


Figure 5.7: Effect of liquid hold-up in absorber on PZ aerosol growth

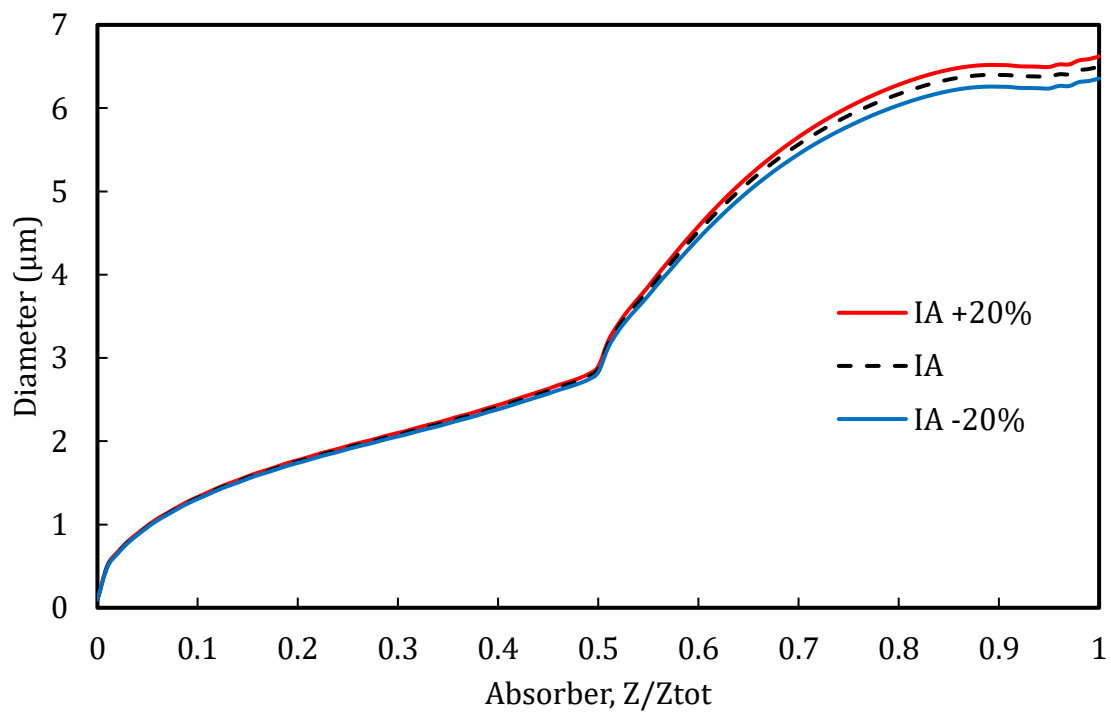


Figure 5.8: Effect of interfacial area in absorber on PZ aerosol growth

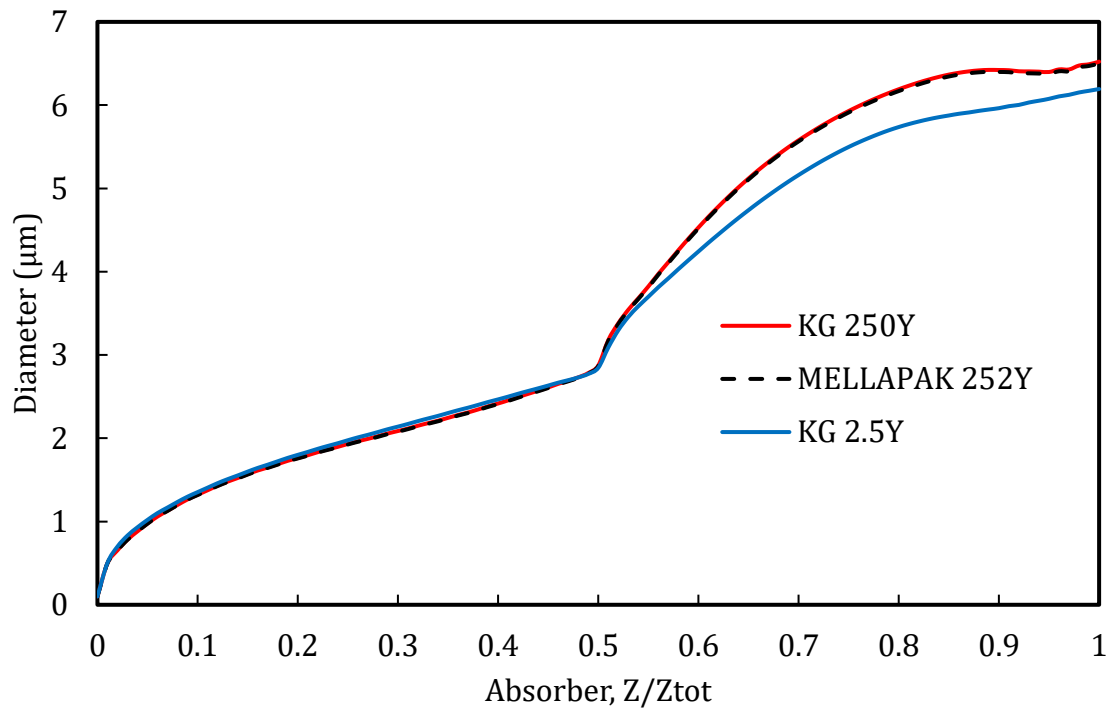


Figure 5.9: Effect of absorber packing type on PZ aerosol growth

5.4.4 Water Wash Operating Conditions

Figure 5.10 shows the results of the sensitivity analysis in the water wash. For colder gas entering the water wash, the water wash temperature has a greater impact on aerosol size than the ratio of liquid to gas flow rates. This observation is reversed for hot gas entering the water wash. Regardless of the absorber conditions, running the water wash at higher temperatures increased drop size. This increase in aerosol size is due to the greater driving force for water transfer from gas to drop at higher temperatures.

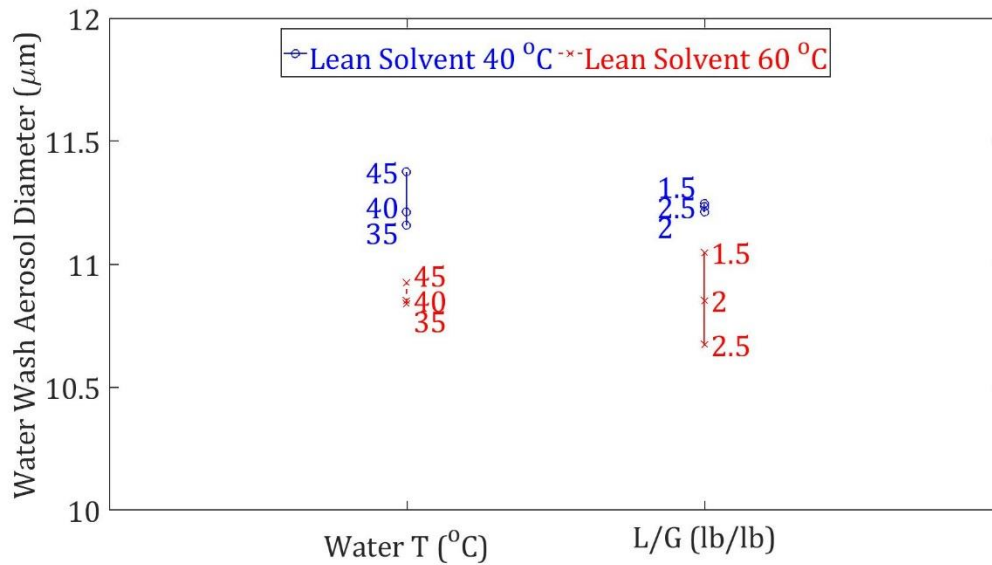


Figure 5.10: Effect of changes in water wash operating conditions on PZ aerosol leaving the water wash

5.5 EFFECT OF PARAMETRIC CHANGES IN ABSORBER OPERATING CONDITIONS ON PZ AEROSOL

Quick, short-term, and reversible changes in operating conditions are desirable for aerosol mitigation during episodes. Such changes affect PZ aerosol, CO₂ absorption, and energy costs. Step changes in the lean solvent temperature and intercooling temperatures were made to the base condition in Table 5.1 while constantly holding all other operating conditions. The analysis in this section differs from the previous in that the solvent rate was held constant through the changes, and no design specification on CO₂ removal was set.

5.5.1 Lean Solvent Temperature

An increase in lean solvent temperature from 40 to 60 °C while holding the solvent flow rate and all other base conditions increased the aerosol size by 6% (Figure 5.11). While this is favorable for aerosol control, it results in a 4% penalty on CO₂ removal (Table

5.8). The tradeoff between emission control and CO₂ removal might be acceptable in the short term to mitigate emissions during episodes. Although the temperature profiles are similar, the bulge increases with lean temperature due to the limited CO₂ absorption at higher temperatures (Figure 5.12). The driving force for PZ transfer from gas to drop is positive throughout most of the column (Figure 5.13) and follows the temperature profile with a slight reversal at the absorber top due to contact with the colder solvent.

Table 5.8: Results of parametric test on lean solvent temperature at constant solvent flow rate simulated in Aspen Plus®

Run	Lean T °C	Lean Loading mol CO ₂ /mol alk.	Rich Loading	Removal %	L/G lb/lb	IC T °C	Drop Diameter m
1	40	0.24	0.383	90	3.7	40	6.4
2	50	0.24	0.378	87	3.7	40	6.6
3	60	0.24	0.376	86	3.7	40	6.9

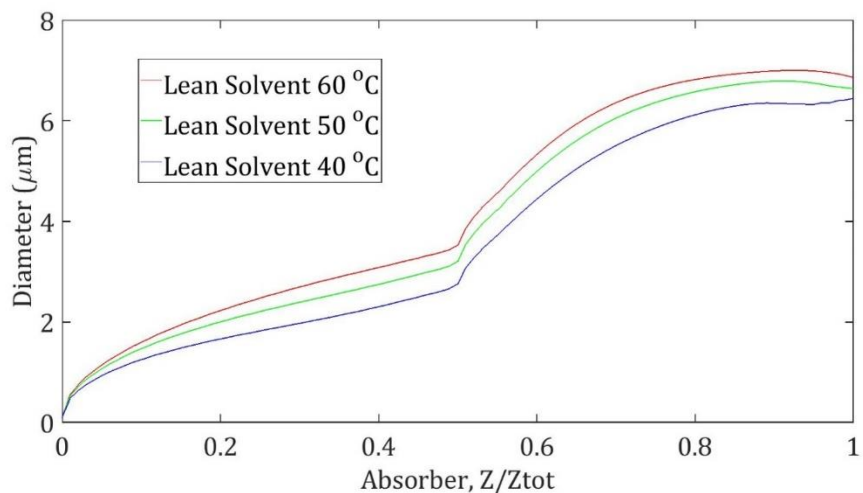


Figure 5.11: Effect of lean solvent temperature on PZ aerosol in the absorber. Constant: 40 °C IC, 0.24 lldg, 5 m PZ, and solvent flow rate. Varied: lean solvent (40–60 °C).

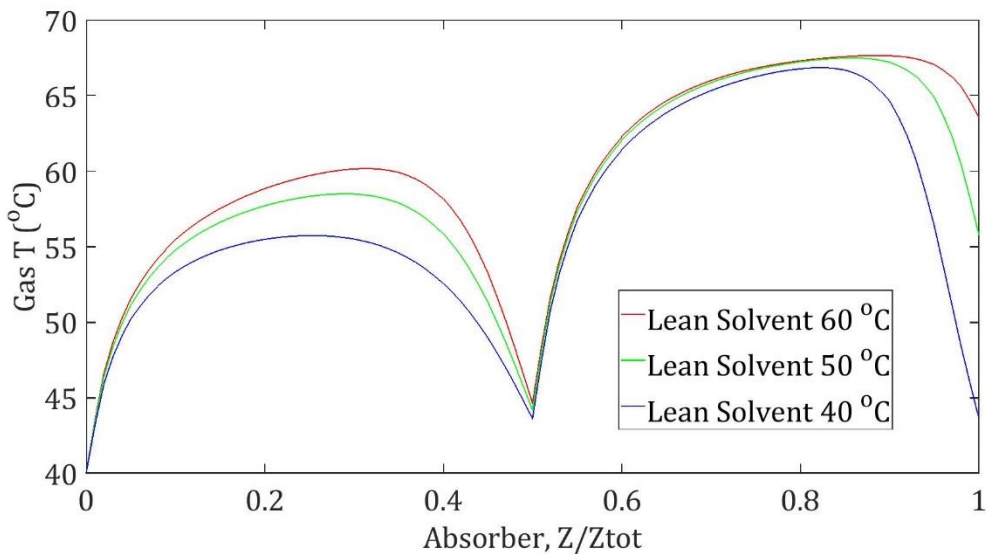


Figure 5.12: Gas temperature profile in absorber at different lean solvent temperatures. Constant: 40 °C IC, 0.24 lldg, 5 m PZ, and solvent flow rate. Varied: lean solvent (40–60 °C).

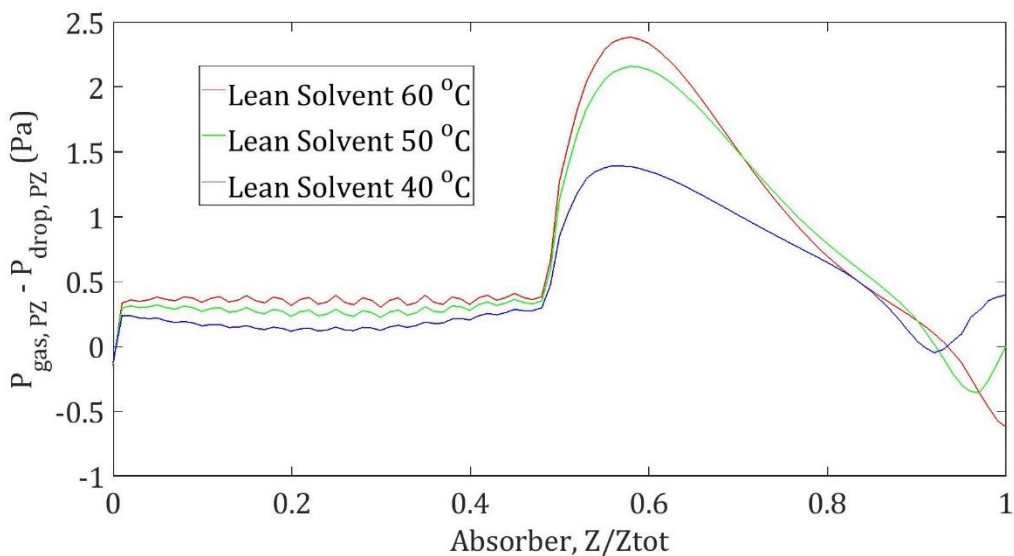


Figure 5.13: Driving force for PZ transfer from gas to aerosol in absorber at different lean solvent temperatures. Constant: 40 °C IC, 0.24 lldg, 5 m PZ, and solvent flow rate. Varied: lean solvent (40–60 °C).

5.5.2 Intercooling Temperature

PZ aerosol grew by 15% with no intercooling (Figure 5.14). The significant increase in aerosol size is favorable for emission control but comes with a 15% penalty in CO₂ removal (Table 5.9). The colder the intercooling temperature, the smaller the temperature bulge in the absorber (Figure 5.15). When intercooling is used, the aerosol grows due to large driving forces at the mid and top sections of the absorber; however, without intercooling, the growth is steepest at the absorber bottom (Figure 5.16).

Table 5.9: Results of parametric test on intercooling T at constant solvent flow rate simulated in Aspen Plus[®]

Run	Lean	Rich	Removal	L/G	IC T	Drop	
	Lean T	Loading					Loading
	°C	mol CO ₂ /mol alk.	%	lb/lb	°C	m	
1	40	0.24	0.383	90	3.7	40	6.4
2	40	0.24	0.374	85	3.7	50	6.9
3	40	0.24	0.361	76	3.7	N/A	7.4

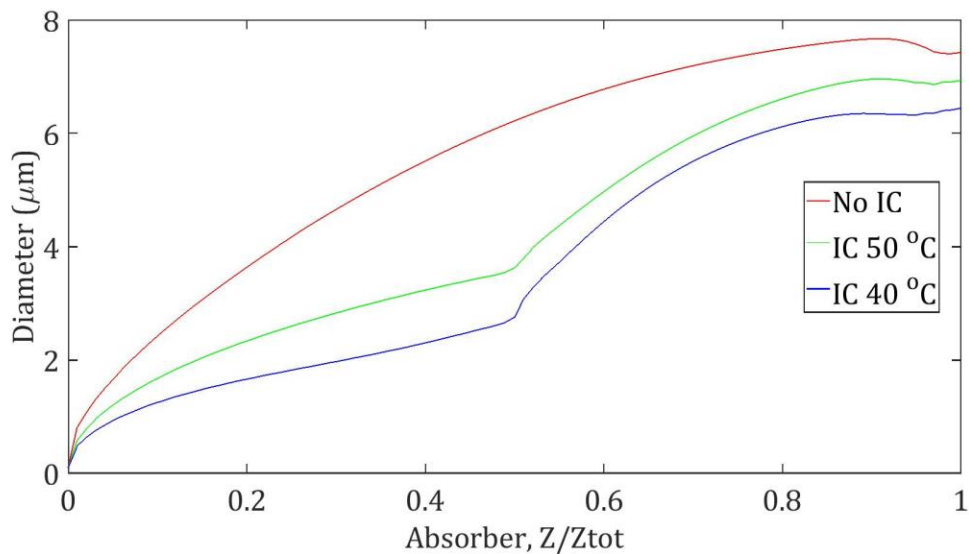


Figure 5.14: Effect of intercooling temperature on PZ aerosol in the absorber. Constant: 40 °C lean solvent, 0.24 lldg, 5 m PZ, and solvent flow rate. Varied: intercooler (35–45 °C).

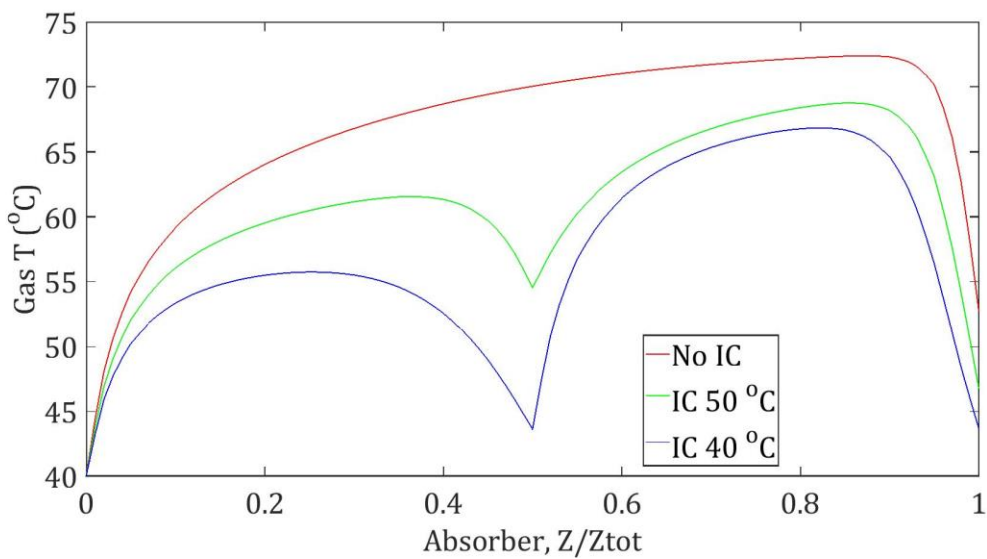


Figure 5.15: Gas temperature profile in absorber at different intercooling temperatures with base case conditions. Constant: 40 °C lean solvent, 0.24 lldg, 5 m PZ, and solvent flow rate. Varied: intercooler (35–45 °C).

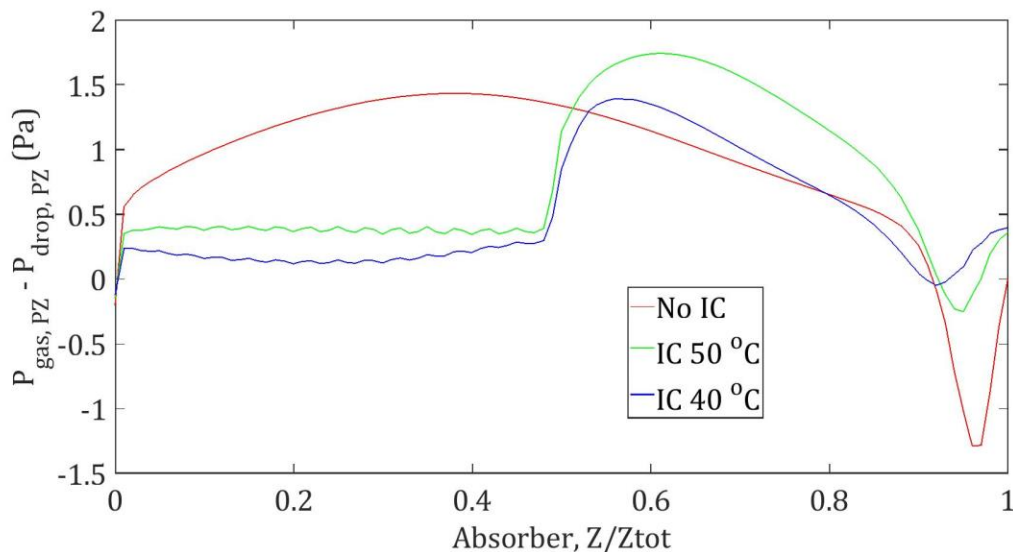


Figure 5.16: Driving force for PZ transfer from gas to aerosol in absorber at different intercooling temperatures with base case conditions. Constant: 40 °C lean solvent, 0.24 lldg, 5 m PZ, and solvent flow rate. Varied: intercooler (35–45 °C).

5.6 EFFECT OF INPUT MODELS ON PZ AEROSOL

5.6.1 Equilibrium Model

An equilibrium model was regressed from Aspen Plus[®] using the electrolyte NRTL model and the Independence[™] developed by Frailie (2014). The results from Aspen Plus[®] were compared to empirical models by Xu (2011) and pure water vapor pressure from the DIPPR chemical databank (DIPPR, 1998).

The equilibrium partial pressures of CO₂, PZ, and H₂O were developed using 55 equilibrium data points generated from Aspen Plus[®] at temperature and composition conditions expected in the aerosol. The ranges were 0.2–0.4 mol CO₂/mol alkalinity and 30–70 °C for loading and temperature, respectively.

The regression results for the equilibrium models are shown in Equations 5.1–5.3 and Table 5.10.

$$P_{CO_2}^* = EXP \left(A + \frac{B}{T} + C\alpha^2 + D\frac{\alpha}{T} + E\frac{\alpha^2}{T} \right) \quad (5.1)$$

$$P_{PZ}^* = x_{PZ}^{app} EXP \left(A + B\ln T + C\alpha + D\frac{\alpha^2}{T} \right) \quad (5.2)$$

$$P_{H_2O}^* = x_{H_2O}^{app} EXP \left(A + \frac{B}{T} + C\ln T + DT^2 \right) \quad (5.3)$$

where:

$P_{CO_2}^*, P_{PZ}^*, P_{H_2O}^*$ = Equilibrium partial pressures of CO₂, PZ, and H₂O (Pa)

T = Temperature (K)

α = CO₂ loading (mol CO₂/mol alkalinity)

$x_{H_2O}^{app}$ = apparent H₂O mole fraction

x_{PZ}^{app} = apparent PZ mole fraction

Table 5.10: Empirical models for CO₂, PZ, and water equilibrium partial pressures from experimental data and Aspen Plus[®]

	P* _{CO2}		P* _{PZ}		P* _{H2O}	
	Independence (Aspen Plus [®])	Empirical Xu (2011)	Independence (Aspen Plus [®])	Empirical Xu (2011)	Independence (Aspen Plus [®])	Empirical Raoult
A	39.55	35.5	-144.70	-123	27.93	73.65
B	-11624.8	-11082	25.37	21.6	-5707.66	-7258.20
C	-51.39	-22.5	16.09	20.2	0	-7.30
D	0	4713	-16167.3	-18174	7.78E-6	4.17E-6
E	28647	11722				
R ²	99.9%	99.3%	99.9%	99.6%	99.9%	

In Figure 5.17, the growth of the PZ drop is compared for both equilibrium models. Although the drop growth profiles are similar for both equilibrium models, the drop grows

20% larger with the predictions from Aspen Plus[®]. This increased growth is due mainly to the differences in CO₂ solubility and PZ volatility predictions from both models. Xu (2011) underpredicts CO₂ solubility and PZ volatility up to 50% compared to Aspen Plus[®] (Figures 5.18 and 5.19), resulting in a lower driving force for PZ transfer from gas to drop. The water vapor pressure predictions by DIPPR (1998) and Aspen Plus[®] within 4% error (Figure 5.20). The models from Aspen Plus[®] are more reliable given that the gas phase partial pressures are calculated using the same Aspen Plus[®] model. However, it should be noted that the rate-based model in Aspen Plus[®] uses rate constants that might not accurately reflect the equilibrium predictions by eNRTL. Based on these results, the modeling approach for PZ aerosol by Zhang (2018) is corrected using equilibrium models regressed from Aspen Plus[®] in this work.

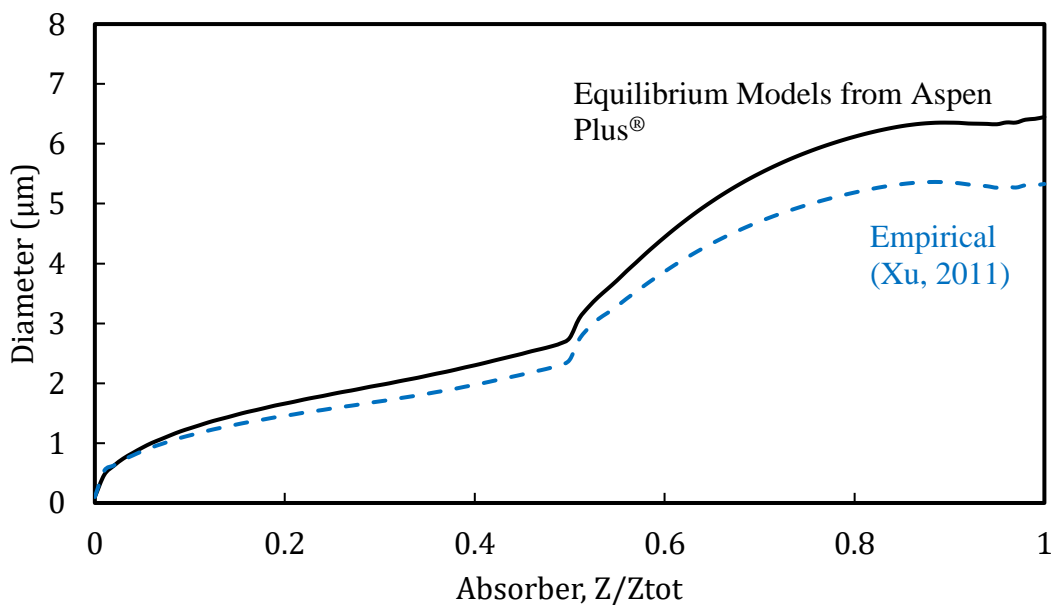


Figure 5.17: Drop growth comparison between equilibrium models from Aspen Plus[®] (solid lines) and empirical correlations (dashed lines) at base case conditions defined in Table 5.1

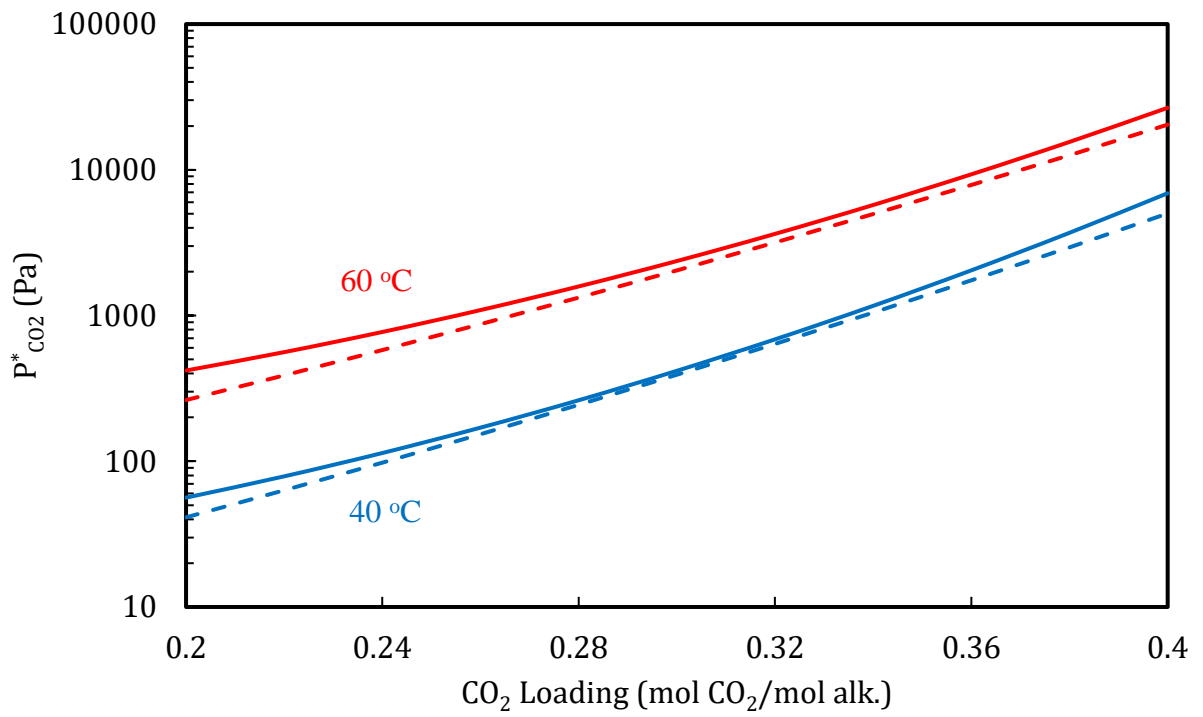


Figure 5.18: CO₂ solubility comparison between Aspen Plus[®] regressed model (solid lines) and empirical correlation by Xu (2011) (dashed lines)

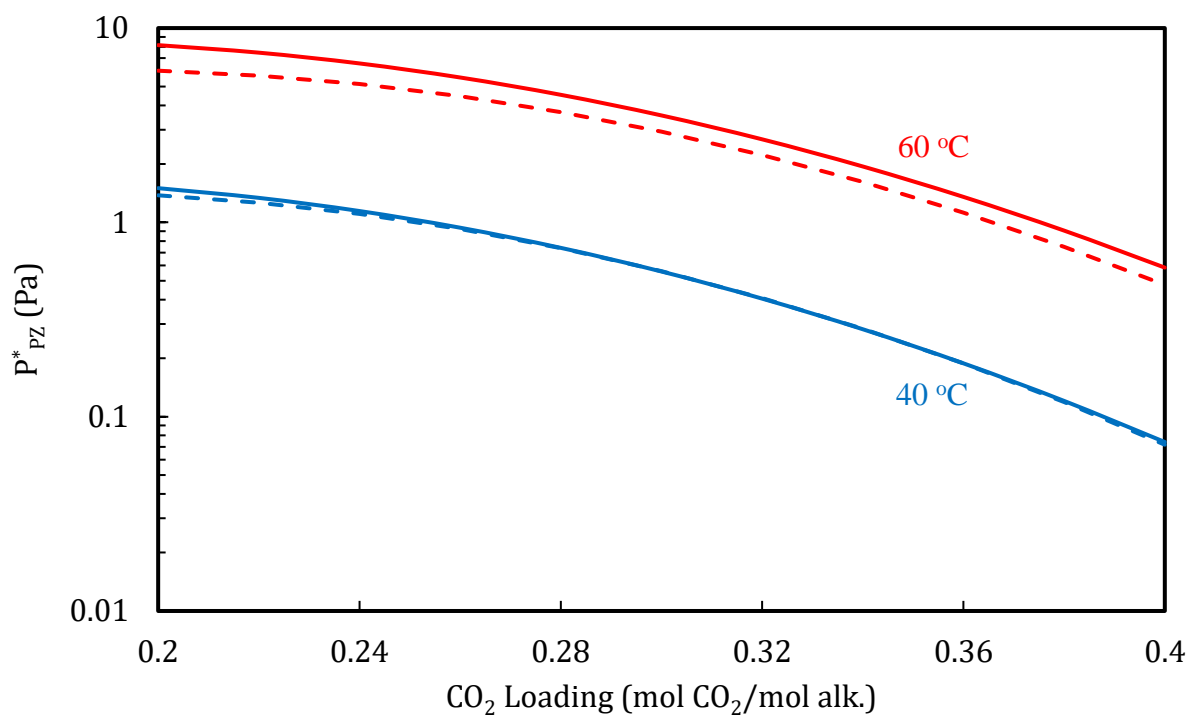


Figure 5.19: PZ volatility comparison between Aspen Plus[®] regressed model (solid lines) and empirical correlation by Xu (2011) (dashed lines)

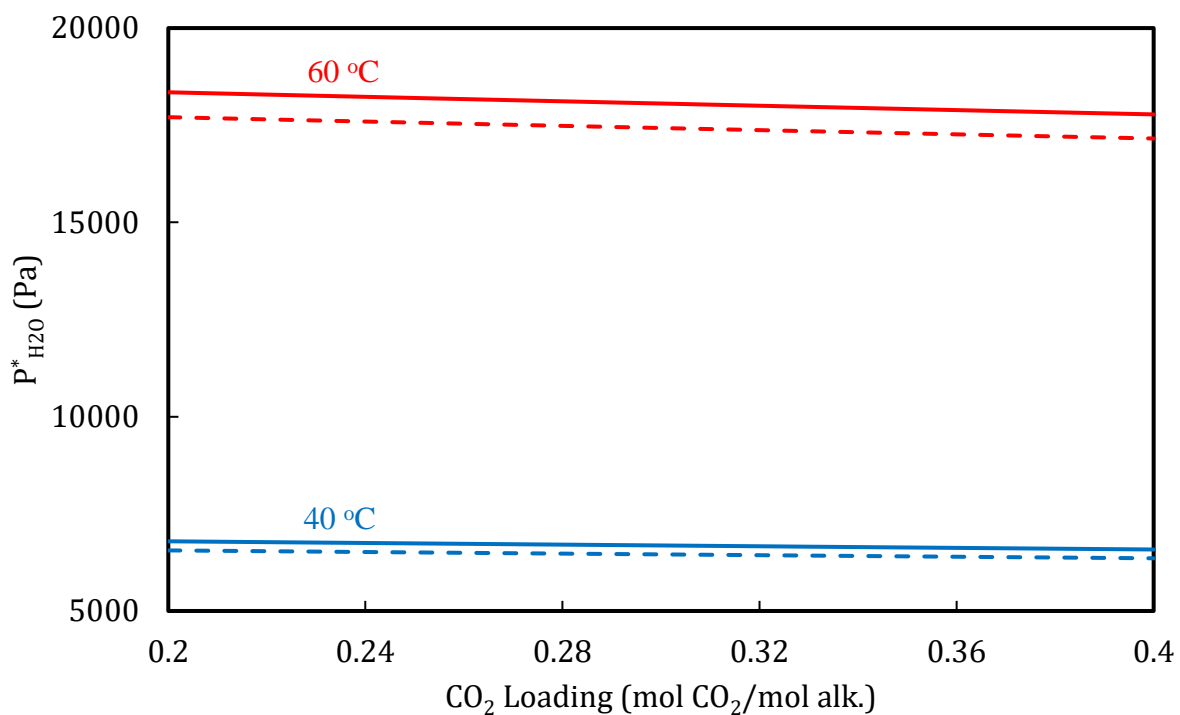


Figure 5.20: Water vapor pressure comparison between Aspen Plus[®] regressed model (solid lines) and empirical correlation by DIPPR (1998) (dashed lines)

5.6.2 Flow Model

The effect of the flow model on aerosol growth was evaluated in this study. The four flow models are shown in Table 5.11. Each case was simulated in Aspen Plus[®] at the base case conditions presented in Table 5.1 with 60 computational stages. The liquid and vapor phases were simulated as well mixed, countercurrent, and plug flow.

Table 5.11: Flow models in Aspen Plus[®]

Flow Model	Description
Countercurrent	Liquid and Vapor phases are countercurrent
Mixed	Liquid and vapor phases are well mixed
VPlug	Liquid is well mixed; vapor is plug flow

The effect of the flow models on absorber bulk gas and liquid temperatures is shown in Figures 5.21 and 5.22. The more well-mixed the flows are, the lower the temperature bulge in the absorber. The countercurrent flow gives the most significant disparity between gas and drop temperatures at the intercooling, causing the drop to grow rapidly (Figures 5.23 and 5.24). The oscillations in Figure 5.22 are due to convergence issues that can be corrected by increasing the computational stages, particularly at the bottom half of the column. These oscillations are not present when the liquid phase is well mixed, indicating a more significant convergence challenge for the plug and countercurrent flow methods. Overall, the flow model used in modeling CO₂ absorption does not significantly affect the outlet aerosol size.

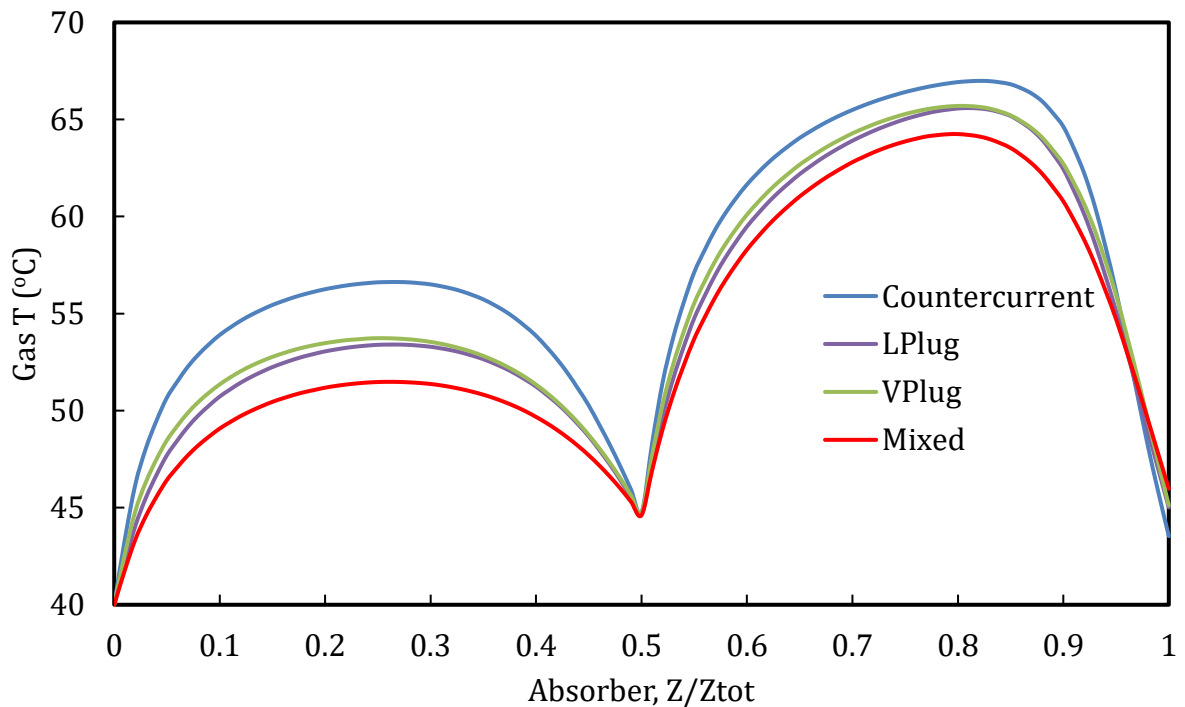


Figure 5.21: Gas temperature profile in the absorber at different flow models

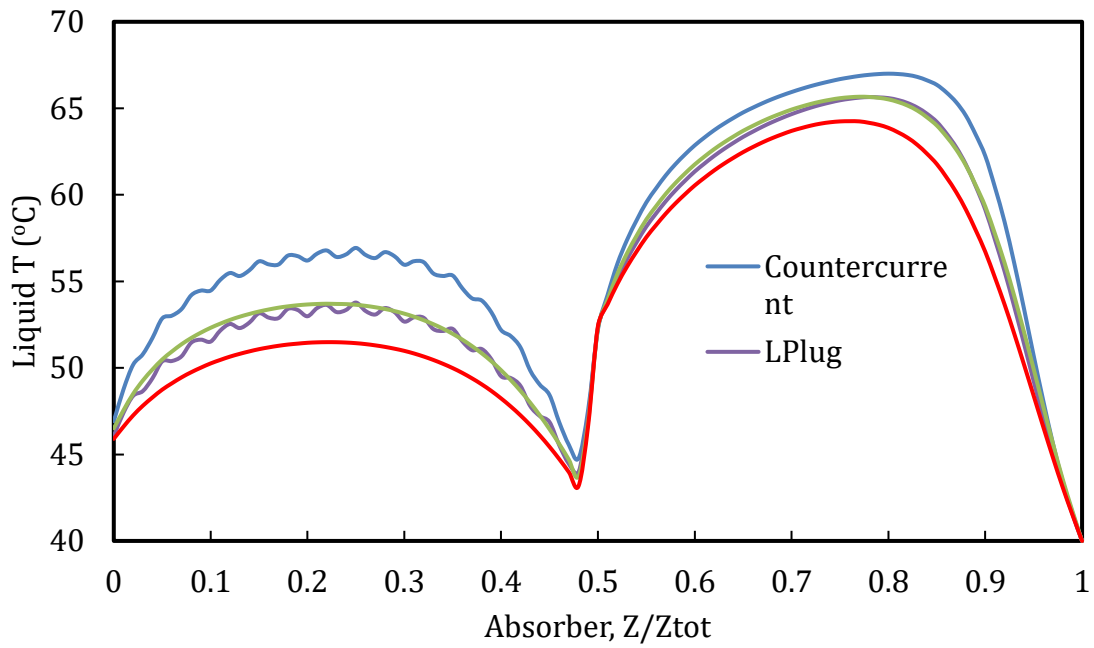


Figure 5.22: Liquid temperature profile in the absorber at different flow models

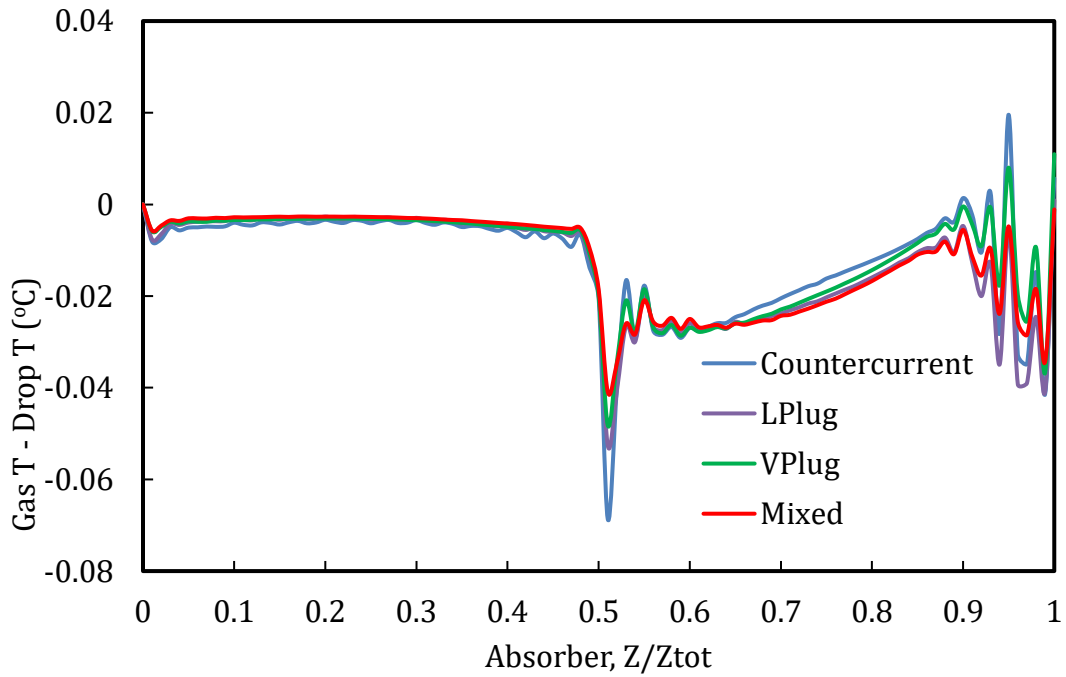


Figure 5.23: Temperature difference between gas and drop in the absorber at different flow models

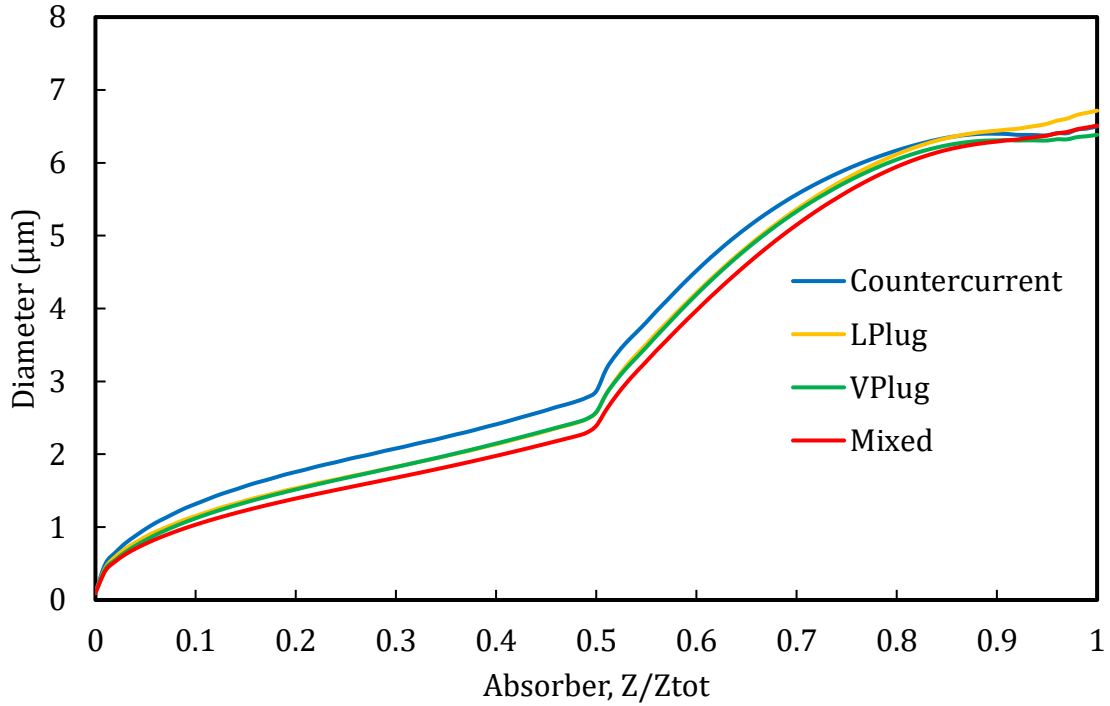


Figure 5.24: Effect of flow models in Aspen Plus® on PZ aerosol growth

5.6.3 Heat and Mass Transfer Models

The effect of heat and mass transfer coefficients calculated by Aspen Plus® on aerosol growth is studied in this work. Aspen Plus® calculates heat and mass transfer coefficients using the Chilton-Colburn weighting parameter.

The Chilton-Colburn j-factor for heat transfer is:

$$j_H = NuRe^{-1}Pr^{-1/3} = \frac{h}{\rho C_p v_0} \left(\frac{\hat{C}_p \mu}{k} \right)^{2/3} \quad (5.4)$$

while that for mass transfer is:

$$j_D = ShRe^{-1}Sc^{-1/3} = \frac{k_x}{c v_0} \left(\frac{\mu}{\rho D_{AB}} \right)^{2/3} \quad (5.5)$$

The Chilton-Colburn analogy is represented by equating the j-factors for heat and mass transfer.

$$j_H = j_D \quad (5.6)$$

Aspen Plus[®] uses a weighting parameter to calculate the average diffusivity and average binary mass transfer coefficient as a factor of the Chilton-Colburn analogy. The default value is 1E-4, and a larger value diminishes the impact of compositions. Changes in the weighting parameter only slightly affect the gas and liquid temperature profiles (Figures 5.25 and 5.26). A higher weighting parameter value results in a greater temperature delta between gas and drop at the intercooling and absorber top (Figure 5.27) and increases outlet aerosol size by 1% (Figure 5.28). Changes in the weighting parameter used by other process simulators should not significantly affect the aerosol growth profile results.

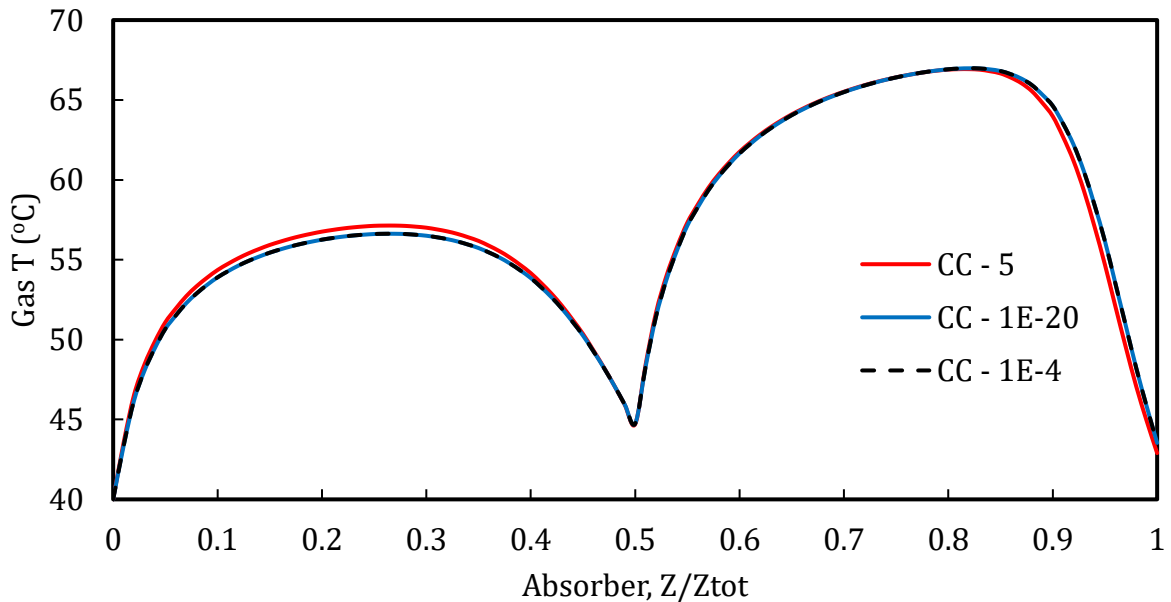


Figure 5.25: Gas temperature profile in the absorber for different Chilton-Colburn weighting parameter values

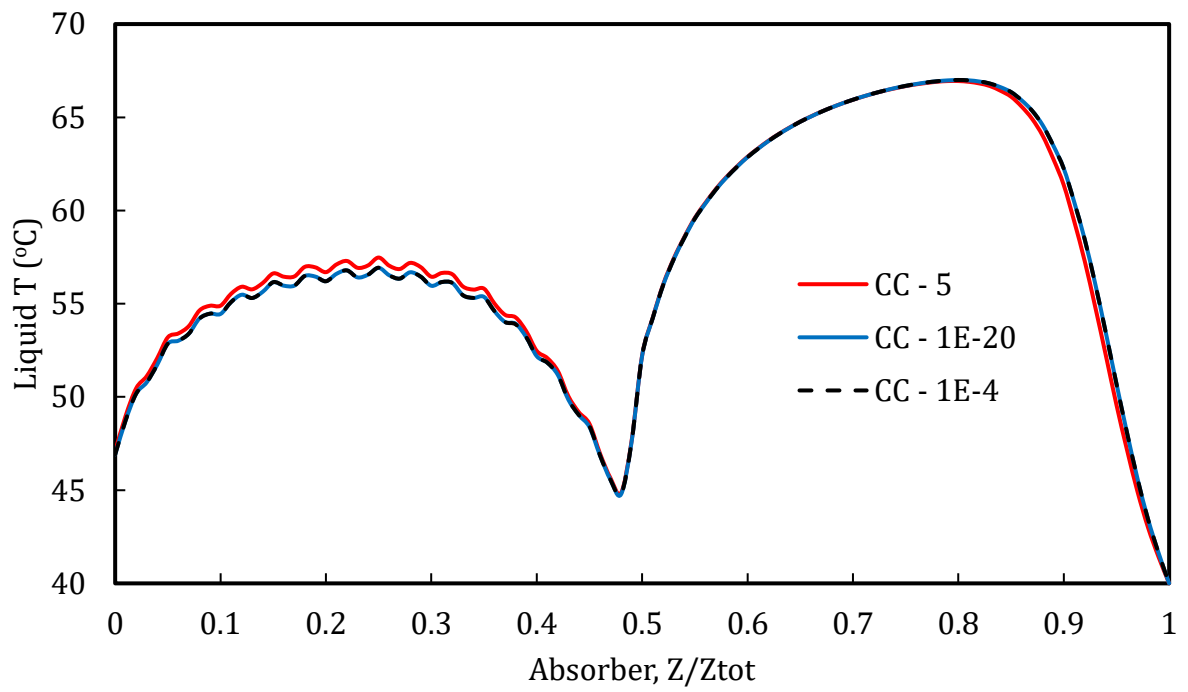


Figure 5.26: Liquid temperature profile in the absorber for different Chilton-Colburn weighting parameter values

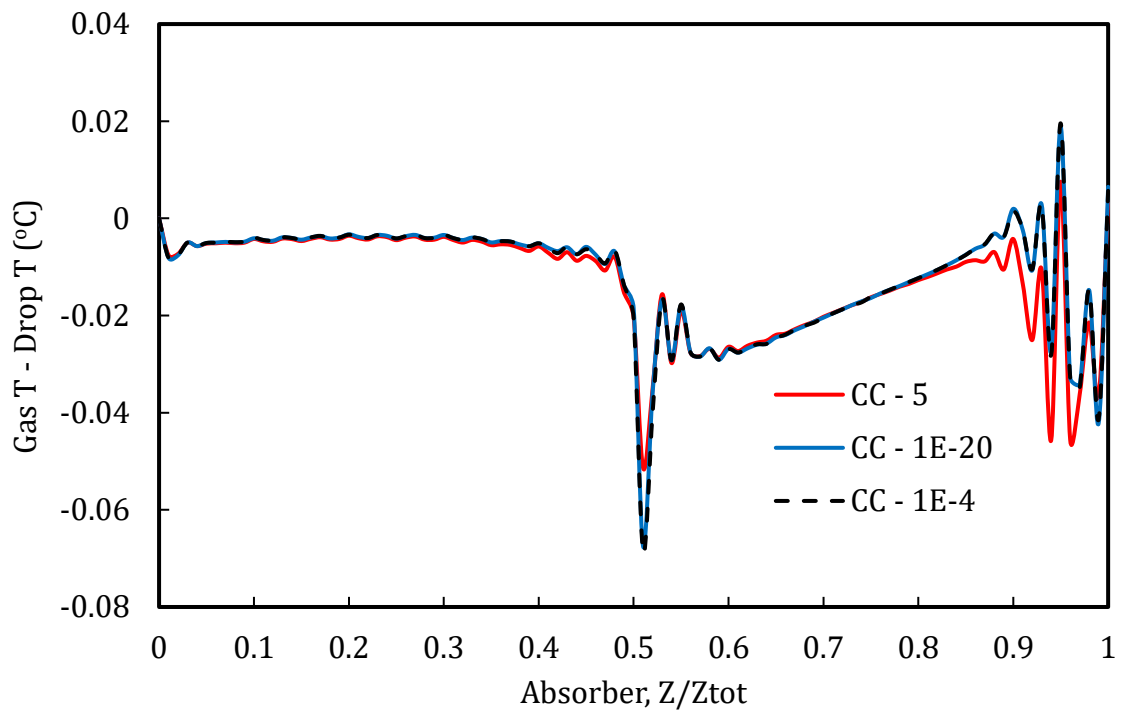


Figure 5.27: Difference between gas and drop temperatures in the absorber for different Chilton-Colburn weighting parameter values

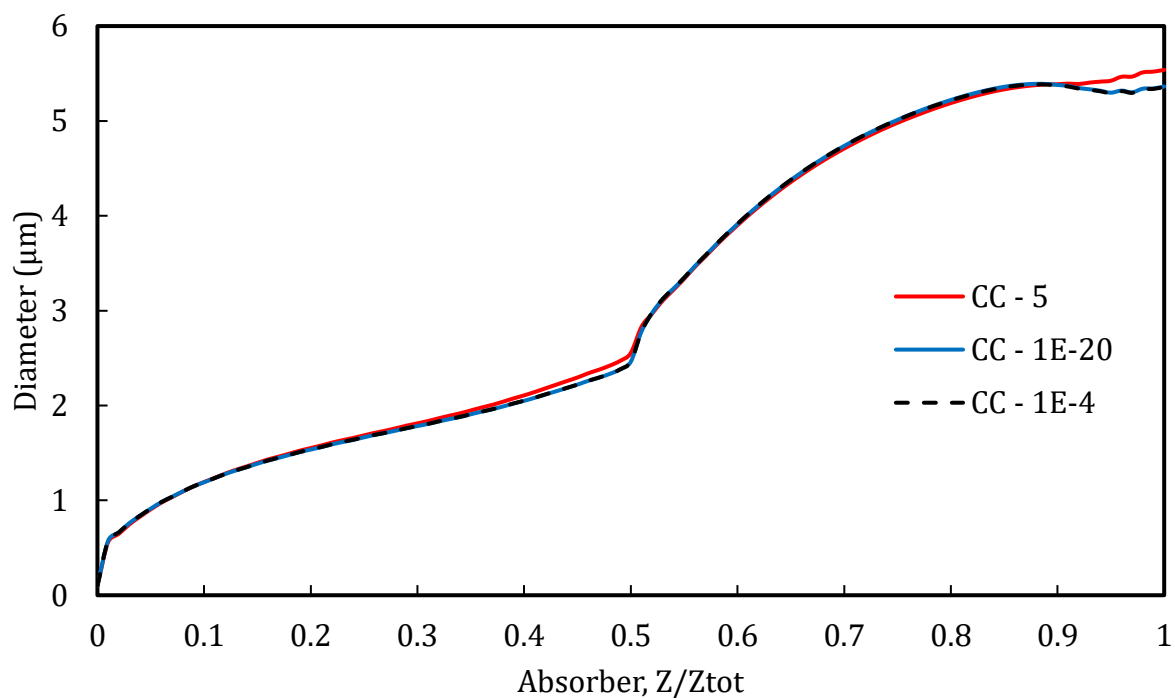


Figure 5.28: Effect of Chilton-Colburn weighting parameter in Aspen Plus[®] on PZ aerosol growth

5.6.4 Physical Property Models

The use of average values from literature or first principle derivations to approximate physical properties is desirable for solvents with limited experimental data. This possibility is evaluated with PZ by comparing temperature, and composition-dependent physical properties from Aspen Plus[®] subroutines and the DIPPR database to constant averaged values (Table 5.12).

Table 5.12: Effect of assuming constant values in physical property models on aerosol calculations. Base case conditions are defined in Table 5.1.

Property	Dependent variables	Range	Assumed Value	Units	Final dp (μm)	%Error
Base Case					6.44	-
Heat Capacity, C_p	T, x_i	79–86	83	J/molK	6.45	0.1%
Heat of absorption ΔH_{abs}	T, α	58–79	69	kJ/mol	6.45	0.1%
Surface tension, σ	T	10.3–11.3	10.8	mN/m	6.45	0.2%
Density, ρ	T, x_i , α	1063–1106	1090	kg/m ³	6.43	0.2%
Mass transfer coefficient, kg^*	T, x_i , α	2E-6–5E-6	3.5E-6	mol/Pa.s.m ²	6.40	0.8%

The error from assuming average values for all the physical properties was less than 1%. Of the properties analyzed, the mass transfer coefficient is the most sensitive. The assumption of a constant value can be used on the physical property data with reasonable accuracy.

5.7 CONCLUSIONS AND RECOMMENDATIONS

From a design standpoint, the following conditions will increase PZ aerosol size and help mitigate emission: (1) higher lean solvent temperature, (2) higher intercooling temperature, (3) lower lean loading, (4) higher PZ molality, (5) greater absorber packing volume, (6) packing with lower hold-up and higher interfacial areas, and (7) higher water wash temperatures.

There is a tradeoff between capital or energy costs and PZ aerosol control. Design conditions that lead to larger drop sizes require more solvent flow to maintain CO₂ removal specifications (higher lean solvent and higher intercooling temperatures), require higher energy cost for solvent regeneration in the stripper (lower lean loading), or require bigger columns to increase residence time for drop growth (greater packing volume).

From an operational standpoint, short-term episodes of PZ aerosol can be controlled by increasing the lean solvent or intercooling temperatures at the cost of lower CO₂ removal. Model results show that PZ aerosol size increased by 6% and reduced CO₂ removal by 4% when the lean solvent temperature was changed from 40 to 60 °C. Similarly, PZ aerosol size increased by 15% and CO₂ removal by 15% with no intercooling. These model results agree with experimental results from the PZ aerosol tests at NCCC.

Changes in the flow models and the Chilton-Colburn averaging factor used in process simulators do not significantly impact drop calculations.

PZ aerosol model with updated VLE resulted in 20% increase in PZ drop diameter compared to previous work with empirical correlations. This improvement is mainly due to differences in CO₂ solubility and PZ volatility predictions from both models. The regressed equations used in this work are more reliable because they better represent the temperature and composition of the PZ drop.

The mass transfer coefficient is the physical property with the most significant effect on aerosol growth. Assumptions of a constant value for all other physical property models are accurate within 1% error.

Chapter 6: Modeling Aerosol Growth for Solvent Blends

This chapter presents a framework for modeling aerosol growth for solvent blends. Two solvents: an aqueous blend (AB) of AM1 and AM2 and a non-aqueous blend (NAB) of Amine A and Organic B, were evaluated in this study. The aerosol growth profile and composition were calculated for both systems at specified absorber and water wash conditions. Part of this work was prepared as a deliverable for Cooperative Agreement DE-FE-0031583, “UK CAER Heat-Integrated Transformative CO₂ Capture Process for Pulverized Coal Power Plants”. The objective of the cooperative agreement was to design a pilot-scale (10MWe) post-combustion carbon capture system at a pulverized coal-fired power plant using the UK CAER technology and a proprietary solvent. This work supports that goal by evaluating amine loss through aerosol for the proprietary solvent at the UK CAER design conditions.

6.1 INTRODUCTION

Several 2nd and 3rd generation CO₂ capture technologies have gained attention in recent years. The UK CAER technology uses a proprietary solvent, which is an aqueous blend of two amines: AM1 and AM2. The proprietary solvent can reduce the cost of CO₂ capture by 50% compared to existing technologies and has been tested at the Technology Centre Mongstad (TCM) pilot plant. In addition, UK CAER has validated their heat-integrated solvent system by operating for more than 4,000 hours using a 0.7 MWe slipstream of flue gas at the E.W. Brown Power Generating Station (Thompson et al., 2017). Combining the proprietary solvent with the heat integrated technology provides the potential for significant energy savings and improved absorber performance.

Management of aerosol requires the modeling of aerosol growth at the absorber and water wash conditions. If the amine aerosol grows well above 3 μm, it is collected through

impaction on the packing and mist eliminator. Although aerosol models for single amine solvents have been developed, none have been reported for blended amine solvents. Previous work on PZ-CO₂ (Fulk, 2016; Kang et al., 2017) and MEA-CO₂ (Kang et al., 2020; Majeed et al., 2017b) do not consider mass and heat transfer for a solvent blend. Also, the models are solvent-specific and cannot model the aerosol dynamics for other commercial solvents. The presence of a second amine in the bulk liquid might affect the current understanding of aerosol growth mechanisms, composition, and size. Finally, without a model for an amine blend, it is challenging to identify operating conditions that can grow the aerosol to larger sizes for mitigation.

This work simulates aerosol growth for an aqueous solvent blend of amines AM1 and AM2, and a non-aqueous solvent blend of Amine A and Organic B. Aerosol Transport Models (ATM) were developed for both solvents with drop profiles simulated at conventional run conditions in the absorber and water wash. The models calculate the size and composition of an aerosol drop with 10⁷ particles/cm³ traveling through the absorber and water wash. In addition, it tracks the water, CO₂, and amines in the bulk gas and aerosol phase, with mass transfer occurring at the bulk gas-drop interface and the bulk gas-solvent interface.

6.2 MODELING APPROACH

The approach to modeling aerosol growth in the absorber and water wash involved two steps: (1) process modeling with ProTreat[®] and Aspen Plus[®] and (2) aerosol transport modeling with gPROMS[®]. The output from the process model was fed into user-defined equations in the aerosol model.

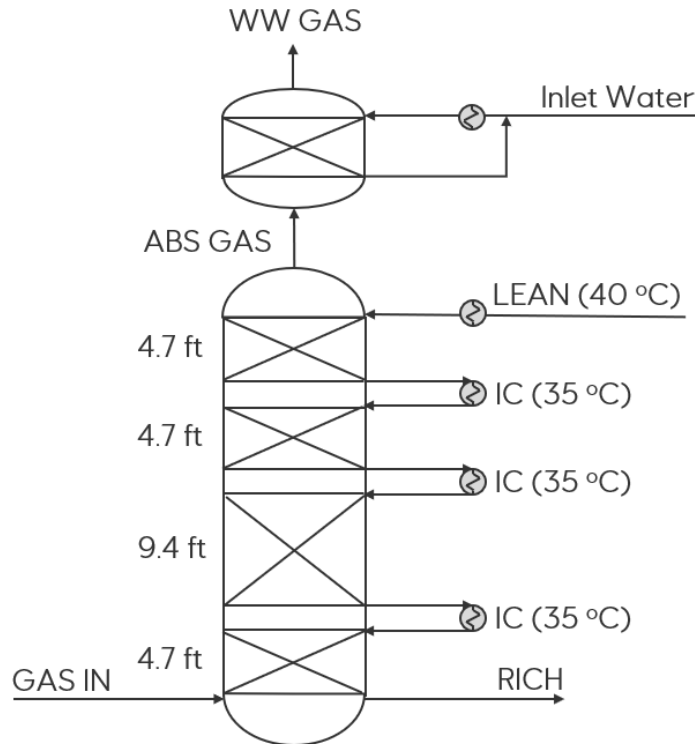


Figure 6.2: Process flow diagram for the non-aqueous blend (NAB)

Table 6.1: Summary of run conditions for the aqueous blend (AB)

	Run 1, lean 40 °C, IC 40 °C				Run 2, Lean 60 °C, IC 30 °C			
	ABS Gas In	ABS Gas Out	Lean	IC	ABS Gas In	ABS Gas Out	Lean	IC
T (°C)	40	46	40	40	40	62	60	30
H ₂ O (mol %)	8	11	84	83	8	23	84	83
CO ₂ (mol %)	16	1.7	4.5	5.8	16	1.5	4.4	5.7
Solvent (mol %)	0	0.02	11.8	11.2	0	0.06	11.8	11.3
Flow (lb/hr)	93000	74000	391000	369000	93000	81000	381000	355000

Table 6.2: Summary of run conditions for the non-aqueous blend (NAB)

	ABS Gas In	ABS Gas Out	Lean
T (°C)	40	40	40

H ₂ O (mol %)	3	3	41
CO ₂ (mol %)	14	2	5
Solvent (mol %)	0	0.3	54
Flow (lb/hr)	36	30	215

6.2.3 Stage-wise Composition and Physical Properties

Gas-phase compositions and physical properties at each computational stage of the absorber and water wash were extracted from the process models and fed into user-defined equations in the aerosol model. The following properties were extracted: vapor temperature, vapor volumetric flow rate, vapor thermal conductivity, partial pressures of water, CO₂, and amine in the vapor, diffusion coefficients of water and amine in the vapor, mass transfer coefficients of amine, interfacial area, liquid temperature, liquid hold-up, and liquid mole fraction of water, CO₂, and amine.

6.3 DEVELOPMENT OF AEROSOL TRANSPORT MODEL (ATM) FOR SOLVENT BLENDS

An Aerosol Transport Model (ATM) was developed for both solvent blend systems using gPROMS ProcessBuilder. The model calculates the size and composition of an aerosol with 10^7 particles/cm³ traveling through the absorber and water wash. It tracks the water, CO₂, and organics in the bulk gas and aerosol phases, with mass transfer occurring at the bulk gas-drop interfaces and the bulk gas-solvent interfaces. Aerosol mass transfer fluxes for the individual amines were calculated separately. The assumptions made to simplify the calculation of aerosol bulk properties were tested in Section 5.6.4 and have a negligible impact on the aerosol profiles.

6.3.1 gPROMS ProcessBuilder

The gPROMS ProcessBuilder was found to be a suitable process modeling environment for this work. Compared to traditional flow sheeting packages, it offers the

ability to create custom models of processes published in libraries for deployment to multiple users (PSE, n.d.). In addition, it uses an equation-oriented (EO) modeling approach instead of sequential modeling. With the EO approach, the process flowsheet is treated as equations to be solved simultaneously, not sequentially. This provides faster solutions and a more powerful optimization and custom modeling capability without programming the mathematical solution. Although the numerical solvers may fail to find an initial solution if wrong guesses are provided, its inherent directionality of computation means that it can be solved with any valid degree-of-freedom specification, making it very robust and efficient.

A total of 69 unknown variables were solved with the model. Sixty-two algebraic and seven differential equations were defined within the model to solve the variables. Seven initial conditions were specified for the differential equations. The simulation took 5 minutes on average for each case to converge.

6.3.2 Model Equations

The model equations developed for solvent blends are presented in this section using the aqueous blend (AB) as a reference. Analogous equations were developed for the non-aqueous blend (NAB). The ATM tracks water, CO₂, AM1, and AM2 in the bulk gas and aerosol phases, with mass transfer occurring at the bulk gas-drop interface and the bulk gas-solvent interface. Aerosol mass transfer fluxes are calculated using Equations 6.1 to 6.4, and heat transfer flux using Equations 6.19 and 6.20.

The mass transfer coefficients for water, AM1, and AM2 are calculated as a function of the Sherwood number, diffusivity, and drop diameter (Equation 6.5). The coefficient of CO₂ is calculated as a function of the free amine, diffusivity, rate constant, and Henry constant (Equation 6.6). For simplicity, a constant value was assumed for the

kg' in this work. The fluxes are corrected using the Fuchs-Sutugin correlation, a function of the Knudsen number and mean free path of the drop. The partial pressures of CO₂ and water are obtained from the absorber stage-wise profiles in ProTreat[®]. The partial pressures for AM1 and AM2 are initialized at the absorber bottom and re-calculated along the absorber height to account for their gas-phase partial pressures. The individual gas-phase partial pressures for AM1 and AM2 are re-calculated by individual amine mass transfer fluxes between the gas-drop interface and the gas-solvent interface, shown in Equations 6.7–6.10. The equilibrium partial pressure for each component over the aerosol is calculated using surrogate models (Equations 6.11–6.14). The models are corrected for the Kelvin effect due to the assumption of a spherical drop (Equations 6.15–6.18).

The heat transfer from gas to aerosol is calculated as a function of the fluxes of each component, gas and drop temperatures, heat transfer coefficient, and heat of absorption/vaporization (Equation 6.19). The heat transfer coefficient for each component is calculated as a function of the Nusselt number, the thermal conductivity of the gas, and drop diameter (Equation 6.20).

$$N_{gd,H_2O} = k_{g,H_2O} \frac{(P_{g,H_2O} - P_{d,H_2O}^*)}{RT_g} \varphi(Kn) \quad (6.1)$$

$$N_{gd,AM1} = k_{g,AM1} \frac{(P_{g,AM1} - P_{d,AM1}^*)}{RT_g} \varphi(Kn) \quad (6.2)$$

$$N_{gd,AM2} = k_{g,AM2} \frac{(P_{g,AM2} - P_{d,AM2}^*)}{RT_g} \varphi(Kn) \quad (6.3)$$

$$N_{gd,CO_2} = k'_g (P_{g,CO_2} - P_{d,CO_2}^*) \quad (6.4)$$

$$k_{g,i} = \frac{Sh_i D_{g,i}}{d_{drop}} \quad (6.5)$$

$$k'_g = \frac{\sqrt{k_2 [AM1 + AM2]^{free} D_{CO_2, mx}}}{H_{CO_2}} \quad (6.6)$$

$$\frac{v_{drop}}{H_{col}} \frac{dP_{AM1}}{d\tau_D} = -(N_{gl,AM1}a_{gl} + N_{gd,AM1}A_dN_p)RT_g \quad (6.7)$$

$$\frac{v_{drop}}{H_{col}} \frac{dP_{AM2}}{d\tau_D} = -(N_{gl,AM2}a_{gl} + N_{gd,AM2}A_dN_p)RT_g \quad (6.8)$$

$$N_{gl,AM1} = k_{g,AM1} \frac{(P_{g,AM1} - P_{l,AM1}^*)}{RT_g} \quad (6.9)$$

$$N_{gl,AM2} = k_{g,AM2} \frac{(P_{g,AM2} - P_{l,AM2}^*)}{RT_g} \quad (6.10)$$

$$\ln P_{AM1,liq}^* = 24 - \frac{7146}{T_{liq}} - 2389 \frac{\alpha^2}{T_{liq}} + 53X_{AMINE} - 230X_{AMINE}^2 - 3.1 \frac{X_{AM2}}{X_{AMINE}} \quad (6.11)$$

$$\ln P_{AM2,liq}^* = 18 - \frac{8226}{T_{liq}} - 6202 \frac{\alpha^2}{T_{liq}} + 22X_{AMINE} - 94X_{AMINE}^2 + 14 \frac{X_{AM2}}{X_{AMINE}} - 15 \left(\frac{X_{AM2}}{X_{AMINE}} \right)^2 \quad (6.12)$$

$$\ln P_{CO2,liq}^* = 31 - \frac{10445}{T_{liq}} + 9225 \frac{\alpha}{T_{liq}} - 6848 \frac{\alpha^2}{T_{liq}} + 31X_{AMINE} - 146X_{AMINE}^2 + 1.3 \frac{X_{AM2}}{X_{AMINE}} \quad (6.13)$$

$$\ln P_{H2O,liq}^* = 25 - \frac{5186}{T_{liq}} + 0.9X_{H2O} \quad (6.14)$$

$$P_{AM1,drop}^* = P_{AM1,liq}^* \times e^{\left(\frac{4 \times \sum (x_i \times \sigma) \times \text{Molar Volume}_{AM1}}{kB \times T_{drop} \times d_{drop}} \right)} \quad (6.15)$$

$$P_{AM2,drop}^* = P_{AM2,liq}^* \times e^{\left(\frac{4 \times \sum (x_i \times \sigma) \times \text{Molar Volume}_{AM2}}{kB \times T_{drop} \times d_{drop}} \right)} \quad (6.16)$$

$$P_{CO2,drop}^* = P_{CO2,liq}^* \times e^{\left(\frac{4 \times \sum (x_i \times \sigma) \times \text{Molar Volume}_{CO2}}{kB \times T_{drop} \times d_{drop}} \right)} \quad (6.17)$$

$$P_{H2O,drop}^* = P_{H2O,liq}^* \times e^{\left(\frac{4 \times \sum (x_i \times \sigma) \times \text{Molar Volume}_{H2O}}{kB \times T_{drop} \times d_{drop}} \right)} \quad (6.18)$$

$$Q_d = N_{gd,H2O} \Delta H_{H2O} - N_{gd,AM1} \Delta H_{AM1} - N_{gd,AM2} \Delta H_{AM2} + N_{gd,CO2} \Delta H_{CO2} + h_g (T_g - T_d) \quad (6.19)$$

$$h_g = \frac{Nu \times K}{d_{drop}} \quad (6.20)$$

6.3.3 Model Assumptions

1. The aerosol drop was assumed to be a well-mixed spherical drop with an initial concentration similar to that of the rich bulk liquid, an initial diameter of 0.1 μm , and 10^7 particles/ cm^3 .
2. There is no convective flux in the aerosol, so molar density at each layer is assumed to be the same.
3. The drop velocity is assumed to equal to gas velocity because the drop is small.
4. Sherwood and Nusselt numbers are both assumed to be equal to 2.
5. The CO_2 mass transfer coefficient from gas to drop is assumed to be constant throughout the absorber.
6. The density, heat capacity, heat of absorption of CO_2 , and heat of vaporization of the amines in the drop were all assumed constant.

6.3.4 Surrogate Equilibrium Model

The flux for water, CO_2 , and amines from gas to aerosol depends on the difference between the gas and aerosol partial pressures. Due to the unavailability of experimentally determined vapor-liquid equilibrium (VLE) for the CO_2 -loaded amine, surrogate models were developed by regressing equilibrium data from process models. ProTreat[®] was used for the aqueous blend (AB), while Aspen Plus[®] was used for the non-aqueous blend (NAB). While the gas-phase partial pressures at each computational stage are extracted from the process model for each run, the equilibrium pressures must be represented by a semi-empirical model in gPROMS[®]. The semi-empirical models predict the equilibrium partial

pressures of CO₂, water, and the solvent at bulk liquid and aerosol conditions in the absorber.

6.3.4.1 Surrogate Equilibrium Model Development for Aqueous Blend (AB)

The aqueous blend (AB) models were developed using equilibrium data generated from ProTreat[®] and are shown in Equation 6.21 and Table 6.3. The equations were regressed at a loading range of 0.2–0.4 mol CO₂/mol alkalinity, temperature of 30–70 °C, concentration of 0.6–7.6, X_{ALKALINITY} of 0.01–0.2, and X_{AM2}/X_{ALKALINITY} of 0.05–0.23. The resulting models predict the volatilities over operationally significant conditions in the absorber and water wash with R² ranging from 0.95 to 0.99. In the absorber, the bulk liquid has average alkalinity of 0.2 and X_{AM2}/X_{ALKALINITY} of 0.23. However, these values will be much lower in the aerosol and water wash due to the low volatility of AM2 and higher activity of water, respectively.

$$P_{i, drop}^* = x_{i, drop}^{app} \exp \left(A + \frac{B}{T_{drop}} + CT^2 + D \frac{\alpha}{T_{drop}} + E \frac{\alpha^2}{T_{drop}} + FX_{Alkalinity} + G \frac{X_{AM2}}{X_{Alkalinity}} \right) \quad (6.21)$$

Table 6.3: Regressed equilibrium partial pressures for the aqueous blend (AB) over bulk liquid and aerosol conditions

	P _{AM1} [*]	P _{AM2} [*]	P _{CO2} [*]	P _{H2O} [*]
A	28.79	26.20	31.66	27.75
B	-7145.61	-7694.32	-9874.78	-5673.24
C	0	0	0	-7.26E-6
D	0	-3771.54	5116.08	0
E	-2388.98	0	0	0
F	1.35	-13.35	13.57	0
G	-1.76	0.72	1.26	0

R ²	0.98	0.95	0.96	0.99
----------------	------	------	------	------

where:

$P_{CO_2}^*, P_{AM1}^*, P_{AM2}^*, P_{H_2O}^*$ = Equilibrium partial pressures of CO₂, AM1, AM2, and H₂O (Pa)

T = Temperature (K)

$X_{Alkalinity} = X_{AM1} + 3X_{AM2}$

α = CO₂ loading (mol CO₂/mol alkalinity)

$x_{H_2O}^{app}$ = apparent H₂O mole fraction

X_{AM1}^{app} = apparent AM1 mole fraction

X_{AM2}^{app} = apparent AM2 mole fraction

6.3.4.2 Surrogate Equilibrium Model Development for Non-Aqueous Blend (NAB)

The surrogate equilibrium model for the non-aqueous blend (NAB) are shown in Equation 6.22 and Table 6.4. The equilibrium models were regressed using thermodynamic data in the proprietary Aspen Plus[®] process model. Only the binary (amine-water) VLE was regressed to represent the absence of the non-volatile Organic B in the aerosol. Figure 6.4 compares the volatilities of both aqueous and non-aqueous blends to PZ and MEA at bulk liquid conditions.

$$P_{i, drop}^* = x_{i, drop}^{app} \exp\left(A + \frac{B}{T_{drop}} + C\alpha^2 + D\frac{\alpha}{T_{drop}} + E\frac{\alpha^2}{T_{drop}}\right) \quad (6.22)$$

Table 6.4: Regressed equilibrium partial pressures for the non-aqueous blend (NAB) over aerosol conditions

	P* _{Amine A}	P* _{CO2}	P* _{H2O}
A	21.89	29.20	26.65
B	-4748.97	-7091.07	-5195.14

C	0	-20.41	0
D	470.41	-5017.9	0
E	-2542.26	14623.9	0
R ²	0.99	0.99	0.85

where:

$P_{CO_2}^*$, $P_{Amine A}^*$, and $P_{H_2O}^*$ = Equilibrium partial pressures of CO₂, Amine A, and H₂O (Pa)

T = Temperature (K)

α = CO₂ loading (mol CO₂/mol alkalinity)

$x_{H_2O}^{app}$ = apparent H₂O mole fraction

$X_{Amine A}^{app}$ = apparent Amine A mole fraction

Figure 6.3 compares the solvent volatility obtained from this work (Equations 6.21 and 6.22) to PZ and MEA at bulk liquid conditions of each solvent system. AM1 in the aqueous blend is one order of magnitude more volatile than PZ, while AM2 is less volatile by 2–3 orders of magnitude. For the non-aqueous blend, Amine A is 2–3 orders of magnitude more volatile than PZ, while Organic B is non-volatile.

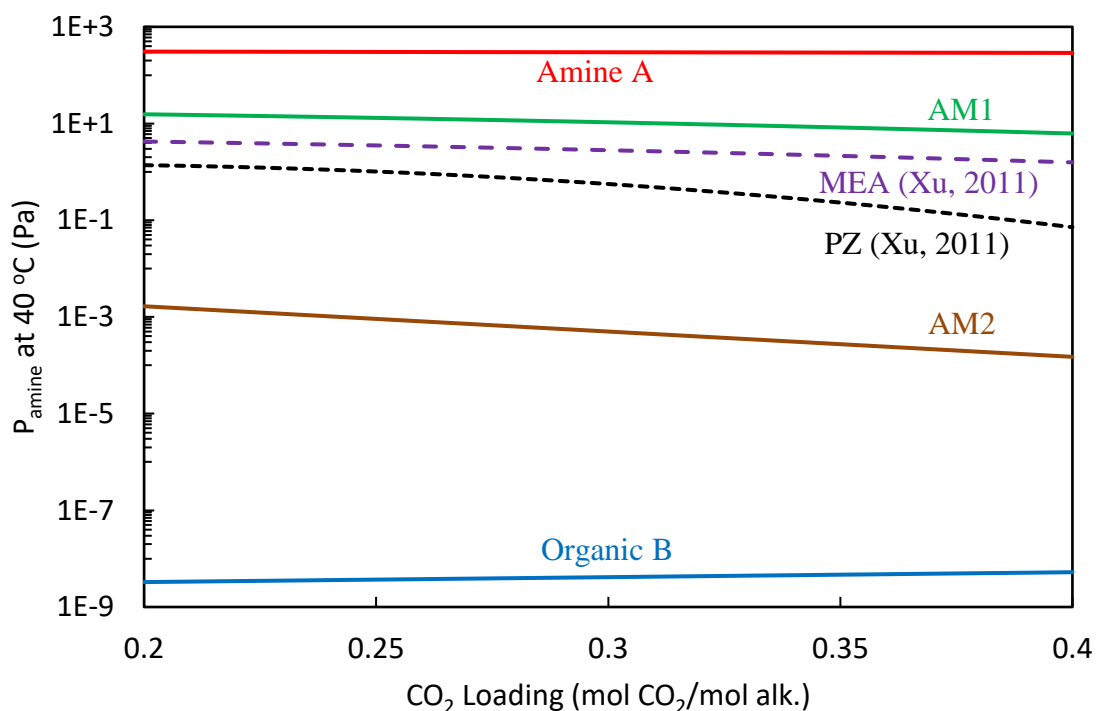


Figure 6.3: Solvent volatility regressed in this work compared to PZ (Xu, 2011) and MEA (Xu, 2011) at bulk liquid conditions. Aqueous blend (AM1 and AM2). Non-aqueous blend (Amine A and Organic B).

6.4 RESULTS AND DISCUSSION

The growth of aerosol of aqueous and non-aqueous solvent blends with 10^7 particles/cm³ traveling through the absorber and water wash is presented in this section. The non-aqueous blend (NAB) was simulated using the run defined in Table 6.2, while the aqueous blend (AB) was simulated at the two runs defined in Table 6.1. For the AB, Run 1 was modeled with lean solvent and intercooling at 40 °C, while Run 2 was modeled with a lean solvent at 60 °C and intercooling at 30 °C. The water wash was modeled for water balance by adjusting the circulation water flow rate to produce equal amounts of water in the gas streams exiting the water wash and entering the absorber. Finally, a sensitivity analysis was done on the water temperature and water wash packed height.

6.4.1 Amine Aerosol Growth Profile

Figure 6.4 compares aerosol growth at 10^7 particles/cm³ for the aqueous and non-aqueous blends to PZ. The AB and NAB drops grow to 15 and 20 μm respectively, about 3–4 times PZ and well above the 3 μm threshold for collection by packing or mist eliminators. Figures 6.5 and 6.6 show the composition of the aqueous and non-aqueous blend drops, respectively. For AB, the drop grows in the absorber by picking up large amounts of water, AM1, and CO₂. Due to its much lower volatility, the AM2 picked up is 4–6 orders less than the other components. The AB drop grows in the water wash by picking up only water. This composition profile in absorber and water wash is quite similar to PZ (Zhang, 2018), with water being the dominant fraction in the drop. The drop grows in the absorber for the NAB by picking up only Amine A, CO₂, and water. The Organic B has very low volatility and remains at the initial concentration of the inlet drop. The composition profile for the NAB differs from AB and PZ in that Amine A and not water is the dominant fraction in the drop. Also, a much larger fraction of CO₂ is picked up by the NAB drop compared to AB and PZ.

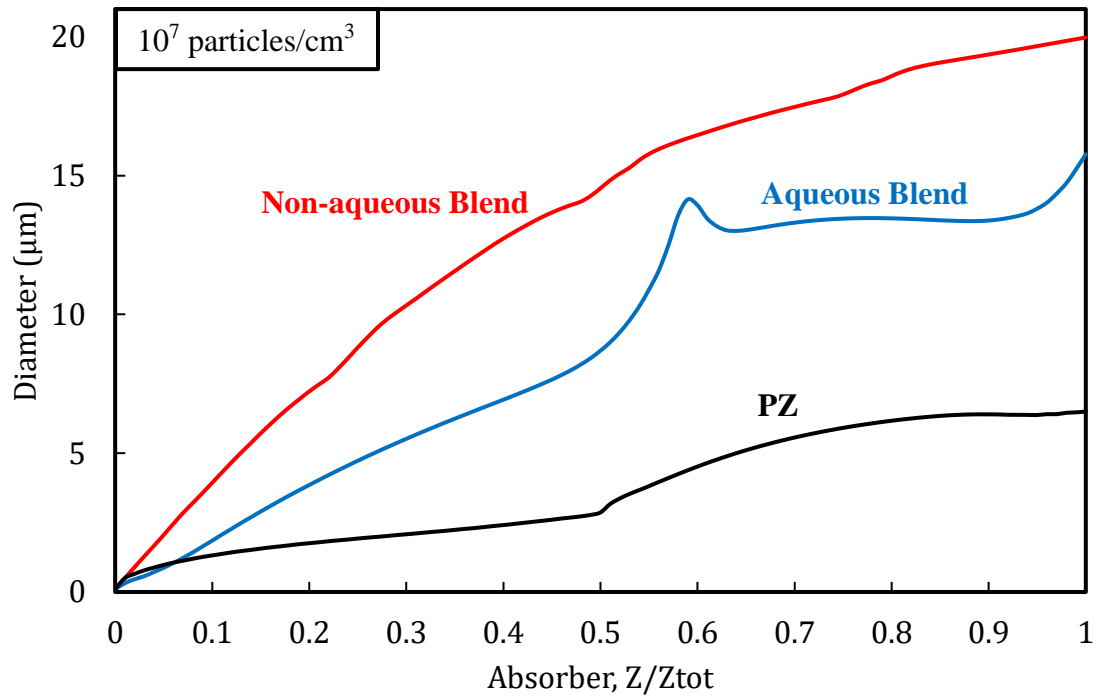


Figure 6.4: Aerosol growth in absorber for Aqueous Blend (AB), Non-aqueous blend (NAB), and PZ at base conditions and 10^7 particles/ cm^3 . AB and NAB grow to 15 and 20 μm in the absorber, respectively.

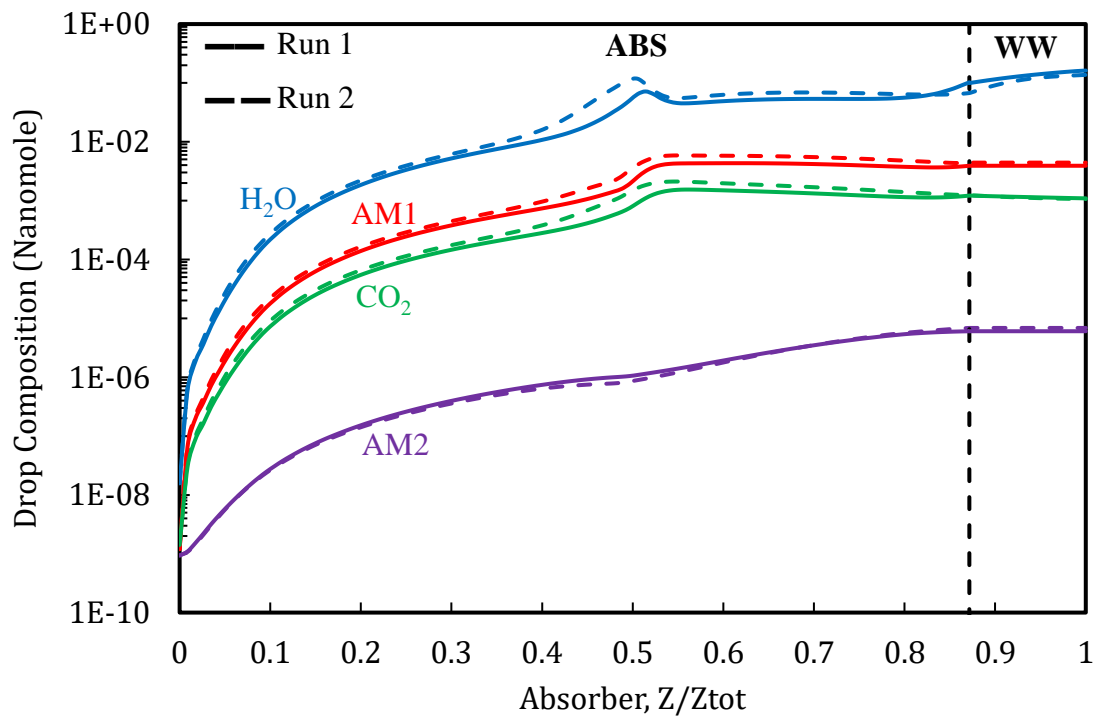


Figure 6.5: AB Drop composition in the absorber and water wash for Run 1 (solid lines) and Run 2 (dashed lines). AB Drop grows by picking large amounts of water, AM1, and CO₂ in the absorber; only water in the water wash.

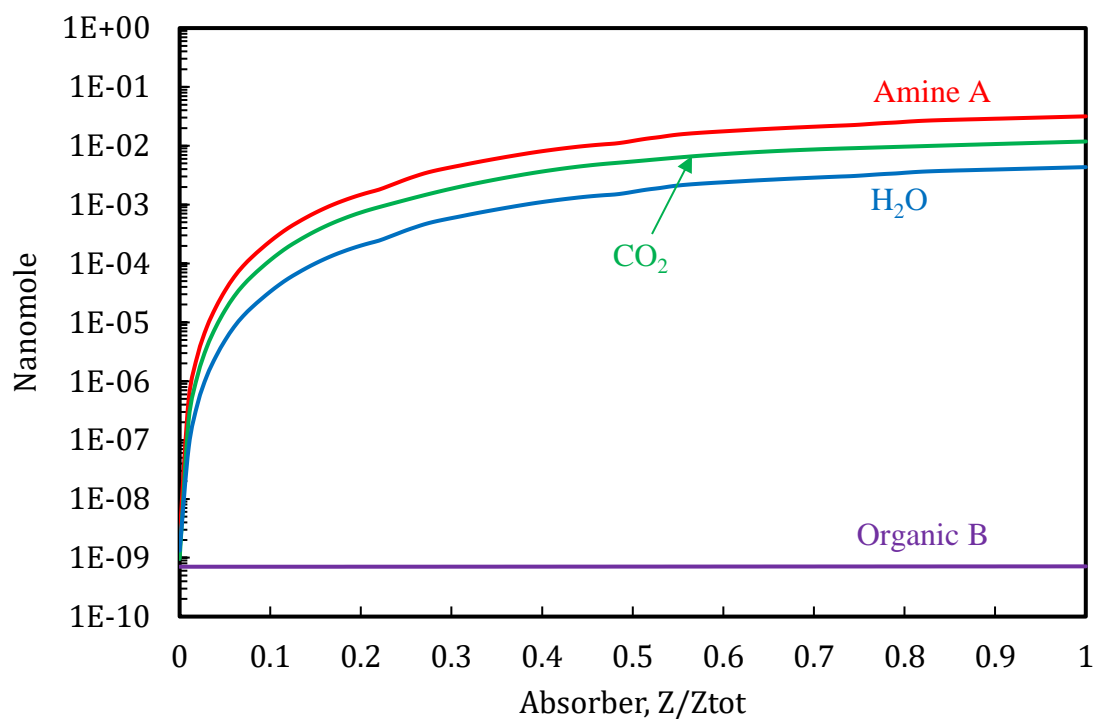


Figure 6.6: NAB Drop composition in the absorber. Drop grows by picking up only Amine A, CO₂, and water.

6.4.2 Limiting Mechanisms for Aerosol Growth

Figure 6.7 shows that the aerosol growth for all three solvents decreases at higher aerosol concentrations and that the NAB aerosol is least sensitive to changes in aerosol concentration. This effect can be explained by identifying the limiting mechanism for aerosol growth for each solvent. A similar analysis to previous work by Zhang (2018) is extended here for PZ, AB, and NAB solvents using Equation 6.23.

$$\emptyset_i = \frac{P_{gas,i} - P_{drop,i}^*}{P_{liq,i} - P_{drop,i}^*} \quad (6.23)$$

where:

\emptyset_i = Relative driving force of component i

$i = \text{PZ, AM1 (AB), Amine A (NAB), and water}$

$P_{gas,i}$ = Partial pressure of component i

$P_{drop,i}^*$ = Equilibrium partial pressure of component i over the aerosol (Pa)

$P_{liq,i}^*$ = Equilibrium partial pressure of component i over the bulk liquid (Pa)

A 0% value for the relative driving force of a component indicates equilibrium between the aerosol and bulk gas phases of that component. Similarly, a 100% value indicates equilibrium between its bulk gas and bulk liquid phases. Table 6.5 shows the average \emptyset_{amine} and \emptyset_{H2O} for PZ, AB, and NAB. The values were obtained at the base run conditions for PZ presented in Table 5.1, Run 1 for the AB solvent (Table 6.1), and the base conditions for the NAB solvent (Table 6.2). The results show that aerosol growth for all three solvents is driven by amine-limited diffusion since the \emptyset_{amine} is always greater than \emptyset_{H2O} (Table 6.5). The average \emptyset_{H2O} is 0% at all aerosol concentrations, indicating that the aerosol is in equilibrium with water in the bulk gas phase. The amine relative driving force (\emptyset_{amine}) for each solvent system is shown in Figures 6.8–6.10. The \emptyset_{amine} is 100% at 1 particle/cm³ and diminishes with aerosol concentration, indicating that the bulk gas is initially at equilibrium with the amine in the bulk liquid but depletes with increased aerosol concentration. Figure 6.11 shows that the amine driving force between gas and aerosol for AB and NAB is several orders of magnitude greater than PZ. This is due to the significantly higher volatility of AB and NAB over PZ and explains the diminished effect of higher aerosol concentration on AB and NAB aerosol size. Therefore, the effect of aerosol concentration on aerosol growth is more pronounced in less volatile solvents.

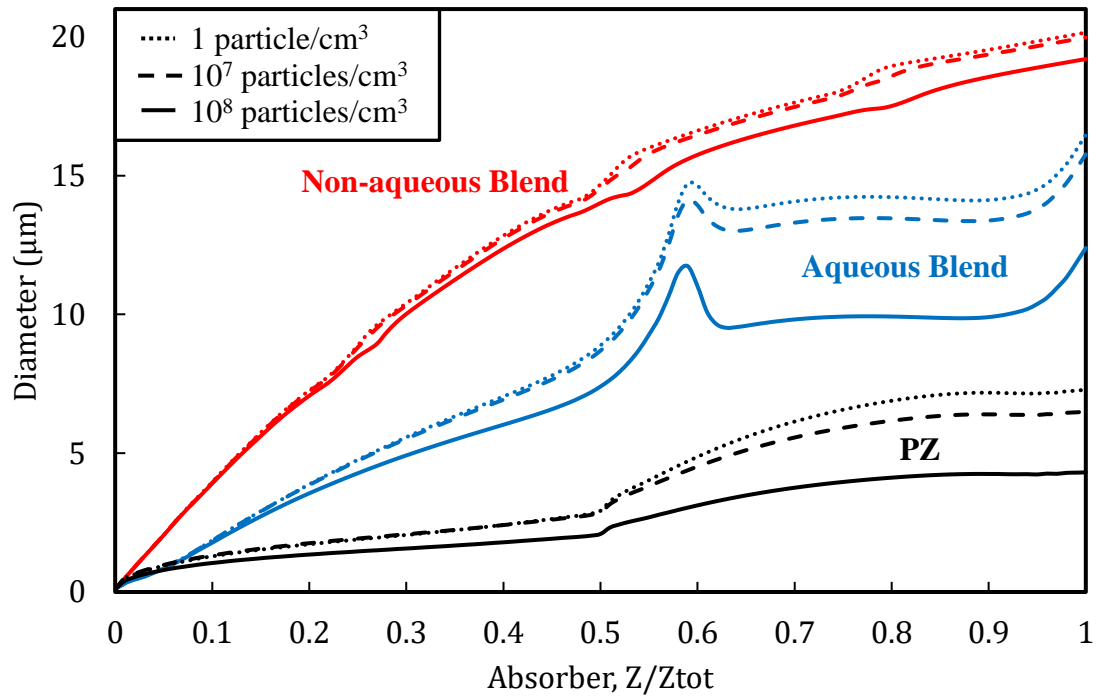


Figure 6.7: Higher aerosol concentration (1–10⁸ particles/cm³) reduces the growth of the non-aqueous blend, aqueous blend, and PZ in the absorber by 5, 25, and 41%, respectively.

Table 6.5: Average amine and H₂O relative driving force for PZ, aqueous blend (AB), and non-aqueous blend (NAB) solvents in the absorber at 1–10⁸ particles/cm³

Solvent	Relative Driving Force (\emptyset_i)	Aerosol Concentration		
		1 particle/cm ³	10 ⁷ particles/cm ³	10 ⁸ particles/cm ³
PZ	\emptyset_{PZ}	100%	81%	41%
	\emptyset_{H_2O}	0%	0%	0%
Aqueous Blend (AB)	\emptyset_{AM1}	100%	72%	31%
	\emptyset_{AM2}	100%	73%	32%
	\emptyset_{H_2O}	0%	0%	0%
Non-aqueous Blend (NAB)	$\emptyset_{Amine A}$	100%	78%	34%
	\emptyset_{H_2O}	0%	0%	0%

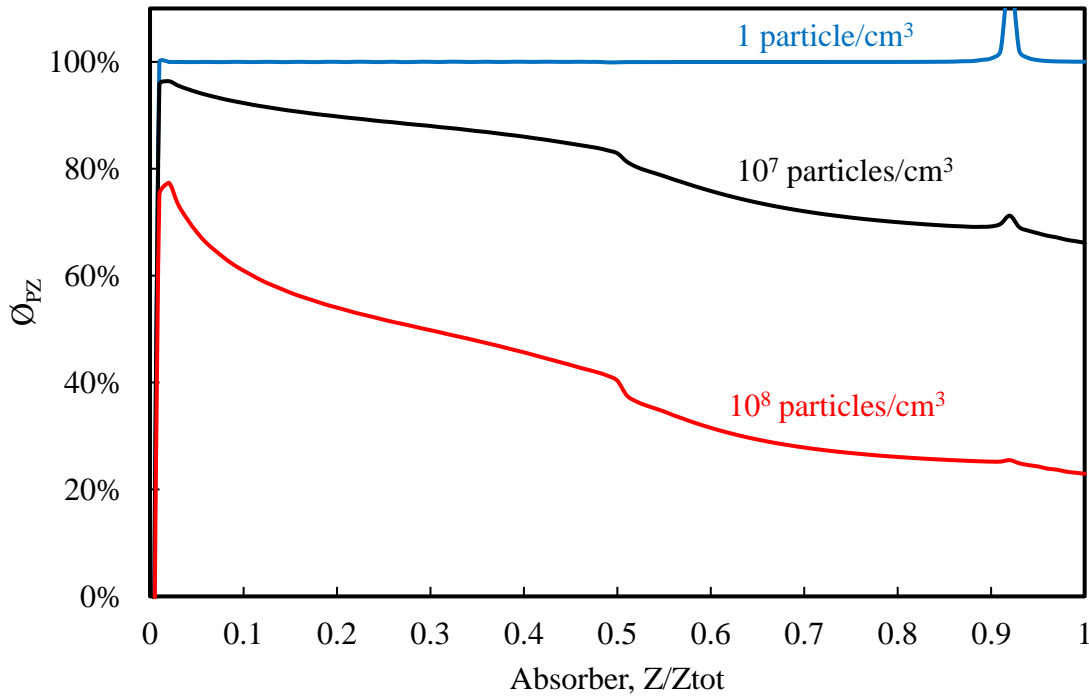


Figure 6.8: PZ relative driving force (\emptyset_{PZ}) in the absorber at 1–10⁸ particles/cm³. Higher aerosol concentration decreases gas-phase amine driving force.

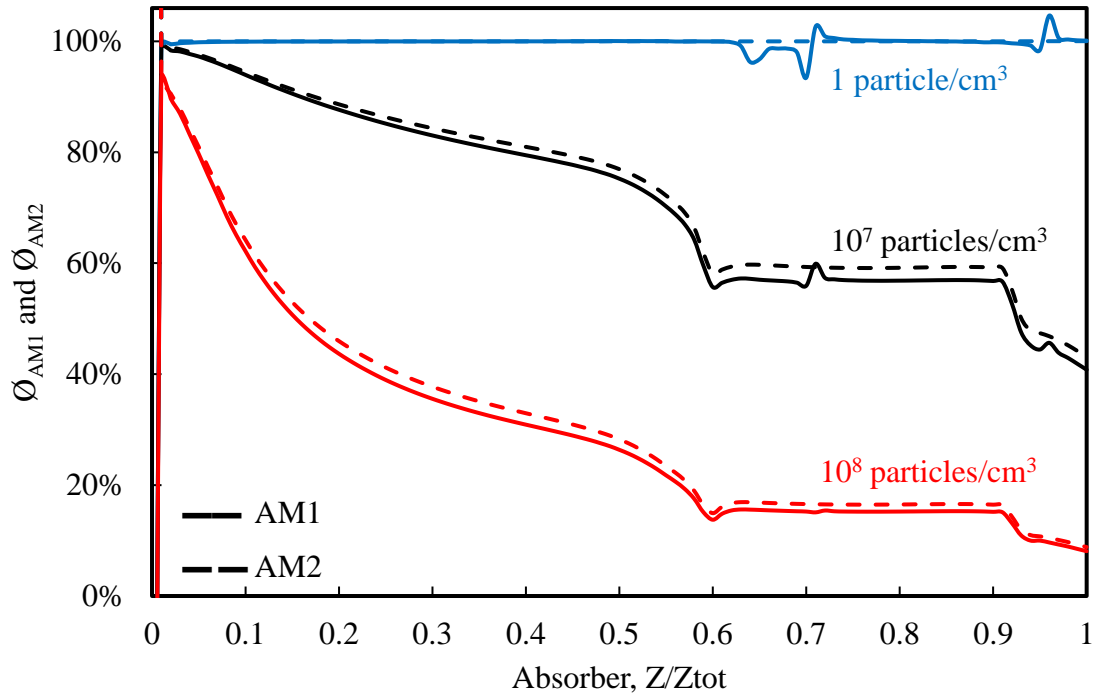


Figure 6.9: Amine relative driving force (\varnothing_{AM1} and \varnothing_{AM2}) for the aqueous blend (AB) in the absorber at $1-10^8$ particles/cm³. Higher aerosol concentration decreases gas-phase amine driving force.

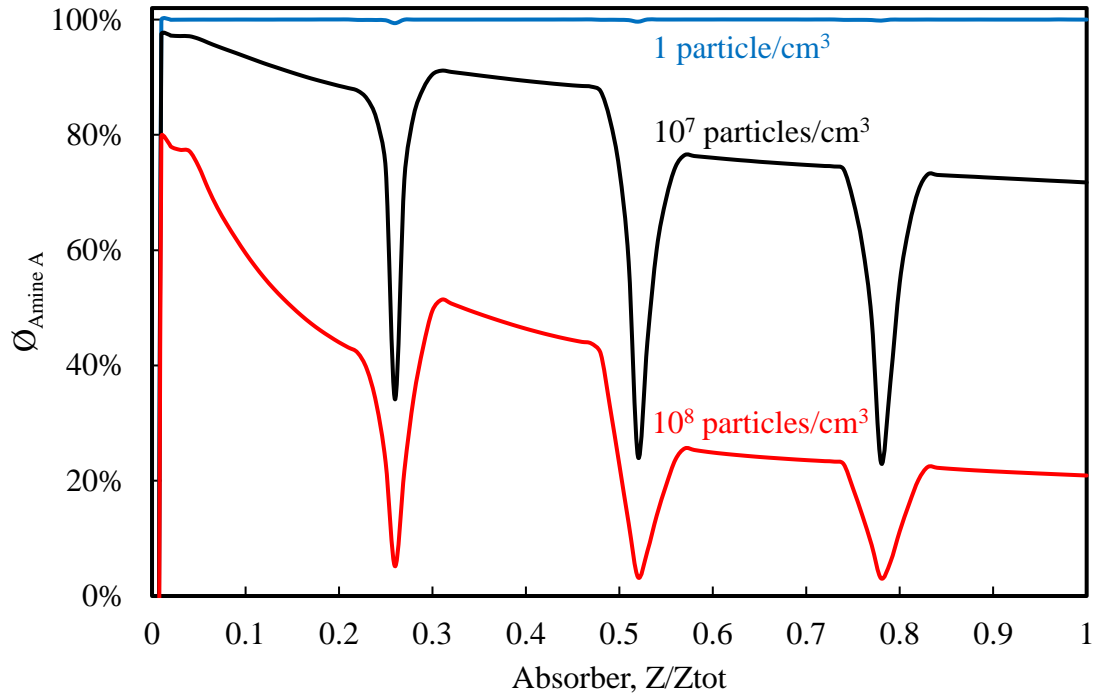


Figure 6.10: Amine relative driving force ($\varnothing_{\text{Amine A}}$) for the non-aqueous blend (NAB) in the absorber at $1-10^8$ particles/cm³. Higher aerosol concentration decreases gas-phase amine driving force.

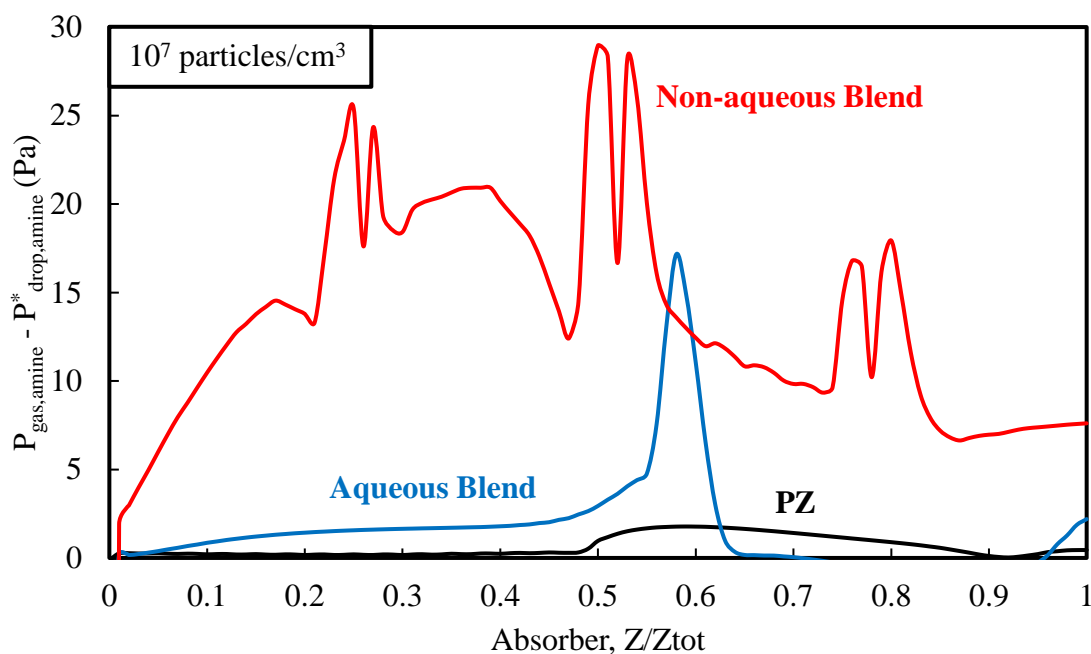


Figure 6.11: Gas-phase amine driving force for Aqueous Blend (AB), Non-aqueous blend (NAB), and PZ at base conditions and 10^7 particles/cm³. The driving force is greatest for NAB.

Figure 6.12 evaluates the effect of changes in absorber operating conditions on AB aerosol growth. Two run conditions in the absorber at differing lean temperatures presented in Table 6.2 were assessed. The results show that changes in the run conditions do not significantly affect the AB drop size, contrasting with previous observations for PZ presented in Chapter 5 of this dissertation (Figures 5.2 and 5.10). Since both AB and NAB aerosol grow well beyond the 3 μm threshold for collection, emission control with mist eliminators and no changes to operating conditions should be feasible. The water wash operation will be critical as vapor emissions will likely form a greater fraction of the overall emissions due to the high volatilities. In fact, as the volatility of the amine in a solvent system increases, the controlling phase for emission will shift from aerosol to vapor.

The effect of kg' on aerosol growth was more pronounced on NAB than AB and PZ (Figure 6.13). Increasing the kg' by a factor of two increased the NAB drop by 85% compared to 10 and 16% for AB and PZ, respectively. This observation indicates that the value of the kg' used in NAB aerosol growth calculations is critical for accurate modeling. An experimentally determined kg' at relevant aerosol conditions is recommended to improve the accuracy of the model results.

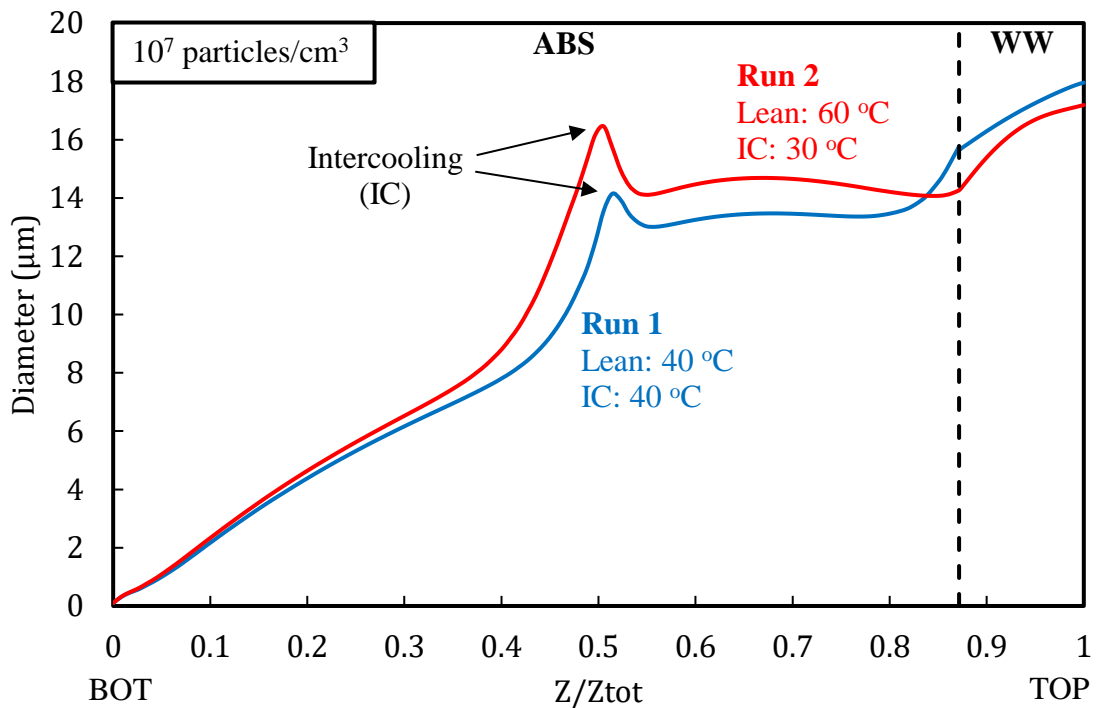


Figure 6.12: Aerosol growth in the absorber and water wash for the Aqueous Blend (AB) at Run 1 (lean solvent, intercooler, and water wash at 40 °C) and Run 2 (lean solvent at 60 °C, intercooler at 30 °C, and water wash at 40 °C). Drop grows to 18 μm in Run 1 and 17 μm in Run 2.

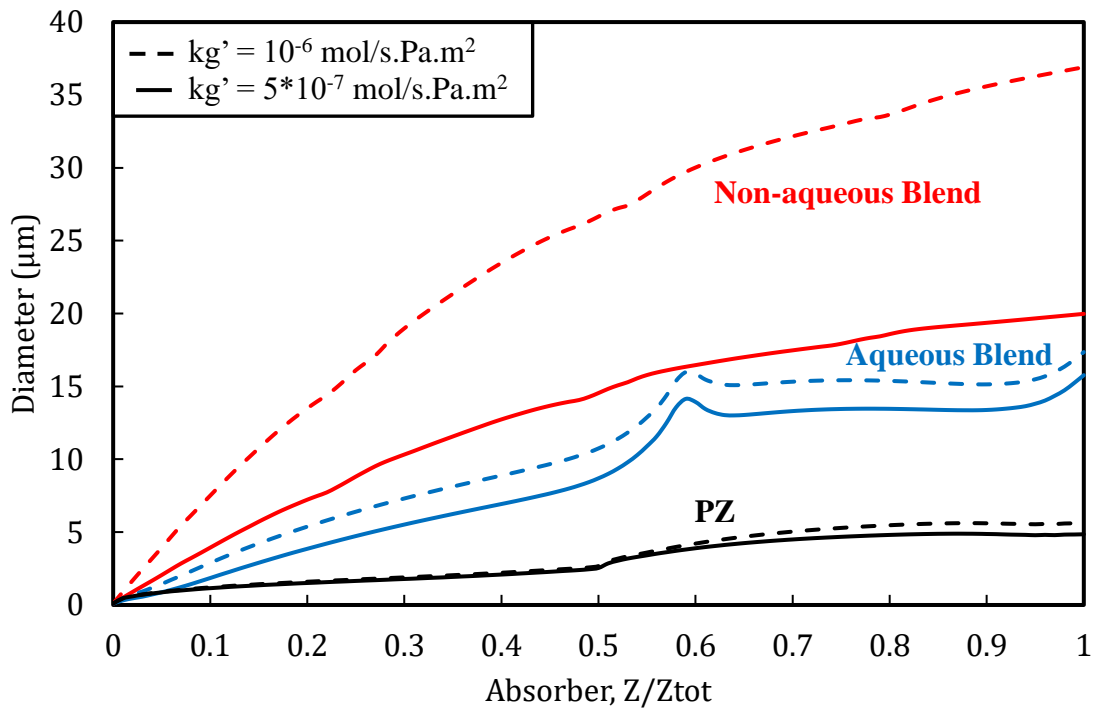


Figure 6.13: Higher kg' (2x) increases the growth of the non-aqueous blend (NAB), Aqueous Blend (AB), and PZ in the absorber by 85, 10, and 16%, respectively.

6.4.3 Effect of Water Wash Temperature and Packed Height on Aerosol Growth for the Aqueous Blend (AB)

The temperature of the circulation water in the water wash was modeled at 30 °C, 35 °C, and 40 °C to model its effect on aerosol growth in the water wash. The water balance was maintained by adjusting the circulation flow rate to produce equal amounts of water in the gas streams exiting the water wash and entering the absorber. Figure 6.14 shows that more circulation water was required as the water wash temperature was increased. This water requirement is larger for Run 2 because the gas entering the water wash is warmer. Colder water wash temperatures produced slightly larger drops exiting the water wash (Figure 6.15). The magnitude of increase in drop size was more pronounced for

Run 2. Reducing the water temperature by 10 °C only increased the drop size in Run 1 by 0.1%, while Run 2 increased by 1%. Figure 6.16 shows the effect of additional water wash packing on aerosol growth. More packing increases the residence time for growth and produces bigger aerosol—the drop size increases by 4% and 5% for Runs 1 and 2, respectively.

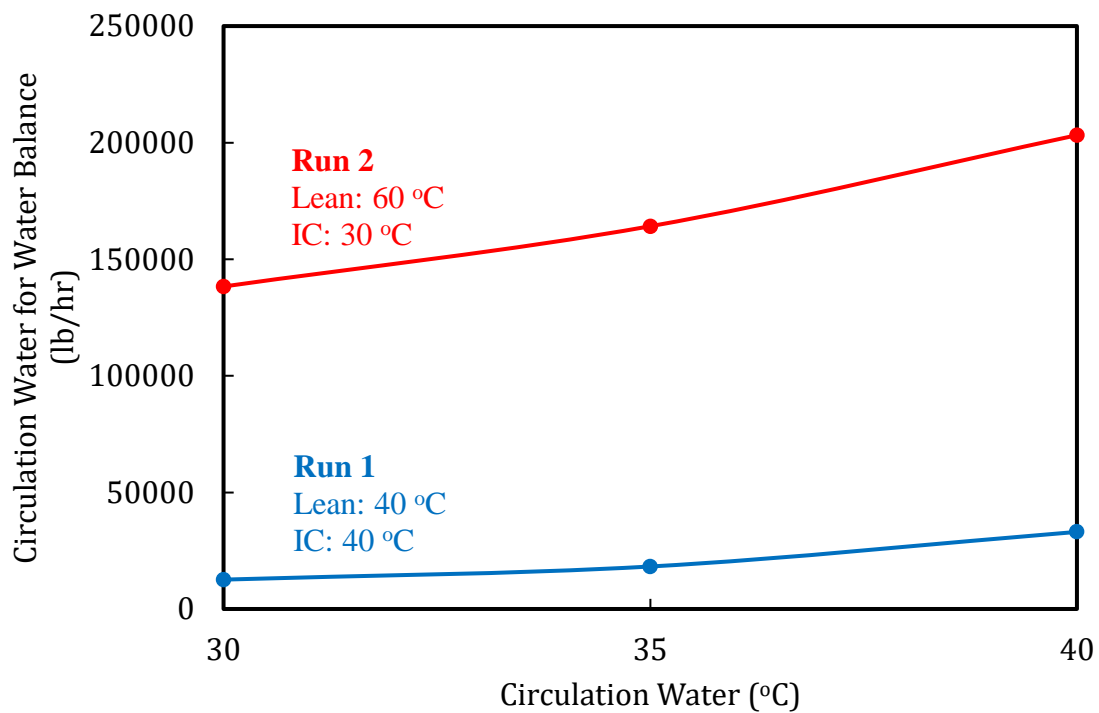


Figure 6.14: Circulation water flow required to maintain water balance for Runs 1 and 2 with AB solvent at temperature set points.

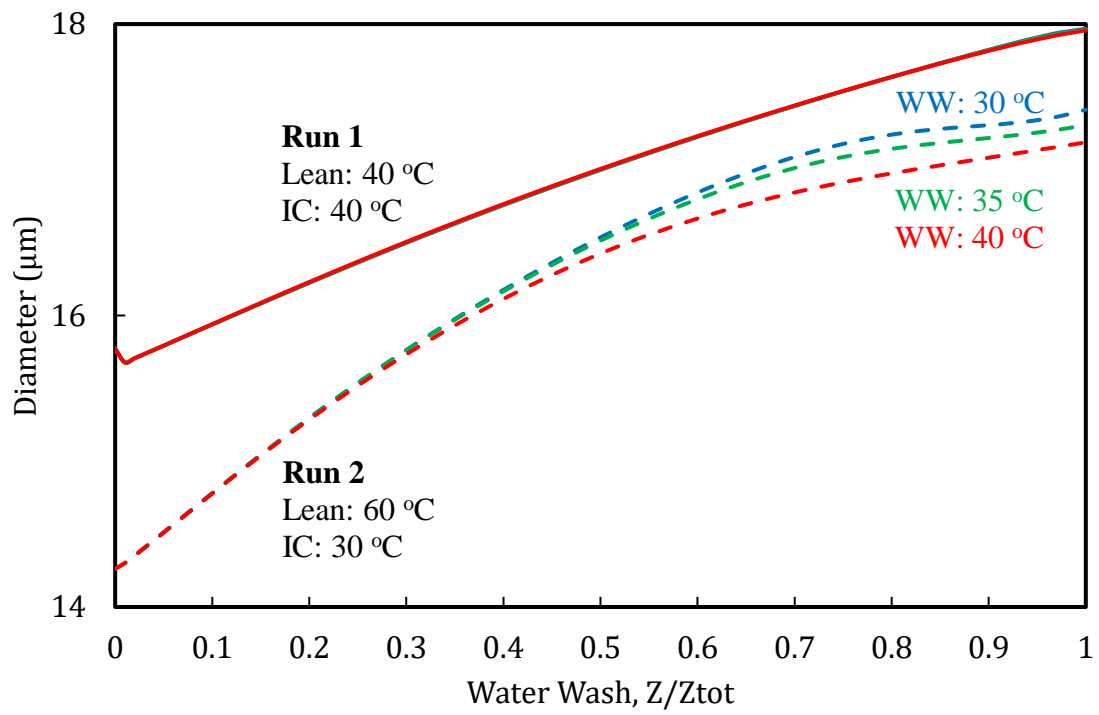


Figure 6.15: Effect of water wash temperature on AB aerosol growth in the water wash. Colder water wash grows bigger drops for Run 2 (dashed lines); minimal effect for Run 1 (solid lines).

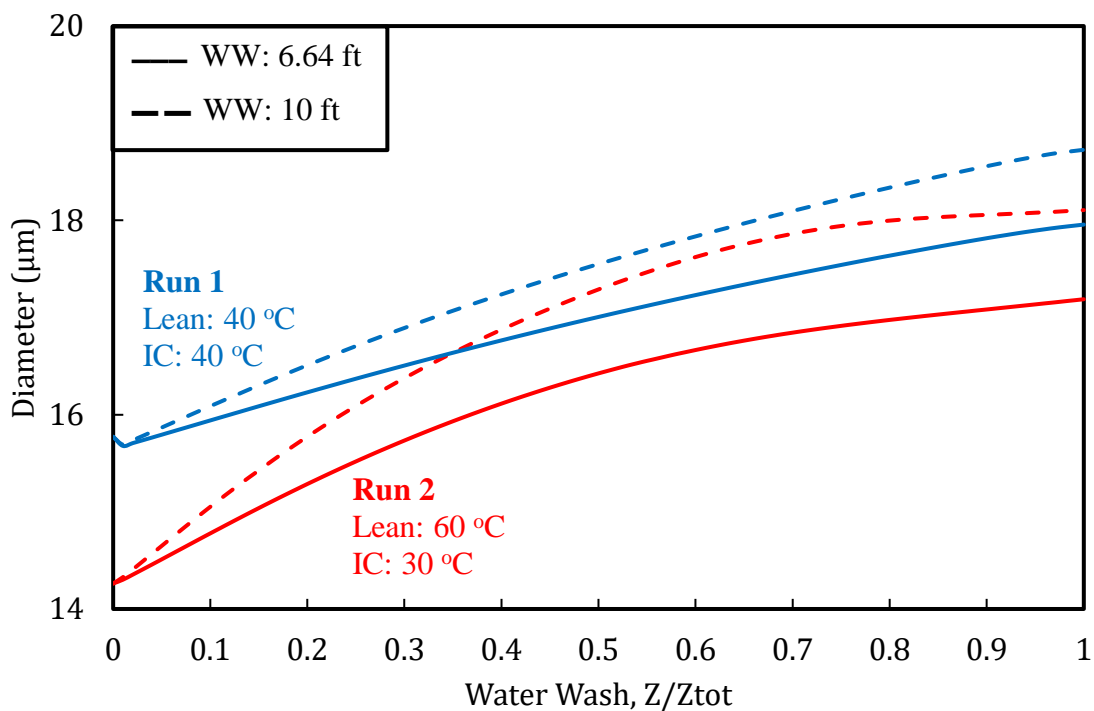


Figure 6.16: Effect of water wash packed height on AB aerosol growth in the water wash. 6.64 ft (solid lines) and 10ft (dashed lines). More packing grows bigger drops.

6.5 CONCLUSIONS AND RECOMMENDATIONS

The aqueous blend (AB) and non-aqueous blend (NAB) aerosol grow in the absorber by picking up water, the more volatile amine component, and CO₂. Their compositions differ in that while water is the dominant fraction for AB aerosol, the amine (Amine A) is the dominant fraction for NAB aerosol due to the reduced concentration of water in the bulk liquid of the NAB and its highly volatile amine.

Aerosol grows faster for more volatile amines due to the larger driving force for amine transfer. Like PZ, the growth of AB and NAB aerosol is driven by amine-limited diffusion, and the aerosol is in equilibrium with water in the bulk gas phase. The diminutive effect of aerosol concentration on the relative amine driving force for all three

solvent systems was similar; however, its overall effect on aerosol size was less pronounced for the more volatile solvents because of the significantly greater amine driving force between gas and aerosol phases.

Vapor emissions will be more significant than aerosol emissions for the AB and NAB systems. AB and NAB aerosol grow to 15 and 20 μm respectively, about 3 times PZ and well above the 3 μm threshold for collection by packing or mist eliminators. Since both AB and NAB aerosol grow well beyond the 3 μm threshold for collection, emission control with mist eliminators and no changes to operating conditions should be feasible. The water wash operation will be critical as vapor emissions will form a greater fraction of the overall emissions due to the high volatilities of the dominant amines in both AB and NAB. As the volatility of the amine in a solvent system increases, the controlling phase for emission will shift from aerosol to vapor.

Additional packing and colder circulation water in the water wash will enable further aerosol growth for aqueous solvents. Increasing the water wash packed height from 6.64 ft to 10 ft increased AB aerosol size by 4% in Run 1 and 5% in Run 2. Also, lowering the circulation water temperature by 10 $^{\circ}\text{C}$ while maintaining water balance in the water wash increased AB aerosol size by 0.1% in Run 1 and 1% in Run 2.

The model of aerosol size for the NAB was found to be extremely sensitive to kg' . Therefore, it is recommended that an experimentally determined kg' at relevant aerosol conditions be obtained to improve the model accuracy. The binary VLE approximation used to obtain surrogate equilibrium models for the NAB solvent needs to be improved with experimentally determined models. More accurate volatility data will also be required to improve the VLE predictions for both the AB and NAB solvents.

Chapter 7: Conclusions and Recommendations

This section presents the summary, conclusions, and recommendations from this work and some future directions for amine aerosol research.

7.1 SUMMARY

- Amine aerosol generation and injection into flue gas was demonstrated at pilot scale over extended periods
- Amine aerosol mitigation was demonstrated for PZ at pilot scale with flue gas at varying SO₃
- Emissions from PZAS™ were evaluated at coal and NGCC conditions through pilot studies during the 2018 coal and 2019 NGCC campaigns at the National Carbon Capture Center (NCCC)
- An aerosol model for solvent blends was developed and used to predict growth mechanisms for two proprietary solvents

7.2 CONCLUSIONS AND RECOMMENDATIONS

7.2.1 Conclusions from the Demonstration of Amine Aerosol Generation and Measurement at Pilot-Scale

1. The catalytic bed is highly effective for amine aerosol generation at pilot scales

The catalytic bed was proven reliable for aerosol tests at CO₂ capture facilities by demonstrating up to 8 ppm SO₃ generation and injection into 4000 lb/hr flue gas flow for more than 15 hrs over 2 weeks. A greater average conversion was achieved at the pilot-scale (97%) compared to previous bench-scale work (90%), confirming that the catalytic bed is highly efficient, more so at larger scales.

2. SO₃ generation by plasma oxidation is better suited for bench-scale aerosol experiments but needs future modifications

This work designed and fabricated a custom-made dielectric-barrier discharge (DBD) for SO₃ production by plasma oxidation of SO₂. The conversion varied inversely with inlet flow and peaked at 15% for the run conditions tested. Despite the low conversion, the DBD shows promise because of certain advantages over the catalytic bed and previous Liquid Vaporizer Injector (LVI). It is cheaper to construct, instant to start-up/shut-down, and operates at a much lower temperature than the other two. Future upgrades should focus on improving the conversion by increasing the intensity of the plasma or increasing the residence time for reaction. The plasma intensity can be increased by reducing the discharge gap between the electrodes, selecting better electrodes, or increasing the power supply. The residence time can be increased by increasing the reactor length or fabricating a series/cascade reactor configuration.

3. Gas sampling by FTIR is reliable for total amine sampling at CO₂ capture facilities

The Gaset CX-4000 and DX-4000 analyzers were reliable for sampling total PZ vapor and aerosol exiting the absorber and water wash gas during the 2018 coal and 2019 NGCC campaigns. Data loss and sampling interruptions can be minimized by ensuring proper weather protection, routine electrical checks on the connections, and temperature control of the probes and sample lines at 180 °C.

4. The particulate (fly ash and SO₃) concentration in the flue gas at Wyoming ITC should be measured to establish a baseline of fewer than 10⁵ particles/cm³

The potential for amine emissions was evaluated for the Wyoming ITC facility with a recommendation for initial particulate (fly ash and SO₃) concentration measurement to

establish a baseline of fewer than 10^5 particles/cm³. A PFD was also developed with recommended gas and aerosol sampling setup for the UK CAER CO₂ capture pilot plant.

7.2.2 Conclusions from the Demonstration of Amine Aerosol Mitigation at Pilot-Scale

5. Hydrated lime is the critical indicator in Baghouse operations for SO₃ reduction and inlet aerosol mitigation

While previous work by Beaudry (2018) concluded that the baghouse installed at NCCC reduced inlet SO₃, it was unclear what particular baghouse operations led to the SO₃ removal and subsequent amine emission reduction. Findings from this work improve previous conclusions by showing that SO₃ slippage correlates with hydrated lime injection upstream of the baghouse. Therefore, hydrated lime is the critical function in baghouse operations for SO₃ reduction and inlet aerosol mitigation. There is a threshold for hydrated lime injection rates beyond which SO₃ slippage occurs into the CO₂ capture plant. For the NCCC, that threshold is at 0.5 of normal hydrated lime rates.

6. As inlet flue gas SO₃ increases, amine emissions increase, and water wash performance decreases

PZ emissions exiting both the absorber and water wash were proportional to inlet SO₃. Without SO₃ injection, the baseline concentration was 11 ppm in the absorber and 2 ppm in the water wash. However, with SO₃ in the flue gas, the PZ in the absorber gas outlet increased by 14 times the inlet SO₃. This factor was reduced to 11 in the water wash. The water wash was most effective at mitigating vapor emissions (zero SO₃ concentration in the flue gas), and its efficiency diminished with SO₃ load from 80% at zero inlet SO₃ to 30% at 4 ppm SO₃.

7. Increasing the lean solvent temperature, turning off the intercooler, and increasing the water wash stages help mitigate PZ aerosol emission

Increasing the lean solvent from 43 to 58 °C resulted in a 65% reduction in PZ exiting the absorber. Likewise, the avoidance of intercooling also reduced PZ emission by 65%. Overall, PZ emissions were reduced to 1 ppm for flue gas with 2 ppm SO₃ by increasing the lean solvent temperature and water wash stages. Compared to the case with cold solvent at 44 °C and no water wash, a 98% reduction in PZ emission was achieved for flue gas with two ppm SO₃ by increasing the lean solvent to 58 °C and using a 2-stage water wash. Greater lean solvent temperatures would be even more effective at mitigating amine emissions.

8. Higher lean solvent temperature mitigates PZ emission because it grows PZ aerosol and increases the collection of aerosol within the column

The ELPI aerosol concentration measurements at the water wash outlet showed that runs at higher lean solvent temperatures shifted the aerosol size distribution to the larger size and reduced the total number count. The fraction of larger particles ($D_p > 0.1 \mu\text{m}$) increased from 39 to 68% by increasing the lean solvent temperature, confirming growth due to amine condensation at the higher temperature. Also, increasing the lean solvent temperature resulted in a 47% decrease in the total aerosol number count, confirming that many particles had grown above the 3 μm threshold for removal and were collected in the packing and mist eliminator of the column.

9. Long-term operations at aerosol mitigation conditions of an elevated lean solvent temperature can be sustained

Although running the absorber at higher lean solvent temperatures does not favor CO₂ absorption, 90% CO₂ removal was maintained by intensive solvent intercooling to 32 °C. A large amount of packing in the NCCC absorber also helped sustain CO₂ absorption

at the operating conditions evaluated during the aerosol tests. The water balance of the system was maintained by increasing the circulation water flow to cool the gas exiting the water wash within 4–7 °C of the absorber inlet gas temperature.

7.2.3 Conclusions from the Evaluation of Amine Emissions at NGCC Conditions

10. For the same SO₃ penetration, amine emissions from NGCC operations are much lower than coal

PZ emissions exiting the water wash at NGCC conditions had a maximum of 2 ppm and an overall average below 1 ppm. The results suggest that the capture conditions of NGCC suppressed emissions even at significant SO₃ penetration. This could also have resulted because the inlet aerosol got diluted as the coal flue gas was diluted with air to meet the 4% CO₂ spec for NGCC.

11. Bypassing the DCC resulted in a five-fold increase in PZ due to possible aerosol formation from the quenching of hot gas in the absorber

When the DCC was bypassed, inlet gas at 76 °C was introduced to the absorber, resulting in a five-fold increase in PZ emission. This increase in emission is possibly due to aerosol formation from the quenching of hot gas with cold solvent in the absorber. Despite this, the average PZ emission was still below 1 ppm.

12. The water wash efficiency at NGCC conditions is high and inversely correlated with inlet PZ

The average removal efficiency for PZ at NGCC conditions was 94%. This efficiency is significantly higher than coal conditions which ranged from 30–80%, although at a more significant inlet SO₃ load. The water wash efficiency correlated inversely with the PZ concentration entering the water wash.

7.2.4 Conclusions from the Improvement of PZ Aerosol Model and Development of New Aerosol Models for Solvent Blends

13. PZ aerosol model with updated VLE resulted in a 20% increase in PZ drop diameter compared to previous work with empirical correlations

This work improved previous work by using CO₂ solubility and PZ volatility predictions from the Independence model in Aspen Plus[®]. The regressed equations used in this work are more reliable than previous work because they better represent the temperature and composition ranges of the PZ drop.

14. There is a tradeoff between capital or energy costs and PZ aerosol control

Design conditions that lead to larger drop sizes require more solvent flow to maintain CO₂ removal specifications (higher lean solvent and higher intercooling temperatures), require higher energy cost for solvent regeneration in the stripper (lower lean loading), or require bigger columns to increase residence time for drop growth (greater packing volume).

From an operational standpoint, short-term episodes of PZ aerosol can be controlled by increasing the lean solvent or intercooling temperatures at the cost of lower CO₂ removal. Model results show that PZ aerosol size increased by 6% and CO₂ removal decreased by 4% when the lean solvent temperature was changed from 40 to 60 °C. Similarly, PZ aerosol size increased by 15% and CO₂ removal by 15% with no intercooling. These model results agree with experimental results from the PZ aerosol tests at NCCC.

15. The aqueous blend (AB) and non-aqueous blend (NAB) aerosol grow in the absorber by picking up water, the more volatile amine component, and CO₂

Aerosol from the solvent blends grows similarly to PZ aerosol by picking up water, amine, and CO₂. Their compositions differ in that while water is the dominant fraction for

AB aerosol, the amine (Amine A) is the predominant fraction for NAB aerosol due to the reduced concentration of water in the bulk liquid of the NAB and its highly volatile amine.

16. More volatile solvents grow bigger drops due to the larger driving force for amine transfer, and the effect of aerosol concentration is diminished

AB and NAB aerosol grow to 15 and 20 μm respectively, about 3 times PZ. The diminutive effect of aerosol concentration on the relative amine driving force for all three solvent systems was similar; however, its overall effect on aerosol size was less pronounced for the more volatile solvents because of the significantly greater amine driving force between gas and aerosol phases.

17. Vapor emissions will be more significant than aerosol emissions for the AB and NAB systems

Since both AB and NAB aerosol grow well beyond the 3 μm threshold for collection, emission control with mist eliminators and no changes to operating conditions should be feasible. The water wash operation will be critical as vapor emissions will likely form a greater fraction of the overall emissions due to the high volatilities of the dominant amines in both AB and NAB. As the volatility of the amine in a solvent system increases, the controlling phase for emission will shift from aerosol to vapor. Since the volatility is critical, future work should improve the binary VLE approximation used to obtain surrogate equilibrium models for the NAB solvent with experimentally determined models. More accurate volatility data should also be used to improve the VLE predictions for both the AB and NAB solvents.

18. Additional packing and colder circulation water in the water wash will enable further aerosol growth for aqueous solvents

Increasing the water wash packed height from 6.64 ft to 10 ft increased AB aerosol size by 4% in Run 1 and 5% in Run 2. Also, lowering the circulation water temperature

by 10 °C while maintaining water balance in the water wash increased AB aerosol size by 0.1% in Run 1 and 1% in Run 2.

7.3 FUTURE DIRECTIONS FOR AMINE AEROSOL RESEARCH

1. Improve aerosol transport models to account for collection and size distribution

The models modified and developed in this work only predict a final drop size that does not account for collection in the mist eliminators and packing or predict a size distribution. While the model as-is helps identify at a high level the response of aerosol to the operating conditions in the absorber and potential for aerosol control, it fails at representing experimentally measured distributions and sizes. Future work should incorporate drop cut-off efficiencies at the end of each packing section and absorber/water wash top to account for collection.

2. Design experiments to validate aerosol transport models

While the experimental design implemented in this work helped validate amine aerosol growth and capture in the absorber, further work is required to confirm the changes in aerosol size as it travels through the absorber stages. This will require extractive sampling of gas between sections of absorber packing for particle size and concentration measurements.

3. Investigate amine aerosol in CO₂ stripper overhead

Much attention has been on the amine concentrations exiting the absorber and water wash columns, with very little being paid to the pure CO₂ stream exiting the top of the stripper column. The stripper operates at higher temperature and pressure than the absorber, so significant amine vapor could escape in the pure CO₂ stream. More so, when quenched in the condenser, amine aerosol could form and be challenging to collect back into the liquid stream.

Appendix A: Codes for PZ Aerosol Transport Model in gPROMS® ModelBuilder

The PZ aerosol growth model used for the sensitivity analysis and PZ aerosol growth prediction is presented in this appendix. The model was coded initially by Fulk (2016) in MATLAB and then transferred to gPROMS ModelBuilder by Kang et al. (2017) with the inclusion of gas-phase PZ depletion. This work improves Kang et al. (2017) with updated equilibrium and thermodynamic models for PZ.

A.1 AEROSOL INTEGRATION

```
# Aerosol Transport Model for Piperazine (PZ ATM)
# Aerosol Integration
# Last Revised by: Korede Akinpelumi
# Date Modified: 5/21/2021

PARAMETER
Column_Stages AS INTEGER DEFAULT 30 # No of computational stages used
in Aspen run
Stages AS INTEGER DEFAULT 100
Layers AS INTEGER DEFAULT 3
Aspen_Profile AS FOREIGN_OBJECT "ExcelFO" #Gas profile from Aspen
Comps AS ORDERED_SET DEFAULT ["N2", "H2O", "CO2", "PZ"] #Components in
gas/liquid/aerosol
#Const
pi AS REAL DEFAULT 3.14159265359
g AS REAL DEFAULT 9.80665 # [m/s^2]
R_const AS REAL DEFAULT 8.3144621 #m3·Pa·K-1·mol-1
#Column Parameters
H_col AS REAL DEFAULT 1.74625 #m, Column height
D_col AS REAL DEFAULT 0.0427228 #m, Column diameter
vfrac AS REAL DEFAULT 0.96 # Void fraction of the packing from Aspen
initial_Diameter_Drop AS REAL DEFAULT 2.3 #um
Num_Drop AS REAL DEFAULT 1e6 # Num/cm3
MW AS ARRAY(Comps) OF REAL #Component molecular weight
initial_LDG_Drop AS REAL DEFAULT 0.4 #molCO2/mol alkalinity
initial_xApp AS ARRAY(COMPS) OF REAL #mol/mol
initial_MW AS REAL #g/mol
initial_Rho AS REAL #kg/m3
initial_Conc_tot AS REAL #mol/m3
initial_Vol_drop AS REAL #m3
initial_T_Drop AS REAL DEFAULT 313 # K

UNIT
Phy_Props AS Phy_Props
```

VARIABLE

```
# Parameters of Column
T_BulkG AS temperature
T_BulkL AS temperature
#y_BulkG AS ARRAY(Comps) OF molar_fraction
pp_BulkG AS ARRAY(Comps) OF pressure
#MW_BulkG AS molecular_weight
RHO_BulkG AS mass_density
K_BulkG AS thermo_conductivity
#CP_BulkG AS molar_specific_heat_capacity
MU_BulkG AS dynamic_viscosity
Diff_BulkG AS ARRAY(Comps) OF diffusion_coefficient
VOLFL_BulkG AS volume_flowrate
#FN2_BulkG AS molar_flowrate
#FH2O_BulkG AS molar_flowrate
#FCO2_BulkG AS molar_flowrate
#FPZ_BulkG AS molar_flowrate
Kg_Bulk AS ARRAY(Comps) OF mass_transfer_coefficient
IA_Bulk AS specific_surface_area
x_BulkL AS ARRAY(Comps) OF molar_fraction
C_BulkL AS ARRAY(Comps) OF molar_concentration
LDG_BulkL AS loading
HOLDUP_BulkL AS no_type

#Parameters of Gas Side
#Conc_BulkG AS ARRAY(Comps) OF molar_concentration
ppeq_BulkL AS ARRAY(Comps) OF pressure # Equilibrium pressure of each
component over bulk liquid
N_gl AS ARRAY(Comps) OF no_type #Flux of each component

#Parameters of Aerosol Side
T_Drop AS temperature #Drop temperature, K
n AS ARRAY(Comps) OF nanomoles # mole of component in drop, nano mole
n_tot AS nanomoles# mole of drop, nano mole
Conc_Drop AS ARRAY(Comps) OF molar_concentration # concentration of
drop, mole/m3
Conc_Drop_Free AS ARRAY(Comps) OF molar_concentration # concentration
of drop, mole/m3
Conc_tot_Drop AS molar_concentration # concentration of drop, mole/m3
Rds AS Radius_Drop # Radius of drop, um
Diff_Drop_CO2 AS diffusion_coefficient # diffusion coefficient of drop,
m2/s
Ngd AS ARRAY(Comps) OF no_type #mass transfer flux between gas and
drop, mol/m2-s
v_Drop AS velocity #velocity of drop, m/s
v_BulkG AS velocity #velocity of gas, m/s

#If want to consider relative velocity between aerosols and gas flow,
turn on the following equations##

##turn on the following equations##
#v_Rel AS no_type # related velocity, m/s
d_drop AS Radius_Drop # diameter of drop, um
```

```

RHO_Drop AS mass_density #density of drop, kg/m3
##turn on the following equations##
#Cc AS no_type
##turn on the following equations##
#avgKn AS no_type
Kn AS ARRAY(Comps) OF no_type
##turn on the following equations##
#avgmfp AS no_type
mfp AS ARRAY(Comps) OF no_type #mean free path
LDG_Drop AS loading #CO2 loading in drop, mol CO2/mol alk.
Cplmx AS molar_specific_heat_capacity #heat capacity, J/mol-K
xApp AS ARRAY(Comps) OF molar_fraction #mole/mole, apparent mole
fractions in drop, Accounts for speciation.
Qd AS heat_flux #heat transfer flux, J/m2-s
delHd AS ARRAY(Comps) OF molar_specific_enthalpy #heat of vaporation
and absorption, J/mol
hg AS heat_transfer_coefficient #heat transfer coeff.
kg AS ARRAY(Comps) OF mass_transfer_coefficient #mass transfer coeff.
kgprime_Drop AS mass_transfer_coefficient #mass transfer coeff.
A_Drop AS area_Drop
agd AS specific_surface_area #specific surface area of aerosol
Vol_Drop AS volume
Fuchs AS ARRAY(Comps) OF no_type
ppeq_Drop_Outlayer AS ARRAY(Comps) OF pressure
k2d AS no_type
Henry_Drop AS no_type
Nu AS Dimentionless
##turn on the following equations##
#Re AS Dimentionless
#Pr AS Dimentionless
#Sc AS ARRAY(Comps) OF Dimentionless
Sh AS ARRAY(Comps) OF Dimentionless
v_gmol AS ARRAY(Comps) OF no_type
molal_PZ_Drop AS molal_concentration
h AS length
#Thermal_Conductivity_Drop AS thermo_conductivity
MW_Drop AS molecular_weight

```

SELECTOR

```

MT_Mode AS (DefaultMode,InitializationMode) DEFAULT DefaultMode
kgprime_Mode AS (DefaultMode,InitializationMode) DEFAULT DefaultMode

```

SET

```

Phy_Props.Stages := Stages;
Phy_Props.Layers := Layers;
Phy_Props.Comps := Comps;
MW := [28.0134, 18.01528, 44.0095, 86.1356]; #g/gmol, (N2, H2O, CO2,
PZ)
initial_xApp('N2') := 0; # No N2 in drop
initial_xApp('H2O') := Aspen_Profile.xH2O(0); #initial drop
concentration assumed equal to rich solvent conc
initial_xApp('CO2') := Aspen_Profile.xCO2(0); #initial drop
concentration assumed equal to rich solvent conc

```

```
initial_xApp('PZ') := Aspen_Profile.xPZ(0); #initial drop concentration
assumed equal to rich solvent conc
```

```
initial_LDG_Drop := Aspen_Profile.LDG(0);
initial_T_Drop := Aspen_Profile.TG(0);
initial_MW :=
initial_xApp('H2O')*MW('H2O')+initial_xApp('CO2')*MW('CO2')+initial_xAp
p('PZ')*MW('PZ');#g/gmol
initial_Rho := 1000*((1.5494 +(-0.0005728 *initial_T_Drop))*LOG((2.676
*initial_xApp('CO2'))+(-0.030977 *initial_xApp('PZ'))+(-0.0726176
*initial_LDG_Drop)+ 2.102569));#kg/m3, Solvent density for PZ from
Fawkes model, Frailie 2011. fn(T,xco2,xpz,ldg)
initial_Conc_tot := initial_Rho/(initial_MW/1000);#mol/m^3
initial_Vol_drop := 1/6*pi*initial_Diameter_Drop^3; #um^3
```

EQUATION

```
# Model equations
```

```
#-----
#-----
#-----
#GAS Profiles extracted from ASPEN via VBA script
#-----
#-----
#-----
```

```
T_BulkG = Aspen_Profile.TG(h);
#y_BulkG('N2') = Aspen_Profile.yN2(h);
#y_BulkG('H2O') = Aspen_Profile.yH2O(h);
#y_BulkG('CO2') = Aspen_Profile.yCO2(h);
#y_BulkG('PZ') = Aspen_Profile.yPZ(h);
pp_BulkG('N2') = Aspen_Profile.ppN2(h);
pp_BulkG('H2O') = Aspen_Profile.ppH2O(h);
pp_BulkG('CO2') = Aspen_Profile.ppCO2(h);
#pp_BulkG('PZ') = Aspen_Profile.ppPZ(h);
#MW_BulkG = Aspen_Profile.MW(h);
RHO_BulkG = Aspen_Profile.RHOG(h); #Not currently used. Only useful for
v_Rel and Re/Sc
K_BulkG = Aspen_Profile.K(h);
#CP_BulkG = Aspen_Profile.CPG(h);
MU_BulkG = Aspen_Profile.MUG(h); #Not currently used. Only useful for
Sh/Re/Sc
Diff_BulkG('N2') = Aspen_Profile.DGN2(h);
Diff_BulkG('H2O') = Aspen_Profile.DGH2O(h);
Diff_BulkG('CO2') = Aspen_Profile.DGCO2(h);
Diff_BulkG('PZ') = Aspen_Profile.DGPZ(h);
VOLFL_BulkG = Aspen_Profile.VOLFLG(h);
#FN2_BulkG = Aspen_Profile.FGN2(h);
#FH2O_BulkG = Aspen_Profile.FGH2O(h);
#FCO2_BulkG = Aspen_Profile.FGCO2(h);
#FPZ_BulkG = Aspen_Profile.FGPZ(h);
Kg_Bulk('N2') = Aspen_Profile.KGN2(h); #Not used at all
Kg_Bulk('H2O') = Aspen_Profile.KGH2O(h); #Not used at all
Kg_Bulk('CO2') = Aspen_Profile.KGCO2(h); #Not used at all
Kg_Bulk('PZ') = Aspen_Profile.KGPZ(h);
```

```

IA_Bulk = Aspen_Profile.IA(h)/(pi*D_col^2/4*H_col/Column_Stages);
x_BulkL('N2') = Aspen_Profile.xN2(h);
x_BulkL('H2O') = Aspen_Profile.xH2O(h);
x_BulkL('CO2') = Aspen_Profile.xCO2(h);
x_BulkL('PZ') = Aspen_Profile.xPZ(h);
C_BulkL('N2') = Aspen_Profile.CLN2P(h); #Not used at all
C_BulkL('H2O') = Aspen_Profile.CLH2OP(h); #Not used at all
C_BulkL('CO2') = Aspen_Profile.CLCO2P(h); #Not used at all
C_BulkL('PZ') = Aspen_Profile.CLPZP(h); #Not used at all
LDG_BulkL = Aspen_Profile.LDG(h);
T_BulkL = Aspen_Profile.TL(h);
HOLDUP_BulkL =
Aspen_Profile.HOLDUPL(h)/(pi*D_col^2/4*H_col/Column_Stages); # Fraction
of free volume occupied by liquid (Total volume - Packing volume)
#-----
#-----
#Physical Properties (input parameters from Phy_Props model)
#-----
#-----
Phy_Props.T_BulkG = T_BulkG;
Phy_Props.T_BulkL = T_BulkL;
Phy_Props.T_Drop = T_Drop;
Phy_Props.xApp = xApp;
Phy_Props.x_BulkL = x_BulkL;
Phy_Props.LDG_Drop = LDG_Drop;
Phy_Props.LDG_BulkL = LDG_BulkL;
Phy_Props.d_drop = d_drop;
Phy_Props.n = n;

#Properties of Aerosol side
Diff_Drop_CO2 = Phy_Props.Diff_Drop_CO2;

Cplmx = Phy_Props.Cplmx;

delHd('N2') = Phy_Props.delHd('N2');
delHd('H2O') = Phy_Props.delHd('H2O');
delHd('CO2') = Phy_Props.delHd('CO2');
delHd('PZ') = Phy_Props.delHd('PZ');

#Thermal_Conductivity_Drop = Phy_Props.Thermal_Conductivity_Drop;

ppeq_Drop_Outlayer = Phy_Props.ppeq_Drop_Outlayer;

v_gmol = Phy_Props.v_gmol; #velocity in kinetic mass transfer regime
RHO_Drop = Phy_Props.RHO_Drop;
k2d = Phy_Props.k2d;
Henry_Drop = Phy_Props.Henry_Drop;
MW_Drop =
xApp('H2O')*MW('H2O')+xApp('CO2')*MW('CO2')+xApp('PZ')*MW('PZ');

```

```

#-----
#-----
#Algebraic Equations of Aerosol Side
#-----
#-----

# CO2 Loading in aerosol drop
If xApp('PZ')>0 Then
LDG_Drop = xApp('CO2')/(2*xApp('PZ'));
Else
LDG_Drop=0;
End
# PZ molality in aerosol drop
molal_PZ_Drop = (1000/MW('H2O'))*xApp('PZ')/xApp('H2O');

#Calc. Kn
mfp = 3*Diff_BulkG/(v_gmol);
##turn on the following equations##
#avgmfp = sigma(mfp)/Comps.Card;
d_drop = 2*Rds;
Kn = (2*mfp/(d_drop*(1E-6)));
##turn on the following equations##
#avgKn = (2*avgmfp/(d_drop*(1E-6)));
##turn on the following equations##
#Calc. Cc
#Cc = 1+avgKn*(1.246+0.418*exp(-0.867/avgKn));#Cunningham slip used to
correct Stokes' Law.
#Calc. Fuchs(i)
Fuchs = (0.75*1*(1+Kn))/(Kn^2+Kn+0.283*Kn*1+0.75*1);#alpha = 1;

# Calc. v_Drop
v_BulkG = 4*VOLFL_BulkG/((vfrac-HOLDUP_BulkL)*pi*(D_col^2));
##turn on the following equations##
#v_Rel = (d_drop*(1E-6))^2*(RHO_DropMix-RHO_BulkG)*g*Cc/(18*MU_BulkG);
v_Drop= v_BulkG;
##change the following equations##
#v_Drop= v_BulkG -v_Rel;

#Calc. Dimensionless Numbers
##turn on the following equations##
#Sc = MU_BulkG/RHO_BulkG/Diff_BulkG;
#Pr = (MU_BulkG*CP_BulkG)/(K_BulkG*MW_BulkG);
#Re = ABS(RHO_BulkG*v_Rel*d_drop*(1E-6)/MU_BulkG);
Sh = 2;#+0.6*(Re^(1/2))*(Sc^(1/3));
Nu = 2;#+0.6*(Re^(1/2))*(Pr^(1/3));

#Calc. kg
kg = Sh*Diff_BulkG/(d_drop*(1E-6));
#Calc. kgprime
#kgprime_Drop = 3*10^(-6);
If Conc_Drop_Free('PZ')>0 Then

```

```

kgprime_Drop = (k2d*Conc_Drop_Free('PZ')
*Diff_Drop_CO2)^(1/2)/Henry_Drop;
Else
kgprime_Drop = 0;
End
#Calc. hg
hg = Nu*K_BulkG/(d_drop*(1E-6));
#Calc. Ngd
Ngd('N2') = 0;
Ngd('H2O') = Fuchs('H2O')*kg('H2O')/(R_const*T_BulkG)*(pp_BulkG('H2O')-
ppeq_Drop_Outlayer('H2O'));
Ngd('CO2') = kgprime_Drop*(pp_BulkG('CO2')-ppeq_Drop_Outlayer('CO2'));
Ngd('PZ') = Fuchs('PZ')*kg('PZ')/(R_const*T_BulkG)*(pp_BulkG('PZ')-
ppeq_Drop_Outlayer('PZ'));
#Calc. Qd
Qd = (Ngd('H2O')*delHd('H2O')-
Ngd('PZ')*delHd('PZ')+Ngd('CO2')*delHd('CO2'))+hg*(T_BulkG-T_Drop);

#Total number of moles of all components in drop
n_tot = SIGMA(n);
#Mole fraction of each component in drop
xApp = n/n_tot;
#Total concentration of all components in drop
Conc_tot_Drop = RHO_Drop/(MW_Drop/1000);
#Concentration of each component in drop
Conc_Drop = xApp*Conc_tot_Drop;
#Not sure what this is
Conc_Drop_Free('N2') = 0;
Conc_Drop_Free('H2O') = Conc_Drop('H2O');
Conc_Drop_Free('CO2') = 0;
Conc_Drop_Free('PZ') = Conc_Drop('PZ')-Conc_Drop('CO2');

#Aerosol size calculations
#Aerosol volume and diameter calculation
Vol_Drop = 4/3*pi*Rds^3 = (n_tot*(1E-9)/Conc_tot_Drop)*(1E6)^3; #um^3
#Area of aerosol drop
A_Drop = 4*pi*Rds^2; #um^2
#Specific surface area of aerosol drop
agd = 4*pi*Rds^2/(4/3*pi*Rds^3)*(1E-6)^2/(1E-6)^3;

#-----
#-----
#-----
#Differential Equations of Aerosol Side
#-----
#-----
#-----
#Calculation for number of moles of each component in aerosol drop
n('N2') = 0;
For i in ['H2O', 'CO2', 'PZ'] Do
    v_Drop/H_col*$n(i)*(1E-9) = Ngd(i)*A_Drop*(1E-6)^2;
End

```

```

v_Drop/H_col*$T_Drop ==
v_Drop/H_col*T_Drop/n_tot*SIGMA($n('H2O':'PZ'))+Qd*A_Drop*(1E-
6)^2/(Cplmx*n_tot*(1E-9));

#Properties of Gas side
ppeq_BulkL=Phy_Props.ppeq_BulkL;
#Algebraic Equations of Gas Side
N_gl('N2') = 0;
N_gl('H2O') = 0;
N_gl('CO2') = 0;
N_gl('PZ') = Kg_Bulk('PZ')*(pp_BulkG('PZ')-ppeq_BulkL('PZ'));

#Differential Equations of Gas Side
v_Drop/H_col*$pp_BulkG('PZ') = (-Ngd('PZ')*A_Drop*(1E-
6)^2*Num_Drop*(1E2)^3-N_gl('PZ')*IA_Bulk)*R_const*T_BulkG;

ASSIGN
h := TIME;

INITIAL
#STEADY_STATE
T_Drop = initial_T_Drop;
n('CO2')*(1E-9)= initial_xApp('CO2')*
initial_Conc_tot*initial_Vol_drop*(1E-6)^3;
n('PZ')*(1E-9)= initial_xApp('PZ')*
initial_Conc_tot*initial_Vol_drop*(1E-6)^3;
n('H2O')*(1E-9)= initial_xApp('H2O')*
initial_Conc_tot*initial_Vol_drop*(1E-6)^3;
pp_BulkG('PZ') = Aspen_Profile.ppPZ(0);

```

A.2 PHYSICAL PROPERTIES MODEL

```

# Aerosol Transport Model for Piperazine (PZ ATM)
# Physical Properties
# Last Revised by: Korede Akinpelumi
# Date Modified: 5/21/2021

PARAMETER
Stages AS INTEGER
Layers AS INTEGER
Comps AS ORDERED_SET DEFAULT ["N2", "H2O", "CO2", "PZ"]
pi AS REAL DEFAULT 3.14159265359
R_const AS REAL DEFAULT 8.3144621 #m3·Pa·K-1·mol-1
MW AS ARRAY(Comps) OF REAL

DISTRIBUTION_DOMAIN
#Height AS [ 0 : 1 ]
Radius AS [ 0 : 1 ]

VARIABLE
T_Drop AS temperature #Aerosol temperature
T_BulkG AS temperature #Bulk gas temperature

```

```

T_BulkL AS temperature #Bulk solvent temperature
LDG_Drop AS loading #CO2 loading in aerosol
LDG_BulkL AS loading #CO2 loading in bulk solvent
xApp AS ARRAY(Comps) OF molar_fraction #mole/mole, apparent mole
fractions in drop, Accounts for speciation.
xwApp AS ARRAY(Comps) OF mass_fraction #mass fraction of components in
aerosol
x_BulkL AS ARRAY(Comps) OF molar_fraction #mole fraction of components
in bulk solvent
d_drop AS Radius_Drop #drop diameter
n AS ARRAY(Comps) OF nanomoles # mole of component in drop, nano mole
ppeq_BulkL AS ARRAY(Comps) OF pressure #Equilibrium pressure of each
component over bulk solvent
Diff_Drop_CO2 AS diffusion_coefficient
ppeq_Drop_Outlayer AS ARRAY(Comps) OF pressure #Equilibrium pressure of
each component over aerosol
v_gmol AS ARRAY(Comps) OF no_type
RHO_Drop AS mass_density
k2d AS no_type #CO2 reaction rate constant for calculating kg'
Henry_Drop AS no_type #Henry constant for CO2 in drop
MUDH2O AS dynamic_viscosity #viscosity of pure water in aerosol
MUDMIX AS dynamic_viscosity # viscosity of amine solution in aerosol
Vmold AS ARRAY(Comps) OF no_type
TAUD AS ARRAY(Comps) OF no_type #Surface tension
Cp_Drop AS ARRAY (Comps) OF molar_specific_heat_capacity
Cp_Ex_Drop AS molar_specific_heat_capacity
Cplmx AS molar_specific_heat_capacity
delHd AS ARRAY(Comps) OF molar_specific_enthalpy
#Thermal_Conductivity_Drop AS thermo_conductivity

```

SET

```

#Height := [BFDM,Stages];
Radius := [OCFEM,2,Layers];
MW := [28.0134, 18.01528, 44.0095, 86.1356];

```

EQUATION

```

#Model equations; Properties of Aerosol side

```

```

#convert molefraction of each component in aerosol to mass fraction;
molefraction not yet calculated
xwApp('N2') = MW('N2')*xApp('N2')/(MW('N2')
*xApp('N2')+MW('H2O')*xApp('H2O')+MW('CO2')*xApp('CO2')+MW('PZ')*xApp('
PZ'));
xwApp('H2O') = MW('H2O')*xApp('H2O')/(MW('N2')
*xApp('N2')+MW('H2O')*xApp('H2O')+MW('CO2')*xApp('CO2')+MW('PZ')*xApp('
PZ'));
xwApp('CO2') = MW('CO2')*xApp('CO2')/(MW('N2')
*xApp('N2')+MW('H2O')*xApp('H2O')+MW('CO2')*xApp('CO2')+MW('PZ')*xApp('
PZ'));
xwApp('PZ') = MW('PZ')*xApp('PZ')/(MW('N2')
*xApp('N2')+MW('H2O')*xApp('H2O')+MW('CO2')*xApp('CO2')+MW('PZ')*xApp('
PZ'));

```

```

#viscosity of pure water in aerosol; from DIPPR 101
MUDH2O = EXP(-52.843+(3703.6 /T_Drop)+5.866 *LOG(T_Drop)-5.88E-29
*T_Drop^10);
# viscosity of amine solution in aerosol
MUDMIX = MUDH2O*EXP(((487.52 *xwApp('PZ')+1389.31 *T_Drop+(1.58
*xwApp('PZ')+4.5 ))*(LDG_Drop*(8.73 *xwApp('PZ')-0.0038 *T_Drop-0.3
)+1)*xwApp('PZ'))/T_Drop^2);

#Diffusion coefficient of CO2 in amine solution; = (Diffusion
coefficient of CO2 in pure water * ratio of pure water viscosity to
amine solvent viscosity)
Diff_Drop_CO2 = (1/100^2)*0.024*EXP(-2122/T_Drop)*(MUDH2O/MUDMIX)^0.72;
#m2/s

#molecular volume
Vmold('N2') = 0;
Vmold('H2O') = (1/(6.0221415*10^23*1000))*(-13.851 +0.64038 *T_Drop-
0.0019124 *T_Drop^2+1.82E-06 *T_Drop^3)^(-1);
Vmold('CO2') = (1/(6.0221415*10^23*1000))*(2.768 /0.26212 ^ (1+(1-
(304.21/304.21 ))^0.2908 ))^(-1);
Vmold('PZ') = (1/(6.0221415*10^23*1000))*(1.0425 /0.323 ^ (1+(1-
(T_Drop/638 ))^0.28571 ))^(-1);

#Surface tension for Water and PZ in amine solution
TAUD('N2') = 0;
TAUD('H2O') = 0.17766 *(1-T_Drop/647.096 )^(2.567 -3.3377
*T_Drop/647.096 +1.9699 *(T_Drop/647.096 )^2);
TAUD('CO2') = 0;
TAUD('PZ') = 0.024853*(1-T_Drop/638)^(1.1667 +0*T_Drop/638
+0*(T_Drop/638)^2);
#TAUD('PZ') = 0.0108;

#velocity for kinetic theory assumption of mass transfer
v_gmol('N2') = ((1000*6.0221415*10^23*8*1.3806503*10^(-
23)*T_BulkG)/(pi*MW('N2')))^ (1/2);
v_gmol('H2O') = ((1000*6.0221415*10^23*8*1.3806503*10^(-
23)*T_BulkG)/(pi*MW('H2O')))^ (1/2);
v_gmol('CO2') = ((1000*6.0221415*10^23*8*1.3806503*10^(-
23)*T_BulkG)/(pi*MW('CO2')))^ (1/2);
v_gmol('PZ') = ((1000*6.0221415*10^23*8*1.3806503*10^(-
23)*T_BulkG)/(pi*MW('PZ')))^ (1/2);

#amine solution density in aerosol from Fawkes model (vl2u2.f), Frailie
2011. fn(T,xco2,xpz,ldg)
RHO_Drop =1000*(1.5494 -0.0005728 *T_Drop)*LOG(2.676 *xApp('CO2')-
0.030977 *xApp('PZ')-0.0726176 *LDG_Drop+2.102569 );
#RHO_Drop = 1090;

#CO2 reaction rate constant
k2d = 65700000 *EXP(-34100 /(8.3144621*T_Drop));

```

```

#Henry constant for CO2 in aerosol; assumed to be equal to CO2 in
water, i.e activity coefficient is neglected
Henry_Drop = 17107000 *EXP(-1886.1 /T_Drop)*101325/(100^3);

#Heat capacity of components in aerosol
Cp_Drop('N2') = 0;
Cp_Drop('H2O') = 276370 -2090.1 *T_Drop+8.125 *T_Drop^2-0.014116
*T_Drop^3+9.37E-06 *T_Drop^4;
Cp_Drop('CO2') = 0;
Cp_Drop('PZ')=46690 +431.5*T_Drop+0*T_Drop^2+0*T_Drop^3+0*T_Drop^4;

#Excess heat capacity H2O/CO2 in aerosol
Cp_Ex_Drop = (xApp('PZ')*xApp('CO2')*((-8722.163507 +36.220997
*T_Drop)+(40762.0731 -173.383544 *T_Drop)*(xApp('PZ')-
xApp('CO2')))+xApp('H2O')*xApp('CO2')*((4604.181038 -17.76459089
*T_Drop)+(-5368.404949 +20.37895136 *T_Drop)*(xApp('H2O')-
xApp('CO2'))))*1000;

#Heat capacity of mixture in aerosol
Cplmx =
1/1000*((Cp_Drop('N2')*xApp('N2')+Cp_Drop('H2O')*xApp('H2O')+Cp_Drop('C
O2')*xApp('CO2')+Cp_Drop('PZ')*xApp('PZ'))+Cp_Ex_Drop);#J/mol K
#Cplmx = 84;

#Heat of absorption for all components
delHd('N2') = 0;
delHd('H2O') = (1/1000)*51546000 *(1-T_Drop/647.096)^(0.28402 -0.15843
*(T_Drop/647.096)+0.2375 *(T_Drop/647.096)^2);
delHd('CO2') = (1/1000)*(-R_const)*(-11624.8+28647.04*LDG_Drop^2);
delHd('PZ')= (1/1000)*(-R_const)*(-25.37*T_Drop-16167.3 *LDG_Drop^2);
#delHd('CO2') = (1/1000)*(-R_const)*(-11082 +4713 *LDG_Drop+11722
*LDG_Drop^2);
#delHd('PZ')= (1/1000)*(-R_const)*(-21.6*T_Drop-18027 *LDG_Drop^2);
#delHd('CO2') = 72;
#delHd('PZ')= -39;

#Thermal conductivity of drop
#Thermal_Conductivity_Drop = 0.6;

#Properties of Gas side
#Equilibrium partial pressure over the bulk solvent fn(x, T, vapor
pressure, ldg)
#Surrogate Equilibrium Model regressed from Aspen Plus (eNRTL and
Independence)

ppeq_BulkL('N2')=0;
ppeq_BulkL('H2O')=x_BulkL('H2O')*EXP(27.932+(-5707.66/T_BulkL)+(-7.8E-
6*T_BulkL^2));
ppeq_BulkL('CO2')=EXP(39.549+(-11624.8/T_BulkL)+(-
51.395*LDG_BulkL^2)+(28647.04*LDG_BulkL^2/T_BulkL));
ppeq_BulkL('PZ') =x_BulkL('PZ')*EXP(-
144.017+(25.37*LOG(T_BulkL)))+(16.094*LDG_BulkL)-
(16167.3*LDG_BulkL^2/T_BulkL));

```

```

#Equilibrium partial pressure over the aerosol fn(x, molarvolume,
surface tension, T, vapor pressure, ldg, d_drop)
#Surrogate Equilibrium Model regressed from Aspen Plus (eNRTL and
Independence)

ppeq_Drop_Outlayer('N2')=0;
ppeq_Drop_Outlayer('H2O')=xApp('H2O')*EXP(27.932+(-5707.66/T_Drop)+(-
7.8E-
6*T_Drop^2))*EXP(4*SIGMA(xApp('H2O')*TAUD('H2O')+xApp('CO2')*TAUD('CO2'
)+xApp('PZ')*TAUD('PZ'))*Vmold('H2O')/(1.38065E-23 *T_Drop*d_drop*1E-
6));
ppeq_Drop_Outlayer('CO2')=EXP(39.549+(-11624.8/T_Drop)+(-
51.395*LDG_Drop^2)+(28647.04*LDG_Drop^2/T_Drop))*EXP(4*SIGMA(xApp('H2O'
)*TAUD('H2O')+xApp('CO2')*TAUD('CO2')+xApp('PZ')*TAUD('PZ'))*Vmold('CO2
')/(1.38065E-23 *T_Drop*d_drop*1E-6));
ppeq_Drop_Outlayer('PZ')=xApp('PZ')*EXP(-
144.017+(25.37*LOG(T_Drop))+(16.094*LDG_Drop) -
(16167.3*LDG_Drop^2/T_Drop))*EXP(4*SIGMA(xApp('H2O')*TAUD('H2O')+xApp('
CO2')*TAUD('CO2')+xApp('PZ')*TAUD('PZ'))*Vmold('PZ')/(1.38065E-23
*T_Drop*d_drop*1E-6));

#Empirical/Experimental data from Xu (PZ and CO2) and Raoult (H2O)
#ppeq_Drop_Outlayer('H2O')=xApp('H2O')/(xApp('PZ')+xApp('H2O'))*EXP(73.
649+(-7258.2/T_Drop)+(-7.3037*LOG(T_Drop)))+(4.17E-
6*T_Drop^2))*EXP(4*SIGMA(xApp('H2O')*TAUD('H2O')+xApp('CO2')*TAUD('CO2'
)+xApp('PZ')*TAUD('PZ'))*Vmold('H2O')/(1.38065E-23 *T_Drop*d_drop*1E-
6));
#ppeq_Drop_Outlayer('CO2')=EXP(35.5+(-11082/T_Drop)+(-
22.5*LDG_Drop^2)+(4713*LDG_Drop/T_Drop)+(11722*LDG_Drop^2/T_Drop))*EXP(
4*SIGMA(xApp('H2O')*TAUD('H2O')+xApp('CO2')*TAUD('CO2')+xApp('PZ')*TAUD
('PZ'))*Vmold('CO2')/(1.38065E-23 *T_Drop*d_drop*1E-6));
#ppeq_Drop_Outlayer('PZ') =xApp('PZ')/(xApp('H2O')+xApp('PZ'))*EXP(-
123+(21.6*LOG(T_Drop))+(19.9*LDG_Drop) -
(18027*LDG_Drop^2/T_Drop))*EXP(4*SIGMA(xApp('H2O')*TAUD('H2O')+xApp('CO
2')*TAUD('CO2')+xApp('PZ')*TAUD('PZ'))*Vmold('PZ')/(1.38065E-23
*T_Drop*d_drop*1E-6));

#Equilibrium partial pressure over the aerosol fn(x, molarvolume,
surface tension, T, vapor pressure, ldg, d_drop)
#Empirical/Experimental data from Xu (PZ and CO2) and Raoult (H2O)
#ppeq_BulkL('H2O')=x_BulkL('H2O')/(x_BulkL('PZ')+x_BulkL('H2O'))*EXP(73
.649+(-7258.2/T_BulkL)+(-7.3037*LOG(T_BulkL)))+(4.17E-6*T_BulkL^2));
#ppeq_BulkL('CO2')=EXP(35.5+(-11082/T_BulkL)+(-
22.5*LDG_BulkL^2)+(4713*LDG_BulkL/T_BulkL)+(11722*LDG_BulkL^2/T_BulkL)
);
#ppeq_BulkL('PZ') =x_BulkL('PZ')/(x_BulkL('H2O')+x_BulkL('PZ'))*EXP(-
123+(21.6*LOG(T_BulkL))+(19.9*LDG_BulkL)-(18027*LDG_BulkL^2/T_BulkL));

```

A.3 PROCESS FLOWSHEET

UNIT

Flowsheet AS Process_Flowsheet

SET

```
# Start Unit Specifications
  WITHIN Flowsheet DO
    WITHIN Aerosol001 DO
      Aspen_Profile := "C:\Users\akinp\Box Sync\Research\Aerosol
Modeling\PZ\Case Study 1\gPROMS Runs\Case 4\Profiles to
gPROMS_Absorber.xls" ;
      Column_Stages := 60 ; # 60
      Comps := ["N2", "H2O", "CO2", "PZ"] ;
      D_col := 0.6604 ; # 0.6604 m
      H_col := 3.048*4 ; # 3.048*4
      initial_Diameter_Drop := 0.1 ; # 0.1 um
      Layers := 5 ; # 5
      Num_Drop := 1E7 ; # 1E7 #/cm3
      vfrac := 0.98 ; # 0.98 m3/m3
    END # WITHIN Aerosol001
  END # WITHIN Flowsheet
# End Unit Specifications
```

INITIALISATION_PROCEDURE

```
# Start Default Initialisation Procedure
  USE
      : DEFAULT;
  END
  SAVE "Process_Flowsheet_InitialGuess";
# End Default Initialisation Procedure
```

SOLUTIONPARAMETERS

```
ReportingInterval := 1.0E-2
DASolver := "DASOLV" [
    "AbsoluteTolerance" := 1.0E-3
]
```

SCHEDULE

```
SEQUENCE
  CONTINUE FOR 1
  SAVE "Initial"
  MESSAGE "DONE!!!"
END
```

Appendix B: Codes for Aerosol Transport Model of Solvent Blends in gPROMS® ModelBuilder

This work presents an aerosol transport model for solvent blends developed and applied to model two proprietary solvents: aqueous blend (AB) and non-aqueous blend (NAB). Fundamental physical properties of the solvent systems have been retracted to maintain proprietary.

B.1 AEROSOL INTEGRATION

```
# Aerosol Transport Model for Solvent Blend
# Absorber
# Aerosol Integration
# Last Revised by: Korede Akinpelumi
# Date Modified: 2/15/2021

PARAMETER
Column_Stages AS INTEGER DEFAULT 30 # No of computational stages used
in Aspen run
Stages AS INTEGER DEFAULT 100
Layers AS INTEGER DEFAULT 3
Aspen_Profile AS FOREIGN_OBJECT "ExcelFO" #Gas profile from Aspen
Comps AS ORDERED_SET DEFAULT ["N2", "H2O", "CO2", "AM1", "AM2"] #Components
in gas/liquid/aerosol
Comp AS ORDERED_SET DEFAULT ["N2", "H2O", "CO2", "SolventBlend"] #Solvent
blend as SolventBlend (AM1+AM2)
#Const
pi AS REAL DEFAULT 3.14159265359
g AS REAL DEFAULT 9.80665 # [m/s^2]
R_const AS REAL DEFAULT 8.3144621 #m3·Pa·K-1·mol-1
#Column Parameters
H_col AS REAL DEFAULT 1.74625 #m, Column height
D_col AS REAL DEFAULT 0.0427228 #m, Column diameter
vfrac AS REAL DEFAULT 0.96 # Void fraction of the packing from Aspen
initial_Diameter_Drop AS REAL DEFAULT 2.3 #um
Num_Drop AS REAL DEFAULT 1e6 # Num/cm3
MW AS ARRAY(Comps) OF REAL #Component molecular weight
initial_LDG_Drop AS REAL DEFAULT 0.4 #molCO2/mol alkalinity
initial_xApp AS ARRAY(COMPS) OF REAL #mol/mol
initial_MW AS REAL #g/mol
initial_Rho AS REAL #kg/m3
initial_Conc_tot AS REAL #mol/m3
initial_Vol_drop AS REAL #m3
initial_T_Drop AS REAL DEFAULT 313 # K

UNIT
Phy_Props AS Phy_Props
```

VARIABLE

```
# Parameters of Column
T_BulkG AS temperature
T_BulkL AS temperature
#y_BulkG AS ARRAY(Comps) OF molar_fraction
pp_BulkG AS ARRAY(Comps) OF pressure
#MW_BulkG AS molecular_weight
RHO_BulkG AS mass_density
K_BulkG AS thermo_conductivity
#CP_BulkG AS molar_specific_heat_capacity
MU_BulkG AS dynamic_viscosity
Diff_BulkG AS ARRAY(Comps) OF diffusion_coefficient
VOLFL_BulkG AS volume_flowrate
#FN2_BulkG AS molar_flowrate
#FH2O_BulkG AS molar_flowrate
#FCO2_BulkG AS molar_flowrate
#FPZ_BulkG AS molar_flowrate
Kg_Bulk AS ARRAY(Comps) OF mass_transfer_coefficient
IA_Bulk AS specific_surface_area
x_BulkL AS ARRAY(Comps) OF molar_fraction
#C_BulkL AS ARRAY(Comp) OF molar_concentration
LDG_BulkL AS loading
HOLDUP_BulkL AS no_type

#Parameters of Gas Side
#Conc_BulkG AS ARRAY(Comps) OF molar_concentration
ppeq_BulkL AS ARRAY(Comps) OF pressure # Equilibrium pressure of each
component over bulk liquid
N_gl AS ARRAY(Comps) OF no_type #Flux of each component

#Parameters of Aerosol Side
T_Drop AS temperature #Drop temperature, K
n AS ARRAY(Comps) OF nanomoles # mole of component in drop, nano mole
n_tot AS nanomoles# mole of drop, nano mole
Conc_Drop AS ARRAY(Comps) OF molar_concentration # concentration of
drop, mole/m3
#Conc_Drop_Free AS ARRAY(Comps) OF molar_concentration # concentration
of drop, mole/m3
Conc_tot_Drop AS molar_concentration # concentration of drop, mole/m3
Rds AS Radius_Drop # Radius of drop, um
#Diff_Drop_CO2 AS diffusion_coefficient # diffusion coefficient of
drop, m2/s
Ngd AS ARRAY(Comps) OF no_type #mass transfer flux between gas and
drop, mol/m2-s
v_Drop AS velocity #velocity of drop, m/s
v_BulkG AS velocity #velocity of gas, m/s

#If want to consider relative velocity between aerosols and gas flow,
turn on the following equations##

##turn on the following equations##
#v_Rel AS no_type # related velocity, m/s
```

```

d_drop AS Radius_Drop # diameter of drop, um
RHO_Drop AS mass_density #density of drop, kg/m3
##turn on the following equations##
#Cc AS no_type
##turn on the following equations##
#avgKn AS no_type
Kn AS ARRAY(Comps) OF no_type
##turn on the following equations##
#avgmfp AS no_type
mfp AS ARRAY(Comps) OF no_type #mean free path
LDG_Drop AS loading #CO2 loading in drop, mol CO2/mol alk.
Cplmx AS molar_specific_heat_capacity #heat capacity, J/mol-K
xApp AS ARRAY(Comps) OF molar_fraction #mole/mole, apparent mole
fractions in drop, Accounts for speciation.
Qd AS heat_flux #heat transfer flux, J/m2-s
delHd AS ARRAY(Comps) OF molar_specific_enthalpy #heat of vaporation
and absorpction, J/mol
hg AS heat_transfer_coefficient #heat transfer coeff.
kg AS ARRAY(Comps) OF mass_transfer_coefficient #mass transfer coeff.
kgprime_Drop AS mass_transfer_coefficient #mass transfer coeff.
A_Drop AS area_Drop
agd AS specific_surface_area #specific surface area of aerosol
Vol_Drop AS volume
Fuchs AS ARRAY(Comps) OF no_type
ppeq_Drop_Outlayer AS ARRAY(Comps) OF pressure
#k2d AS no_type
#Henry_Drop AS no_type
Nu AS Dimentionless
##turn on the following equations##
#Re AS Dimentionless
#Pr AS Dimentionless
#Sc AS ARRAY(Comps) OF Dimentionless
Sh AS ARRAY(Comps) OF Dimentionless
v_gmol AS ARRAY(Comps) OF no_type
molal_SolventBlend_Drop AS molal_concentration
h AS length
#Thermal_Conductivity_Drop AS thermo_conductivity
MW_Drop AS molecular_weight

```

SELECTOR

```

MT_Mode AS (DefaultMode,InitializationMode) DEFAULT DefaultMode
kgprime_Mode AS (DefaultMode,InitializationMode) DEFAULT DefaultMode

```

SET

```

Phy_Props.Stages := Stages;
Phy_Props.Layers := Layers;
Phy_Props.Comps := Comps;
Phy_Props.Comp := Comp;
MW := [28.0134, 18.01528, 44.0095, ###, ###]; #g/gmol, (N2, H2O, CO2,
AM1, AM2)
initial_xApp('N2') := 0; # No N2 in drop
initial_xApp('H2O') := Aspen_Profile.xH2O(0); #initial drop
concentration assumed equal to rich solvent conc

```

```

initial_xApp('CO2') := Aspen_Profile.xCO2(0); #initial drop
concentration assumed equal to rich solvent conc
initial_xApp('AM1') := Aspen_Profile.xAM1(0); #initial drop
concentration assumed equal to rich solvent conc
initial_xApp('AM2') := Aspen_Profile.xAM2(0); #initial drop
concentration assumed equal to rich solvent conc

initial_LDG_Drop := Aspen_Profile.LDG(0);
initial_T_Drop := Aspen_Profile.TG(0);
initial_MW :=
initial_xApp('H2O')*MW('H2O')+initial_xApp('CO2')*MW('CO2')+initial_xAp
p('AM1')*MW('AM1')+initial_xApp('AM2')*MW('AM2');#g/gmol
initial_Rho := ###; #kg/m3, From Pilot H&M Case 1. Average of Lean and
Rich solvent density. Assumption instead of regressing as a
fn(T,xco2,xAM1,xAM2,ldg)
initial_Conc_tot := initial_Rho/(initial_MW/1000);#mol/m^3
initial_Vol_drop := 1/6*pi*initial_Diameter_Drop^3; #um^3

```

EQUATION

```

# Model equations
#-----
#-----
#-----
#GAS Profiles extracted from ASPEN via VBA script
#-----
#-----
#-----
T_BulkG = Aspen_Profile.TG(h);
#y_BulkG('N2') = Aspen_Profile.yN2(h);
#y_BulkG('H2O') = Aspen_Profile.yH2O(h);
#y_BulkG('CO2') = Aspen_Profile.yCO2(h);
#y_BulkG('SolventBlend') = Aspen_Profile.ySolventBlend(h);
pp_BulkG('N2') = Aspen_Profile.ppN2(h);
pp_BulkG('H2O') = Aspen_Profile.ppH2O(h);
pp_BulkG('CO2') = Aspen_Profile.ppCO2(h);
#pp_BulkG('AM1') = Aspen_Profile.ppAM1(h);
#pp_BulkG('AM2') = Aspen_Profile.ppAM2(h);
#MW_BulkG = Aspen_Profile.MW(h);
RHO_BulkG = Aspen_Profile.RHOG(h); #Not currently used. Only useful for
v_Rel and Re/Sc
K_BulkG = Aspen_Profile.K(h);
#CP_BulkG = Aspen_Profile.CPG(h);
MU_BulkG = Aspen_Profile.MUG(h); #Not currently used. Only useful for
Sh/Re/Sc
Diff_BulkG('N2') = Aspen_Profile.DGN2(h); #Not Used
Diff_BulkG('H2O') = Aspen_Profile.DGH2O(h);
Diff_BulkG('CO2') = Aspen_Profile.DGCO2(h); #Not used
Diff_BulkG('AM1') = Aspen_Profile.DGAM1(h);
Diff_BulkG('AM2') = Aspen_Profile.DGAM2(h);
VOLFL_BulkG = Aspen_Profile.VOLFLG(h);
#FN2_BulkG = Aspen_Profile.FGN2(h);
#FH2O_BulkG = Aspen_Profile.FGH2O(h);
#FCO2_BulkG = Aspen_Profile.FGCO2(h);

```

```

#FSolventBlend_BulkG = Aspen_Profile.FGSolventBlend(h);
Kg_Bulk('N2') = Aspen_Profile.KGN2(h); #Not used at all
Kg_Bulk('H2O') = Aspen_Profile.KGH2O(h); #Not used at all
Kg_Bulk('CO2') = Aspen_Profile.KGCO2(h); #Not used at all
Kg_Bulk('AM1') = Aspen_Profile.KGAM1(h);
Kg_Bulk('AM2') = Aspen_Profile.KGAM2(h);
IA_Bulk = Aspen_Profile.IAVF(h); #m2/m3
#IA_Bulk = Aspen_Profile.IA(h)/(pi*D_col^2/4*H_col/Column_Stages);
x_BulkL('N2') = Aspen_Profile.xN2(h);
x_BulkL('H2O') = Aspen_Profile.xH2O(h); #not used
x_BulkL('CO2') = Aspen_Profile.xCO2(h); #not used
x_BulkL('AM1') = Aspen_Profile.xAM1(h);
x_BulkL('AM2') = Aspen_Profile.xAM2(h);
#C_BulkL('N2') = Aspen_Profile.CLN2P(h); #Not used at all
#C_BulkL('H2O') = Aspen_Profile.CLH2OP(h); #Not used at all
#C_BulkL('CO2') = Aspen_Profile.CLCO2P(h); #Not used at all
#C_BulkL('SolventBlend') = Aspen_Profile.CLSolventBlendP(h); #Not used
at all
LDG_BulkL = Aspen_Profile.LDG(h);
T_BulkL = Aspen_Profile.TL(h);
HOLDUP_BulkL = Aspen_Profile.HOLDUPLVF(h);
#HOLDUP_BulkL =
Aspen_Profile.HOLDUPL(h)/(pi*D_col^2/4*H_col/Column_Stages); # Fraction
of free volume occupied by liquid (Total volume - Packing volume)
#-----
-----
#Physical Properties (input parameters from/to Phy_Props model)
#-----
-----
Phy_Props.T_BulkG = T_BulkG;
Phy_Props.T_BulkL = T_BulkL;
Phy_Props.T_Drop = T_Drop;
Phy_Props.xApp = xApp;
Phy_Props.x_BulkL = x_BulkL;
Phy_Props.LDG_Drop = LDG_Drop;
Phy_Props.LDG_BulkL = LDG_BulkL;
Phy_Props.d_drop = d_drop;

#Properties of Aerosol side
#Diff_Drop_CO2 = Phy_Props.Diff_Drop_CO2;

Cplmx = Phy_Props.Cplmx;

delHd('N2') = Phy_Props.delHd('N2');
delHd('H2O') = Phy_Props.delHd('H2O');
delHd('CO2') = Phy_Props.delHd('CO2');
delHd('AM1') = Phy_Props.delHd('AM1');
delHd('AM2') = Phy_Props.delHd('AM2');

#Thermal_Conductivity_Drop = Phy_Props.Thermal_Conductivity_Drop;

```

```

ppeq_Drop_Outlayer = Phy_Props.ppeq_Drop_Outlayer;

v_gmol = Phy_Props.v_gmol; #velocity in kinetic mass transfer regime
RHO_Drop = Phy_Props.RHO_Drop;
#k2d = Phy_Props.k2d;
#Henry_Drop = Phy_Props.Henry_Drop;
MW_Drop =
xApp('H2O')*MW('H2O')+xApp('CO2')*MW('CO2')+xApp('AM1')*MW('AM1')+xApp(
'AM2')*MW('AM2');

#-----
#-----
#-----
#Algebraic Equations of Aerosol Side
#-----
#-----

# CO2 Loading in aerosol drop
#LDG_Drop = 0.3;
If (xApp('AM1')+xApp('AM2'))>0 Then
LDG_Drop = xApp('CO2')/(xApp('AM1')+3*xApp('AM2'));
Else
LDG_Drop=0;
End
# SolventBlend molality in aerosol drop
molal_SolventBlend_Drop =
(1000/MW('H2O'))*(xApp('AM1')+xApp('AM2'))/xApp('H2O');

#Calc. Kn
mfp = 3*Diff_BulkG/(v_gmol);
##turn on the following equations##
#avgmfp = sigma(mfp)/Comps.Card;
d_drop = 2*Rds;
Kn = (2*mfp/(d_drop*(1E-6)));
##turn on the following equations##
#avgKn = (2*avgmfp/(d_drop*(1E-6)));
##turn on the following equations##
#Calc. Cc
#Cc = 1+avgKn*(1.246+0.418*exp(-0.867/avgKn));#Cunningham slip used to
correct Stokes' Law.
#Calc. Fuchs(i)
Fuchs = (0.75*1*(1+Kn))/(Kn^2+Kn+0.283*Kn*1+0.75*1);#alpha = 1;

# Calc. v_Drop
v_BulkG = 4*VOLFL_BulkG/((vfrac-HOLDUP_BulkL)*pi*(D_col^2));
##turn on the following equations##
#v_Rel = (d_drop*(1E-6))^2*(RHO_DropMix-RHO_BulkG)*g*Cc/(18*MU_BulkG);
v_Drop= v_BulkG;
##change the following equations##
#v_Drop= v_BulkG -v_Rel;

#Calc. Dimensionless Numbers
##turn on the following equations##

```

```

#Sc = MU_BulkG/RHO_BulkG/Diff_BulkG;
#Pr = (MU_BulkG*CP_BulkG)/(K_BulkG*MW_BulkG);
#Re = ABS(RHO_BulkG*v_Rel*d_drop*(1E-6)/MU_BulkG);
Sh = 2;#2+0.6*(Re^(1/2))*(Sc^(1/3));
Nu = 2;#2+0.6*(Re^(1/2))*(Pr^(1/3));

#Calc. kg
kg = Sh*Diff_BulkG/(d_drop*(1E-6));
#Calc. kgprime
kgprime_Drop = ###;
#If (Conc_Drop_Free('AM2'))>0 Then
#kgprime_Drop = (k2d*(Conc_Drop_Free('AM2'))
*Diff_Drop_CO2)^(1/2)/Henry_Drop;
#Else
#kgprime_Drop = 0;
#End
#Calc. hg
hg = Nu*K_BulkG/(d_drop*(1E-6));
#Calc. Ngd
Ngd('N2') = 0;
Ngd('H2O') = Fuchs('H2O')*kg('H2O')/(R_const*T_BulkG)*(pp_BulkG('H2O')-
ppeq_Drop_Outlayer('H2O'));
Ngd('CO2') = kgprime_Drop*(pp_BulkG('CO2')-ppeq_Drop_Outlayer('CO2'));
Ngd('AM1') = Fuchs('AM1')*kg('AM1')/(R_const*T_BulkG)*(pp_BulkG('AM1')-
ppeq_Drop_Outlayer('AM1'));
Ngd('AM2') = Fuchs('AM2')*kg('AM2')/(R_const*T_BulkG)*(pp_BulkG('AM2')-
ppeq_Drop_Outlayer('AM2'));
#Calc. Qd
Qd = (Ngd('H2O')*delHd('H2O')-Ngd('AM1')*delHd('AM1')-
Ngd('AM2')*delHd('AM2')+Ngd('CO2')*delHd('CO2'))+hg*(T_BulkG-T_Drop);

#Total number of moles of all components in drop
n_tot = SIGMA(n);
#Mole fraction of each component in drop
xApp = n/n_tot;
#Total concentration of all components in drop
Conc_tot_Drop = RHO_Drop/(MW_Drop/1000);
#Concentration of each component in drop
Conc_Drop = xApp*Conc_tot_Drop;

#Conc_Drop_Free('N2') = 0;
#Conc_Drop_Free('H2O') = Conc_Drop('H2O');
#Conc_Drop_Free('CO2') = 0;
#Conc_Drop_Free('AM1') = Conc_Drop('AM1');
#Conc_Drop_Free('AM2') = Conc_Drop('AM2');

#Aerosol size calculations
#Aerosol volume and diameter calculation
Vol_Drop = 4/3*pi*Rds^3 = (n_tot*(1E-9)/Conc_tot_Drop)*(1E6)^3; #um^3
#Area of aerosol drop
A_Drop = 4*pi*Rds^2; #um^2
#Specific surface area of aerosol drop
agd = 4*pi*Rds^2/(4/3*pi*Rds^3)*(1E-6)^2/(1E-6)^3;

```

```

#-----
#-----
#Differential Equations of Aerosol Side
#-----
#-----

#Calculation for number of moles of each component in aerosol drop
n('N2') = 0;
For i in ['H2O', 'CO2', 'AM1', 'AM2'] Do
    v_Drop/H_col*$n(i)*(1E-9) = Ngd(i)*A_Drop*(1E-6)^2;
End
v_Drop/H_col*$T_Drop ==
v_Drop/H_col*T_Drop/n_tot*SIGMA($n('H2O':'AM2'))+Qd*A_Drop*(1E-
6)^2/(Cplmx*n_tot*(1E-9));

#Properties of Gas side
ppeq_BulkL=Phy_Props.ppeq_BulkL;
#Algebraic Equations of Gas Side
N_gl('N2') = 0;
N_gl('H2O') = 0;
N_gl('CO2') = 0;
N_gl('AM1') = Kg_Bulk('AM1')*(pp_BulkG('AM1')-ppeq_BulkL('AM1'));
N_gl('AM2') = Kg_Bulk('AM2')*(pp_BulkG('AM2')-ppeq_BulkL('AM2'));

#Differential Equations of Gas Side
v_Drop/H_col*$pp_BulkG('AM1') = (-Ngd('AM1')*A_Drop*(1E-
6)^2*Num_Drop*(1E2)^3-N_gl('AM1')*IA_Bulk)*R_const*T_BulkG;
v_Drop/H_col*$pp_BulkG('AM2') = (-Ngd('AM2')*A_Drop*(1E-
6)^2*Num_Drop*(1E2)^3-N_gl('AM2')*IA_Bulk)*R_const*T_BulkG;

ASSIGN
h := TIME;

INITIAL
#STEADY_STATE
T_Drop = initial_T_Drop;
n('CO2')*(1E-9)= initial_xApp('CO2')*
initial_Conc_tot*initial_Vol_drop*(1E-6)^3;
n('H2O')*(1E-9)= initial_xApp('H2O')*
initial_Conc_tot*initial_Vol_drop*(1E-6)^3;
n('AM1')*(1E-9)= initial_xApp('AM1')*
initial_Conc_tot*initial_Vol_drop*(1E-6)^3;
n('AM2')*(1E-9)= initial_xApp('AM2')*
initial_Conc_tot*initial_Vol_drop*(1E-6)^3;

pp_BulkG('AM1') = Aspen_Profile.ppAM1(0);
pp_BulkG('AM2') = Aspen_Profile.ppAM2(0);

```

B.2 PHYSICAL PROPERTIES MODEL

```
# Aerosol Transport Model for SolventBlend Solvent
# Absorber
# Physical Properties
# Last Revised by: Korede Akinpelumi
# Date Modified: 2/15/2021

PARAMETER
Stages AS INTEGER
Layers AS INTEGER
Comps AS ORDERED_SET DEFAULT ["N2", "H2O", "CO2", "AM1", "AM2"]
Comp AS ORDERED_SET DEFAULT ["N2", "H2O", "CO2", "SolventBlend"]
pi AS REAL DEFAULT 3.14159265359
R_const AS REAL DEFAULT 8.3144621 #m3·Pa·K-1·mol-1
MW AS ARRAY(Comps) OF REAL

DISTRIBUTION_DOMAIN
#Height AS [ 0 : 1 ]
Radius AS [ 0 : 1 ]

VARIABLE
T_Drop AS temperature #Aerosol temperature
T_BulkG AS temperature #Bulk gas temperature
T_BulkL AS temperature #Bulk solvent temperature
LDG_Drop AS loading #CO2 loading in aerosol
LDG_BulkL AS loading #CO2 loading in bulk solvent
xApp AS ARRAY(Comps) OF molar_fraction #mole/mole, apparent mole
fractions in drop, Accounts for speciation.
xwApp AS ARRAY(Comps) OF mass_fraction #mass fraction of components in
aerosol
x_BulkL AS ARRAY(Comps) OF molar_fraction #mole fraction of components
in bulk solvent
d_drop AS Radius_Drop #drop diameter

ppeq_BulkL AS ARRAY(Comps) OF pressure #Equilibrium pressure of each
component over bulk solvent
#Diff_Drop_CO2 AS diffusion_coefficient
ppeq_Drop_Outlayer AS ARRAY(Comps) OF pressure #Equilibrium pressure of
each component over aerosol
v_gmol AS ARRAY(Comps) OF no_type
RHO_Drop AS mass_density
#k2d AS no_type #CO2 reaction rate constant for calculating kg'
#Henry_Drop AS no_type #Henry constant for CO2 in drop
#MUDH2O AS dynamic_viscosity #viscosity of pure water in aerosol
#MUDMIX AS dynamic_viscosity # viscosity of amine solution in aerosol
Vmold AS ARRAY(Comps) OF no_type #molar volume
TAUD AS ARRAY(Comps) OF no_type #Surface tension
#Cp_Drop AS ARRAY (Comp) OF molar_specific_heat_capacity
#Cp_Ex_Drop AS molar_specific_heat_capacity
Cplmx AS molar_specific_heat_capacity
delHd AS ARRAY(Comps) OF molar_specific_enthalpy
#Thermal_Conductivity_Drop AS thermo_conductivity
```

```

SET
#Height := [BFDM,Stages];
Radius := [OCFEM,2,Layers];
MW := [28.0134, 18.01528, 44.0095, ###, ###]; #g/gmol, (N2, H2O, CO2,
AM1, AM2)

EQUATION
#Model equations; Properties of Aerosol side

#convert molefraction of each component in aerosol to mass fraction;
molefraction not yet calculated
xwApp('N2') = MW('N2')*xApp('N2')/(MW('N2')
*xApp('N2')+MW('H2O')*xApp('H2O')+MW('CO2')*xApp('CO2')+MW('AM1')*xApp(
'AM1')+MW('AM2')*xApp('AM2'));
xwApp('H2O') = MW('H2O')*xApp('H2O')/(MW('N2')
*xApp('N2')+MW('H2O')*xApp('H2O')+MW('CO2')*xApp('CO2')+MW('AM1')*xApp(
'AM1')+MW('AM2')*xApp('AM2'));
xwApp('CO2') = MW('CO2')*xApp('CO2')/(MW('N2')
*xApp('N2')+MW('H2O')*xApp('H2O')+MW('CO2')*xApp('CO2')+MW('AM1')*xApp(
'AM1')+MW('AM2')*xApp('AM2'));
xwApp('AM1') = MW('AM1')*xApp('AM1')/(MW('N2')
*xApp('N2')+MW('H2O')*xApp('H2O')+MW('CO2')*xApp('CO2')+MW('AM1')*xApp(
'AM1')+MW('AM2')*xApp('AM2'));
xwApp('AM2') = MW('AM2')*xApp('AM2')/(MW('N2')
*xApp('N2')+MW('H2O')*xApp('H2O')+MW('CO2')*xApp('CO2')+MW('AM1')*xApp(
'AM1')+MW('AM2')*xApp('AM2'));

#viscosity of pure water in aerosol; from DIPPR 101
#MUDH2O = EXP(-52.843+(3703.6 /T_Drop)+5.866 *LOG(T_Drop)-5.88E-29
*T_Drop^10);
# viscosity of amine solution in aerosol
#MUDMIX = ###; #Pa.s, From Pilot H&M Case 1. Average of Lean and Rich
solvent viscosity. Assumption instead of regressing as a
fn(T,xco2,xAM1,xAM2,ldg)

#Diffusion coefficient of CO2 in amine solution; = (Diffusion
coefficient of CO2 in pure water * ratio of pure water viscosity to
amine solvent viscosity)
#Diff_Drop_CO2 = (1/100^2)*0.024*EXP(-
2122/T_Drop)*(MUDH2O/MUDMIX)^0.72; #m2/s

#molecular volume
Vmold('N2') = 0;
Vmold('H2O') = (1/(6.0221415*10^23*1000))*(-13.851 +0.64038 *T_Drop-
0.0019124 *T_Drop^2+1.82E-06 *T_Drop^3)^(-1);#from DIPPR Equation #105
Vmold('CO2') = (1/(6.0221415*10^23*1000))*(2.768 /0.26212 ^ (1+(1-
(304.21/304.21 ) )^0.2908 ) )^(-1);#from DIPPR Equation #105
Vmold('AM1') = ###; #from DIPPR Equation #105
Vmold('AM2') = ###; #from DIPPR Equation #105

#Surface tension for Water and PZ in amine solution
TAUD('N2') = 0;

```

```

TAUD('H2O') = 0.17766 * (1-T_Drop/647.096 )^(2.567 -3.3377
*T_Drop/647.096 +1.9699 *(T_Drop/647.096 )^2); #from DIPPR Equation 106
TAUD('CO2') = 0;
TAUD('AM1') = ###; #from DIPPR Equation 106 #N/m
TAUD('AM2') = ###; #from DIPPR Equation 106 #N/m

#velocity for kinetic theory assumption of mass transfer
v_gmol('N2') = ((1000*6.0221415*10^23*8*1.3806503*10^(-
23)*T_BulkG)/(pi*MW('N2')))^ (1/2);
v_gmol('H2O') = ((1000*6.0221415*10^23*8*1.3806503*10^(-
23)*T_BulkG)/(pi*MW('H2O')))^ (1/2);
v_gmol('CO2') = ((1000*6.0221415*10^23*8*1.3806503*10^(-
23)*T_BulkG)/(pi*MW('CO2')))^ (1/2);
v_gmol('AM1') = ((1000*6.0221415*10^23*8*1.3806503*10^(-
23)*T_BulkG)/(pi*MW('AM1')))^ (1/2);
v_gmol('AM2') = ((1000*6.0221415*10^23*8*1.3806503*10^(-
23)*T_BulkG)/(pi*MW('AM2')))^ (1/2);

#amine solution density in aerosol
RHO_Drop = ###; #kg/m3, From Pilot H&M Case 1. Average of Lean and Rich
solvent density. Assumption instead of regressing as a
fn(T,xco2,xAM1,xAM2,ldg)

#CO2 reaction rate constant
#k2d = ###; #average of AM1-CO2 and AM2-CO2

#Henry constant for CO2 in aerosol; assumed to be equal to CO2 in
water, i.e activity coefficient is neglected
#Henry_Drop = 17107000 *EXP(-1886.1 /T_Drop)*101325/(100^3);

#Heat capacity of components in aerosol
#Cp_Drop('N2') = 0;
#Cp_Drop('H2O') = 276370 -2090.1 *T_Drop+8.125 *T_Drop^2-0.014116
*T_Drop^3+9.37E-06 *T_Drop^4;
#Cp_Drop('CO2') = 0;
#Cp_Drop('SolventBlend')= ###; #J/molK Avg heat capacity of rich and
lean SolventBlend solvent from H&M Case 1

#Excess heat capacity H2O/CO2 in aerosol
#Cp_Ex_Drop = ((xApp('AM1')+xApp('AM2'))*xApp('CO2'))*((-8722.163507
+36.220997 *T_Drop)+(40762.0731 -173.383544
*T_Drop)*((xApp('AM1')+xApp('AM2'))-
xApp('CO2')))+xApp('H2O')*xApp('CO2'))*((4604.181038 -17.76459089
*T_Drop)+(-5368.404949 +20.37895136 *T_Drop)*(xApp('H2O')-
xApp('CO2'))))*1000;

#Heat capacity of mixture in aerosol
#Cplmx =
1/1000*((Cp_Drop('N2')*xApp('N2')+Cp_Drop('H2O')*xApp('H2O')+Cp_Drop('C
O2')*xApp('CO2')+Cp_Drop('SolventBlend')*(xApp('AM1')+xApp('AM2')))+Cp_
Ex_Drop);#J/mol K

```

```

Cplmx = ###; #J/molK Avg heat capacity of rich and lean SolventBlend
solvent from H&M Case 1

#Heat of absorption for all components
delHd('N2') = 0;
delHd('H2O') = (1/1000)*51546000 *(1-T_Drop/647.096)^(0.28402 -0.15843
*(T_Drop/647.096)+0.2375 *(T_Drop/647.096)^2);
delHd('CO2') = (1/1000)*(-R_const)*(-9874.78+5116.083*LDG_Drop);
delHd('AM1')= (1/1000)*(-R_const)*(-7145.61-2388.98*LDG_Drop^2);
delHd('AM2')= (1/1000)*(-R_const)*(-7694.32-3771.54*LDG_Drop);
#delHd('CO2') = 64;
#delHd('AM1') = ###;
#delHd('AM2') = ###;

#Thermal conductivity of drop
#Thermal_Conductivity_Drop = 0.6;

#Properties of Gas side
#Equilibrium partial pressure over the bulk solvent fn(x, T, vapor
pressure, ldg)
ppeq_BulkL('N2')=0;
ppeq_BulkL('H2O')=x_BulkL('H2O')*EXP(27.75+(-5673.24/T_BulkL)+(-7.3E-
6*T_BulkL^2));
ppeq_BulkL('CO2')=EXP(31.657+(-
9874.78/T_BulkL)+(5116.083*LDG_BulkL/T_BulkL)+(13.567*(x_BulkL('AM1')+(
3*x_BulkL('AM2')))+(1.263*x_BulkL('AM2')/(x_BulkL('AM1')+(3*x_BulkL('A
M2'))))););
ppeq_BulkL('AM1')=x_BulkL('AM1')*EXP(28.786+(-7145.61/T_BulkL)+(-
2388.98*LDG_BulkL^2/T_BulkL)+(1.354*(x_BulkL('AM1')+(3*x_BulkL('AM2'))
)+(-1.755*x_BulkL('AM2')/(x_BulkL('AM1')+(3*x_BulkL('AM2'))))););
ppeq_BulkL('AM2')=x_BulkL('AM2')*EXP(26.2+(-7694.32/T_BulkL)+(-
3771.54*LDG_BulkL/T_BulkL)+(-
13.345*(x_BulkL('AM1')+(3*x_BulkL('AM2')))+(0.723*x_BulkL('AM2')/(x_Bu
lkL('AM1')+(3*x_BulkL('AM2'))))););

#Equilibrium partial pressure over the aerosol fn(x, molarvolume,
surface tension, T, vapor pressure, ldg, d_drop)
ppeq_Drop_Outlayer('N2')=0;
ppeq_Drop_Outlayer('H2O')=xApp('H2O')*EXP(27.75+(-5673.24/T_Drop)+(-
7.3E-
6*T_Drop^2))*EXP(4*SIGMA(xApp('H2O')*TAUD('H2O')+xApp('CO2')*TAUD('CO2'
)+xApp('AM1')*TAUD('AM1')+xApp('AM2')*TAUD('AM2'))*Vmold('H2O')/(1.3806
5E-23 *T_Drop*d_drop*1E-6));
ppeq_Drop_Outlayer('CO2')=EXP(31.657+(-
9874.78/T_Drop)+(5116.083*LDG_Drop/T_Drop)+(13.567*(xApp('AM1')+(3*xApp
('AM2')))+(1.263*xApp('AM2')/(xApp('AM1')+(3*xApp('AM2'))))) *EXP(4*SIG
MA(xApp('H2O')*TAUD('H2O')+xApp('CO2')*TAUD('CO2')+xApp('AM1')*TAUD('AM
1')+xApp('AM2')*TAUD('AM2'))*Vmold('CO2')/(1.38065E-23
*T_Drop*d_drop*1E-6));
ppeq_Drop_Outlayer('AM1')=xApp('AM1')*EXP(28.786+(-7145.61/T_Drop)+(-
2388.98*LDG_Drop^2/T_Drop)+(1.354*(xApp('AM1')+(3*xApp('AM2')))+(
1.755*xApp('AM2')/(xApp('AM1')+(3*xApp('AM2'))))) *EXP(4*SIGMA(xApp('H2O

```

```

')*TAUD('H2O')+xApp('CO2')*TAUD('CO2')+xApp('AM1')*TAUD('AM1')+xApp('AM
2')*TAUD('AM2')*Vmold('AM1')/(1.38065E-23 *T_Drop*d_drop*1E-6));
ppeq_Drop_Outlayer('AM2')=xApp('AM2')*EXP(26.2+(-7694.32/T_Drop))+(-
3771.54*LDG_Drop/T_Drop)+(-
13.345*(xApp('AM1')+(3*xApp('AM2')))+(0.723*xApp('AM2')/(xApp('AM1')+(
3*xApp('AM2'))))*EXP(4*SIGMA(xApp('H2O')*TAUD('H2O')+xApp('CO2')*TAUD(
'CO2')+xApp('AM1')*TAUD('AM1')+xApp('AM2')*TAUD('AM2'))*Vmold('AM2')/(1
.38065E-23 *T_Drop*d_drop*1E-6));

```

B.3 PROCESS FLOWSHEET

UNIT

```
Flowsheet AS Process_Flowsheet
```

SET

```

# Start Unit Specifications
  WITHIN Flowsheet DO
    WITHIN Aerosol001 DO
      Aspen_Profile := "C:\Users\akinp\Box Sync\Research\Aerosol
Modeling\Solvent Blend\Absorber Profile - Case 1.xls" ;
      Comps := ["N2", "H2O", "CO2", "AM1", "AM2"] ;
      initial_Diameter_Drop := 0.1 ; # 0.1 um
      Layers := 5 ; # 5
      Num_Drop := 1E7 ; # 1E7 #/cm3
      vfrac := 0.98 ; # 0.98 m3/m3

      ##Case 1
      Column_Stages := 46;
      D_col := 3.42900; #m
      H_col := 13.716; #m

      ##Case 2
      #Column_Stages := 47;
      #D_col := 3.40553; #m
      #H_col := 13.716; #m

    END # WITHIN Aerosol001
  END # WITHIN Flowsheet
# End Unit Specifications

```

INITIALISATION_PROCEDURE

```

# Start Default Initialisation Procedure
  USE
    : DEFAULT;
  END
  SAVE "Process_Flowsheet_InitialGuess";
# End Default Initialisation Procedure

```

SOLUTIONPARAMETERS

```
ReportingInterval := 1.0E-2
```

```
        DASolver := "DASOLV" [
                                "AbsoluteTolerance" := 1.0E-3
        ]
SCHEDULE
  SEQUENCE
    CONTINUE FOR 1
    SAVE "Initial"
    MESSAGE "DONE!!!"
  END
```

References

- Akinpelumi, K., Saha, C., & Rochelle, G. T. (2019). Piperazine aerosol mitigation for post-combustion carbon capture. *International Journal of Greenhouse Gas Control*, *91*, 102845. <https://doi.org/10.1016/j.ijggc.2019.102845>
- Anderlohr, C., Brachert, L., Mertens, J., & Schaber, K. (2015). Collection and Generation of Sulfuric Acid Aerosols in a Wet Electrostatic Precipitator. *Aerosol Science and Technology*, *49*(3), 144–151. <https://doi.org/10.1080/02786826.2015.1008624>
- Bade, O. M., Woodhouse, S., Gorset, O., & Andersson, V. (2015). *Method for mist control* (United States Patent No. US9180404B2). <https://patents.google.com/patent/US9180404B2/en>
- Beaudry, M., Akinpelumi, K., & Rochelle, G. (2019). *Impacts of Aerosol Nuclei on Amine-Scrubbing CO₂ Capture Process Emissions* (SSRN Scholarly Paper ID 3365816). Social Science Research Network. <https://papers.ssrn.com/abstract=3365816>
- Beaudry, M. R. (2018). *Aerosol measurement and mitigation in CO₂ capture by amine scrubbing* [The University of Texas at Austin]. <https://repositories.lib.utexas.edu/handle/2152/67989>
- Bottoms, R. R. (1930). *Separating acid gases* (Patent No. 1783901).
- Brachert, L., Kochenburger, T., & Schaber, K. (2013). Facing the Sulfuric Acid Aerosol Problem in Flue Gas Cleaning: Pilot Plant Experiments and Simulation. *Aerosol Science and Technology*, *47*(10), 1083–1091. <https://doi.org/10.1080/02786826.2013.824549>
- DIPPR. (1998). *Thermophysical Properties in the DIPPR 801 Database*. /dippr/events-products/801-database/thermophysical-properties
- Frailie, P. T. (2014). *Modeling of carbon dioxide absorption/stripping by aqueous methyldiethanolamine/piperazine* [The University of Texas at Austin]. <https://repositories.lib.utexas.edu/handle/2152/25019>
- Fulk, S. M. (2016). *Measuring and modeling aerosols in carbon dioxide capture by aqueous amines* [The University of Texas at Austin]. <https://repositories.lib.utexas.edu/handle/2152/41723>
- Fulk, S. M., & Rochelle, G. T. (2014). Quantification of Gas and Aerosol-phase Piperazine Emissions by FTIR Under Variable Bench-scale Absorber Conditions. *Energy Procedia*, *63*, 871–883. <https://doi.org/10.1016/j.egypro.2014.11.097>
- Gao, T., Selinger, J. L., & Rochelle, G. T. (2019). Demonstration of 99% CO₂ removal from coal flue gas by amine scrubbing. *International Journal of Greenhouse Gas Control*, *83*, 236–244. <https://doi.org/10.1016/j.ijggc.2019.02.013>
- Glitsch, K. (2012). Mist Elimination and Phase Separations. Retrieved September, 2021, from <https://koch-glitsch.com/products/mist-elimination/demister-mist-eliminator->

- ts?productcategory=Mist-Elimination&categoryname=DEMISTER-Mist-Eliminators&product=true&level=3
- Guo, H., Li, C., Shi, X., Li, H., & Shen, S. (2019). Nonaqueous amine-based absorbents for energy efficient CO₂ capture. *Applied Energy*, *239*, 725–734. <https://doi.org/10.1016/j.apenergy.2019.02.019>
- Heldebrant, D. J., Koech, P. K., Glezakou, V.-A., Rousseau, R., Malhotra, D., & Cantu, D. C. (2017). Water-Lean Solvents for Post-Combustion CO₂ Capture: Fundamentals, Uncertainties, Opportunities, and Outlook. *Chemical Reviews*, *117*(14), 9594–9624. <https://doi.org/10.1021/acs.chemrev.6b00768>
- IEA. (2021). *Net Zero by 2050—Analysis and key findings. A report by the International Energy Agency*. <https://www.iea.org/reports/net-zero-by-2050>
- Kamijo, T., Kajiya, Y., Endo, T., Nagayasu, H., Tanaka, H., Hirata, T., Yonekawa, T., & Tsujiuchi, T. (2013a). SO₃ Impact on Amine Emission and Emission Reduction Technology. *Energy Procedia*, *37*, 1793–1796. <https://doi.org/10.1016/j.egypro.2013.06.056>
- Kamijo, T., Kajiya, Y., Endo, T., Nagayasu, H., Tanaka, H., Hirata, T., Yonekawa, T., & Tsujiuchi, T. (2013b). SO₃ impact on amine emission and emission reduction technology. *Energy Procedia*, *37*, 1793–1796.
- Kang, J.-L., Liu, K.-T., Wong, D. S.-H., Jang, S.-S., & Tsai, D.-H. (2020). Multi-Scale Modeling and Study of Aerosol Growth in an Amine-based CO₂ Capture Absorber. *Environments*, *7*(8), 58. <https://doi.org/10.3390/environments7080058>
- Kang, J.-L., Zhang, Y., Fulk, S., & Rochelle, G. T. (2017). Modeling Amine Aerosol Growth in the Absorber and Water Wash. *Energy Procedia*, *114*, 959–976. <https://doi.org/10.1016/j.egypro.2017.03.1241>
- Khakharia, P. (2015). *Aerosol-based emission, solvent degradation, and corrosion in post combustion CO₂ capture*.
- Khakharia, P., Brachert, L., Mertens, J., Anderlohr, C., Huizinga, A., Fernandez, E. S., Schallert, B., Schaber, K., Vlught, T. J. H., & Goetheer, E. (2015). Understanding aerosol based emissions in a Post Combustion CO₂ Capture process: Parameter testing and mechanisms. *International Journal of Greenhouse Gas Control*, *34*, 63–74. <https://doi.org/10.1016/j.ijggc.2015.01.001>
- Khakharia, P., Brachert, L., Mertens, J., Huizinga, A., Schallert, B., Schaber, K., Vlught, T. J. H., & Goetheer, E. (2013). Investigation of aerosol based emission of MEA due to sulphuric acid aerosol and soot in a Post Combustion CO₂ Capture process. *International Journal of Greenhouse Gas Control*, *19*, 138–144. <https://doi.org/10.1016/j.ijggc.2013.08.014>
- Khakharia, P., Mertens, J., Abu-Zahra, M. R. M., Vlught, T. J. H., & Goetheer, E. L. V. (2016). Overview of aerosols in post-combustion CO₂ capture. In *Absorption-*

- Based Post-combustion Capture of Carbon Dioxide* (pp. 465–485). Elsevier.
<https://doi.org/10.1016/B978-0-08-100514-9.00019-6>
- Lail, M., Tanthana, J., & Coleman, L. (2014). Non-Aqueous Solvent (NAS) CO₂ Capture Process. *Energy Procedia*, 63, 580–594.
<https://doi.org/10.1016/j.egypro.2014.11.063>
- Majeed, H., Knuutila, H., Hillestad, M., & Svendsen, H. F. (2017a). Gas phase amine depletion created by aerosol formation and growth. *International Journal of Greenhouse Gas Control*, 64, 212–222. <https://doi.org/10.1016/j.ijggc.2017.07.001>
- Majeed, H., Knuutila, H. K., Hillestad, M., & Svendsen, H. F. (2017b). Characterization and modelling of aerosol droplet in absorption columns. *International Journal of Greenhouse Gas Control*, 58, 114–126. <https://doi.org/10.1016/j.ijggc.2017.01.006>
- Mertens, J., Brachert, L., Desagher, D., Schallert, B., Khakharia, P., & Goetheer, E. (2014). Predicting Amine Mist Formation Based on Aerosol Number Concentration and Size Measurements in Flue Gas. *Energy Procedia*, 63, 893–901.
<https://doi.org/10.1016/j.egypro.2014.11.099>
- Mertens, J., Brachert, L., Desagher, D., Thielens, M. L., Khakharia, P., Goetheer, E., & Schaber, K. (2014). ELPI+ measurements of aerosol growth in an amine absorption column. *International Journal of Greenhouse Gas Control*, 23, 44–50.
<https://doi.org/10.1016/j.ijggc.2014.02.002>
- Mertens, J., Lepaumier, H., Desagher, D., & Thielens, M.-L. (2013). Understanding ethanolamine (MEA) and ammonia emissions from amine based post combustion carbon capture: Lessons learned from field tests. *International Journal of Greenhouse Gas Control*, 13, 72–77. <https://doi.org/10.1016/j.ijggc.2012.12.013>
- Moser, P., Schmidt, S., Stahl, K., Vorberg, G., Lozano, G. A., Stoffregen, T., & Rösler, F. (2014). Demonstrating Emission Reduction – Results from the Post-combustion Capture Pilot Plant at Niederaussem. *Energy Procedia*, 63, 902–910.
<https://doi.org/10.1016/j.egypro.2014.11.100>
- PSE: Products—GPROMS ProcessBuilder—Advanced Process Simulation*. (n.d.). Retrieved April 4, 2020, from <https://www.psenterprise.com/products/gproms/processbuilder>
- Rochelle, G., Akinpelumi, K., Gao, T., Liu, C.-T., Suresh Babu, A., & Wu, Y. (2021). *Pilot Plant Results With the Piperazine Advanced Stripper at NGCC Conditions* (SSRN Scholarly Paper ID 3819261). Social Science Research Network. <https://papers.ssrn.com/abstract=3819261>
- Rochelle, G., Chen, E., Freeman, S., Van Wagener, D., Xu, Q., & Voice, A. (2011). Aqueous piperazine as the new standard for CO₂ capture technology. *Chemical Engineering Journal*, 171(3), 725–733. <https://doi.org/10.1016/j.cej.2011.02.011>

- Rochelle, G. T. (2009). Amine scrubbing for CO₂ capture. *Science*, 325(5948), 1652–1654.
- Rochelle, G. T., Wu, Y., Chen, E., Akinpelumi, K., Fischer, K. B., Gao, T., Liu, C.-T., & Selinger, J. L. (2019). Pilot plant demonstration of piperazine with the advanced flash stripper. *International Journal of Greenhouse Gas Control*, 84, 72–81. <https://doi.org/10.1016/j.ijggc.2019.03.014>
- Saha, C., & Anthony, J. H. (2018). Real-Time Aerosol Measurements in Post-Combustion CO₂ Capture Using ELPI⁺™ and Smooth and Sintered Collection Plates. *Journal of Energy Resources Technology*, 140(6), 062001. <https://doi.org/10.1115/1.4038782>
- Saha, C., & Irvin, J. H. (2017). Real-time aerosol measurements in pilot scale coal fired post-combustion CO₂ capture. *Journal of Aerosol Science*, 104, 43–57. <https://doi.org/10.1016/j.jaerosci.2016.11.005>
- Sardja, I., & Dhali, S. K. (1990). Plasma oxidation of SO₂. *Applied Physics Letters*, 56(1), 21–23. <https://doi.org/10.1063/1.102651>
- Saveliev, A. B., Pietsch, G. J., Murtazin, A. R., & Fried, A. (2007). SO₂ removal from air with dielectric barrier discharges. *Plasma Sources Science and Technology*, 16(3), 454–469. <https://doi.org/10.1088/0963-0252/16/3/005>
- Shao, R., & Stangeland, A. (2009). Amines Used in CO₂ Capture. *Oslo, Norway: The Bellona Foundation Technical Report*.
- Song, D. (2017). *Effect of Liquid Viscosity on Liquid Film Mass Transfer for Packings*.
- Srivastava, R. K., Miller, C. A., Erickson, C., & Jambhekar, R. (2004). Emissions of Sulfur Trioxide from Coal-Fired Power Plants. *Journal of the Air & Waste Management Association*, 54(6), 750–762. <https://doi.org/10.1080/10473289.2004.10470943>
- Thompson, J. G., Combs, M., Abad, K., Bhatnagar, S., Pelgen, J., Beaudry, M., Rochelle, G., Hume, S., Link, D., Figueroa, J., Nikolic, H., & Liu, K. (2017). Pilot testing of a heat integrated 0.7 MWe CO₂ capture system with two-stage air-stripping: Emission. *International Journal of Greenhouse Gas Control*, 64, 267–275. <https://doi.org/10.1016/j.ijggc.2017.08.003>
- U.S. Energy Information Administration (EIA). (2019). *U.S. Energy-Related Carbon Dioxide Emissions, 2018*. <https://www.eia.gov/environment/emissions/carbon/archive/2018/>
- Xu, Q. (2011). *Thermodynamics of CO₂ loaded aqueous amines* [Thesis]. <https://tdl-ir.tdl.org/handle/2152/ETD-UT-2011-12-4819>
- Yuan, Y., & Rochelle, G. T. (2018). CO₂ absorption rate in semi-aqueous monoethanolamine. *Chemical Engineering Science*, 182, 56–66. <https://doi.org/10.1016/j.ces.2018.02.026>

- Zhang, Y. (2018). *Absorber and aerosol modeling in amine scrubbing for carbon capture* [The University of Texas at Austin].
<https://repositories.lib.utexas.edu/handle/2152/71424>
- Zhang, Y., Kang, J.-L., Fulk, S., & Rochelle, G. (2017). Modeling Amine Aerosol Growth at Realistic Pilot Plant Conditions. *Energy Procedia*, 114, 1045–1060.
<https://doi.org/10.1016/j.egypro.2017.03.1251>
- Zhou, S. J., Tanthana, J., Mobley, P., Rayer, A. V., Gupta, V., Soukri, M., Lail, M., Tobiesen, A., Mejdell, T., Aronu, U. E., Grimstvedt, A., Hjarbo, K., & Hovdahl, L. (2018). *Pilot Testing of a Non-Aqueous Solvent (NAS) CO₂ Capture Process*. 10.

Vita

Korede Fiyinfoluwa Akinpelumi was born in Lagos, Nigeria, in January 1994. He graduated as valedictorian from both the International School, Lagos, in 2009 and the University of Lagos, Nigeria, in 2014. At the University of Lagos, he studied Chemical Engineering, interned with Chevron, and briefly worked as a graduate assistant upon graduation. He began his graduate studies in Chemical Engineering under the supervision of Dr. Gary Rochelle at the University of Texas at Austin in 2016. During his time at UT Austin, he worked on-site at the National Carbon Capture Center for several months in 2018 and 2019 and had internships with Equinor and ExxonMobil in the summers of 2019 and 2020, respectively. He was a member of the departmental safety board and departmental intramural soccer team. Outside the department, he served as vice president of the Longhorn Energy Club (LEC) and was on the advisory committee of the Texas Advanced Degree 2 Consulting (AD2C) Club. Upon graduation, he will be joining the Boston Consulting Group (BCG) as a consultant in Houston.

Permanent email: kakinpelumi@utexas.edu

This dissertation was typed by the author.